X-ray Spectroscopy of Neutron Star Low-Mass X-ray Binaries

by

Miriam Ilana Krauss

B.A. Astronomy
Columbia University (1999)

Submitted to the Department of Physics
in partial fulfillment of the requirements for the degree of

Doctor of Philosophy

at the

MASSACHUSETTS INSTITUTE OF TECHNOLOGY

September 2007

© Miriam Ilana Krauss, MMVII. All rights reserved.

The author hereby grants to MIT permission to reproduce and distribute publicly
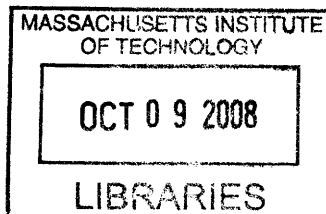paper and electronic copies of this thesis document in whole or in part.

Author . .   ⋯⋯⋯⋯⋯⋯⋯
Department of Physics
August 10, 2007

Certified by. . .   ⋯⋯⋯⋯⋯⋯
Deepto Chakrabarty
Associate Professor of Physics
Thesis Supervisor

Accepted by . . . .
/ Thomas Greytak
Professor of Physics
Interim Department Head

X-ray Spectroscopy of Neutron Star Low-Mass X-ray Binaries

by
Miriam Ilana Krauss

Submitted to the Department of Physics
on August 10, 2007, in partial fulfillment of the
requirements for the degree of
Doctor of Philosophy

Abstract

In this thesis, I present work spanning a variety of topics relating to neutron star low-mass X-ray binaries (LMXBs) and utilize spectral information from X-ray observations to further our understanding of these sources. First, I give an overview of important X-ray astrophysics relevant to the work I present in subsequent chapters, as well as information about the X-ray observatories from which I obtained my data. In the next three chapters, I consider spectra—both high- and low-resolution—of accretion-powered millisecond X-ray pulsars, a unique and relatively new class of objects. In addition to analysis of the pulsar XTE J1814−338, I compare a broader sample of pulsars with a sample of atoll sources in order to better understand why the latter class do not contain persistently pulsating neutron stars. In particular, I test the hypothesis that pulsations in the atoll sources are suppressed by a high–optical-depth scattering region. Using X-ray color-color diagrams to define a selection criterion based on spectral state, I analyze *Rossi X-ray Timing Explorer* (*RXTE*) spectra from all the sources, and use a Comptonization model to obtain measurements of their optical depths.

I then discuss efforts to spatially resolve X-ray jets from the accretion-powered millisecond pulsar SAX J1808.4−3658 and the Z source XTE J1701−462. Each was observed by the *Chandra X-ray Observatory* to produce a high–spatial-resolution image. This work was motivated in part by my analysis of XTE J1814−338, which found an apparent excess of infrared flux which could be attributed to jet emission.

Next, I discuss the measured temperatures of thermonuclear X-ray bursts. The detection of line features in these bursts, and hence from the surfaces of neutron stars, has been an important goal for high-resolution X-ray spectroscopy. A measurement of the wavelengths of identified line features would yield a measurement of the neutron star's gravitational redshift, which would help constrain current models for the neutron star equation of state. Although such a measurement has been made for one source, other searches have not been able to repeat this measurement. I consider the effects of burst temperature on the formation of discrete spectral features, using a large sample of bursts observed by the *RXTE* PCA.

Finally, I present analysis of high-resolution *Chandra* HETG spectra of a sample of Galactic LMXBs. High-resolution spectra are able to resolve line features, such as the prominent Ne and O emission lines in the ultracompact X-ray binary 4U 1626−67. They also allow for more precise measurements of photoelectric absorption edges, which can otherwise hinder the determination of continuum spectral components, particularly in the lower-energy spectral regions.

Thesis Supervisor: Deepto Chakrabarty
Title: Associate Professor of Physics

Acknowledgments

Contents

List of Figures

List of Tables

Chapter 1

Introduction

The end product of most branches of stellar evolution, when nuclear burning ceases to be a viable means of support, is the birth of a compact stellar remnant. Therefore, any galaxy that has been forming stars for longer than the lifetime of its most massive stellar types is populated with these objects. They are often referred to as *compact objects*, a class which includes white dwarfs, neutron stars and black holes. The white dwarfs and neutron stars are supported by, respectively, electron degeneracy pressure and the repulsive nuclear force between the neutrons arising from the Pauli exclusion principle. The black holes are not supported (as far as anyone knows) by anything at all, and collapse to form a singularity.

Left alone, compact objects will radiate away their birth energy and end up as cold and largely invisible relics. However, if they are able to accrete material, they can begin new lives as active emitters. There are a few different means by which compact objects can accrete material, the most common being a companion star. If the compact object is in a binary system, and its companion is losing mass either via a stellar wind or Roche lobe overflow, some fraction of the mass will accrete onto the compact object. As this occurs, the material will radiate a large amount of gravitational potential energy; the energetic processes through which this takes place will result in copious quantities of high-energy radiation, and the system will appear as an X-ray source.

The first cosmic X-rays were discovered in 1962, and the young field of X-ray astronomy developed very rapidly. In the last 45 years, the level of sophistication of X-ray detectors and observatories has increased enormously. At first, observations were limited to rocket or balloon experiments which scanned the sky for bright sources, and these observations only lasted for minutes to hours. Now, orbiting observatories such as the *Chandra X-ray Observatory*, *Rossi X-ray Timing Explorer* (*RXTE*), and *XMM-Newton* are operational for many years, and are able to provide X-ray data that have arcsecond spatial resolution and microsecond timing resolution. In this thesis, we present analyses of a large sample of Galactic low-mass X-ray binaries (LMXBs) using data from these highly sophisticated observatories. First, this chapter reviews the astrophysics of LMXB systems, the physics of their X-ray emission, and the basic characteristics of the X-ray observatories from which our data were acquired. All formulae are in c.g.s. units unless otherwise indicated.

1.1 Relevant X-ray astrophysics

1.1.1 Types of Galactic low-mass X-ray binaries

Broadly defined, an LMXB comprises a compact object, either a neutron star or black hole, and a low-mass ($\lesssim 1\ M_\odot$) stellar companion from which it is accreting material. We review the physics of mass transfer in these systems and their X-ray emission mechanisms in § 1.1.2 and § 1.1.3.

In this thesis, we consider only systems with neutron star primaries. Most neutron star LMXBs can be classified as either *atoll* or *Z* sources. This classification is based on their X-ray timing behavior and their appearance on an X-ray *color-color diagram*. A color-color diagram is constructed by grouping source counts into broad spectral bands and taking their ratios, resulting in *hard* (higher-energy) and *soft* (lower-energy) colors. These values are plotted against each other, and the resulting diagrams show that sources generally trace out distinct patterns over time. The timescale over which the source colors change, the shape of the pattern, and the fast timing behavior at a given color location all help classify a system as being either an atoll or Z source (see, e.g., Schulz et al. 1989; Hasinger and van der Klis 1989). We show color-color diagrams of a representative system from each class in Figure 1-1.

Although there may be other distinctions as well, it appears that the main difference between atoll and Z sources is their accretion rate. Z sources have, overall, higher X-ray luminosities than atoll sources, and all (save perhaps one, the recently discovered XTE J1701$-$462—see Chapter 5) are persistent systems, whereas many atolls are transients. This suggests that systems with higher rates of mass transfer have fundamentally different geometries and/or emission mechanisms, leading to the observed distinctions in their timing and color behavior.

Once the binary orbital period $P_{\mathrm{orb}} \lesssim 3$ hr, orbital decay (and thus mass transfer) is driven by gravitational radiation. For a system with a hydrogen-rich companion, there is a minimum period to which its orbit can decay of ≈ 80 min (see the discussion in § 1.1.2). Systems with shorter orbital periods necessarily have companions rich in elements heavier than hydrogen: the fraction of their mass comprised of hydrogen $X \lesssim 0.5$. Often, these are white dwarfs which may be enriched in helium, oxygen, and neon. One such system is the 42-min binary 4U 1626$-$67, pictured in Figure 1-2, which shows the likely Ne- and O-rich white dwarf, the accretion stream and disk, the truncated inner disk edge (indicating the location of the magnetospheric radius), and the bright neutron star. 4U 1626$-$67 is discussed in more detail in Chapter 7.

As a neutron star accretes material from its companion, it also gains angular momentum, causing its spin frequency to increase. Although this scenario was suggested shortly after the discovery of the first pulsar in a binary system (Hulse and Taylor 1975), it was not until the discovery of persistent pulsations from SAX J1808.4$-$3658 that a millisecond pulsar was found in an actively accreting system (Wijnands and van der Klis 1998). Since then, seven more accretion-powered millisecond pulsars (AMPs) have been discovered. Furthermore, burst oscillations in SAX J1808.4$-$3658 have been found to occur at the same frequency as the persistent pulsations, showing that this phenomenon traces the spin of the neutron star. Therefore, we know the neutron star spin frequency of all the burst oscillation sources as well. Analysis of the spin distribution of this larger sample leads to the discovery of an apparent "speed limit", likely enforced by the emission of gravitational radiation (Chakrabarty et al. 2003).
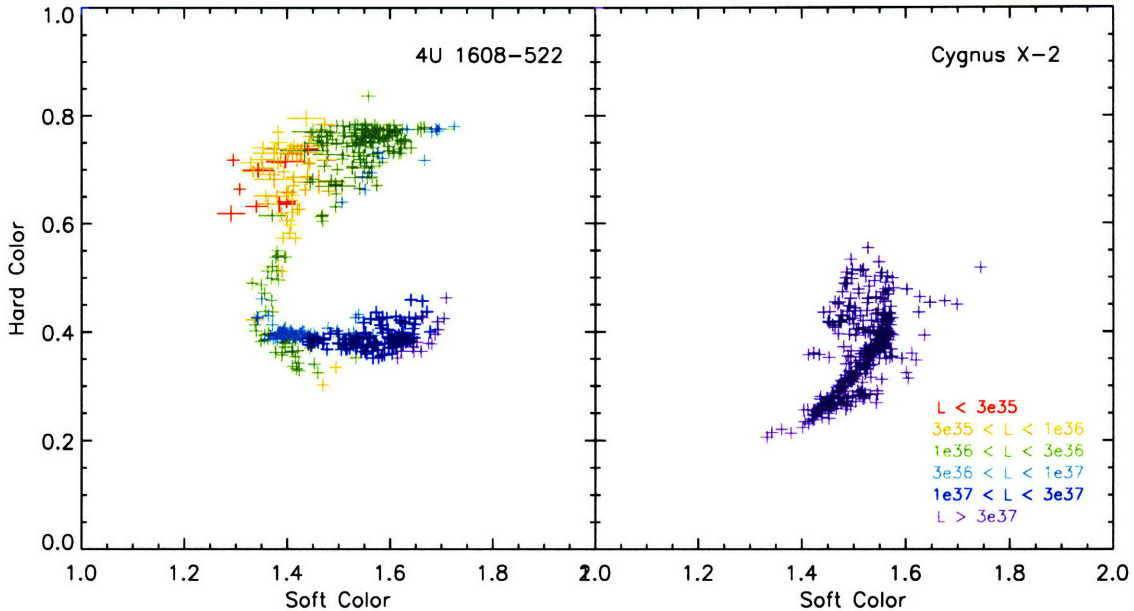
Figure 1-1: Color-color diagrams of the atoll source 4U 1608−522 and the Z source Cygnus X-2. Note that the color bands we have defined for the *RXTE* data has resulted in an atoll diagram which has a relatively Z-like shape, whereas the long timescale over which the data from Cyg X-2 were acquired has smeared out what would otherwise be an elongated Z tilted somewhat to the left. Ultimately, the choice of energy cuts as well as the instrumental response function will affect how a given source appears in the X-ray color-color diagram.

1.1.2 Mass transfer in X-ray binaries

Mass transfer in X-ray binaries can occur via two primary mechanisms, wind accretion and Roche lobe overflow. The first takes place in a binary system where the companion (secondary) is losing mass in a stellar wind. If the orbit of the primary takes it through a sufficiently dense portion of the wind, it will accrete enough material to become X-ray bright. Since this form of accretion takes place primarily in high-mass X-ray binaries, which are outside the scope of this thesis, we do not discuss it further. The other mechanism, Roche lobe overflow, is what facilitates accretion in low-mass X-ray binaries. In order to understand this method of accretion, one must first consider the gravitational potential of such a system.

A stellar binary system can be approximated by two point masses in a circular orbit. The latter is a reasonable assumption because the timescale over which the orbital eccentricity becomes zero and the orbit becomes circular is substantially shorter than the timescale over which accretion takes place. The gravitational potential for this configuration is known as the *Roche potential*; see Figure 1-3 for a diagram of the resulting equipotential surfaces in the plane of the binary orbit. These surfaces can be used to determine the behavior of a test particle placed anywhere in the system; for example, the points labeled $L_1 - L_5$ are *Lagrange points* and indicate locations of gravitational equilibria. All the equilibria at these points are unstable, with the exception of L_4 and L_5 if the mass ratio $M_1/M_2 > 24.96$.

If the radius of the secondary reaches the inner Lagrange point (L_1), it is known as
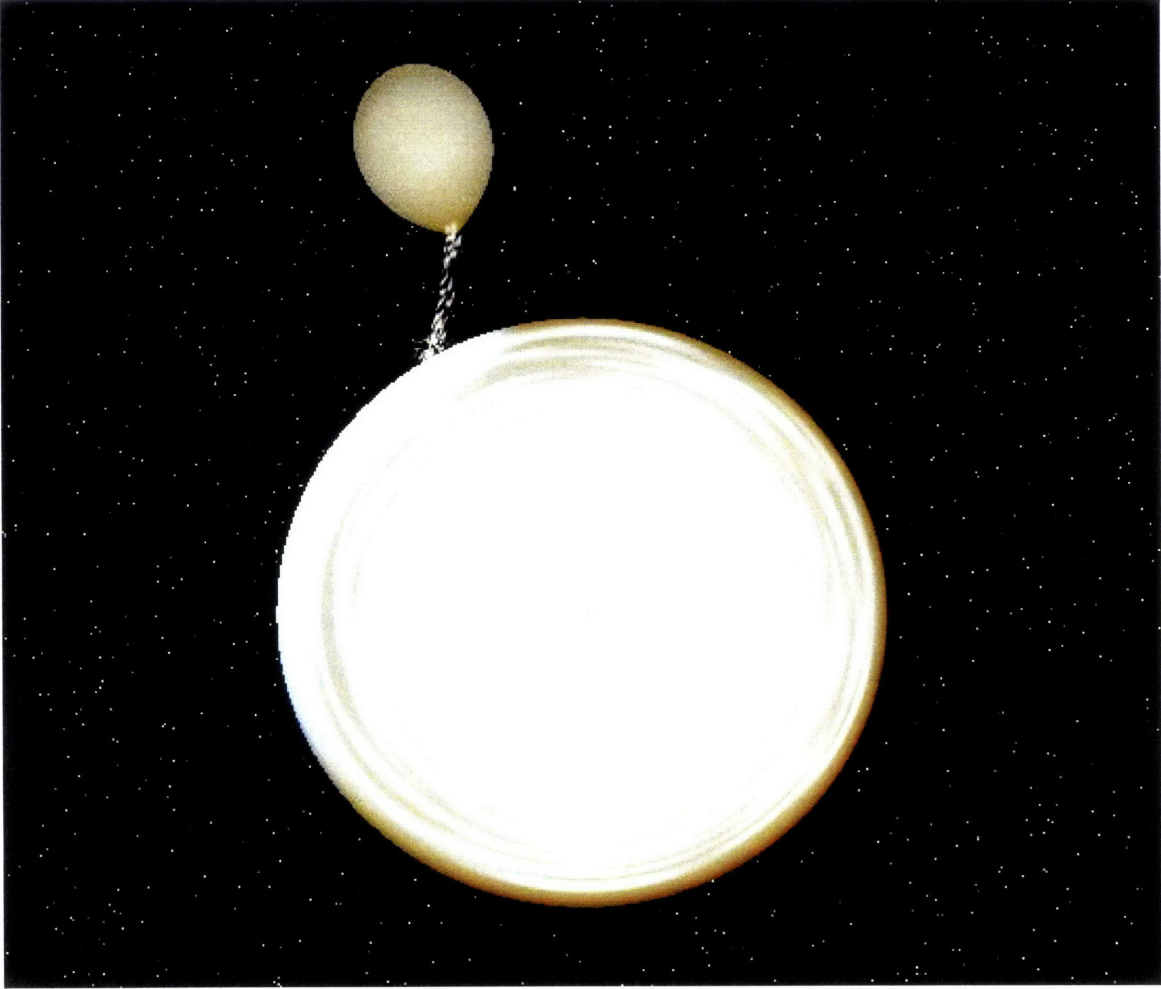
Figure 1-2: Visualization of the ultracompact binary system 4U 1626−67 using the known system parameters. Image produced with the `BinSim` utility (http://www.phys.lsu.edu/~rih/binsim/).

Roche-lobe filling. Under this condition, material from the secondary will spill over and fall under the gravitational influence of the primary, beginning the process of mass transfer. The Roche lobe radius of the secondary can be closely approximated by (Paczyński 1971)

$$\frac{R_2}{a} \cong 0.46224 \left(\frac{M_2}{M_1 + M_2} \right)^{1/3}, \tag{1.1}$$

where a is the relative semi-major axis and (M_1, M_2) are the masses of the primary and secondary. It should also be noted that from Equation 1.1 and Kepler's third law, one can derive the mean density of the secondary as a function only of the orbital period of the system:

$$\bar{\rho} \cong 110 P_{\mathrm{hr}}^{-2} \ \mathrm{g} \ \mathrm{cm}^{-3}. \tag{1.2}$$

This relationship can be very useful for determining possible companion types; see, e.g., the discussion in § 2.4.

18
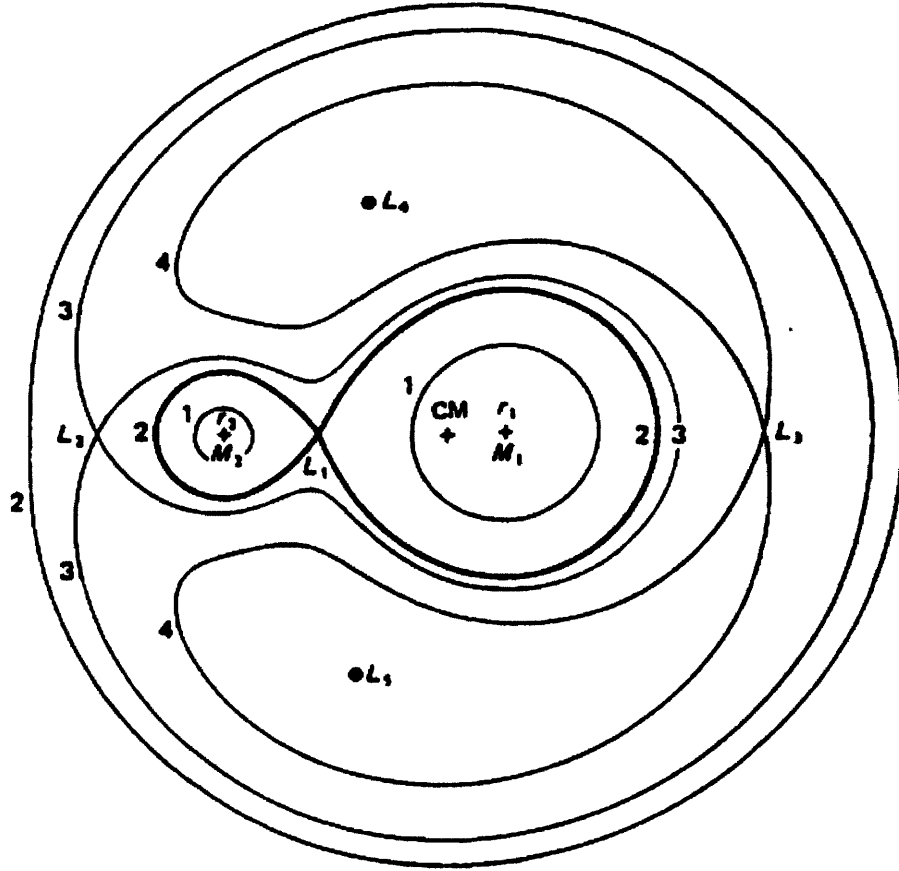
Figure 1-3: Roche equipotential surfaces for a binary system. (Figure from Frank et al. 2002).

Before mass transfer can commence, there must be a physical mechanism which causes the secondary to fill its Roche lobe. Either its radius must increase, which can happen as a result of stellar evolution, or the binary orbit must shrink. The timescale over which the radius of the secondary will increase is very short, commensurate with its nuclear evolution timescale, and is not relevant to the current state of the LMXB sources considered in this thesis. However, orbital decay in LMXB systems will occur over a much longer timescale, and is generally the result of gravitational radiation or rotational/magnetic braking.

All binary systems will produce gravitational radiation, and it is the dominant mechanism driving orbital decay and mass transfer for short-period systems ($P_{orb} \lesssim 3$ hr). The instantaneous period change due to gravitational radiation—neglecting any resulting mass transfer and thus assuming that M_1 and M_2 remain constant—is given by (Paczyński 1967)

$$\dot{P}_{orb} = -3.68 \times 10^{-6} \frac{M_1 M_2}{(M_1 + M_2)^{1/3}} P_{orb}^{-5/3} \text{ s s}^{-1}, \tag{1.3}$$

Where M_1 and M_2 are in units of solar mass and P and $\dot{P}$ are in seconds. Neglecting stellar evolution, the two stars would ultimately merge. However, the secondary is losing mass in the process, and must evolve to reestablish its own thermodynamic equilibrium.

19

This occurs on its Kelvin-Helmholtz time scale, which is a function of the stellar mass and radius. As can be seen from Equation 1.3, the time scale for the mass loss is also dependent on the mass of the secondary and the period of the system; at $P_{orb} \approx 80$ min, these two are comparable, and the secondary becomes adiabatic. Therefore, the mass-radius relation becomes negative, and mass loss causes an increase of the stellar radius and an increase of the orbital period. This results in the 80-min *period minimum* seen in systems with hydrogen-rich donors (Rappaport et al. 1982). However, hydrogen-depleted donors may have $P_{orb} < 80$ min; these are known as the "ultracompact" sources—see § 1.1.1.

For systems with $P_{orb} \gtrsim 3$ hr, a likely mechanism for the shedding of orbital angular momentum is through rotational braking (Rappaport et al. 1983). Here, the secondary expels a stellar wind which, for a small amount of mass loss, carries off a large quantity of angular momentum. Since tidal forces act rapidly to bring the primary and secondary back into a synchronous orbit, the more slowly-rotating secondary will be spun up at the expense of orbital angular momentum and the orbital period will decrease, driving mass transfer.

Mass lost from the secondary will not immediately accrete onto the primary, since it will still posses a significant quantity of angular momentum. As a result, it will form an accretion disk in the plane of the binary orbit. The most basic model for an accretion disk is that of Shakura and Syunyaev (1973). This is also known as the *α-disk model*, since viscosity, the means by which gravitational potential energy is converted to kinetic energy and radiated out of the system, is parametrized by the dimensionless quantity α. Two observationally important characteristics of an α-disk model is that the disk is geometrically thin: its scale height is much less than its radius, and optically thick: it will radiate like a blackbody. The temperature of the disk will depend strongly on the accretion rate, since viscous heating by the dissipation of gravitational potential energy from the inflowing material is the main heating mechanism. In systems where the primary is an X-ray bright neutron star, its radiation will provide an additional heat source for the disk, causing the inner regions to swell as a result of radiation pressure. The resulting temperature will be a function of the disk radius, and the temperature profile can be described by two terms, the first due to viscous heating and the second due to irradiation from the primary (Wang et al. 2001):

$$T^4(r) = \frac{3GM_1\dot{M}}{8\pi\sigma r^3} + \frac{L_{1,X}(1-\eta_d)}{4\pi\sigma r^2}\left(\frac{dH}{dr} - \frac{H}{r}\right),\tag{1.4}$$

where $\dot{M}$ is the mass transfer rate, $L_{1,X}$ is the X-ray luminosity of the neutron star primary, η_d is the albedo of the accretion disk, and H is its scale height. This equation can be useful in determining the spectrum of the disk, which can then be used to constrain other parameters in the observed binary system, such as its inclination angle (see, e.g., Chapter 2). However, it is not clear that most accretion disks emit thermally, so care must be taken when applying this model to astrophysical observations.

The behavior of material in the inner regions of the accretion disk and its flow onto the neutron star surface depends primarily on the strength of the neutron star's magnetic field. If the magnetic field is strong enough at a given disk radius to dominate the accretion flow, the disk will become truncated and the disk material will travel along the magnetic field lines to the neutron star surface. As it approaches the surface, an accretion column will form, although the physics that takes place in this region is not well understood. In systems with weak magnetic fields, the disk could extend all the way to the neutron star surface, forming an X-ray bright *boundary layer* where the two meet (Pringle 1977).

Ultimately, the material will merge with the neutron star, imparting not only its mass

but also the angular momentum it had at the inner edge of the accretion disk. This will cause the neutron star spin to increase, and is the reason why the measured spin frequencies of neutron stars in LMXBs (typically $\approx$ 400 Hz) are substantially faster than the frequencies of isolated radio pulsars (typically $\approx$ 1 Hz). Accretion also seems to result in a weaker neutron star magnetic field, though exactly how this happens—whether it is a result of field decay, suppression, or some combination of the two—is a matter of debate (see Bhattacharya and Srinivasan 1995 for a review). The combination of mass transfer and a diminished magnetic field will lead to a rapidly rotating neutron star, and the cessation of mass transfer will result in the birth of a millisecond radio pulsar.

If material is deposited onto the surface of the neutron star at a sufficiently high rate, it will undergo stable nuclear burning. This critical rate is determined by the composition of the material; in particular, the mass fraction of carbon, nitrogen, and oxygen (Z_{CNO}):

$$\dot{M}_{crit} = 900 \left(\frac{Z_{CNO}}{0.01} \right)^{1/2} \text{ g cm}^{-2} \text{ s}^{-1}. \tag{1.5}$$

Below this rate, accreted material will build up on the surface of the neutron star until it reaches sufficiently high temperature and density to undergo nuclear burning, and a thermonuclear runaway will ensue (see Strohmayer and Bildsten 2006 for a review). This event is observed as a thermonuclear, or *type-I*, X-ray burst, and usually has a duration on the order of tens of seconds, with a fast rise and exponential decay. Since the burning commences over a finite area of the neutron star surface, the emission is sometimes modulated at the spin frequency of the neutron star, a phenomenon known as a *burst oscillation*.

Thermonuclear burst spectra are well-described by a blackbody, and a spectral fit to the emission at any given time can measure the neutron star's surface temperature as well as its radius given its distance.[1] Interestingly, some bursts show a pronounced increase in radius and decrease in temperature as the flux peaks. This occurs when the burst luminosity at the surface of the neutron star exceeds the Eddington limit: the outward force due to the burst radiation is greater than the gravitational attraction of the neutron star. Assuming spherical geometry, the Eddington luminosity is given by

$$L_{Edd} = \frac{4\pi GM m_p c}{\sigma_T} \cong 1.3 \times 10^{38} (M/M_\odot) \text{ erg s}^{-1} \tag{1.6}$$

where m_p is the mass of a proton and σ_T is the Thomson cross-section (see, e.g., Frank et al. 2002). Note that the Eddington limit is relevant to a wide array of astrophysical processes where high luminosities are concerned. In the case of thermonuclear X-ray bursts, the violation of this limit causes the burning layer of the neutron star to expand, resulting in the observed increase in radius and decrease in temperature. Bursts in which show this behavior are known as *radius-expansion* bursts, and the association of their peak luminosity with the Eddington luminosity can provide an important measure of the distance to the neutron star (see, e.g., Basinska et al. 1984).

We show the lightcurves, power spectra, and blackbody fits of two thermonuclear X-ray bursts observed by the *RXTE* PCA in Figure 1-4. Both bursts contain burst oscillations, and the burst from 4U 1608−52 also shows evidence of radius expansion. In can be seen

---

[1]Note, however, there are large uncertainties associated with this measurement: first, it is based on the *color temperature* of the blackbody, which will generally be higher than the actual *effective* temperature (see Section 1.1.4), although the amount by which it differs in not well known. Furthermore, the distances to most thermonuclear burst sources are known, at best, to $\approx$ 30%.
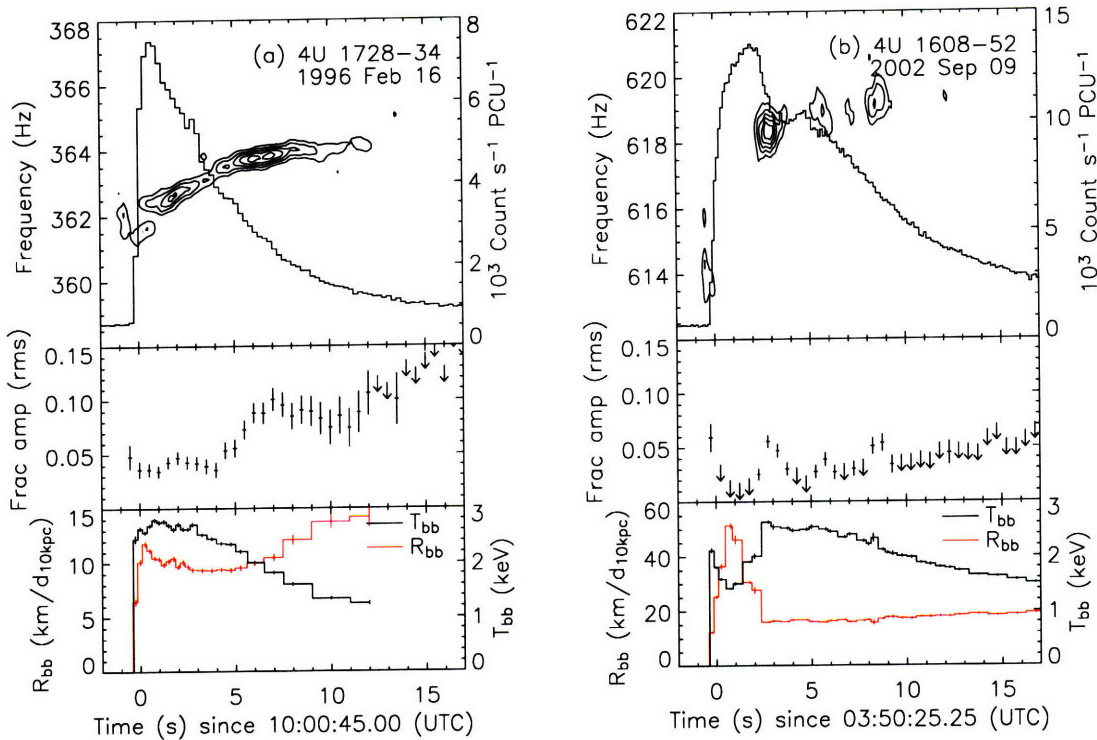
Figure 1-4: Lightcurves, dynamic power spectra, and blackbody fits of two thermonuclear (type-I) X-ray bursts. For (a), the power spectra were determined using overlapping 2 s intervals separated by 0.25 s; for (b), 1 s intervals separated by 0.125 s were used. The plotted contours are unit-norm powers in multiples of 8, and the fractional amplitudes are relative to the count rate above the persistent emission level. Figure courtesy J. Hartman.

that the emission timescale for both bursts is ≈ 10 s, a fairly typical value.

1.1.3 Astrophysical X-ray emission mechanisms

X-rays fall between ultraviolet light and γ-rays in the electromagnetic spectrum, with wavelengths in the range 0.1–100 Å (corresponding to energies of $\approx$ 0.1–120 keV). Earth's upper atmosphere is opaque to X-rays, which precludes any study of astrophysical sources from ground-based experiments. As a result, none (aside from the Sun) were known until 1962, when a team led by Riccardo Giacconi launched an X-ray detector on a sounding rocket to look for reflected Solar X-ray emission from the Moon. This led to the unexpected discovery of the first extrasolar X-ray source, the LMXB system Sco X-1.

There are several mechanisms by which astrophysical sources can generate and modify X-ray emission, and any given system may radiate as a result of more than one process. These include blackbody radiation, bremsstrahlung, inverse Compton scattering, synchrotron emission, and radiative atomic transitions. We describe each of these processes below.
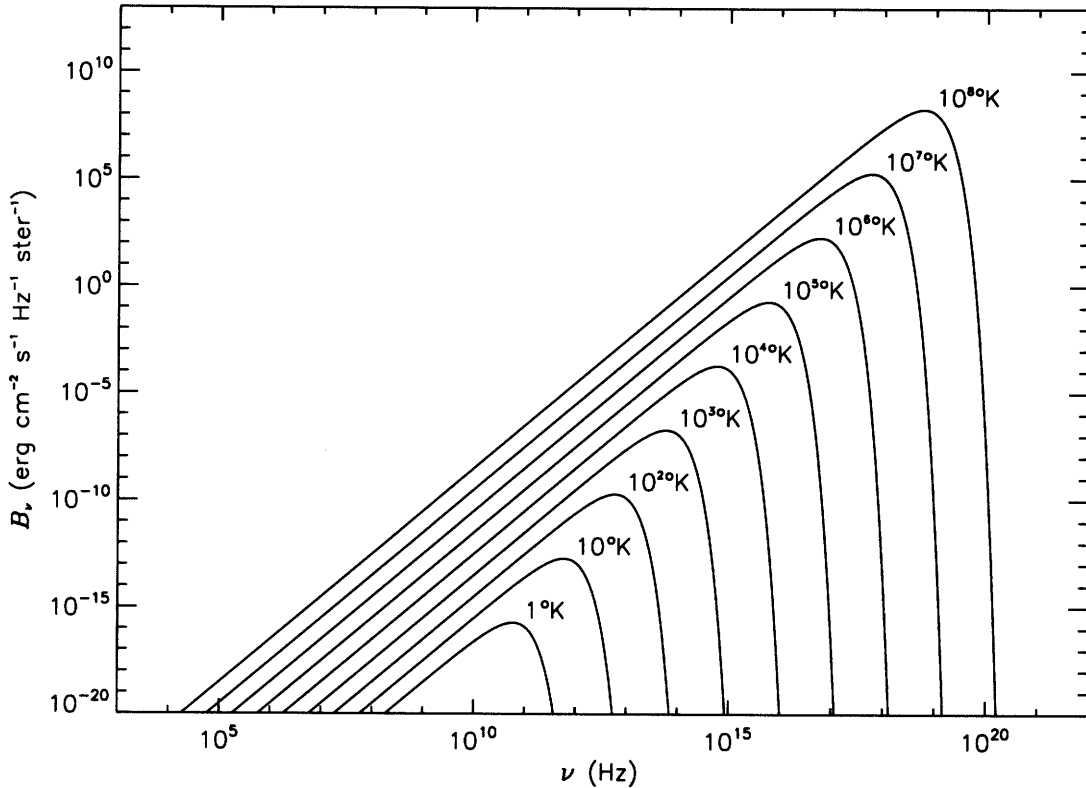
Figure 1-5: Blackbody spectra for emitters of varying temperatures. Adapted from Kraus (1966).

1.1.4 Blackbody radiation

Blackbody emission is produced by material whose radiation is in thermal equilibrium. This emission is independent of the material from which the blackbody itself is composed, depending only its temperature and emitting area. The spectrum is described by

$$B_\nu(T) = \frac{2h\nu^3/c^2}{e^{\frac{h\nu}{kT}} - 1} \text{ erg cm}^{-2} \text{ s}^{-1} \text{ Hz}^{-1} \text{ ster}^{-1} \tag{1.7}$$

where h is the Planck constant, k is the Boltzmann constant, and c is the speed of light.

Blackbody spectra have several important properties (see Figure 1-5). The low-frequency regime (i.e., radio frequencies when astrophysical sources are considered) is known as the *Rayleigh-Jeans tail*, and can be approximated by $B_\nu \propto \nu^2$. The high-frequency regime can only be understood via a quantum mechanical description, and results in an exponential cutoff of the spectrum. For a given blackbody temperature, the peak of the curve is given by the *Wien displacement law*,

$$h\nu_{\text{max}} = 2.82 \ kT. \tag{1.8}$$

As can be seen in Figure 1-5, a blackbody of fixed area but greater temperature has both a higher peak frequency as well as a greater brightness at any given frequency.

Although many astrophysical processes can be closely approximated with a blackbody

23

description, most astrophysical blackbodies are less than ideal, causing the measured *color temperature* to differ from the effective temperature. For example, emission arising from the surface of a neutron star may be subject to subsequent Compton scattering as well as bremsstrahlung and bound-free interactions, resulting in an overall spectral hardening. Therefore, correction factors must be applied in order to derived physical quantities from spectral fits. In addition to emission from the surface of neutron stars, important astrophysical sources of X-ray blackbody emission include optically thick accretion disks and thermonuclear X-ray bursts.

1.1.5 Bremsstrahlung

Literally "braking radiation" in German, bremsstrahlung occurs when an electron passes near an ion and experiences an acceleration. Since an accelerating charge radiates electromagnetically, radiation will be emitted whose properties will depend on the speed of the electron, its impact parameter (the distance of closest approach to the ion), and the charge of the ion with which it interacts. By extension, a collection of such electrons and ions will have a spectrum that is characteristic of its ensemble properties. For astrophysical sources, the most relevant example is the spectrum which arises from a thermal distribution of electrons. This results in an emissivity of

$$\varepsilon_\nu = 6.8 \times 10^{-38} Z^2 n_e n_i T^{-1/2} e^{-h\nu/kT} \bar{g}_{ff} \text{ erg cm}^{-3} \text{ s}^{-1} \text{ Hz}^{-1} \tag{1.9}$$

where Z is the atomic number of the ion; n_e and n_i are, respectively, the number densities of electrons and ions; and $\bar{g}_{ff}$ is the velocity averaged Gaunt factor, which to first order can usually be set equal to one (Rybicki and Lightman 1979). Figure 1-6 shows representative bremsstrahlung spectra for several different values of temperature and electron density. The curves are generally flat, with an abrupt cutoff that is strongly dependent on the temperature of the electron distribution. The electron density controls the overall normalization of the spectrum.

Astrophysical bremsstrahlung often arises from hot, optically thin plasmas, and is a main source of cooling for hot gas sinking in the potential well of galaxy clusters. Along with radiation from inverse Compton scattering, bremsstrahlung also plays an important role in the cooling of neutron star accretion columns when the accretion rate is "subcritical" (i.e., less than the local Eddington rate; see, e.g., Frank et al. 2002).

1.1.6 Inverse Compton scattering

Compton scattering occurs when a photon scatters off an electron, resulting in an increase in the momentum of the electron and a decrease in the energy of the photon. If the electron has enough kinetic energy, the opposite will occur, and the photon will gain energy from the interaction; this is known as inverse Compton scattering. (Note that in this thesis, the result of inverse Compton scattering is often simply referred to as *Comptonization*.) Inverse Compton scattering can play an important role in the generation of high-energy photons when a seed photon field traverses a region of energetic electrons. Any given photon may scatter multiple times; the number and strength of these interactions will determine the change in the photon's energy. The amount that the energy changes is described by the Compton y parameter:

$$y = \overline{\Delta\varepsilon} \times \overline{N}, \tag{1.10}$$
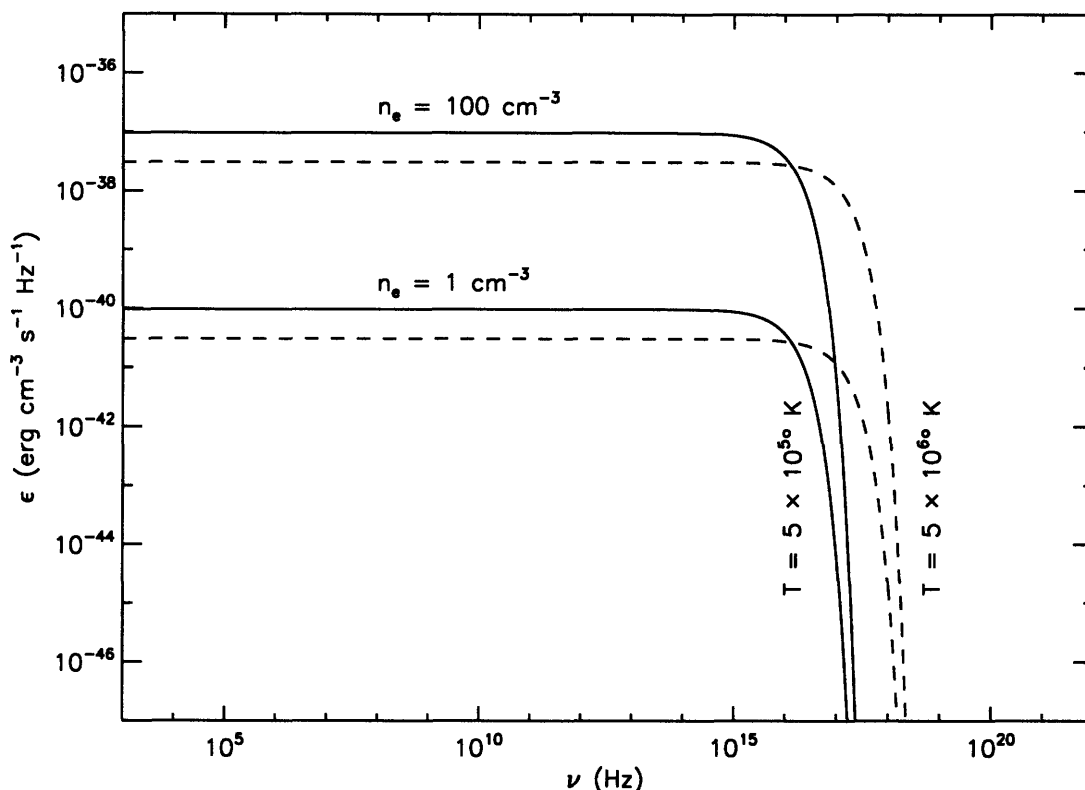
Figure 1-6: Bremsstrahlung curves for emitters of varying temperature and electron density. The upper (lower) curves are for an emitter of density $n_e = 100$ (1) cm^{-3}, and the solid (dashed) curves are for $T = 5 \times 10^5$ (5×10^6)° K.

where $\overline{\Delta\varepsilon}$ is the average fractional energy change of the photon for each interaction, and $\overline{N}$ is the mean number of scatterings (Rybicki and Lightman 1979). The actual mathematical form for y will depend on the electron distribution (e.g., thermal, non-thermal; relativistic, non-relativistic) as well as the optical depth τ of the material. The resulting spectrum can be quite varied, depending not only on the nature of the scattering medium and the input photon field, but also on the geometry of the scattering region. The scattering due to non-relativistic thermal electrons is of particular relevance to X-ray astrophysics, in which case the y parameter is given by

$$y = \frac{4kT_e}{m_e c^2}\text{Max}(\tau, \tau^2),$$ (1.11)

where T_e and m_e are the temperature and mass of the electrons, and the number of scatterings is approximately equal to the greater of either τ or τ^2. In Figure 1-7, we plot a set of spectra resulting from the Comptonization of blackbody radiation with $kT = 0.1$ keV by a spherical distribution of thermal electrons. These spectra have been generated using the comptt model in XSPEC (Titarchuk 1994). We vary both the optical depth and the temperature of the electron distribution to show the effects of these two parameters. It should be noted that increasing the optical depth affects the spectrum in a very similar way to increasing the electron temperature. When fitting X-ray data, this often results in

25
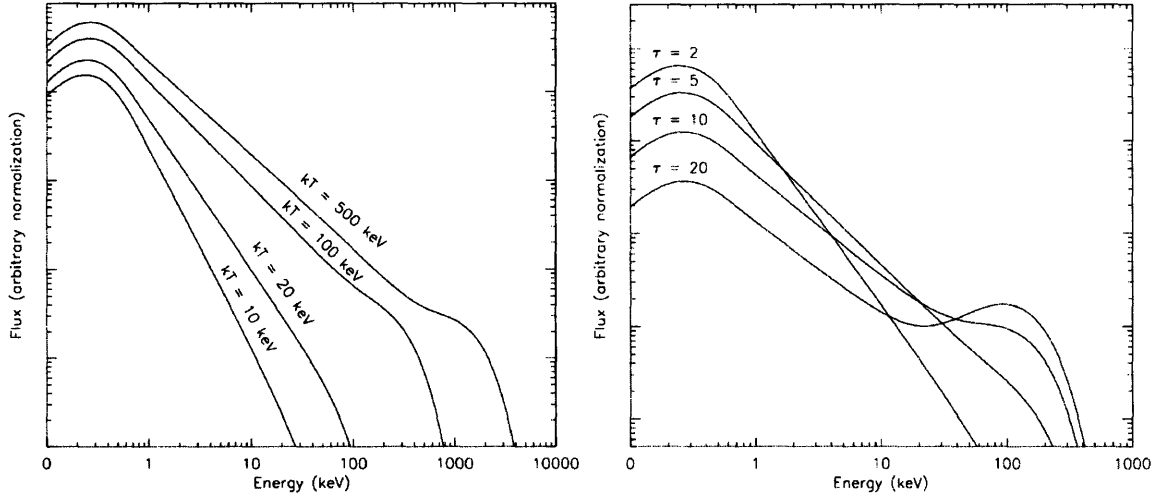
Figure 1-7: Inverse Compton spectra with an input 0.1 keV blackbody distribution of photons and a spherical distribution of thermal electrons. **Left panel:** the optical depth is fixed at $\tau = 5$ while the electron temperature is varied. **Right panel:** the electron temperature is fixed at $kT = 50$ keV while the optical depth is varied.

a degeneracy, since the same spectrum may be well fit by both a high-temperature plasma of low optical depth and a low-temperature plasma of high optical depth.

Comptonization plays an important role in the production and modification of high-energy spectra. Photons which traverse a region that contains highly energetic electrons, such as an accretion disk corona or the accretion column of a neutron star, will be Compton scattered, sometimes greatly affecting the transmitted spectrum.

1.1.7 Synchrotron emission

A charged particle traversing a region containing a magnetic field where $q(\vec{v} \times \vec{B}) \neq 0$ will experience a force and thus an acceleration, causing it to radiate. When $v \ll c$, this will result in cyclotron emission of frequency $\omega_c = qB/m$ as the particle radiates away its energy. However, as $v \to c$, relativistic corrections need to be taken into account, and the spectrum becomes more complex. The emission from such a charge is known as synchrotron radiation.

Of particular interest for astrophysical applications is the synchrotron spectrum of a power-law distribution of electrons. In this case, the spectrum is given by

$$P(\omega) = \frac{\sqrt{3}q^3 CB \sin \alpha}{2\pi mc^2 (p+1)} \, \Gamma\left(\frac{p}{4} + \frac{19}{12}\right) \Gamma\left(\frac{p}{4} - \frac{1}{12}\right) \left(\frac{mc\omega}{3qB \sin \alpha}\right)^{-(p-1)/2} \text{erg s}^{-1} \text{ cm}^{-3} \text{ Hz}^{-1},$$

(1.12)

where q and m are the electron charge and mass, C is a dimensionless constant governing the electron number density, p is power-law index, B is the magnetic field, α is the pitch angle of the electron with respect to the magnetic field, and $\Gamma(x)$ are gamma functions of argument x (see, e.g., Rybicki and Lightman 1979). Figure 1-8 shows a set of spectra where p and B are varied: changing p results in a change in the spectral index, whereas a variation
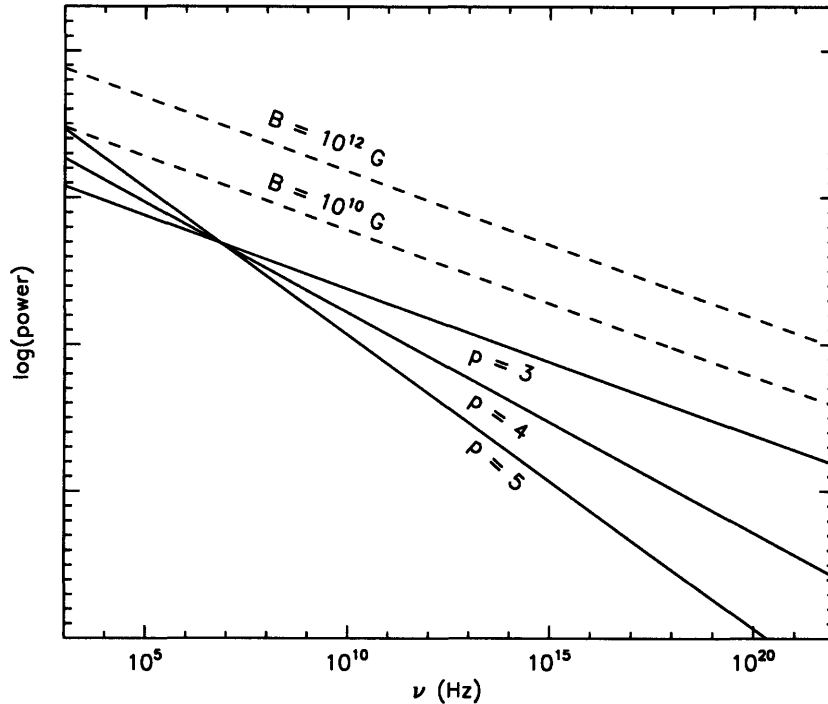
Figure 1-8: Synchrotron curves (power cm^{-3} Hz^{-1}; arbitrary normalization) for several different values of the magnetic field B (resulting in a change of normalization) and power-law index p (resulting in a change of slope).

in B changes the overall normalization.

Synchrotron emission plays a major role in many astrophysical processes. Jets of all scales are thought to radiate primarily via synchrotron emission, producing spectra that can span all the way from radio to X-ray frequencies. The expanding shells of supernova remnants likely radiate as a result of synchrotron processes, and it may also contribute to the emission from the accretion column of magnetized neutron stars. Also important is the closely related *synchrotron self-Compton* process, through which synchrotron photons are inverse Compton scattered by the same population of electrons from which they were initially created, resulting in a more significant proportion of high-energy photons.

1.1.8 Radiative atomic transitions

As required by quantum mechanics, atomic electrons must occupy distinct energy levels. Transitions between these levels will result in the emission of, or result from the absorption of, energy in the form of a photon. Since the levels are discrete, a large number of transitions between the same pair of levels will result in, or from, a large number of photons of the same energy, which will then be observable in the form of an emission or absorption line.

The lines which arise from a given medium will necessarily depend on the species, and excitation level, of ions that are present. In the simplest scenario, the medium will be in thermodynamic equilibrium, in which case the relative ion populations can be determined using the Saha equation,

$$\frac{N_{i+1}}{N_i} = \frac{2Z_{i+1}}{n_e Z_i} \left(\frac{2\pi m_e kT}{h^2}\right)^{3/2} e^{-\chi_i/kT}, \tag{1.13}$$

where N_i are the number of atoms and Z_i the partition function for the atoms in ionization stage i, n_e is the number density of free electrons, m_e is the electron mass, χ_i is the ionization energy needed to take the atom from ionization state i to $i+1$. In order to determine the relative excitations of the ions, one can use the Boltzmann equation,

$$\frac{N_b}{N_a} = \frac{g_b}{g_a} e^{-(E_b - E_a)/kT}, \tag{1.14}$$

where $N_{a,b}$ are the number of atoms in states with energies $E_{a,b}$ and degeneracies $g_{a,b}$ (Carroll and Ostlie 1996).

For atoms with only a single electron, also known as *hydrogen-like* ions, the non-relativistic quantum mechanical equations can be solved analytically. Furthermore, hydrogen-like ions such as Ne X, O VIII, and Si XIV are often responsible for some of the strongest astrophysical X-ray emission lines, generally resulting from transitions to the innermost electron orbital, $n = 1$, also known as *Lyman series* transitions. Atoms which retain two electrons are known as *helium-like* ions, and there is not an exact analytical description of these systems. Furthermore, the energy levels are dependent on the spin of the electrons. This results in a splitting of the levels and transition energies, resulting in distinct *resonance*, *intercombination*, and *forbidden* lines. Since the relative populations of these levels are dependent on the temperature, density, and radiation environment of the plasma, they can be used as diagnostics to determine the physical environments of line formation regions (see, e.g., Porquet and Dubau 2000 as well as the discussion in Chapter 7).

Radiative atomic transitions which give rise to absorption and emission lines are important in many astrophysical systems. For example, absorption lines could form during thermonuclear X-ray bursts, in which case they could provide a measurement of the gravitational redshift from a neutron star (see, e.g., Chapter 6).

1.1.9 Understanding X-ray spectra from neutron star LMXBs

There are several regions in a neutron star LMXB system which could either emit or affect X-ray photons. These include: the accretion disk, an accretion disk corona, hot electrons in various locations acting as a Comptonizing medium, a jet, a boundary layer where the accretion disk meets the neutron star, and the neutron star surface itself. If the neutron star has an appreciable magnetic field, there will be X-rays generated in an accretion column, and the disk will never reach the neutron star surface. Obviously, since a neutron star has a solid surface, the number of regions which can produce X-rays are greater in a neutron star than a black hole LMXB system.

Not all of these elements will be present in any given system, and their existence may be dependent on the accretion rate. As would be expected, high and low rates of accretion (associated with softer and harder spectra, respectively; see Chapter 3) lead to different source geometries and dominant emission mechanisms. An accretion disk is present at all times, but likely extends closer to the neutron star during periods of high accretion, perhaps even extending to the neutron star surface and creating a boundary layer where the two meet (see, e.g., Popham and Sunyaev 2001). However, some favored neutron star equations of state result in $R_{\rm NS} \lesssim 10$ km. In this case, the radius of the innermost stable circular orbit (ISCO) will be greater than the radius of the neutron star, and the portion

of the disk which would inhabit this region will be disturbed, precluding the formation of a classical boundary layer (Kluzniak and Wagoner 1985). Alternatively, if the neutron star has a sufficiently strong magnetic field, this will truncate the accretion disk and channel the accretion flow onto the magnetic poles.

The X-ray spectra from higher-accretion rate states are dominated by a soft component which can be modeled as a single-temperature blackbody or a multi-temperature disk, but may also contain a higher-energy component and in some cases a broad iron line (see Barret 2004 for a review). There have historically been two main branches of modeling and interpretation, dubbed *Eastern* and *Western*. The Eastern model, first presented by Mitsuda et al. (1984), describes the spectra as a combination of multi-temperature blackbody emission from the accretion disk as well as weakly-Comptonized single-temperature blackbody emission from the surface of the neutron star (see also Mitsuda et al. 1989). Although the origin of the Comptonizing electrons is not specified, the authors mention the possibility of an optically thin but geometrically thick high-temperature plasma surrounding the neutron star (see also Hirano et al. 1984). This disk-dominated model is supported by the observational evidence that there are correlations observed between the strength of the blackbody component and the kHz QPO frequencies (Ford and van der Klis 1998). Alternatively, the Western model attributes the thermal component to a single-temperature blackbody from an optically thick boundary layer, and the hard component to Comptonization occurring in the inner disk region (White et al. 1988).

The hard, low-accretion rate spectra can generally be described by Comptonized emission, though in some cases an additional blackbody and/or iron line component is needed. The disk likely recedes from the neutron star when the accretion rate is lower, and therefore does not contribute much to the spectrum, so the remaining blackbody component is due to emission from the neutron star surface (see, e.g., Gierliński and Done 2002). This picture is supported by observations that the timing properties of LMXBs in the low/hard state are not correlated with spectral changes (see, e.g., Olive et al. 2003).

There may also be a jet contribution in the hard state (see Fender 2006 for a review), though exactly how much (and in what way) it might contribute to the X-ray spectrum is not clear. Markoff et al. (2005) suggest that the base of the jet could be the source of Comptonizing photons in the hard state. Synchrotron photons at the base could also contribute to the X-ray spectrum or act as seed photons for the Comptonizing region (*synchrotron self-Compton* emission). We discuss X-ray jets in neutron star X-ray binaries further in Chapter 5.

The accretion geometry will also be affected by the neutron star's magnetic field. A strong dipole field will truncate the accretion disk and channel accreting material to the magnetic poles, forming an accretion column as it approaches the neutron star and ultimately creating hotspots on its surface (see, e.g., Pringle and Rees 1972). If the magnetic axis is not aligned with the spin axis, the rotation of the neutron star will result in modulated X-ray emission, and the source will appear as a pulsar (see, e.g. Meszaros et al. 1980).

Although there have been numerous observations of neutron star LMXBs, there is still no consensus regarding the exact physical origin of their X-ray spectra. Much of the difficulty in interpreting these spectra lies in the ambiguity of the spectral components: often a number of different models provide equally good fits, as surveys of LMXBs from *Einstein*, *ROSAT*, and *ASCA* have shown (Christian and Swank 1997; Schulz 1999; Church and Balucińska-Church 2001). Recently, Lin et al. (2007) analyzed ~ 800 *RXTE* spectra of two well-known LMXBs, Aql X-1 and 4U 1608−522, and found that their spectra can be well described by

several different models. However, the authors point out that some of these models conflict with other known or expected properties of the systems. For example, when fits include a disk model (MCD), the fitted inner disk radius is sometimes less than the expected radius of the neutron star, which is physically impossible. Ultimately, large-scale spectral studies such as this hold promise for truly understanding the origin of X-ray emission from LMXB systems.

1.2 X-ray observatories

1.2.1 The *Rossi X-ray Timing Explorer*

The *Rossi X-ray Timing Explorer* (*RXTE*) is an X-ray mission dedicated to high time and moderate energy resolution observations, as well as the continual long-term monitoring of variable sources. *RXTE* has the ability to quickly respond to target of opportunity requests, making it the ideal observatory with which to pursue observations of bright transients. In December 1995, *RXTE* was placed in an $\approx$ 90-min low-Earth orbit by a Delta II launch vehicle, and has been performing science observations for over ten years, far surpassing its nominal lifetime of two years. It carries two instruments used for pointed observations, the Proportional Counter Array (PCA) and the High Energy X-ray Timing Experiment (HEXTE), as well as the All-Sky Monitor (ASM), which observes $\approx$ 80% of the sky during every spacecraft orbit. During each orbit, the spacecraft passes through the South Atlantic Anomaly, a region of enhanced charged particle density, resulting in gaps in data collection. A diagram of *RXTE* is presented in Figure 1-9.

The PCA comprises five proportional counter units (PCUs), each of which includes an X-ray collimator and three layers of xenon gas sandwiched between two layers of propane gas which serve as veto layers to reject non–X-ray events. It is capable of extremely high (1 μs) time resolution observations, and is sensitive over the energy range 2–60 keV. The collimator results in 1° FWHM spatial resolution, which is sufficient for observations of relatively isolated sources, although at times bright events (e.g., X-ray bursts) from nearby sources are included in the data stream. The PCA also has moderate energy resolution, $R \equiv E/\Delta E \approx 6$ at 6 keV which is well-calibrated for energies in the 2.5–25 keV range, and a substantial collecting area of 6500 cm^2. For any given observation, data are recorded in a number of different modes of varying time and energy resolution. Two of these modes are known as *standard* and are used for all observations, whereas the others are chosen by the observer to be most relevant for the expected source behavior and the science goals. Since the start of the mission, two of the PCUs have lost their outer propane veto layers: PCU0 in May 2000, and PCU1 in December 2006. Although they still perform observations, this has resulted in some degradation of their spectral information.

The HEXTE includes two clusters (*A* and *B*) of four NaI/CsI phoswich scintillation detectors each. The detectors are equipped with collimators to provide the spatial resolution of 1° FWHM, and the clusters rock independently and orthogonally between the source position and a background position to provide contemporaneous measurements of nearby background information. Each cluster provides 800 cm^2 of collecting area, and covers the energy range 15–250 keV with a resolution $R \approx 7$ at 60 keV. The HEXTE also has very high time resolution of 8 μs.

The ASM is a coded-mask instrument capable of determining source positions with a spatial resolution of 3′ × 15′. It is comprised of three shadow cameras, each with a 6° × 90° field of view and 60 cm^2 collecting area. The xenon proportional counter detectors are
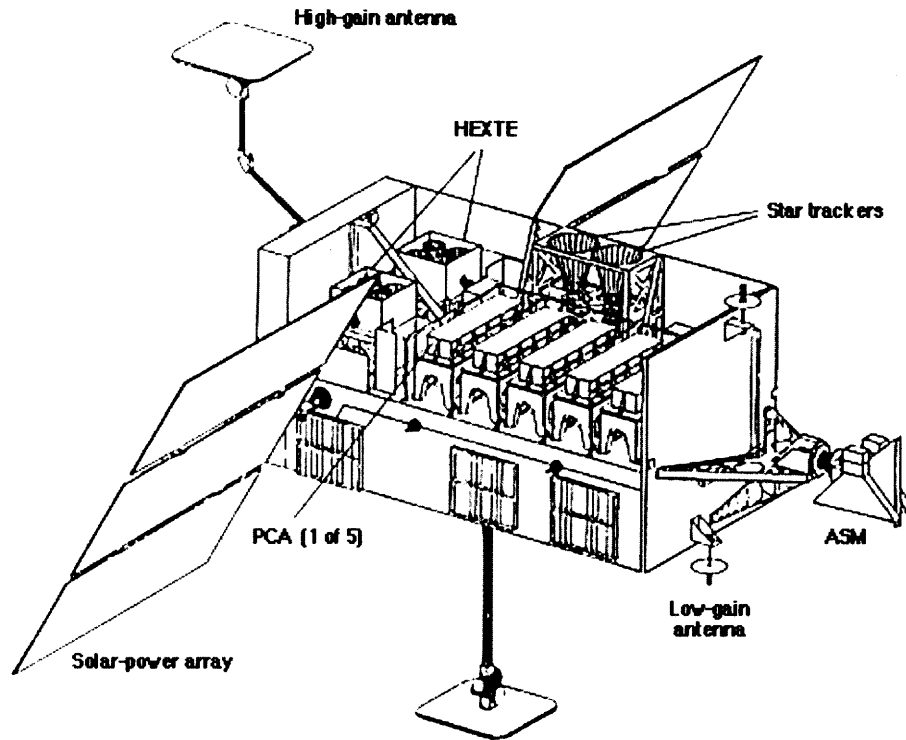
Figure 1-9: Diagram of the *Rossi X-ray Timing Explorer* with major components labeled. Figure courtesy of the NASA High Energy Astrophysics Science Archive Research Center/Goddard Space Flight Center (HEASARC/GSFC).

sensitive over a 2–10 keV energy range and have some spectral resolution (enough to produce 3-band colors). Most importantly, the ASM allows for long-term continuous monitoring of sources with the 90-min time resolution of the spacecraft orbit as well as the detection and positional determination of new transients.

1.2.2 The *Chandra X-ray Observatory*

The third of NASA's Great Observatories, the *Chandra X-ray Observatory* (*CXO*) was launched on the Space Shuttle Columbia in July 1999. To maximize the fraction of time during which it is able to observe astrophysical X-ray sources, *Chandra* is in a highly elliptical 64.3 hr orbit which reaches over a third of the way to the Moon. Figure 1-10 shows a diagram of the Observatory and its major components.

One of the great technological achievements of the *CXO* is the High Resolution Mirror Assembly (HRMA). The HRMA comprises four nested grazing-incidence X-ray mirrors in a Wolter Type-I configuration with a focal length of ≈ 10 m. These mirrors are polished to extremely high precision—the ratio of the size of surface imperfections to the length of the mirrors is $\Delta h/L \approx 5 \times 10^{-8}$, resulting in a diminutive point spread function (PSF) of $0\rlap{.}''5$ FWHM. To maximize the X-ray reflectivity of the mirror surfaces, they are coated with iridium, resulting in effective areas of (800, 400, 100) cm^2 at (0.25, 5.0, 8.0) keV.

There are two focal plane instruments, the High Resolution Camera (HRC) and the Ad-
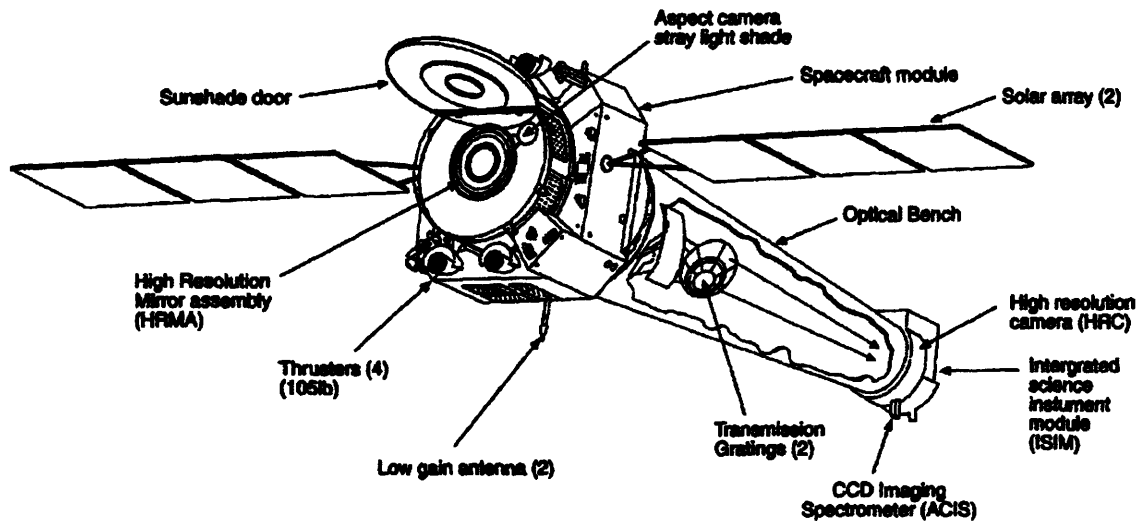
Figure 1-10: Diagram of the *Chandra X-ray Observatory* with major components labeled. Figure from Brissenden (2001).

vanced CCD Imaging Spectrometer (ACIS). These instruments are mounted on the Science Instrument Module (SIM), a moveable bench that allows either to be moved to the focal point of the HRMA. During a science observation, only one of these instruments records data.

The HRC is a microchannel plate detector which allows for, in various operating modes, a very large field of view ($\approx 30' \times 30'$) or high time resolution (16 μs). It is comprised of two arrays, one optimized for imaging (the HRC-I) and one for spectroscopy (the HRC-S). These differ in geometric layout as well as pore size and spacing. The detector readout defines the HRC pixel size to be $0\rlap{.}''13$, which provides a good sampling of the intrinsic HRMA PSF. Although it excels in spatial and time resolution, the energy resolution of the HRC is quite poor ($\Delta E/E \approx 1$ at 1 keV). However, it is very sensitive at low energies (down to ≈ 0.08 keV), making it an optimal choice for use with the Low Energy Transmission Grating (LETG).

ACIS comprises two arrays of CCD detectors, one (ACIS-I) for imaging and one (ACIS-S) primarily for use with the High-Energy Transmission Grating (HETG). Each individual 1024×1024 pixel CCD has a field of view of $\approx 8' \times 8'$, yielding a pixel size of $\approx 0\rlap{.}''5$ pixel^{-1}. ACIS-I is a 2×2 array of CCD detectors, all of which are front-illuminated, whereas ACIS-S is a 1×6 array which includes both back- and front-illuminated (BI and FI) detectors, the former providing better low-energy quantum efficiency. ACIS is well-calibrated over the energy range 0.3–10.0 keV and has moderate intrinsic energy resolution; $R \sim 150$ at 1.5 keV and 30 at 5.9 keV, though these values are somewhat different for the BI and FI chips. Early in the mission, the CCDs suffered significant radiation damage, worsening the effects of charge transfer inefficiency (CTI). This causes a spatially-dependent degradation of energy resolution and increases the charge loss as it is read across the detector. Although this damage continues, its rate has been greatly reduced, and time-dependent corrections are now available in standard data processing. There has also been a reduction in the X-ray throughput to the detector, especially at low energies ($E \lesssim 1.5$ keV), as the result

of a contaminant which has condensed on the optical blocking filter. There are calibration products now available to correct for these time- and energy-dependent effects.

When operating in full-frame imaging modes, the ACIS detectors have a time resolution (frame time) of 3.2 s. If more than one X-ray event occurs in a given pixel over a single frame integration, it will register as a single event of higher energy and possibly of dubious grade.[2] If the latter occurs, it may not be telemetered and will not be included in the science data, resulting in a loss of information. If the former occurs, it will skew the spectrum, depleting the low-energy regime and populating the high-energy regime with incorrectly–energy-tagged events. Furthermore, these events could be assigned grades that are filtered out in standard processing (*grade mitigation*). All of these effects are known as *pileup*, and can be a serious problem for CCD spectra of bright sources. Although it is possible to lessen the impact of pileup by reducing the frame time, this can only be accomplished by also reducing the observed field of view. The extreme of this method is to observe in *continuous-clocking* mode, which provides high time resolution (3 ms) but only a one-dimensional image.

There are two sets of dispersive gratings which may be placed in the optical path. The LETG, for use primarily with the HRC-S, is optimized for low-energy photons and has an wavelength range of 1.2–175 Å (0.07–10.0 keV) with a resolution $\Delta\lambda = 0.05$ Å FWHM. It may also be used with ACIS-S; in this configuration, the range is reduced to 1.2–60 Å (0.2–10 keV). The gratings are constructed of free-standing gold wires held in place with fine and coarse support structures, creating a triangular grating element. Eighty grating elements form a circular grating module, and these modules (180 total) are set in rings which, in order to reduce aberrations, follow the Rowland torus. In order to minimize confusion from overlapping orders, the LETG has been optimized to produce a strong first-order spectrum and to suppress the even-order spectra. This is particularly important since, unlike ACIS, the HRC has insufficient energy resolution to sort the grating orders.

The HETG comprises two sets of gratings: the Medium-Energy Grating (MEG; 2.5–30.0 Å [0.4–5.0 keV], $\Delta\lambda = 0.02$ Å FWHM) and the High-Energy Grating (HEG; 1.2–15.0 Å [0.8–10.0 keV], $\Delta\lambda = 0.01$ Å FWHM). The HETG is used in conjunction with the ACIS-S array, and the MEG and HEG are oriented so as to produce two sets of grating arms with an opening angle of $\approx 10°$. As with the LETG, the HETG is designed to maximize the strength of the odd-order spectra. The gold gratings are supported by a polyimide substrate, and the 192 (144) MEG (HEG) grating facets are placed in concentric rings which follow the Rowland torus of the HRMA. The spectrometer has a resolving power of 80–970 (65–1070) for the MEG (HEG) over the wavelength ranges stated above, and a wavelength scale of 0.011 (0.006) Å pixel^{-1}. Since the ACIS detector has moderate intrinsic energy resolution, it is possible to both extract a spectrum from the zeroth-order image (provided that it is not affected by pileup) and to use the energies of dispersed events to determine their spectral order. If the source is very bright and it is known that the zeroth-order image will be severely piled, it is possible to block it and reduce the telemetry stream. Although the insertion of the HETG naturally reduces pileup, both via dispersion as well as the reduced effective area, it will not necessarily eliminate it, and care must be taken in identifying piled regions when analyzing bright sources.

---

[2]The event grade is a number assigned to each event, which is defined as the local maximum of a 3 × 3 pixel region, based on the analysis of the pattern in the surrounding 3 × 3 pixels. The grade is used to determine if the event is likely a bona fide X-ray detection, or if it is spurious, perhaps due to a cosmic ray or detector noise.
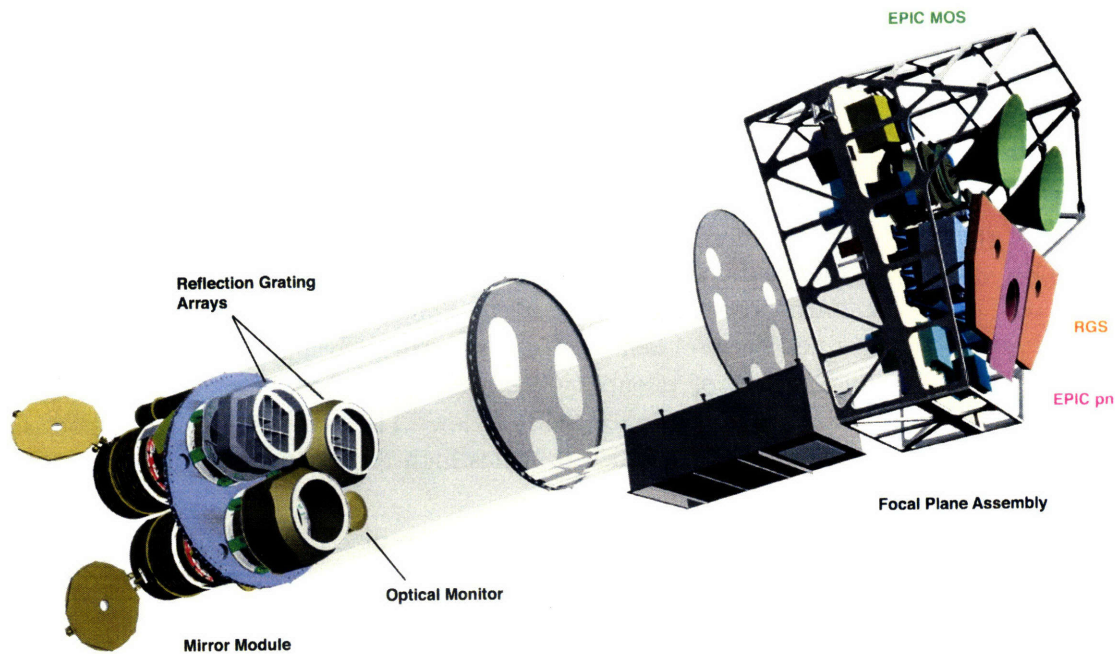
Figure 1-11: Diagram of the *XMM-Newton* payload with major components labeled. The EPIC MOS, EPIC pn, and RGS are color-coded; their radiators are the most visible components. The spacecraft is not shown here. Figure courtesy of Dornier Satellitensysteme GmbH and the European Space Agency (ESA).

1.2.3 The *X-ray Multi-mirror Mission* (*XMM-Newton*)

XMM-Newton is one of the European Space Agency's "cornerstone" missions, and was placed in a highly elliptical 47.9 hr orbit by an Ariane 504 launch vehicle in December 1999. It has three X-ray telescopes, each comprised of 58 nested gold-coated mirrors in a Wolter Type-I configuration, as well as an optical/UV telescope. There are five unique X-ray focal plane instruments that can perform simultaneous observations as described below. A diagram of the *XMM-Newton* telescopes and instruments is presented in Figure 1-11.

The three X-ray telescopes of *XMM-Newton* are optimized to provide high–effective-area, moderate–spatial-resolution images. The thin (0.47–1.07 mm) mirror shells are held in place by radial struts, and each telescope has an entrance and exit baffle to minimize stray light contamination and regulate the thermal environment of the instruments. The telescopes have focal lengths of 7.5 m, and the diameter of the largest mirror on each is 70 cm. The resulting effective area is highest with the EPIC pn detector (see below)—1400 cm^2 at 1.5 keV and 600 cm^2 at 8.0 keV—although there is a prominent Au M photoelectric absorption edge at 2 keV and very little throughput above 12 keV.

Two of the X-ray telescopes are coupled with European Photon Imaging Camera Metal Oxide Semiconductor CCD arrays (EPIC MOS1 and MOS2). These telescopes also have Reflection Grating Units (RGUs) mounted within them, reducing the number of X-ray photons which reach the EPIC MOS detectors (see below for more information on the RGUs). The EPIC MOS arrays have circular fields of view with diameters of 30′ and

operate over the energy range 0.15–15 keV with moderate energy resolution ($R \approx 50$–20). Each array comprises seven $10.'9 \times 10.'9$ front-illuminated overlapping detectors with $1.''1$ pixels to provide good sampling of the $\approx 4''$ FWHM PSF. The arrays can observe in a variety of operating modes with varying fields of view and time resolution. Using the full field of view results in a time resolution of 2.6 s, whereas the *timing uncompressed* mode (similar to the continuous clocking mode of the *Chandra* ACIS detector, see above) has a time resolution of 1.5 ms. The MOS CCDs are susceptible to pileup, although the size of the intrinsic PSF helps to mitigate some of this effect, and telemetry saturation is sometimes a greater concern. In order to reduce the amount of IR, visible, and UV light transmitted to the detectors, EPIC includes a set of three optical blocking filters of varying thickness, the most optimal of which is chosen for a given observation. In March 2005, an event consistent with a micrometeorite impact caused the electronics of MOS1 CCD6 to fail; since this time, it has been switched off and no longer provides science data. Furthermore, the EPIC MOS detectors have suffered an increase in their charge transfer inefficiency (CTI) since launch, resulting in an $\approx 13\%$ decrease in their energy resolution.

The third X-ray telescope images onto the EPIC pn camera, a 2×6 single-wafer array of back-illuminated CCDs with $4.''1$ pixels. The "pn" simply refers to the p-n semiconductor junctions that are an integral part of its CCD detectors. The EPIC pn has very high time resolution; 73.4 ms when operated in full-frame mode, and 7 μs when operated in *burst* mode, which only provides a one-dimensional image and has a low (3%) duty cycle. As with the MOS detectors, it has an $\approx 30'$ field of view and operates over the energy range 0.15–15 keV, although it has a greater overall quantum efficiency (QE) and greater relative QE at the higher energies. The EPIC pn has moderate energy resolution, $R \approx 130$–50, and although it has suffered from increased CTI effects in orbit, this does not appear to have affected the energy resolution.

The Reflection Grating Spectrometer, which includes two units (RGS1 and RGS2), provides high-resolution ($100 \leq R \leq 500$) dispersive X-ray spectra over the wavelength range 5–38 Å (2.5–0.33 keV). Two of the three X-ray telescopes are equipped with RGUs which reflect and disperse $\approx 50\%$ of the incoming X-ray photons. The resulting (negative-order) spectra are imaged by the two RGS Focal cameras (RFCs). The RFCs comprise 1×9 arrays of MOS CCD detectors, which are back-illuminated to provide optimal low-energy response. The energy resolution of the CCDs is utilized to separate the spectral orders. Early in the mission, one of the detectors from each RGS failed, resulting in gaps in wavelength coverage. Fortunately, each gap spans a different wavelength range, so there is no total loss at any given wavelength. The effective area varies substantially as a function of wavelength due to the presence of chip boundaries, bad CCD columns, and instrumental absorption edges. While most of these effects are accounted for in the standard calibration products, residual variations often remain, and care must be taken when analyzing discrete features in the dispersed spectra.

In addition to the X-ray telescopes and instruments, *XMM-Newton* carries a 30-cm optical/UV telescope and imager, the Optical Monitor (OM). This allows for the simultaneous acquisition of data in the wavelength range 1800–6000 Å over a 17' field of view with $\approx 1''$ resolution. The OM detector is a photon-counting microchannel plate intensified CCD, and is able to record either long-duration exposures or event lists with frame times of 500 ms to 20 s. The OM also carries a set of four filters, all optimized for the shorter-wavelength regime ($\lambda \lesssim V$), as well as two grisms—one optical and one UV—for low-resolution ($R \approx 250$) dispersive spectroscopy.

1.3 Organization and content of thesis

This thesis contains a set of seven chapters presenting new scientific results. Although varied, they are linked by a common thread: they are all concerned with neutron star low-mass X-ray binaries in our Galaxy. Therefore, although each system we have studied is unique, they also have many shared properties. In this spirit, we have analyzed data from two individual sources in great depth, as well as several larger sets of sources to compare broader characteristics. Chapter 2 considers the accretion-powered millisecond pulsar (AMP) system XTE J1814−338, including analysis of its high-resolution *Chandra* spectrum as well as optical data. From these data, we are able to provide some constraints on the orbital parameters as well as the type of secondary present in the system. The optical data also suggest an excess of infrared radiation relative to an X-ray heated accretion disk spectrum—this could arise from synchrotron emission from some type of outflow, perhaps in the form of a jet.

In Chapter 3, we consider a larger sample of accretion-powered millisecond pulsars (AMPs), and create X-ray color-color diagrams for them as well as for a sample of atoll sources. We find that the AMPs occupy almost exclusively a distinct subset of color space that corresponds to the extreme island state of the atoll sources. This suggests that they are drawn from a similar, but intrinsically lower-luminosity, population than the atoll sources. This leads one to consider a currently outstanding question in astrophysics: why do only a small subset of neutron star LMXBs contain a pulsar? One theory posits that the sources which appear as pulsars have a less substantial column of scattering material which could otherwise inhibit the pulses from reaching an observer (i.e., a lower optical depth τ). Although X-ray colors can provide some estimate of the spectral properties of our sample, energy-resolved spectra are a more powerful tool for measuring their physical parameters, and in Chapter 4 we analyze the *RXTE* spectra of these sources. We use a Comptonization model, which is able to provide a measure of τ, and find that within our errors, there is no difference in the optical depths of the AMP and atoll sources. The evidence in Chapters 3 and 4 suggests that the mass accretion rate plays an important role in the creation—or suppression—of a pulsar. One possible mechanism is that above some critical rate of accretion, the accreted material substantially diminishes the neutron star's magnetic field. This will result in a dipole field that will no longer be strong enough to direct the accretion flow onto the spatially distinct magnetic poles, resulting in a non-pulsating neutron star.

Another astrophysical phenomenon likely tied to the presence of magnetic fields is the production of jets, although in this case the physics is not quite as simple. Nevertheless, jets are ubiquitous, and there is growing evidence that a substantial number of Galactic LMXBs may produce them at some point during their cycle of activity. In Chapter 5 we consider high-resolution *Chandra* images of two sources, the AMP SAX J1808.4−3658, and unique transient Z source XTE J1701−462. While neither observation contains a statistically significant jet feature, we present analysis techniques to employ when searching for evidence of spatial extension. We also describe a spurious feature which may arise in temporally short observations of bright sources.

An outstanding question in physics concerns the behavior of extremely dense material, and may be one that astrophysical observations can help answer. Neutron stars are the densest known self-supporting objects in the universe, and if we could measure the ratio of a neutron star's mass to its radius, it would provide important constraints on currently proposed equations of state (EOS). One way to measure M/R is by determining the redshift of discrete spectral features arising from the neutron star surface. This has been done for

one system, EXO 0748−676, from red-shifted absorption features seen during thermonuclear X-ray bursts. Ideally, other systems would provide similar measurements, confirming the constraints and furthering our understanding of the neutron star EOS. Since the detectability of line features during bursts depends on the temperature of the burst, this is an important parameter to consider when planning any search strategy. In Chapter 6, we look at the distribution of burst temperatures for all the thermonuclear X-ray bursters observed by *RXTE*. We find a wide distribution of temperature behavior, though there is no single source which emerges as an optimal candidate for a burst line search. This is due primarily to the known neutron star spin frequencies, which are high enough to smear line features beyond the realm of detectability by the current generation of X-ray observatories.

In Chapter 7, we undertake an in-depth study of the high-resolution *Chandra*/HETG and *XMM-Newton*/RGS spectra of the ultracompact X-ray binary pulsar 4U 1626−67, as well as analysis of its recent timing behavior. These data include four observations spanning a baseline of three years and comprising a total of 238 ks. We analyze the prominent Ne and O emission lines, which include the helium-like Ne IX and O VII triplets, allowing us to place some constraints on the physical parameters of the emitting medium. Although the presence of emission lines suggests that the system contains a substantial quantity of Ne and O, neither the Ne K nor O K absorption edges indicate an overabundance of these elements relative to interstellar values. We also find that the pulsar is continuing to spin down, and the system continuing to fade, both in keeping with previously observed trends.

Over its lifetime, *Chandra* has observed a large number of Galactic LMXBs with the HETGS. The majority of these observations are now in the public archive, and to take advantage of this substantial and rich set of data, we have created an IDL database both of the known Galactic LMXBs and of their *Chandra*/HETG observations. In Chapter 8 we describe this database and the procedures we used to reprocess the data. We also present the analysis of a sample of these sources, including an accretion-powered millisecond pulsar, an ultracompact binary, and an atoll source. We use a set of standard spectral models, constraining (when possible) the interstellar absorption values with high-resolution edge modeling. We find that a power-law plus blackbody describes the spectrum of all three quite well, though the physical parameters derived from the blackbody component only make simple physical sense for two of the sources. A larger sample will provide a more coherent picture of the soft emission from LMXBs, and help determine what models and physical interpretations are most likely appropriate.

Chapter 2

The Accretion-Powered Millisecond Pulsar XTE J1814−338

Abstract

We report the precise optical and X-ray localization of the 3.2 ms accretion-powered X-ray pulsar XTE J1814−338 with data from the *Chandra X-Ray Observatory* as well as optical observations conducted during the 2003 June discovery outburst. Optical imaging of the field during the outburst of this soft X-ray transient reveals a star of magnitude $R = 18$ at the X-ray position. This star is absent ($R > 20$) from an archival 1989 image of the field and brightened during the 2003 outburst, and we therefore identify it as the optical counterpart of XTE J1814−338. The best source position derived from optical astrometry is R.A. = $18^h13^m39\overset{s}{.}04$, Dec.= $-33°46'22\overset{''}{.}3$ (J2000). The featureless X-ray spectrum of the pulsar in outburst is best fit by an absorbed power-law (with photon index $\gamma = 1.41 \pm 0.06$) plus blackbody (with $kT = 0.95 \pm 0.13$ keV) model, where the blackbody component contributes approximately 10% of the source flux. The optical spectrum shows evidence for an excess of infrared emission with respect to an X-ray heated accretion disk model, suggesting a significant contribution from the secondary or from a synchrotron-emitting region. A follow-up observation performed when XTE J1814−338 was in quiescence reveals no counterpart to a limiting magnitude of $R = 23.3$. This suggests that the secondary is an M3 V or later-type star, and therefore very unlikely to be responsible for the soft excess, making synchroton emission a more reasonable candidate.

2.1 Introduction

It has long been believed that millisecond radio pulsars are the spun-up products of sustained mass transfer onto neutron stars in low-mass X-ray binaries (e.g., Bhattacharya and van den Heuvel 1991). Their presumed immediate progenitors, accretion-powered millisecond X-ray pulsars, proved elusive for many years, but six such systems are now known: SAX J1808.4−3658 (Wijnands and van der Klis 1998; Chakrabarty and Morgan 1998); XTE J1751−305 (Markwardt et al. 2002); XTE J0929−314 (Galloway et al. 2002); XTE J1807−294 (Markwardt et al. 2003b); XTE J1814−314 (Markwardt and Swank 2003;

Strohmayer et al. 2003); and IGR J00291+5934 (Galloway et al. 2005). In addition, 13 accreting neutron stars also show millisecond oscillations during thermonuclear X-ray bursts (see Strohmayer and Bildsten 2006 for a review). These systems are now understood as nuclear-powered millisecond pulsars, with the burst oscillations tracing the pulsar spin (Strohmayer and Markwardt 2002; Chakrabarty et al. 2003).

The soft X-ray transient XTE J1814−314 ($l = 358°\!.7$, $b = -7°\!.6$) was discovered in outburst on 2003 June 5 during scans of the central Galactic plane with the *Rossi X-Ray Timing Explorer* (*RXTE*; Markwardt and Swank 2003). The outburst lasted for approximately 55 days, and had a peak 2–10 keV flux of around 13 mCrab. *RXTE* observations also established the source as a 314 Hz (3.2 ms) accretion-powered X-ray pulsar (Markwardt and Swank 2003) in a 4.3 hour binary with a main sequence companion of at least 0.17 $M_\odot$ (using the mass function of 0.002016 $M_\odot$ in Markwardt et al. 2003c assuming a neutron star mass of 1.4 $M_\odot$). Over two dozen thermonuclear X-ray bursts with millisecond oscillations at the spin frequency were detected from XTE J1814−338 during the 2003 June outburst (Strohmayer et al. 2003). One of these bursts showed evidence for photospheric radius expansion, allowing Strohmayer et al. (2003) to infer a source distance of 8.0 ± 1.6 kpc.[1]

We obtained a brief observation of the source on 2003 June 20 with the *Chandra X-Ray Observatory* for the purpose of measuring its position, and we used this position to identify the optical counterpart (Krauss et al. 2003). Subsequent optical spectroscopy revealed strong emission lines of H and He including double-peaked Hα emission, indicative of an interacting binary (Steeghs 2003). In this chapter, we present a detailed report on our *Chandra* and optical observations of XTE J1814−338. In § 2.2, we present X-ray and optical imaging and the precise localization and flux measurements of the optical counterpart. We analyze the X-ray spectrum in § 2.3, and in § 2.4 we discuss the implications of the current data in our understanding of the physical parameters of XTE J1814−338.

2.2 X-ray and optical imaging

We observed XTE J1814−338 with *Chandra* for 9.7 ks on 2003 June 20 using the High Energy Transmission Grating Spectrometer (HETGS) with the spectroscopic array of the Advanced CCD Imaging Spectrometer (ACIS-S). The HETGS is comprised of two sets of transmission gratings: the Medium Energy Gratings (MEGs), with a range of 2.5–31 Å (0.4–5.0 keV), and the High Energy Gratings (HEGs), with a range of 1.2–15 Å (0.8–10 keV). The HETGS spectra are imaged by ACIS-S, an array of six CCD detectors. The HETGS/ACIS-S combination provides both an undispersed (zeroth-order) image as well as dispersed spectra from the gratings. The spatially overlapping spectral orders are sorted using the intrinsic energy resolution of the ACIS-S CCDs. The first-order MEG (HEG) spectrum has a spectral resolution of $\Delta\lambda = 0.023$ (0.012) Å FWHM.

All data processing was done with the CIAO analysis package[2] (vers. 2.3). We summed the dispersed first-order events in 500 s time bins to create an X-ray lightcurve, which we searched for signs of orbital modulation. We note that the observation spanned only 60% of the 4.3 hour orbital period, but did cover the time period during which the neutron star was at inferior conjunction. The data were consistent with a constant count rate of

---

[1]This distance estimate should be viewed with some caution, since the burst it is based on has some features which suggest it may not have been Eddington-limited. If the burst was not actually Eddington limited, $L_{\mathrm{burst}} < L_{\mathrm{Edd}}$, and the distance to XTE J1814−338 may be less than 8.0 ± 1.6 kpc. We therefore consider 8.0 kpc to be an upper limit for the source distance.

[2]http://cxc.harvard.edu/ciao/
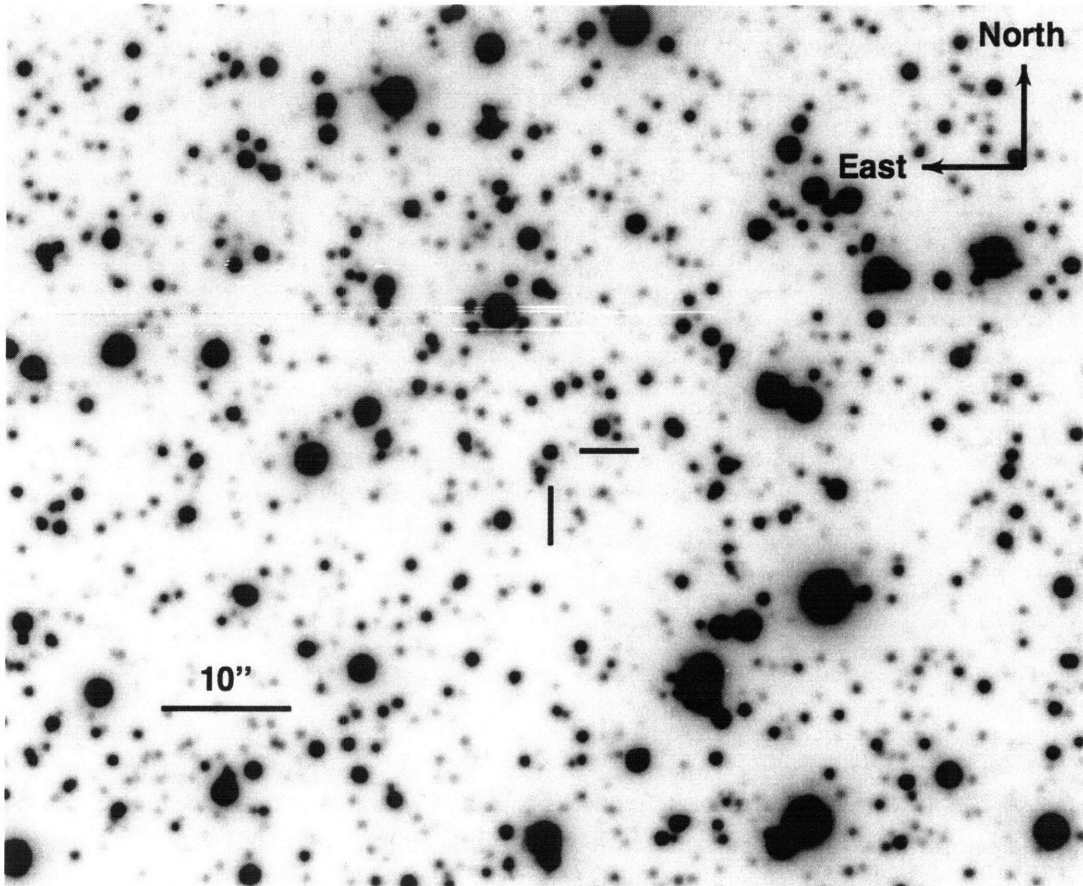
Figure 2-1: I-band MagIC image of the XTE J1814−338 field from 2003 June 21. The $I = 17.4$ optical counterpart is marked near the center of the image. North is up and east is to the left.

4.6 ± 0.1 counts s^{-1}, and we did not detect any evidence of an X-ray eclipse.

We corrected the observation aspect to be consistent with the calibration available as of 2004 March 22. No sources other than XTE J1814−338 were detected in the field. Due to the high source count rate, the zeroth order image is over 75% piled up, which suppresses counts in the image core and results in a characteristic "doughnut" shaped point spread function (see, e.g., Davis 2001). However, this did not affect our ability to use the zeroth-order image to obtain a precise positional measurement with the CIAO tool `wavdetect`. In order to account for the pileup, we used large wavelet scales (8 and 12 pixels), which are not sensitive to the core of the point spread function. The best-fit X-ray position of XTE J1814−338 was R.A. = $18^h13^m39\!\!.\!\!^s02$, Dec. = $-33°46'22\!\!.\!\!''3$ (equinox J2000.0) with a 90% confidence radius of $0\!\!.\!\!''6$.

The precise X-ray source position facilitated the identification of an optical counterpart. We obtained BVR images of the XTE J1814−338 field on 2003 June 6 and BR images on 2003 June 7 using the LDSS2 camera on the 6.5-m Magellan/Clay telescope at the Las Campanas Observatory in Chile (field of view of $2.5' \times 2.5'$ with a scale of $0.38''$/pixel; the seeing on both nights was approximately $0.8''$). An astrometric solution was derived using the USNO-B1.0 catalog (Monet et al. 2003), giving a standard deviation of $0\!\!.\!\!''35$. Using this solution, we find that there is one optical source within the *Chandra* error circle. This

Table 2.1. Optical magnitudes of XTE J1814−338

Observation time (UT)		B	V	R	I
2003 June 6[a]	10:25	18.96	18.59	18.26	⋯
2003 June 7[a]	09:57	18.71	⋯	18.05	⋯
2003 June 21[b]	03:32	18.77	18.48	18.33	17.47
	05:06	18.64	18.39	18.16	17.37
	05:13	18.62	18.34	18.21	17.42
	06:26	18.61	18.33	18.16	17.35
2003 June 24[b]	06:39	18.75	18.48	18.29	17.38
2004 March 15	07:47	⋯	⋯	> 23.3[c]	⋯

[a]Calibration errors are ±0.06 magnitudes; relative uncertainty between these two nights is ±0.01 magnitudes.

[b]Calibration errors are ±0.02 magnitudes.

[c]XTE J1814−338 was not detected; this value is the 3σ limiting magnitude.

source is not present in a 1989 Digitized Sky Survey[3] image to a limiting magnitude of $R \sim 20$: we therefore identify this source as the optical counterpart. Further refinement of the optical position is described below. Flux calibration for the first night was done using the photometric standard star Mark A (Landolt 1992), and calibration for the second night was made by fitting several in-field stars to the previous night's measurements; these values are shown in Table 2.1. Note that these fluxes replace the incorrectly calibrated values reported in Krauss et al. (2003). The optical counterpart brightened slightly over the course of the two days, paralleling the increase in X-ray flux over the same time period as measured by *RXTE*.

On 2003 June 21 and 24 we obtained additional *BVRI* images, again with the 6.5-m Magellan/Clay telescope, this time using the MagIC camera (field of view of $2.4' \times 2.4'$ with a scale of $0.069''$/pixel; the seeing on both nights was approximately $0.6''$—see Figure 2-1). We derived astrometric solutions using 75 sources from the 2MASS catalog (Cutri et al. 2001) and 49 sources from the USNO-B1.0 catalog. The fit using the 2MASS sources is significantly better than the one using the USNO-B1.0 sources, and yields RMS (root-mean-square) residuals of around $0.''07$ in each coordinate. From this, we derive an optical position of R.A.= $18^h13^m39\overset{s}{.}04$, Dec. $= -33°46'22.''3$ (equinox J2000.0) with a 90% confidence radius of $0.''2$ (the uncertainty is based on the astrometric accuracy of 2MASS, see e.g. Cutri et al. 2001). This position is $0.''25$ from the *Chandra*-derived X-ray position, well within the $0.''6$ *Chandra* error circle. This coincidence, the optical source's long-term as well as night-to-night variability, its blue color, and the emission lines seen by Steeghs (2003) argue strongly that it is the counterpart of XTE J1814−338.

The MagIC images were flux calibrated using the standard star Mark A2 (Landolt 1992), and the magnitudes of the counterpart are presented in Table 2.1. The counterpart on these later dates is on average a bit brighter than in the earlier observations, again agreeing with the observed X-ray flux of XTE J1814−338, which brightened from around 10 mCrab to around 12 mCrab before the second set of optical measurements were performed. See

---

[3]http://archive.stsci.edu/dss/index.html

Figure 2-2 for a plot of all optical data.

Finally, on 2004 March 15, while the source was in quiescence, we obtained an R-band image of the XTE J1814−338 field with the ESO Multi-Mode Instrument on the 3.5-m New Technology Telescope at the La Silla Observatory in Chile (field of view of $6.2' \times 6.2'$ with a scale of $0.167''$/pixel; the seeing was approximately $1.0''$). The counterpart was not detected in this observation with a 3σ limiting magnitude of $R = 23.3$.

2.3 X-ray spectroscopy

We extracted separate X-ray spectra for the MEG and HEG data, co-added the ± 1 orders, and constructed the corresponding auxiliary response files (ARFs) and redistribution matrix files (RMFs). We used the contamarf[4] tool to correct the ARF for a decrease in low-energy sensitivity due to contamination on the ACIS CCDs (see, e.g., Marshall et al. 2004). The count rate in the first-order MEG (HEG) spectrum was 2.9 (1.5) cts s^{-1}. To improve statistics, we grouped the spectra such that there was a minimum of 100 counts per bin and assumed Poisson errors. Background spectra were created using the script tg_bkg and subtracted prior to fitting. All fitting was performed using the XSPEC version 11.2 spectral analysis package.

Since the zeroth-order image is severely piled up, all spectral analysis was done on the dispersed first-order spectra, which are not affected by pileup. We fit the MEG and HEG spectra simultaneously over the total energy range 0.5–10 keV, including a normalization factor which was allowed to vary between the two instruments. We found the spectra to be best fit by an absorbed power-law plus blackbody model, where the equivalent hydrogen column density (N_{H}) is fixed to the Galactic value of 1.63×10^{21} cm^{-2} (Dickey and Lockman 1990). We note, however, that the flux in the blackbody component is only about 10% of that in the power-law component. We also fit an absorbed power-law with N_{H} allowed to vary, but the value did not deviate significantly from the Galactic value, justifying fits where this parameter is frozen. The results of spectral fitting are summarized in Table 2.2. Given that the fitted absorption is consistent with a column equal to the integrated Galactic value, it is likely that XTE J1814−338 lies at least 500 pc out of the Galactic plane. At the Galactic latitude of $b = -7.\!^{\circ}6$, this implies a distance of $\gtrsim 3.8$ kpc.

No significant spectral features (lines or edges) were observed. To quantify this, we searched the spectral residuals for Gaussian features of FWHM equal to 800 km s^{-1}, to match the velocity seen in the Hα emission (Steeghs 2003). The 3σ upper limits are approximately 0.05 Å at 15 Å and 0.02 Å at 2.5 Å. To date, high-resolution X-ray spectroscopy has been obtained for four MSPs: XTE J1751−305 (Miller et al. 2003), XTE J0929−314 (Juett et al. 2003), XTE J1807−294 (Campana et al. 2003), and XTE J1814−338. None have shown significant intrinsic spectral features, and the continua are generally well-fit by an absorbed power-law plus blackbody.

2.4 Discussion

2.4.1 Constraints on orbital parameters and companion type

We have identified the optical counterpart of XTE J1814−338. The combined optical and X-ray observations allow us to place several constraints on the system parameters. The

---

[4]Information about contamarf can be found at http://space.mit.edu/CXC/analysis/ACIS_Contam/ACIS_Contam.html
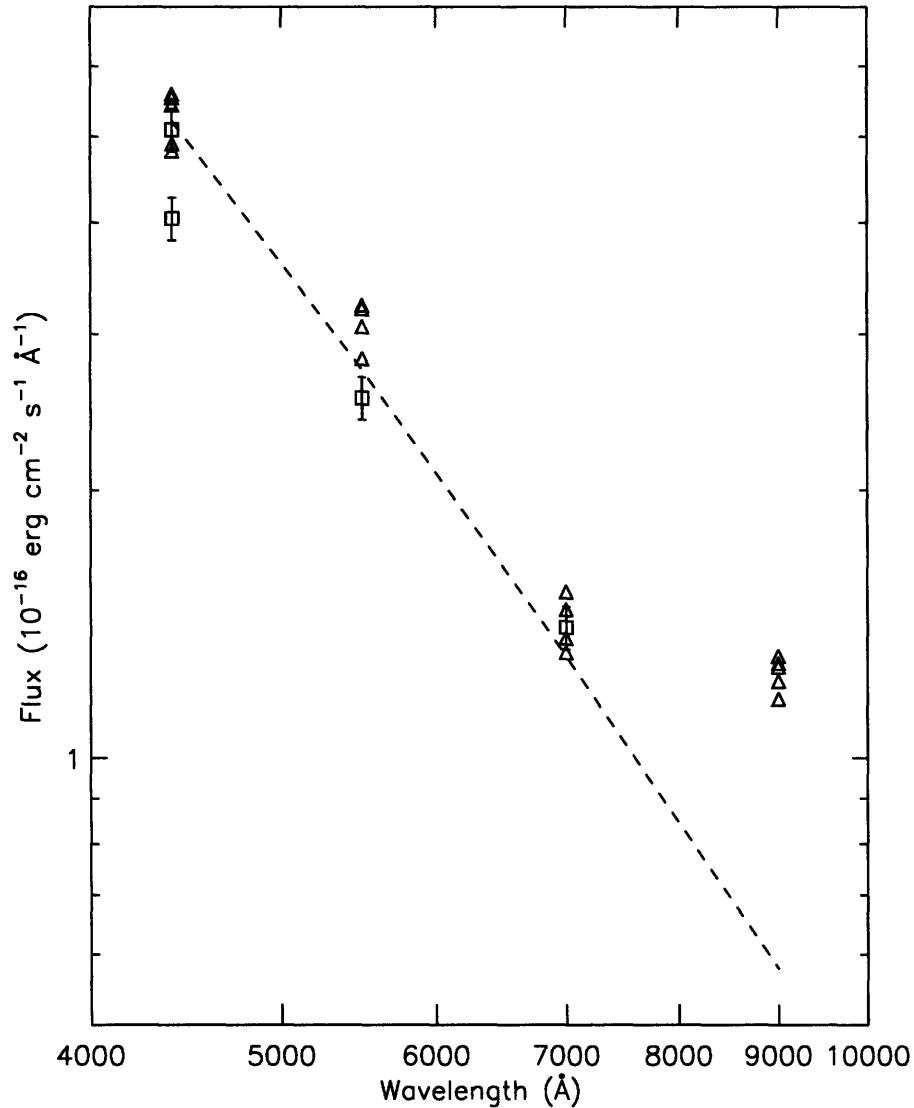
Figure 2-2: Optical data for XTE J1814–338. Measurements taken on 2003 June 6 and 7 are plotted as squares, whereas those from the nights of 2003 June 21 and 24 are shown as triangles (errors are on the order of the symbol size). The observed fluxes were dereddened assuming a Galactic extinction of $A_V = 0.71$. The emission predicted by an X-ray heated accretion disk model is plotted as a dashed line. For this model, we used a source distance of 8 kpc with Galactic extinction, and minimized χ^2 by setting $\cos i = 0.6$. Note that since these parameters are degenerate, the inclination angle fitted here is not well constrained. The I-band flux (9000 Å) lies well above the model prediction.

mass-radius relation for a low-mass Roche-lobe–filling companion in a 4.27 hr binary is $R_c = 0.28 \, (M_c/0.01 M_\odot)^{1/3} \, R_\odot$ (see, e.g., Frank et al. 2002). Given the measured neutron star orbital parameters (Markwardt et al. 2003c), the lack of an X-ray eclipse thus restricts the binary inclination (defined as the angle between the line of sight and the orbital angular momentum vector) to $i < 77°$ ($\cos i > 0.22$) for a Roche-lobe–filling companion. In

44

Table 2.2. Spectral fit parameters

| N_H (10^{21} cm^2) | Power-law[a] | | | Blackbody[a] | | | |
	Γ	A_1[b]	Flux[c]	kT_{in} (keV)	R_{km}[d]	Flux[c]	χ^2_ν (dof)
1.67 ± 0.17	1.36 ± 0.03	3.71 ± 0.15	3.1	$\cdots$	$\cdots$	$\cdots$	1.41 (405)
1.63 (fixed)	1.35 ± 0.02	3.68 ± 0.05	3.1	$\cdots$	$\cdots$	$\cdots$	1.41 (406)
1.63 (fixed)	1.41 ± 0.06	3.32 ± 0.11	2.6	0.95 ± 0.13	1.6 ± 0.3	0.3	1.29 (404)

[a]All errors quoted are the 90%-confidence range.

[b]The amplitude of the power-law is the flux at 1 keV in units of 10^{-2} photons keV^{-1} cm^{-2} s^{-1}.

[c]Fluxes are for the energy range 0.5–10 keV and are in units of 10^{-10} erg cm^{-2} s^{-1}.

[d]Blackbody radius assuming a distance to XTE J1814–338 of 8 kpc.

Figure 2-3, we compare the companion's mass-radius relation with the theoretical relation for low-mass hydrogen main sequence stars (Tout et al. 1996). An ordinary hydrogen-rich companion is consistent with the required relation for a mass $M_c \approx 0.54 M_\odot$ and $i \approx 21°$ ($\cos i \approx 0.93$), although this value has a small a priori probability of 7% for an isotropic sample of binary inclinations. We note, however, that bloating of a hydrogen-rich companion owing to X-ray heating could allow a somewhat less massive companion to fill its Roche lobe (Tout et al. 1989), permitting a slightly larger inclination angle with a higher a priori probability. A hydrogen main sequence companion is also consistent with the observed H and He lines in the optical spectra (Steeghs 2003), whereas a white dwarf companion can be excluded as too small to fill its Roche lobe for any plausible donor mass.

We can check the consistency of our above methods using the brightness of the optical counterpart. In general, optical counterparts of soft X-ray transients brighten in the V-band by $\Delta V \sim 2-7$ mag during outbursts (van Paradijs and McClintock 1995 Table 2.5). Since the counterpart in outburst is $V \approx 18.4$, we can assume $\Delta V < 7$ mag, an extinction of $A_V \geq 0.7$ due to Galactic dust along the line of sight (Schlegel et al. 1998), and a minimum distance of 6.4 kpc (corresponding to the lower limit of the distance estimate derived from the radius expansion burst, see Strohmayer et al. 2003) to estimate a limit on the V magnitude of a main-sequence companion of $V < 25.4$. We used the empirical mass-luminosity relation presented in Delfosse et al. (2000) to determine a minimum companion mass of ≈ 0.4 $M_\odot$ (corresponding to $i < 26°$ and $\cos i \gtrsim 0.90$). This companion mass and high value of $\cos i$ are consistent with the information derived from the period-density relationship. We note that increasing the assumed distance to XTE J1814–338 will increase the minimum companion mass and decrease the maximum inclination angle.

It is also instructive to consider what we can infer about the system given the $R > 23.3$ magnitude limit of the companion in quiescence. We again assume $A_V = 0.7$, and use the upper limit on the distance derived from the radius expansion burst of 9.6 kpc to give an absolute magnitude of $R = 7.9$. This corresponds to a main-sequence spectral type of later than M1 V and a mass of $M \lesssim 0.5$ $M_\odot$ (corresponding to $i > 22°$ and $\cos i \lesssim 0.93$). The significant harmonic content of the burst oscillations allow Bhattacharyya et al. (2005) to use general relativistic models in order to derive 90% confidence intervals on the neutron star inclination of $26° < i < 50°$ ($0.90 > \cos i > 0.64$). This range is in agreement with our
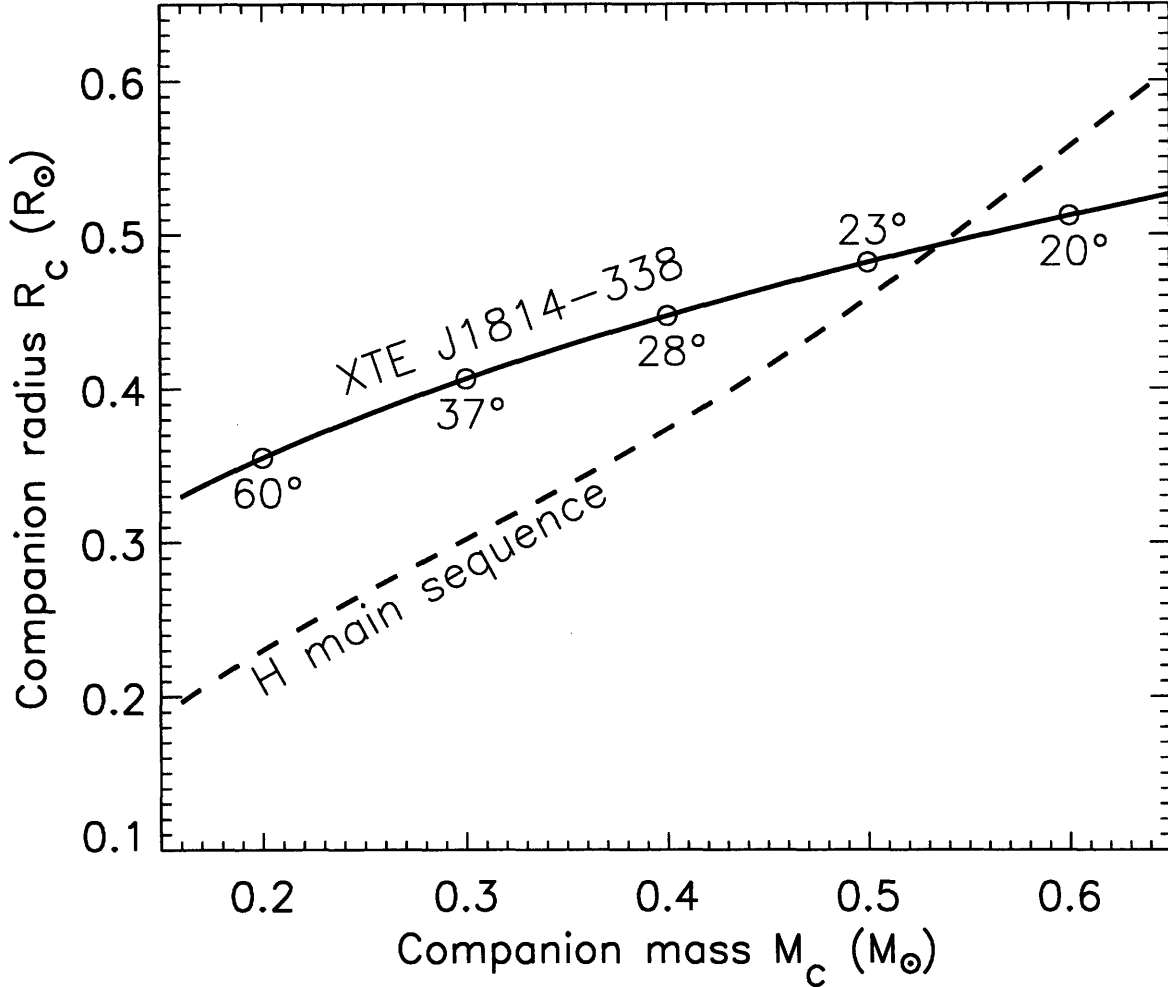
Figure 2-3: The mass-radius relationship for a Roche-lobe–filling companion of XTE J1814–338 (solid curve) and low-mass main-sequence stars (dashed curve) with corresponding inclination angles indicated. The dashed curve is based on the analytic mass-radius function presented in Tout et al. (1996). The intersection of the curves suggests a companion mass of $\approx 0.5~M_{\odot}$.

determination of the inclination angle from the magnitude limit of the optical counterpart ($i > 22°$) and lack of X-ray eclipse ($i < 77°$). However, their lower limit of $i > 26°$ is a bit higher than the value we calculate given the mass-radius relation for an ordinary main-sequence companion of $21°$, suggesting that the companion may be bloated as a result of X-ray heating. Finally, we note that the limit on the inclination angle derived from the empirical relation of $\Delta V_{\text{counterpart}} < 7$ mag of $i < 26°$ seems to be overly constraining, and note that the counterpart for this object may actually have $\Delta V_{\text{counterpart}} > 7$ mag.

2.4.2 Possible infrared excess

We would expect the optical emission from XTE J1814–338 to originate from the combination of an X-ray–heated accretion disk and companion. However, a simple X-ray–heated accretion disk model (Vrtilek et al. 1990; Chakrabarty 1998; Wang et al. 2001) is unable to account for the I-band data, which is systematically higher than predicted. (For a plot of

the optical data with a representative X-ray–heated accretion disk model, see Figure 2-2.) Although we do not have infrared data for XTE J1814−338, the sharp increase in flux in the I-band data suggests an IR excess with respect to the X-ray–heated disk model, similar to what was seen in the accretion-powered millisecond pulsar SAX J1808.4–3658 (Wang et al. 2001). First, let us consider the possibility that this emission arises from the companion: if we take its R-band magnitude to be $R = 23.3$ (the limiting magnitude for its non-detection in quiescence), and assume it to be an M-dwarf (in agreement with previous mass estimates), this corresponds to an I-band magnitude of $I \sim 21.8$ (again assuming $A_V = 0.71$). Although the companion could brighten due to X-ray heating during the outburst, in order for it to account for the excess flux, it would have to brighten to $I \sim 18$, corresponding to a more than 30-fold increase in flux from quiescence. We consider this to be highly unlikely. Furthermore, if the secondary were substantially heated, its surface brightness would be highly anisotropic, and we would expect to see I-band variability at the timescale of the orbital period. The 4.3-hour orbit is well-sampled on 21 June 2003, but we note that there is actually less variability at longer wavelengths (the percent RMS variability in B, V, R, and I is 11%, 9%, 6% and 4%, respectively.) An alternative possibility is that the I-band excess could originate from synchrotron emission related to the outburst (see, e.g., Fender 2001a).

2.5   Conclusions

Our precise X-ray position of the accretion-powered millisecond pulsar XTE J1814−338 has allowed us to identify its optical counterpart as well as obtain optical data during its 2003 outburst. The X-ray spectrum is featureless, and well-described by an absorbed power-law plus blackbody continuum. The lack of X-ray eclipses as well as the magnitude limit of $R > 23.3$ of the quiescent counterpart allow us to place constraints on the inclination of the system to be $22° \lesssim i \lesssim 77°$. Using the X-ray flux and measured radius-expansion burst distance of 8 kpc, we fit the optical data with an X-ray heated accretion disk model, and find that there is an excess of emission at the longest wavelengths, possibly extending into the infrared regime. This suggests that a non-thermal process is also contributing to the emission, which could arise from a jet. Future observations of XTE J1814−338 in outburst which span a large spectral range, including measurements in the visible as well as at IR and radio wavelengths, would further our understanding of the geometry and emission mechanisms of XTE J1814−338.

Chapter 3

X-ray Color-Color Diagrams of Accretion-Powered Millisecond Pulsars

3.1 Introduction: X-ray color-color diagrams

Low-mass X-ray binaries display a varied array of spectral and timing characteristics, but can often be classified as members of one of two groups: either as *Z* or *atoll* sources. As Hasinger and van der Klis (1989) and Schulz et al. (1989) first noted, there are distinctions between these two classes relating to their temporal behavior as well as their gross spectral characteristics, the latter of which which are well-represented on an X-ray color-color diagram.

A color-color diagram is constructed by dividing up the available X-ray bandpass from a given instrument into low-energy and high-energy (*soft* and *hard*) count ratios, which are then called *colors*, recalling a common method used in optical astronomy. However, unlike optical colors, there are no standardized bandpasses for X-ray colors; often, the energy ranges used in a given study depend on the observatory with which the observations were performed, as well as the type of X-ray sources under consideration. Furthermore, this method of analysis is necessarily instrument-dependent, since X-ray counts, not fitted spectral models, are used to determine the colors.

Despite these drawbacks, X-ray color-color diagrams have proven to be very useful in source classification, since Z and atoll sources have very distinct color behavior. These diagrams are also useful in identifying the spectral state a source is in during a particular observation. This ability motivated our exploration of the color-color diagrams of the accretion-powered millisecond pulsars (AMPs), since we use these diagrams to select spectra from comparison atoll sources while they were in a similar region of color space. We present the spectral analysis in Chapter 4.

3.1.1 Behavior of atoll sources

The color-color diagrams of atoll sources have been well-studied and are characterized by a distinctive pattern which is explored over a timescale of days to months. However, some sources are only observed in limited regions of the available color space, presumably because of incomplete sampling or because of an intrinsic lack of luminosity variability (Muno et al.
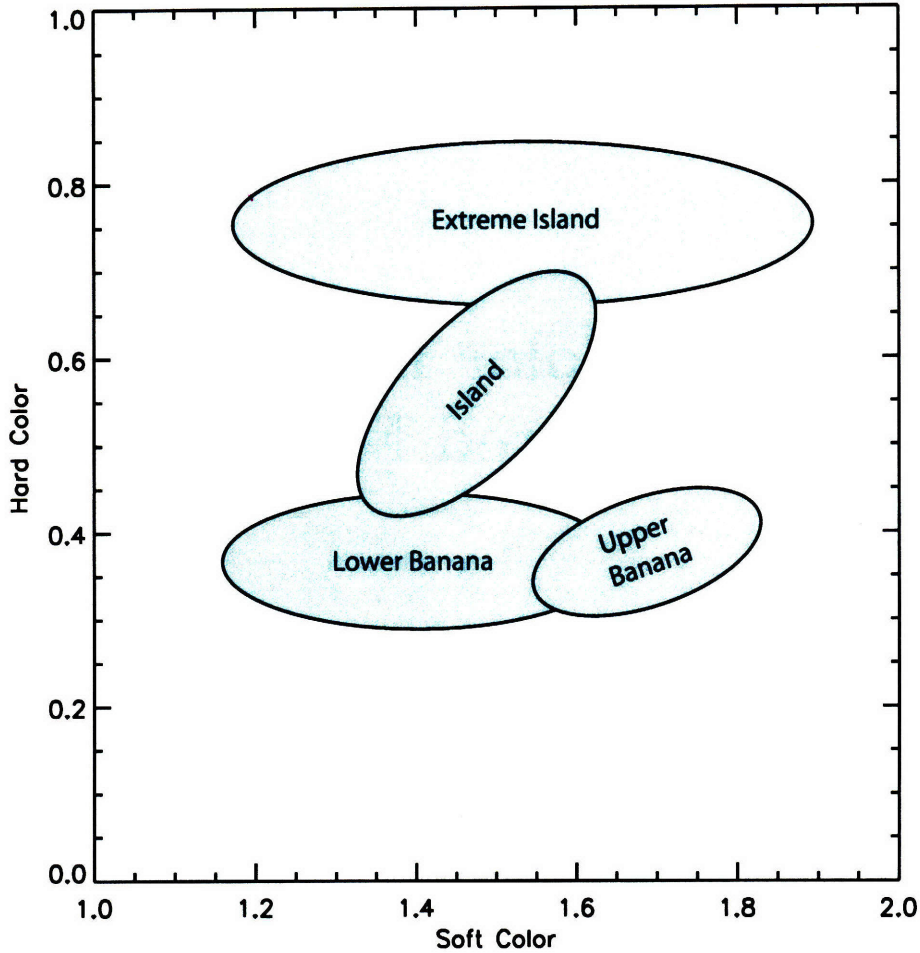
Figure 3-1: A schematic color-color diagram labeling the regions explored by typical atoll sources using the *RXTE* colors defined in this chapter.

2002).

Individual atoll sources can be highly X-ray variable, such as 4U 1608–522, which varies by a factor of $\cong$ 2000 (see, e.g., Muno et al. 2002). This is in contrast with the Z sources, which only vary by a factor of $\cong$ 3, and remain at high luminosities ($L_X \cong L_{Edd} = 3 \times 10^{38}$ ergs cm^{-2} s^{-1}; Ford et al. 2000). The atoll sources, some of which are transients, often become much fainter and do not reach luminosities as high as the Z sources.

The atoll color-color diagrams can be divided into three primary states which are correlated with source luminosity as well as timing behavior. Figure 3-1 shows a schematic representation using the *RXTE* colors defined in this chapter. The states with the hardest colors and lowest luminosities are often referred to as the *island* and *extreme island* states. The extreme island state, which describes the hardest, lowest-luminosity regime, forms a roughly horizontal region (see, e.g., Reig et al. 2000). In the island state, movement in color space is slow, and there is not a strong correlation between soft and hard color, often causing small islands of points to form. The highest-luminosity and softest state is called the *banana branch*, since it has positive curvature, and it can be further divided into upper and lower branches. The transition between states follows (roughly speaking) a path of increasing luminosity from the upper left portion of the diagram to the lower right. However,

the luminosity at which a transition to the extreme island state occurs may be substantially lower than that at which the transition to the banana branch had occurred; this hysteresis effect has been noted by, e.g., Maccarone and Coppi (2003a).

In this chapter, we explore the behavior of a sample of atoll sources as well as the accretion-powered millisecond pulsars on the color-color diagram. Subsequent to our analysis, work on this subject has been published by van Straaten et al. (2005) as well as Gladstone et al. (2007); we discuss our results and then summarize and comment on their papers in § 3.4. We explore the absolute luminosity behavior of these sources on the color-color diagram in § 3.5, and present our conclusions in § 3.6.

3.2 Color determination

As mentioned above, X-ray color-color diagrams are instrument-dependent, and therefore it is advantageous to compare sources which have been observed using the same satellite. All the known AMP sources have been observed multiple times with *RXTE*, as have numerous atoll sources, providing us with a well-sampled dataset. Relevant information about the sources for which we have created color-color diagrams is presented in Table 3.1. With the exception of HETE J1900.1-2455, these are also the sources for which we performed broadband X-ray spectral analysis in Chapter 4.

To create the X-ray color-color diagrams, we used data from the PCA instrument on *RXTE* (see Chapter 1 for more information about the PCA instrument and *RXTE* mission). We defined the hard color to be the background-subtracted counts in the 8.6–18.0 keV band divided by the counts in the 5.0–8.6 keV band, and the soft color to be (3.6–5.0 keV)/(2.2–3.6 keV). With these definitions, movement to the left or downward on the color-color diagram corresponds to a softening spectrum; clearly, the converse is true for spectral hardening. Our choice of colors provides a nice separation of the atoll source tracks in color space, and covers most of the PCA band (2.2–25.0 keV). Although all data are from the same instrument, the PCA detector gain has been varied several times during its operation, and the gain across individual PCUs varies as well. To account for these effects, we used the normalization factors calculated from the Crab spectrum as presented in Muno et al. (2002).

3.3 Source sample and individual behavior on color-color diagrams

Our source sample comprises the seven known AMPs as well as six atoll sources, for which we use 1553 *RXTE* observations totaling 6.11 Ms to create the color-color diagrams. The atoll sources are all known thermonuclear X-ray burst sources, though one (4U 1812-12) has not been seen to burst by *RXTE*. Their nature as bursters unambiguously identifies them as having neutron star primaries, like the AMPs, and also allows the spin period to be determined for the subset which exhibit burst oscillations. Following is a brief description of each source, as well as its color behavior during the *RXTE* observations. The color-color diagrams of individual atoll sources are presented in Figure 3-3; of individual AMPs, Figure 3-4; and of all AMPs and atolls plotted together, Figure 3-5. HETE J1900.1-2455 is presented separately in Figure 3-2.

Table 3.1. Source sample

Source name	$N_{\rm obs}$[a]	$\sum t_{RXTE}$[b] (ks)	Distance[c] (kpc)	Reference(s)[d]
Atoll sources				
4U 1608–522	439	1193	$3.7^{+0.9}_{-0.8}$	1
4U 1705–44	99	352	$6.7^{+1.2}_{-1.1}$	1
KS 1731–261	73	409	$6.4^{+1.8}_{-1.5}$	1
SAX J1748.9–2021	18	112	8.1 ± 1.3	1, 2
4U 1812–12	26	164	4.1 ± 1.2	3
Aquila X-1	312	1206	4.5 ± 1.3	1
Accretion-powered millisecond pulsars				
IGR J00291+5934	22	172	4 ± 2	6, 7
XTE J0929–314	35	119	10 ± 5	4, 5
XTE J1751–305	21	187	8 ± 5	5
XTE J1807–294	88	425	8 ± 5	4
SAX J1808.4–3658	217	1016	3.5 ± 0.1	8
XTE J1814–338	77	342	8 ± 2	1, 9
HETE J1900.1–2455	126	409	$4.2^{+1.2}_{-1.1}$	1

[a]The total number of RXTE observations included in the color-color diagrams. These include observations where both the hard and soft color error are < 5%, and the flux is source-dominated.

[b]The total observing time in the observations used to create the color-color diagram (see above).

[c]The distance determined from radius-expansion bursts depends on whether the burst is pure He or contains H as well. When the composition is unclear and we have information from Galloway et al. (2006), we use a distance that is the average value from models where $X = 0.7$ and $X = 0$.

[d]1—Galloway et al. (2006); 2—Kuulkers et al. (2003); 3—Cocchi et al. (2000); 4—Campana et al. (2005); 5—Wijnands et al. (2005); 6—Galloway et al. (2005); 7—Jonker et al. (2005); 8—Galloway and Cumming (2006); 9—Strohmayer et al. (2003).

3.3.1 Atoll sources

3.3.1.1 4U 1608–522

Thermonuclear X-ray bursts from the atoll soft X-ray transient 4U 1608–522 were first detected by the Vela-5 satellites (Belian et al. 1976), and the source of these bursts was determined by subsequent *Uhuru* observations (Tananbaum et al. 1976). The identification and study of the optical counterpart, QX Nor, indicates that it is either an F- or G-type main sequence star or a lower-mass, evolved star (Grindlay et al. 1978; Wachter et al. 2002). Wachter et al. (2002) also identified an optical periodicity of ≈ 0.55 days, which they identify with either an orbital or a superhump period, the latter of which would require an evolved secondary to satisfy $M_2/M_1 \lesssim 0.33$—a necessary condition if the disk eccentricity is caused by the 3:1 orbital resonance.

The outbursts of 4U 1608–522 have recurrence timescales of a few months to ≈ 2 years, and there is a wide variety in both outburst duration as well as peak intensity (Lochner and Roussel-Dupre 1994; Šimon 2004). This system also exhibits states intermediate to outburst and quiescence, which Wachter et al. (2002) term *low-intensity states*. These states are difficult to explain in the context of the standard disk instability model (see § 1.1.2), but could be related to the stabilizing effects of X-ray irradiation of the disk.

Burst oscillations indicate that the neutron star primary is spinning at a frequency of 619 Hz, making it the fastest known neutron star in an LMXB system (Muno et al. 2001; Hartman et al. 2003). Some bursts from 4U 1608–522 also appear to be Eddington-limited, from which a distance of $3.7^{+0.9}_{-0.8}$ kpc is derived (Nakamura et al. 1989; Galloway et al. 2006).

The frequency with which *RXTE* has observed this source (439 times in 11.7 years, for a total of 1193 ks) allows for a very well-sampled color-color diagram. Over its numerous outbursts, 4U 1608–522 explores color space quite thoroughly, forming a very well-sampled diagram which spans luminosities from $\approx 10^{35}$–4×10^{37} ergs s^{-1}.

3.3.1.2 4U 1705–44

4U 1705–44 was first detected in observations by the *Uhuru* satellite (Forman et al. 1978), and thermonuclear X-ray bursts were subsequently discovered in *EXOSAT* data (Langmeier et al. 1987). The source is persistent but highly variable. Although two possible periodicities have been reported (1.3 hr and 223 days; Sztajno et al. 1985; Priedhorsky 1986), the true orbital period is not known.

Analysis of radius-expansion X-ray bursts leads to a distance estimate of $6.7^{+1.2}_{-1.1}$ kpc (Haberl and Titarchuk 1995; Galloway et al. 2006). However, no burst oscillations have been detected, so the spin of the neutron star has yet to be determined.

The source spectrum contains a broad Fe Kα line (White et al. 1986), and a recent high-resolution spectrum obtained by *Chandra* indicates that there may be several other emission lines from Mg XII and S XVI (Di Salvo et al. 2005). Despite the precise X-ray position from the *Chandra* observation, there is no known optical counterpart.

Since 4U 1705–44 is highly variable, and *RXTE* has observed it 99 times (352 ks) over a period of 9 years, the full pattern of its color-color diagram is nicely traced out. It is seen to vary from $\approx 10^{36}$–6×10^{37} ergs s^{-1}.

3.3.1.3 KS 1731–261

KS 1731–261 is a long-duration X-ray transient, first discovered in 1989 by the *Mir-Kvant* observatory, which also found it to be a source of thermonuclear X-ray bursts (Sunyaev et al. 1990). It exhibits two classes of type-I bursts, short- and long-duration ($\tau \approx 16$ and 7 s, respectively). The former are associated with periods when the source is in the banana branch, and are likely He-dominated, whereas the latter occur during the island states, and are probably fueled by a mix of H and He (Muno et al. 2000). Burst oscillations at 524 Hz have been observed in the short bursts (Smith et al. 1997), and radius-expansion episodes indicate that the system is at a distance of $6.4^{+1.8}_{-1.5}$ kpc (Muno et al. 2000; Galloway et al. 2006). KS 1731–261 also had a 12-hr long *superburst* (thought to be a result of unstable carbon burning) in 1996, following which there were no X-ray bursts for over 35 days (Kuulkers et al. 2002)

Early in the outburst, a 38-day periodicity was detected by Revnivtsev and Sunyaev (2003), but it was not present in the more variable later portions of the outburst. Though these authors do not consider it to be a likely candidate for a binary period, they suggest it could be a disk precession period, which would indicate a binary period of 1–3 days. The infrared counterpart indicates that if the companion is a main sequence star, it is spectral type F or later (Orosz et al. 2001; Mignani et al. 2002).

KS 1731–261 entered quiescence in 2001 after about 12 years of X-ray activity. *Chandra* and *XMM-Newton* observations of the source in quiescence show the neutron star to be very faint. Assuming that it was deeply heated during its period of accretion, this implies that it must have cooled quite rapidly or that the system must undergo extremely long periods of quiescence (thousands of years; Wijnands et al. 2001, 2002). This argues for enhanced cooling of the neutron star core, perhaps due to neutrino production (Rutledge et al. 2002b; Wijnands et al. 2002).

The color-color diagram of KS 1731–261 is relatively well sampled, and includes 73 *RXTE* observations totaling 409 ks. These span the 4.5 years during which the *RXTE* mission overlapped with the outburst (from 1996–2001). The overall luminosity varies by over an order of magnitude ($\approx 10^{36}$–3×10^{37} ergs s^{-1}), and the source displays interesting color behavior similar to what is seen in XTE J1751–305 (see § 3.3.2.3). When KS 1731–261 is in the higher-luminosity portion of the extreme island state, the soft and hard colors are strongly correlated, despite the fact that some of the observations are separated by a substantial period of time.

3.3.1.4 SAX J1748.9–2021

X-rays from the globular cluster NGC 6440 ($d = 8.4^{+1.5}_{-1.3}$ kpc, Kuulkers et al. 2003; Harris 1996; Ortolani et al. 1994) were first observed by the MIT instrument aboard *OSO-7* (Markert et al. 1975). Subsequent analysis of *Uhuru* observations showed that this source behaves much like other Galactic X-ray transients in that it was quiescent throughout the two-year observation window save the ≈ 2 month-long outburst (Forman et al. 1976a).

The next observed outburst from a source in NGC 6440 (though perhaps not the same system) occurred 27 years later in 1998, and was detected both by the instruments on *Beppo-SAX* as well as with the *RXTE* ASM. During the 2-week period of activity, thermonuclear X-ray bursts were observed, confirming that the source is a neutron star X-ray binary (in 't Zand et al. 1999). Following this outburst, Pooley et al. (2002) observed NGC 6440 in quiescence with *Chandra*, and found 24 X-ray sources of which one (CX1) likely corresponds

to the transient ($L_{X,quiesc.} \approx 10^{33}$ ergs s^{-1}). Furthermore, a possible optical counterpart was identified, based on its variability and blue color (source V2, Verbunt et al. 2000). In 2001, another outburst occurred, and NGC 6440 was observed as a target of opportunity by *Chandra*, confirming that SAX J1748.9–2021 is associated with CX1 and with V2 (in 't Zand et al. 2001). During this 20 day outburst, 16 bursts were detected by *RXTE*, one of which has marginally significant burst oscillations at a frequency of 409.7 Hz (Kaaret et al. 2003). Of these bursts, 6 show evidence for radius expansion, and the distance derived (assuming they are He-dominated) of 8.1 ± 1.3 kpc agrees well with the globular cluster distance (Galloway et al. 2006).

Another outburst occurred in 2005, during which 2 bursts were observed by the *RXTE* PCA (in ObsIDs 91050-03-02-00 and 91050-03-03-00), but none of these results have been published and the data are not yet in the burst database, so they are not included in the color-color diagrams presented here.

Since the outbursts from SAX J1748.9–2021 tend to be relatively short, and there have not been many PCA observations, the color-color diagram is rather sparsely sampled (18 observations comprising 112 ks). Nonetheless, this is an interesting source to include in our sample, since it is in a globular cluster and has a well-determined distance. Even with a relatively small dataset, SAX J1748.9–2021 is observed both in the island and banana states, spanning luminosities from 4×10^{36}–3×10^{37} ergs s^{-1}.

3.3.1.5 4U 1812–12

4U 1812–12 is a persistent X-ray source, though it maintains a relatively low luminosity of $L_X \approx 10^{36}$ ergs s^{-1}, and is also somewhat variable. It has been observed by a number of X-ray missions; earlier ones include *Uhuru* (Forman et al. 1976b, 1978), *OSO 7* (Markert et al. 1979), *Ariel V* (Warwick et al. 1981), *HEAO 1* (Wood et al. 1984), *EXOSAT* (Warwick et al. 1988), and *ROSAT* (Voges et al. 1999). Thermonuclear X-ray bursts were first observed by the *Hakucho* satellite as part of a Galactic center monitoring campaign (Murakami et al. 1983), and subsequent observations by the *BeppoSAX* WFC (as part of its Galactic Bulge monitoring campaign) found 8 bursts, 7 of which show signs of radius expansion (Burderi et al. 1997; Cocchi et al. 2000). From these data, Cocchi et al. (2000) derive a distance of 4.1 kpc.

A precise position was obtained by a *Chandra* observation (Wilson et al. 2003), which allowed Bassa et al. (2006) to find an $R = 22.15$ optical counterpart. Given its well-determined distance, this is intrinsically fainter than expected for most LMXBs, implying that it may be an ultracompact system. An ultracompact nature is also supported by its persistent behavior despite its low X-ray luminosity (see, e.g. in 't Zand et al. 2005).

Throughout the lifetime of *RXTE*, 4U 1812–12 has been an ASM source at a level of $\approx$ 20 mCrab (Barret et al. 2003). However, there have not been many pointed PCA observations (26 for a total of 164 ks). This, combined with the low burst rate of the source (Murakami et al. 1983; Cocchi et al. 2000; Tarana et al. 2006; Galloway et al. 2006), makes it unsurprising that no thermonuclear bursts have been detected in any PCA observations. The color-color diagram shows that during this time the source is in the extreme island state.

3.3.1.6 Aquila X-1

Aql X-1 was discovered by early rocket flights (see, e.g., Friedman et al. 1967), and remains an active recurrent transient with an outburst cycle of $\approx$ 10 months (Kaluzienski et al. 1977; Maccarone and Coppi 2003a). The outbursts typically last around a month, during which time the source exhibits thermonuclear X-ray bursts (first seen by *Hakucho*; Koyama et al. 1981), which sometimes display burst oscillations, revealing a neutron star spin period of 549 Hz (Zhang et al. 1998). The 1999 outburst was monitored extensively by Maccarone and Coppi (2003b) with *RXTE*, who found that the X-ray spectra are well-fit by a thermal Comptonization model with spherical geometry and a significantly higher optical depth in the soft state ($\tau \approx 10$) than the hard state ($1 \lesssim \tau \lesssim 4$). We find similar values for the optical depth in Chapter 4. Maccarone and Coppi (2003a) also observed an X-ray burst while the source was in the extreme island state, and find evidence for a significant decrease in the high energy flux following the burst, suggesting that the soft burst photons were able to cool the corona.

The optical counterpart is a K6-M0 V star, but its proximity to a slightly brighter star makes quiescent studies of the system challenging (Thorstensen et al. 1978; Chevalier et al. 1999). A likely orbital period at 19 hr was first reported by Chevalier and Ilovaisky (1991), and recent optical observations of the counterpart in outburst show signs of orbitally-modulated lines (Cornelisse et al. 2007). If these lines do, in fact, originate on the secondary, their properties suggest that the neutron star is relatively massive ($M \geq 1.6 M_\odot$).

Aql X-1 has been observed in quiescence a number of times, with *ROSAT* (Verbunt et al. 1994); *ASCA* (Asai et al. 1998); *BeppoSAX* (Campana et al. 1998); and *Chandra* (Rutledge et al. 2001, 2002b). All observations have been consistent with blackbody emission, though some seem to have a hard tail as well. The *Chandra* observations also show that the quiescent source is variable over the 5 month period of the observations, suggesting that there may be low-level accretion occurring between the outburst states.

RXTE has observed Aql X-1 312 times for a total of 1206 ks and finds that it varies from 9×10^{34}–4×10^{37} ergs s^{-1} over the course of the outbursts, resulting in a quite well sampled color-color diagram. Its movement on the color-color diagram and its state transitions have been extensively studied, and they are found to display hysteresis: the luminosity at which the source transitions to the banana branch is significantly higher than that at which it goes back to the extreme island state (see, e.g., Reig et al. 2004; Maitra and Bailyn 2004).

3.3.2 Accretion-powered millisecond pulsars

3.3.2.1 IGR J00291+5934

IGR J00291+5934 is the sixth accretion-powered millisecond pulsar to be discovered, and the first to be found initially by the *INTEGRAL* observatory as an X/γ-ray source (Shaw et al. 2005; Galloway et al. 2005). At 599 Hz (Markwardt et al. 2004b), it is the fastest known AMP, and has a mass function of $2.81 \pm 0.02 \times 10^{-5}$ $M_\odot$ and an orbital period of 2.46 hr (Markwardt et al. 2004a). Considerations of the orbital parameters and lack of X-ray eclipses or dips indicate that the companion star is likely a hot brown dwarf (Galloway et al. 2005). During its 15-day outburst in December 2004, Falanga et al. (2005b) find a spin-up rate of 8.4(6) $\times 10^{-13}$ Hz s^{-1} .

The distance is not well-constrained, since no burst activity has been observed. Shaw et al. (2005) estimate that it is likely < 3.3 kpc based on the column density of neutral material along the line of sight, whereas Galloway et al. (2005) set the apparent long-term

accretion rate equal to the accretion rate expected from gravitational-radiation-driven mass transfer and find $d \gtrsim 4$ kpc. We adopt a value of 4 kpc for our analysis.

A precise X-ray position obtained by *Chandra* (Paizis et al. 2005) agrees with the position of both the radio and optical counterparts (Fender et al. 2004; Pooley 2004; Fox and Kulkarni 2004). Follow-up *Chandra* observations after IGR J00291+5934 entered quiescence show evidence for spectral variability, and comparison with a serendipitous *ROSAT* observation from 1992 indicates that the source has a comparable quiescent flux after its recent outburst (Jonker et al. 2005).

An apparent hardening at the end of the outburst is due to the presence of the nearby intermediate polar V709 Cas (Falanga et al. 2005b), so we have filtered out times after MJD 53354, leaving a total of 22 PCA observations (172 ks) with which to create the color-color diagram. IGR J00291+5934 remains in a very compact region of the diagram throughout its outburst, with no large changes in hard or soft color.

3.3.2.2 XTE J0929–314

This ultracompact binary system ($P_{orb} = 43.6$ min) was active from April–June 2002, and has the smallest known mass function of any stellar binary system, $f_X = 2.7 \times 10^{-7} M_\odot$ (Galloway et al. 2002). The third AMP to be discovered, it has 185 Hz pulsations, and the companion star has a mass of $\cong 0.01 M_\odot$ and is likely a helium white dwarf. Assuming that the long-term accretion rate is driven by gravitational wave emission, Galloway et al. (2002) find that $d \gtrsim 5$ kpc.

A high-resolution *Chandra* spectrum obtained during the outburst is consistent with the expected amount of interstellar absorption (Juett et al. 2003), and the X-ray position agrees with both the radio and optical counterparts (Rupen et al. 2002; Giles et al. 2005). The optical counterpart shows variability at the binary period, as well as a variable *R*- and *I*-band excess, which could be due to synchrotron emission from outflowing material (Giles et al. 2005 ; see also Chapter 5). *Chandra* has also observed XTE J0929–314 in quiescence, at which time the luminosity was found to be $7^{+5}_{-2} \times 10^{31}$ $(d/10$ kpc$)^2$ (Wijnands et al. 2005).

The color-color diagram comprises 116 ks in 35 PCA observations. XTE J0929–314 remains in the extreme island state for the duration of its outburst, and shows only a small amount of color variability.

3.3.2.3 XTE J1751–305

The Galactic bulge source XTE J1751–305 is an AMP with a frequency of 435 Hz and is in an ultracompact binary orbit ($P_{orb} = 42.4$ min), with a 0.013–0.035 $M_\odot$ companion that is likely a He white dwarf (Markwardt et al. 2002). It was discovered when it went into a 10-day outburst in April 2002. A previous outburst was detected by the *RXTE* ASM in 1998 (Markwardt et al. 2002), and the source was also briefly detected by *INTEGRAL* in 2005 (Grebenev et al. 2005), suggesting a recurrence time of ≈ 3 years. A high-resolution *XMM-Newton* spectrum obtained by (Miller et al. 2003) reveals a featureless continuum. The quiescent source was not detected by *Chandra*, placing an upper limit on the quiescent luminosity of $L_{X,q} \lesssim 10^{32}$ ergs s^{-1} $(d/8$ kpc$)^2$ (Wijnands et al. 2005).

Although there is a precise *Chandra* position for the source, no optical or infrared counterpart has been found. Assuming the mass accretion rate is driven by gravitational wave emission, Markwardt et al. (2002) find that the source is at least 7 kpc away; its association with the Galactic bulge suggests that $d \approx 8$ kpc, which is the value we adopt

here. At this distance, the lack of detection of a counterpart is not unexpected considering the short-period orbit and probable companion type (Jonker et al. 2003).

During its 2002 outburst, the PCA obtained 21 observations of XTE J1751–305 for a total of 187 ks of exposure time. There is a strong correlation between the soft and hard colors, and the color-color diagram traces a straight line from right to left as the source progresses in its outburst. For a source distance of 8 kpc, XTE J1751–305 achieves the highest outburst luminosity of any of the AMPs; however, it remains in the extreme island state and does not make a transition to the banana branch.

3.3.2.4 XTE J1807–294

This Galactic plane ultracompact binary ($P_{orb} = 40.1$ min) was in outburst for 4 months from February–March 2003. Also the fourth accretion-powered millisecond pulsar, it was discovered by *RXTE*, and found to have a spin frequency of 190 Hz (Markwardt et al. 2003b). Its companion is likely a C-O white dwarf, based on considerations of the orbit and inclination constraints (Falanga et al. 2005a). Although a precise *Chandra* position was obtained (Markwardt et al. 2003a), there has been no identification of a longer-wavelength counterpart. A non-detection of XTE J1807–294 in quiescence gives a limit of $L_{X,quiesc.} \lesssim 4 \times 10^{31}$ $(d/8$ kpc$)^2$ ergs s^{-1} (Campana et al. 2005).

A high-resolution *XMM-Newton* spectrum reveals a featureless continuum (Campana et al. 2003), whereas the timing properties of the source are more interesting. XTE J1807–294 contains twin kHz QPOs with a frequency separation approximately equal to the spin frequency of the neutron star ($\Delta\nu \approx 205$ Hz; Linares et al. 2005). This is different from what is seen in SAX J1808.4–3658, where $\Delta\nu \approx \nu_{spin}/2$.

The color-color diagram comprises 88 PCA observations totaling 425 ks. Throughout the outburst, XTE J1807–294 remains in the extreme island state, though there is a softening trend as the source flux declines. There are also three small flare-like events which correspond to a softening of the spectrum. Zhang et al. (2006) found that during these periods, the pulse profile becomes more sinusoidal, and the frequency of the QPOs is seen to increase, suggesting a close link between inner disk instability and activity on the neutron star surface. These events are not visible in the color-color diagram as we have parametrized it, but note that similar behavior is also observed in HETE J1900.1–2455 during which time the hard color is affected.

3.3.2.5 SAX J1808.4–3658

SAX J1808.4–3658 was initially discovered as an X-ray transient by *BeppoSAX* in 1996, during which time it was also found to produce type-I X-ray bursts (in 't Zand et al. 1998). During its second outburst (1998), it was the first source to be identified as a millisecond pulsar, with a spin frequency of 401 Hz (Wijnands and van der Klis 1998). It is in a 2-hour binary orbit, which is also manifested in the X-ray lightcurve as slight dips, suggesting that it is a relatively high-inclination system (Chakrabarty and Morgan 1998). Its companion is likely an X-ray heated, $M \approx 0.05M_{\odot}$ brown dwarf (Bildsten and Chakrabarty 2001). Combining information from the long-term accretion rate as well as Eddington-limited and apparently helium-rich type-I X-ray bursts, Galloway and Cumming (2006) find a distance to SAX J1808.4–3658 of ≈ 3.5 kpc.

Its optical counterpart is also seen to vary at the orbital period (Giles et al. 1999), and often is found to have an infrared excess relative to the spectral shape expected from an X-

ray heated accretion disk (Wang et al. 2001; Greenhill et al. 2006). This excess is sometimes seen to follow a type-I X-ray burst, and may be due to synchrotron emission from ejected material. Furthermore, a radio transient was seen at the position of SAX J1808.4–3658 just after end of its 1998 outburst; this too is likely associated with an ejection event (Gaensler et al. 1999 ; see also Chapter 5).

SAX J1808.4–3658 has a fairly regular outburst recurrence interval of ≈ 2 yr (September 1996, April 1998, January 2000, October 2002, and June 2005), with source activity lasting for about a month. Outbursts often have "ringing" at the end, where the luminosity fluctuates on timescales of $\approx$ a week (Wijnands et al. 2001). *XMM-Newton* observations of SAX J1808.4–3658 in quiescence find $L_{\mathrm{X,quiesc.}} \approx 10^{32}$ ergs s^{-1} (assuming a distance of 3.5 kpc; Campana et al. 2002).

A number of thermonuclear X-ray burst sources are found to have burst oscillations, which were posited to come from the surface of the neutron star and thus indicate its spin frequency. However, without stable pulsations, this was not certain. SAX J1808.4–3658 was the first pulsar to exhibit burst oscillations, which, as expected, were found to be at the spin frequency of the neutron star. This allows for the inference of the neutron star spin in the other burst oscillation sources, which show a distribution in spin frequency that is cut off at just over 600 Hz, suggesting that there is a speed limit, likely enforced by (and therefore an indirect detection of) the emission of gravitational radiation (Chakrabarty et al. 2003).

RXTE has observed SAX J1808.4–3658 217 times for a total of 1016 ks. Despite this extensive coverage, the source occupies a very limited region in color space, remaining in the extreme island state for the duration of its outbursts.

3.3.2.6 XTE J1814–338

XTE J1814–338 was the fifth AMP to be discovered (Markwardt and Swank 2003), and the second found to have burst oscillations at its spin frequency. The burst oscillations also have significant power in the first harmonic, which is not seen in other burst oscillation sources (Strohmayer et al. 2003). This has allowed Bhattacharyya et al. (2005) to use general relativistic models to fit the burst oscillation lightcurves and derive an inclination angle constraint of $i > 20°$. Furthermore, Watts and Strohmayer (2006) find that, unlike what Muno et al. (2003) observed in the other burst oscillation sources, the fractional amplitude of the signal actually decreases with energy. Although numerous thermonuclear X-ray bursts have been observed, only one shows any sign of radius expansion. If this burst is, in fact, Eddington-limited, it places XTE J1814–338 at a distance of ≈ 8 kpc (Strohmayer et al. 2003; Galloway et al. 2006).

A *Chandra* observation found a featureless X-ray spectrum and obtained a precise position that allowed for the identification of the optical counterpart. The counterpart is found to have an infrared excess relative to the prediction for an X-ray heated accretion disk, possibly due to synchrotron emission (see Chapter 2). XTE J1814–338 also has the longest orbital period of any of the known AMPs ($P_{\mathrm{orb}} = 4.3$ hr; Strohmayer et al. 2003), which, combined with the magnitude limit of the quiescent optical counterpart, implies that the companion is likely a H-burning main sequence star of spectral type M3 V or later (Bhattacharyya et al. 2005; Krauss et al. 2005)

During its outburst, *RXTE* observed XTE J1814–338 77 times for a total exposure of 342 ks. Although it remains mostly in the hard portion of the color-color diagram, it explores a bit more of color space as the source fades. There is also one anomalous point with a hard color of 0.67 and soft color of 1.68 which corresponds to ObsID 80418-01-05-04
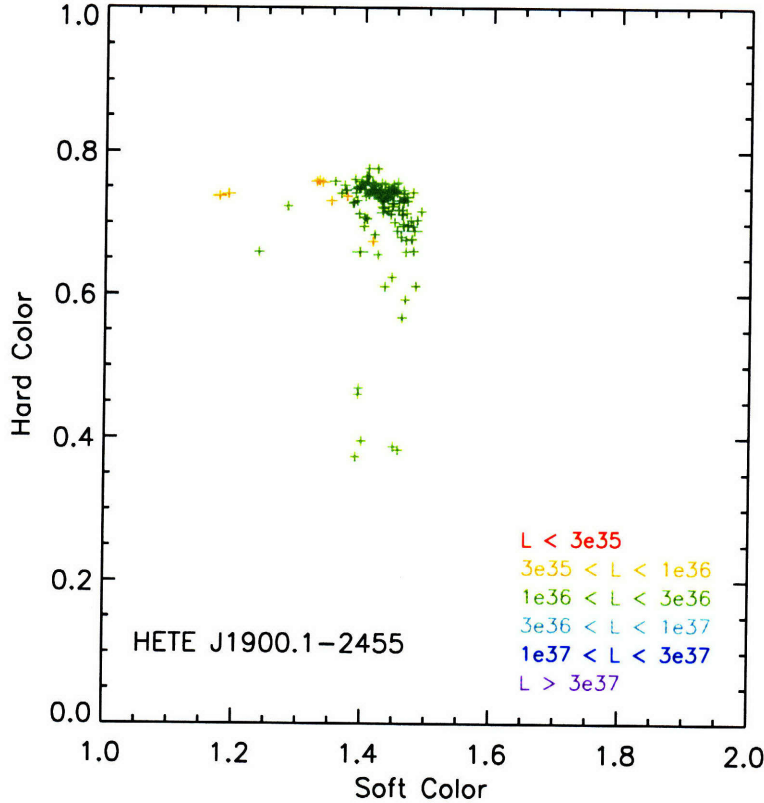
Figure 3-2: The color-color diagram of HETE J1900.1–2455. Note the excursions into the region usually identified as the island state; this is not seen in the other accretion-powered millisecond pulsars.

(MJD 52827.3; a few days before the source flux began to decline precipitously). Although there is a slight increase in flux during this observation, it is quite minimal, and there do not appear to be any missed bursts or other events in the X-ray lightcurve, suggesting that for a brief time the spectral shape was fundamentally different.

3.3.2.7 HETE J1900.1–2455

The most recently discovered AMP source, HETE J1900.1–2455, was initially detected by the *HETE-2* satellite during a bright type-I X-ray burst in June 2005 (Vanderspek et al. 2005). Subsequent observations revealed pulsations at 377 Hz and an orbital period of 83.3 min, as well as a likely brown dwarf companion (Kaaret et al. 2006). From Eddington-limited X-ray bursts, Kawai and Suzuki (2005) and Galloway et al. (2006) derive a distance of $4.2^{+1.2}_{-1.1}$ kpc.

Over the first ≈ 2 months of the outburst, the strength of the persistent pulsations seems to be correlated with the occurrence of the thermonuclear X-ray bursts. The pulsation amplitude decreases over time, then increases substantially after a burst, convolved with a general fading trend. Pulsations have not been detected at all after this time, even following the occurrence of bursts (Galloway et al. 2007b). Nonetheless, the source remains active, and now appears as an ordinary low-luminosity X-ray transient It has been in outburst for over a year and a half, significantly longer than any other AMP (the longest other outburst being that of XTE J1814–338, which lasted ≈ 50 days). A simultaneous *RXTE* and

INTEGRAL spectrum taken after the pulsations turned off found that the X-ray data from 2–200 keV is well-described by blackbody plus Comptonized emission. However, the fitted optical depth is relatively low ($\tau \approx 2$); and not a likely explanation for the suppression of pulsations (Falanga et al. 2007 ; see also Chapter 4)

HETE J1900.1–2455 has also displayed interesting color behavior. This source was intensively monitored by *RXTE* during the early period of its outburst, and has been observed $\approx$ weekly since, for a total of 126 observations (409 ks). Slightly less than a month into the outburst, a single *RXTE* observation caught the source in a higher-luminosity, soft state, during which time Kaaret et al. (2006) also detected a 883 Hz QPO. The source then rapidly faded, accompanied by spectral hardening. This type of behavior has since been observed four more times. The resulting color-color diagram reveals a source that spends most of its time in the extreme island state, but has excursions to what would be considered the island state if the source were a traditional atoll (see Figure 3-2).

3.4   Atoll sources and accretion-powered millisecond pulsars on the color-color diagram

Individual color-color diagrams of our sample of atoll sources are presented in Figure 3-3, and of accretion-powered millisecond pulsars in Figure 3-4. Both sets of sources are plotted in single panes in Figure 3-5. All the plots use a common range for the axes, facilitating easy comparison between the sources. While each source has some unique features, the diagrams show that there is a significant difference in the range of color space explored by the accretion-powered millisecond pulsars compared with the atoll sample. The majority of atoll sources make excursions to the higher-luminosity, softer banana state, but none of the AMPs show this behavior, instead remaining in a hard, lower-luminosity state for the duration of their outbursts. The only possible exceptions to this rule are the brief excursions made by HETE J1900.1-2455 to a softer, but not quite banana, state; see § 3.3.2.7 and Figure 3-2, and evidence from timing behavior that SAX J1808.4–2658 was briefly in the lower-left banana state (van Straaten et al. 2005 ; see below).

Therefore, one would expect the spectra of atoll sources to be most similar to those of the AMPs when they are in the extreme island state. This information provides an important selection criterion for our analysis of their X-ray spectra in Chapter 4 since we want to compare the Compton optical depths of these sources while they are in similar states.

Subsequent to our initial work (Krauss and Chakrabarty 2004), two related papers of note have been presented by other groups. Van Straaten et al. (2005) studied the color and timing features of a set of AMPs (SAX J1808.4–2658, XTE J1751–305, XTE J0929–314, and XTE J1814–338), and found them to be very similar to atoll sources. Of particular interest, they found that during four observations of its 2002 outburst, SAX J1808.4–3658 displayed timing characteristics indicative of the lower left banana state. During this time, the hard color softens, but not as dramatically as what is seen in the atoll sources. While their hard color changes by $\gtrsim$ 30%, it is only $\sim$ 5% for SAX J1808.4–3658, and remains blended with other observations in our color-color diagram. This is interesting behavior, and indicates that state changes among AMPs may affect their colors more subtly than the atoll sources—perhaps detailed timing analysis will be the best way to probe changes in other sources in the future. By the same token, it will be necessary to apply timing analysis to the anomalous softer observations of HETE J1900.1–2455 to determine whether
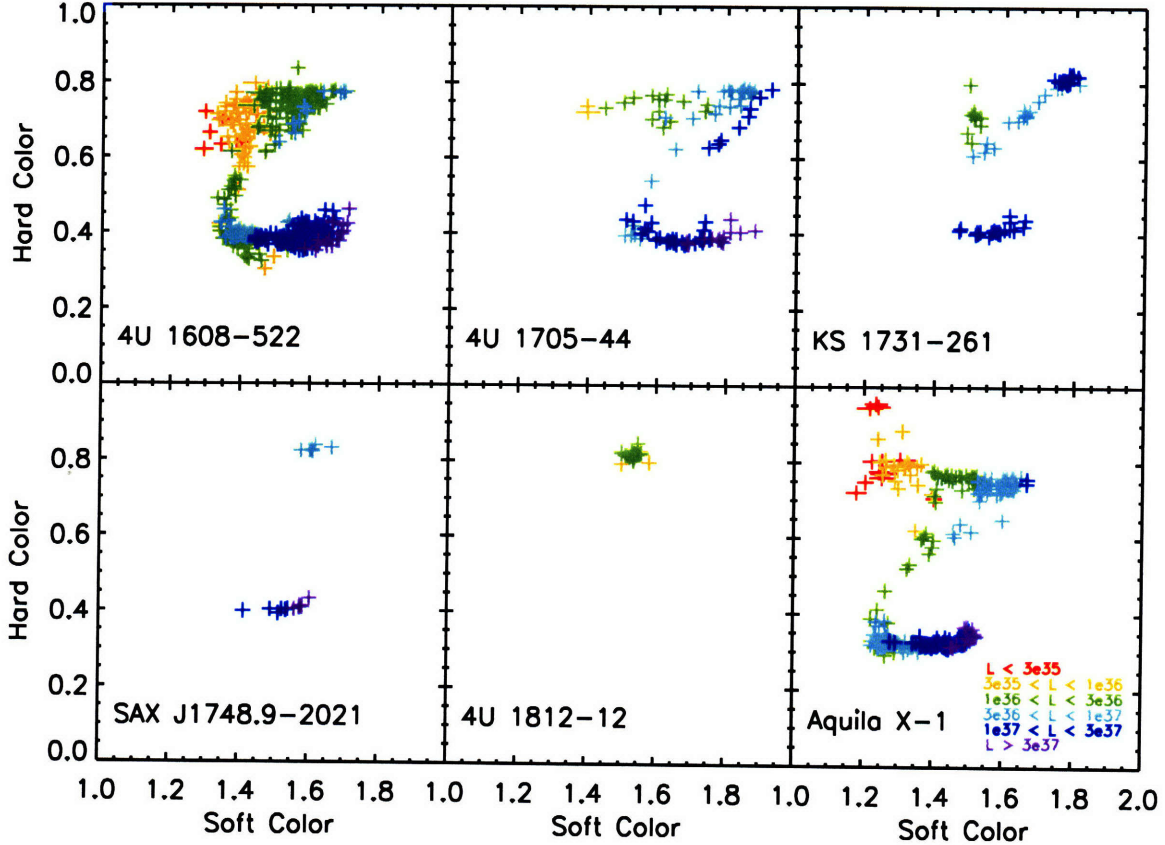
Figure 3-3: Color-color diagrams from *RXTE*/PCA observations of a subset of atoll sources. Each point represents an individual PCA observation, and the luminosity is color-coded based on the distances listed in Table 3.1 and the average PCA flux measurement from 2.5–25.0 keV.

they represent a state transition.

Van Straaten et al. (2005) also note that the hard and soft colors of XTE J1751–305 are highly correlated. They remark that this is different from what is seen in most other AMPs and atoll sources, which typically do not have correlated colors while in the extreme island state. However, we note that it closely resembles the hard portion of the color-color diagram of KS 1731–261. For KS 1731–261, the pattern is traced out over a widely spaced set of observations, rather than observations from a single short-duration outburst like that of XTE J1751–305. Despite this fact, the color and luminosity behaviors of these two sources are quite similar.

The second paper (Gladstone et al. 2007) analyzed all *RXTE* observations of atoll and AMP sources, and created color-color and color-luminosity diagrams. These authors identify two source types based on their behavior on these diagrams: those with vertical and those with diagonal transitions to the banana branch. They find that the diagonal sources transition at a significantly higher luminosity ($L/L_{\rm Edd} \approx 0.1$) than the vertical sources ($L/L_{\rm Edd} \approx 0.02$), and suggest that if the AMPs were to reach a high enough luminosity to make a transition, they would appear as verticals. Gladstone et al. (2007) note that these effects are different from the hysteresis that is seen in some atoll sources, notably Aql X-1 and 4U 1608–52. If, however, SAX J1808.4–2658 did transition to a banana state in its 2002 outburst, the transition it made looked much more diagonal than vertical (see Figure 13 of
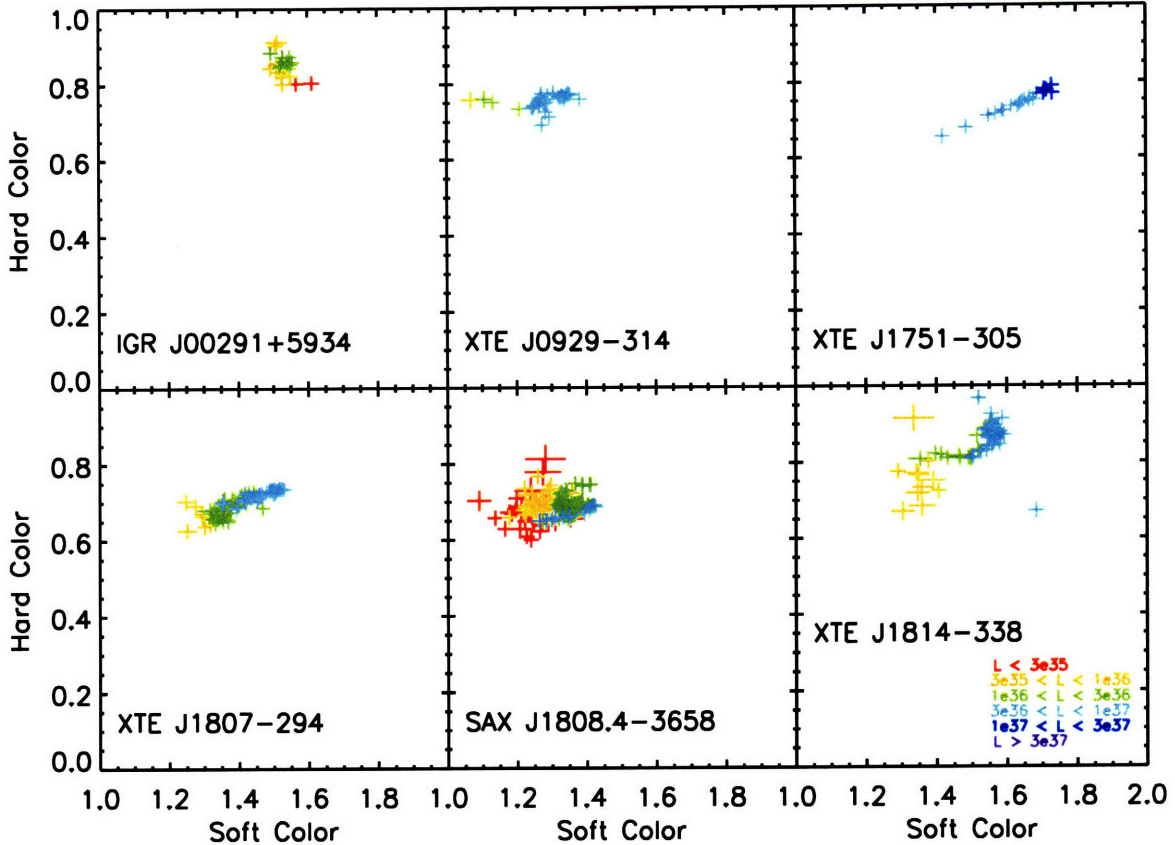
Figure 3-4: Color-color diagrams from *RXTE*/PCA observations of all known accretion-powered millisecond pulsars (except HETE J1900.1–2455, which is shown in Figure 3-2.) Each point represents an individual PCA observation, and the luminosity is color-coded based on the distances listed in Table 3.1 and the average PCA flux measurement from 2.5–25.0 keV.

van Straaten et al. 2005), so the situation may not be so simple. We also note that of their sample of 5 vertical-transition sources, the highest luminosity reached before a transition to the banana state is $L/L_{Edd} \sim 0.05$, whereas 3 out of 7 of the AMP sources are found to exceed this luminosity without making a transition.

3.5 Luminosity regimes of the color-color diagram

The persistent 2.5–25.0 keV flux for each *RXTE* PCA observation has been determined using an absorbed power-law plus blackbody model adding, when necessary, a Gaussian component to account for the presence of a 6.4 keV iron line. For bright sources where this model does not adequately describe the spectral shape, a Comptonized continuum model was used instead (Galloway et al. 2006). Using the best available distances (see Table 3.1), we have converted these fluxes to luminosities, and set the colors of the points on the color-color diagrams according to source luminosity. This reveals some interesting characteristics of both the AMPs and atoll sources. Although there are no regions occupied exclusively by a given luminosity range, it is clear that the upper left portion of the diagram contains only low-luminosity intervals and the lower right only periods of high luminosity. This behavior has already been well-established for the atoll sources, although we are not aware of the
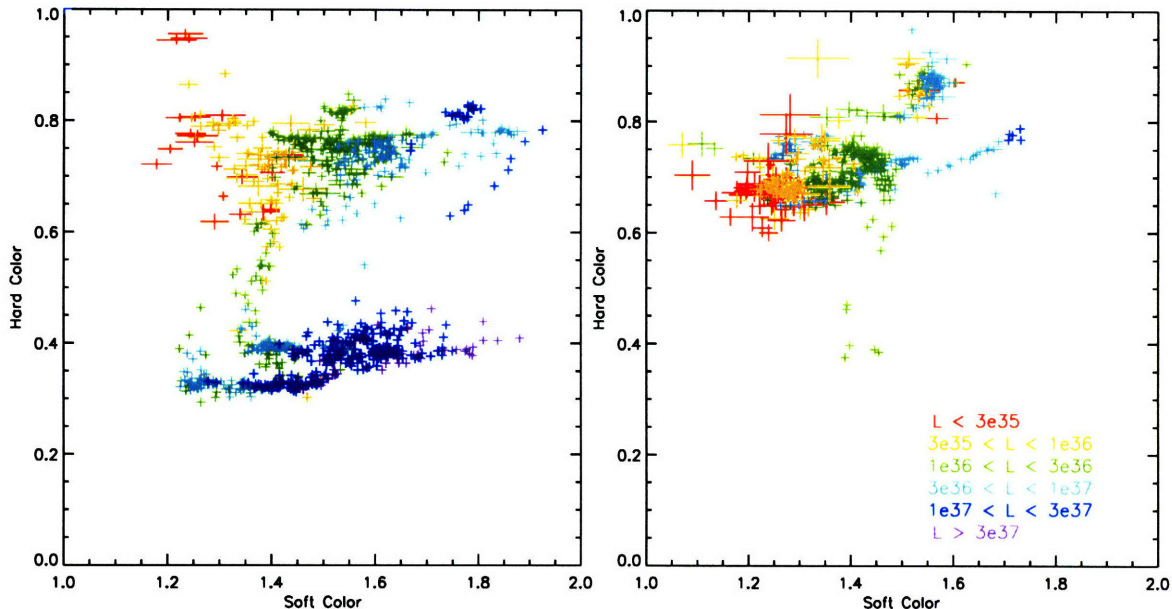
Figure 3-5: Left panel: a color-color diagram that includes all *RXTE*/PCA observations of our sample of atoll sources. **Right panel:** a similar figure for the known accretion-powered millisecond pulsars. Note that they remain in the hard portion of the diagram with the exception of a few observations of HETE J1900.1–2455. The source luminosities of both panels are color-coded according to the key in the lower right.

diagrams having been presented in this fashion. Of more interest is the comparison between the overlapping AMP and atoll diagrams (left and right panels of Figure 3-5). One can see that the color-luminosity relationship is very similar for both source classes, but that the AMPs do not attain the high luminosities seen in some of the atolls and therefore do not explore the color space as fully.

Among the AMP sources, XTE J1751–305 is the only one which appears to exceed a luminosity of 10^{37} ergs s^{-1}, which, among many of the atoll sources, is the luminosity at which a transition to the banana state occurs. However, the only AMP which explores the transition region of color space is HETE J1900.1–2455, and it does so at a significantly lower luminosity. This is still consistent with what is seen in the atoll sample, and in the nomenclature of Gladstone et al. (2007) would classify the source as a "vertical", as these authors suggested the AMP sources would likely be.

3.6   Conclusions

The color-color diagrams of the accretion-powered millisecond pulsars are quite like those of the atoll sources in the extreme island state. Therefore, they exclusively occupy the region where hard color > 0.6. The only exception is the unusual source HETE J1900.1−2455 which has made several excursions to a softer portion of the diagram. This similarity in color suggests a similarity in spectral characteristics between the AMP sources and the atoll sources while they are in the extreme island state.

In addition, the luminosity behavior with respect to color looks much the same for the AMPs and atolls—the lower-luminosity states are associated with the extreme island region, with a softening of the spectrum as the source luminosity decreases further. This

similarity suggests that the most significant difference between these sources is that the accretion-powered millisecond pulsars have lower luminosities than the atoll sources, and therefore are likely to have lower overall accretion rates as well. Since accreted material may significantly diminish the magnetic field of the neutron star, this difference could play a major role in the suppression of persistent pulsations from the atoll sources.

Clearly, while color-color diagrams are a useful tool for exploring the properties of LMXBs, they do not complete the picture—detailed spectral and timing analyses are necessary. A significant question regarding neutron star LMXBs is why the AMP systems show persistent pulsations while atolls do not, despite the fact that we know many contain a neutron star with a millisecond spin period. One possibility is that the pulsations have been rendered undetectable by a scattering medium, which would also alter the overall spectral properties of the system. The color-color diagrams presented here provide a useful tool for selecting comparison spectra from atoll sources while they are in a similar spectral state to the AMP sources. We present further exploration of these spectra in Chapter 4.

Chapter 4

Compton Fitting of Accretion-Powered Millisecond Pulsar and Atoll Spectra

4.1 Introduction

Before concrete evidence emerged, it had long been suspected that neutron stars in accreting binary systems were spinning extremely rapidly as a result of the accretion torque applied to the neutron star. The equilibrium spin period would, of course, depend on a given neutron star's magnetic field, but since the field strengths of neutron stars in LMXBs are generally low ($\sim 10^8$ G), the resulting spin could be in the millisecond range. Quasi-periodic, but highly coherent, oscillations were detected during thermonuclear X-ray bursts from a number of sources, and were generally thought to arise from the neutron star surface. However, without coherent pulsations it was not possible to unequivocally state that they were tracing the spin frequency of the neutron star.

In 1998, coherent millisecond pulsations were discovered from the LMXB SAX J1808.4−3658 (Wijnands and van der Klis 1998). This confirmed theoretical predictions of the expected neutron star spin frequency, and searches continued to find persistent pulsations from other sources. Since then, seven more accretion-powered millisecond pulsars (AMPs) have been found (see Table 4.1), with spin periods ranging from 1.7–5.4 ms. Of these, four systems also exhibit thermonuclear X-ray bursts (SAX J1808.4−3658, XTE J1814−338, IGR J00291+5394, and HETE J1900.1−2455).

In 2003, burst oscillations were seen from SAX J1808.4−3658 at the same frequency as the coherent pulsations (Chakrabarty et al. 2003). This firmly linked the burst oscillation frequency to the spin frequency of the neutron star, establishing that the larger set of burst oscillation sources also have rapidly rotating neutron star primaries. The question remained, however, why more neutron stars in LMXBs are not seen as persistent pulsators.

There are several possible explanations for this observation. One is that the surface dipole magnetic field of the pulsars is stronger than those of the other neutron stars, and more effectively channels accreting material to the magnetic poles. However, considerations of their high-energy spectra suggest that the magnetic fields of non-pulsating neutron stars are similar to the AMP fields (see, e.g., Psaltis and Lamb 1998). This does not eliminate the possibility that short-term processes are changing the field strengths. One such process could be screening of the field by the accreted material, with re-emergence of the field ex-

Table 4.1. Known accretion-powered millisecond X-ray pulsars

Source	NS per. (freq.) ms (Hz)	P_{orb} (min)	Year discovered	Probable binary companion
IGR J00291+5934	1.7 (599)	147.4	2004	Brown dwarf
XTE J0929−314	5.4 (185)	43.6	2002	$\cdots$
XTE J1751−305	2.3 (435)	42.4	2002	He WD
SWIFT J1756.9−2508	5.5 (182)	54	2007	$\cdots$
XTE J1807−294	5.2 (191)	40.1	2003	[C/O WD]
SAX J1808.4−3658	2.5 (401)	120.8	1998	Brown dwarf
XTE J1814−338	3.2 (314)	256.5	2003	Low-mass MS star
HETE J1900.1−2455	2.6 (377)	83.3	2005	Brown dwarf

pected to occur on a timescale of 100-1000 yr after the cessation of accretion. Cumming et al. (2001) consider this possibility, and find that for accretion rates $> 10^{-2}$ $\dot{M}_{Edd}$, screening could effectively bury the field. In fact, this rate may be even lower—Gladstone et al. (2007) found a that the AMPs all have long-term accretion rates $\lesssim 10^{-3}$ $\dot{M}_{Edd}$. At such low accretion rates, it is possible that their magnetic fields remain unburied and thus they remain pulsars.

Another possibility is that all of these sources are, in fact, persistent pulsators, but material in the line of sight obscures the pulses for all but the AMPs (Titarchuk et al. 2002). As the photons travel through this material, they will be Compton-scattered, smearing out any pulses which may be present (see Figure 4-1). The emergent spectrum will be a combination of the thermal photons from the blackbody surface (and perhaps from the disk, see § 1.1.9 for a discussion of X-ray spectra from LMXBs), as well as a Comptonized continuum. The optical depth of the Comptonized component could thus indicate how strong an effect the scattering material would have on emission from the neutron star surface. If this picture is correct, one would expect the measured optical depths of the pulsars to be substantially lower than those of non-pulsating LMXBs.

The most natural set of LMXBs with which to compare the AMPs are the atoll sources. These have the most similar (aperiodic) X-ray timing signatures (van Straaten et al. 2005), and also overlap in X-ray color space, suggesting that the underlying spectra are similar (see Gladstone et al. 2007 as well as Chapter 3). Therefore, we have selected the six known AMPs at the time of analysis as well as six atoll sources, all of which have a substantial number of public *RXTE* observations. The observations we have chosen for analysis are presented in Table 4.2. Information for the individual sources is presented in Chapter 3. We fit all the spectra with a Comptonization model including, where needed, an additional blackbody component and/or an iron line.

4.2 Data analysis and results

For each source, we analyzed two long-duration *RXTE* observations, taking care to select datasets where the atoll sources were in the extreme island state, where the AMP sources reside. We utilize data from both the PCA and HEXTE instruments to get the broadest energy range possible (2.9–250 keV). The high-energy data from HEXTE are important
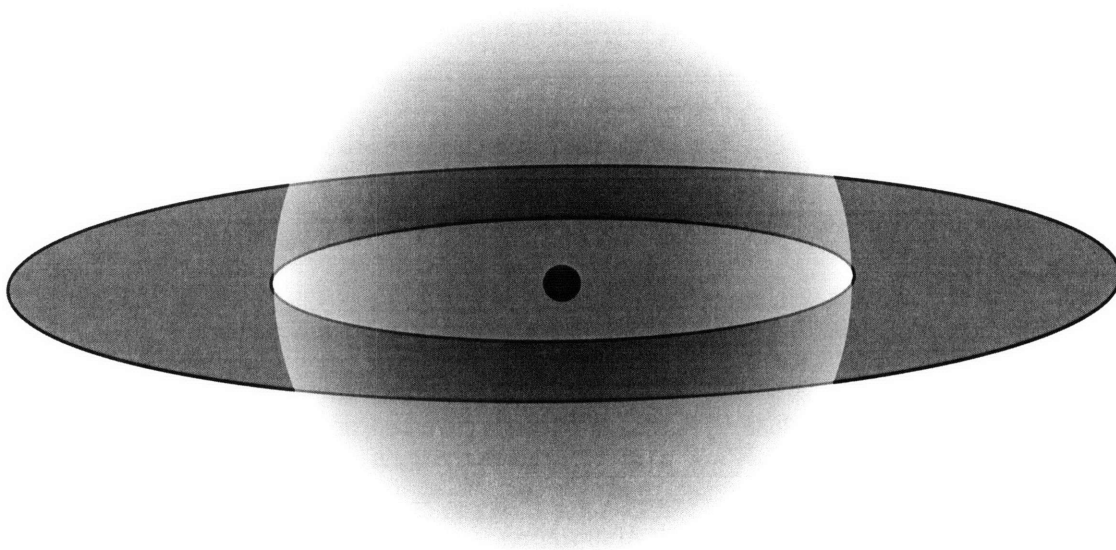
Figure 4-1: Schematic illustration of a neutron star LMXB in the "low/hard", or island, state. The inner edge of the accretion disk has withdrawn from the neutron star, and a Comptonizing region of hot plasma surrounds the neutron star.

because they help constrain the spectral shape in a region where Comptonization often results in a steep decline (see Figure 1-7).

The PCA comprises five proportional counter units (PCUs), each of which provides an independent source spectrum (see Chapter 1 for more information about the *RXTE* instruments). In order to better estimate the systematic errors of our spectral fitting results, we extracted individual spectra from each PCU and fit each spectrum separately. To create the spectra, we used all detector layers, and constructed appropriate response files to match. We subtracted a model background spectrum prior to fitting, applying a count rate threshold of 40 counts s^{-1} pcu^{-1} to determine whether we used the bright or faint background model.[1] We extracted separate spectra for HEXTE Clusters A and B, and used a combination of the "plus" and "minus" background data unless one was contaminated by an off-axis source. We applied appropriate deadtime corrections and created matching response files. All fitting was performed using XSPEC v.11.3.1.

We simultaneously fit the PCA and HEXTE spectra, restricting the energy range for the PCA (HEXTE) to extend from 2.9–25.0 (18.0–250.0) keV. We fit the data with an absorbed Comptonization spectrum (`wabs` × `compTT`), including a blackbody component (bbodyrad) or iron line (modeled as a gaussian) when preferred at the $\geq 3\sigma$ as determined by an f-test. The `compTT` model uses an analytic approximation to represent the Compton β parameter as a function of the optical depth τ (Hua and Titarchuk 1995). For this model, we use spherical geometry, since we expect the hot electrons to reside in a roughly spherical corona surrounding the neutron star. Using a disk geometry would have resulted in lower values of τ for given values of β, but would not have affected our conclusions. In the cases where a blackbody is present, we set the Compton input soft photon temperature equal to the blackbody temperature, since this is a physically reasonable, and because otherwise

---

[1]Further information of PCA background estimation can be found at http://heasarc.gsfc.nasa.gov/docs/xte/pca_news.html.

69

Table 4.2. Source sample

Source	Spin freq. (Hz)	ObsIDs
Accretion-Powered Millisecond Pulsars		
IGR J00291+5934	598	90425-01-01-13, 90425-01-01-10
XTE J0929−314	185	70096-03-06-00, 70096-03-07-01
XTE J1751−305	435	70131-01-04-00, 70131-01-01-00
XTE J1807−294	191	80145-01-02-04, 80145-01-02-06
SAX J1808.4−3658	401	30411-01-06-00, 30411-01-08-00
XTE J1814−338	314	80418-01-03-00, 80418-01-04-00
Atoll sources		
4U 1608−522	620	30062-01-03-00, 50052-05-01-01
4U 1705−44	⋯	20161-01-02-01, 40034-01-09-00
KS 1731−260	524	50031-02-03-030, 50031-02-02-030
SAX J1748.9−2021	410	30425-01-01-00, 60084-02-01-04
4U 1812−12	⋯	30701-13-03-01, 20090-01-02-00
Aquila X-1	549	40048-01-08-00, 40033-10-02-00

these parameters are not well constrained. Where an iron line is present, we limit its width to be < 1 keV, so that it does not interfere with the other spectral components. We present the fit results in Table 4.3.

Table 4.3: Results of Compton fits to AMP and atoll sources[a]

Source	N_H[b] $(10^{22}$ cm$^{-2})$	Blackbody kT (keV)	Amp.	CompTT Photon T (keV)	Electron T (keV)	Opt. Depth (τ)	Norm $(\times 10^{-3})$	χ^2_ν (DOF)
			Accretion-Powered Millisecond Pulsars					
IGR J00291+5934	0.28	$0.43^{+0.05}_{-0.11}$	93^{+76}_{-63}	$0.43^{+0.08}_{-0.21}$	56^{+12}_{-9}	$2.35^{+0.37}_{-0.41}$	$0.0020^{+0.0013}_{-0.0003}$	1.13 (570)
	0.28	$0.37^{+0.05}_{-0.06}$	$270^{+9.5\times10^4}_{-270}$	$0.37^{+0.05}_{-0.07}$	$42.9^{+7.4}_{-7.2}$	$2.93^{+0.48}_{-0.38}$	$0.0017^{+0.0008}_{-0.0004}$	1.08 (566)
XTE J0929−314	0.076	$0.62^{+0.01}_{-0.02}$	47^{+35}_{-15}	$0.62^{+0.09}_{-0.10}$	230^{+290}_{-70}	$0.45^{+0.25}_{-0.18}$	$0.00031^{+0.00017}_{-0.00009}$	1.38 (437)
	0.076	$0.61^{+0.89}_{-0.04}$	58^{+41}_{-26}	0.61 ± 0.03	72^{+25}_{-17}	$1.59^{+0.71}_{-0.27}$	$0.0009^{+0.0032}_{-0.0002}$	0.91 (728)
XTE J1751−305	1.60 ± 0.54	$\cdots$	$\cdots$	$0.55^{+0.03}_{-0.10}$	$57.^{+15}_{-8}$	$1.75^{+0.43}_{-0.23}$	$4.06^{+0.89}_{-0.74}$	0.89 (713)
	3.02 ± 0.13	$\cdots$	$\cdots$	$0.36^{+0.03}_{-0.18}$	$18.9^{+0.8}_{-1.0}$	$4.35^{+0.19}_{-0.16}$	$0.026^{+0.268}_{-0.002}$	0.95 (571)
XTE J1807−294	0.63	$\cdots$	$\cdots$	$0.42^{+0.05}_{-0.06}$	$22.9^{+5.0}_{-1.5}$	$3.47^{+0.22}_{-0.47}$	$6.91^{+0.72}_{-0.88}$	0.90 (432)
	0.63	$0.6^{+1.1}_{-0.1}$	30^{+320}_{-16}	$0.57^{+0.02}_{-0.04}$	44^{+12}_{-7}	$2.04^{+0.50}_{-0.28}$	$0.0024^{+0.0003}_{-0.0005}$	1.02 (571)
SAX J1808.4−3658	0.12	0.64 ± 0.03	98^{+83}_{-35}	$0.64^{+0.12}_{-0.08}$	$25.5^{+4.2}_{-1.4}$	$3.78^{+0.21}_{-0.38}$	$7.1^{+1.1}_{-1.2}$	1.01 (733)
	0.12	0.61 ± 0.02	96^{+93}_{-33}	0.61 ± 0.02	425^{+44}_{-27}	0.18 ± 0.03	$0.00029^{+0.00015}_{-0.00007}$	1.44 (586)
XTE J1814−338	0.17	$\cdots$	$\cdots$	$0.57^{+0.08}_{-0.09}$	$20.5^{+1.7}_{-0.8}$	$5.18^{+0.15}_{-0.23}$	$0.0039^{+0.0003}_{-0.0004}$	1.05 (431)
	0.17	$\cdots$	$\cdots$	$0.06^{+0.18}_{-0.03}$	$20.2^{+1.3}_{-0.8}$	5.07 ± 0.21	$0.02^{+0.13}_{-0.004}$	0.93 (575)

Table **4.3** – Continued

Source	N_H[b] (10^{22} cm^{-2})	Blackbody		CompTT				χ^2_ν (DOF)
		kT (keV)	Amp.	Photon T (keV)	Electron T (keV)	Opt. Depth (τ)	Norm ($\times 10^{-3}$)	
				Atoll Sources				
4U 1608−522	1.5	0.70 ± 0.03	$84._{-35}^{+70}$	$0.70_{-0.08}^{+0.11}$	$29.5_{-2.0}^{+2.2}$	$3.79_{-0.25}^{+0.24}$	$6.97_{-0.65}^{+0.88}$	1.26 (733)
	1.5	$0.61_{-0.03}^{+0.15}$	103_{-27}^{+70}	0.61 ± 0.01	50_{-4}^{+24}	$2.28_{-0.54}^{+0.19}$	$0.0024_{-0.0006}^{+0.0021}$	0.98 (575)
4U 1705−44	1.47 ± 0.31	$\cdots$	$\cdots$	$0.721_{-0.026}^{+0.025}$	$25.5_{-1.7}^{+2.6}$	$3.95_{-0.26}^{+0.24}$	$5.09_{-0.68}^{+0.56}$	0.90 (586)
	2.4 ± 1.2	$0.77_{-0.11}^{+0.12}$	37_{-34}^{+50}	0.77 ± 0.08	19.4 ± 0.8	$4.87_{-0.20}^{+0.21}$	$0.0105_{-0.0010}^{+0.0011}$	0.89 (714)
KS 1731−260	1.0	$0.69_{-0.06}^{+1.27}$	30_{-10}^{+200}	0.69 ± 0.04	83_{-40}^{+83}	$1.43_{-0.43}^{+0.98}$	$0.0006_{-0.0002}^{+0.0024}$	1.03 (713)
	5.9 ± 1.1	$0.52_{-0.04}^{+0.03}$	900_{-380}^{+740}	0.52 ± 0.03	$15.83_{-0.58}^{+0.63}$	$5.44_{-0.22}^{+0.21}$	$0.031_{-0.003}^{+0.014}$	1.16 (567)
SAX J1748.9−2021	3.6 ± 1.0	0.61 ± 0.11	120_{-90}^{+180}	$0.61_{-0.25}^{+0.13}$	$20.7_{-1.2}^{+1.3}$	$4.84_{-0.28}^{+0.27}$	$7.0_{-0.7}^{+1.7}$	1.11 (728)
	3.5 ± 3.5	$0.57_{-0.09}^{+0.12}$	280_{-280}^{+460}	$0.569_{-0.068}^{+0.069}$	$20.0_{-4.6}^{+5.4}$	5.1 ± 1.3	$0.0055_{-0.0017}^{+0.0059}$	0.85 (426)
4U 1812−12	1.1	0.66 ± 0.03	$50._{-15.}^{+42.}$	$0.66_{-0.15}^{+0.19}$	$31._{-20.}^{+42.}$	$4.5_{-1.6}^{+1.7}$	4.5 ± 1.8	0.98 (586)
	1.1	$0.59_{-0.04}^{+0.52}$	35_{-21}^{+86}	0.59 ± 0.04	259_{-22}^{+23}	$0.51_{-0.11}^{+0.18}$	$0.00024_{-0.00005}^{+0.00059}$	1.28 (733)
Aquila X-1	0.5	0.73 ± 0.06	$54._{-19.}^{+34.}$	$0.73_{-0.16}^{+0.10}$	$26.3_{-1.7}^{+1.5}$	$4.10_{-0.16}^{+0.20}$	$6.56_{-0.36}^{+0.82}$	1.26 (429)
	0.5	$0.73_{-0.04}^{+0.10}$	52_{-16}^{+36}	0.73 ± 0.02	$30.2_{-2.5}^{+6.7}$	$3.90_{-0.40}^{+0.29}$	$0.0048_{-0.0007}^{+0.0025}$	1.05 (432)

[a]To determine the total error, we added in quadrature the error on the mean fit value from the different PCUs and the 1σ error as determined by XSPEC. All errors quoted are the 1σ confidence range.

[b]When it was not possible to constrain the value of N_H, it was fixed to a previously determined value. If no error range is provided, the value was fixed, and references for individual sources are as follows: IGR J00291+5934—Nowak et al. (2004); XTE J0929−314—Juett et al. (2003); XTE J1807−294—Campana et al. (2003); SAX J1808.4−3658—Wijnands (2003); XTE J1814−338—Krauss et al. (2005); 4U 1608−522—Christian and Swank (1997); KS 1731−260-Wijnands et al. (2002); 4U 1812−12—Wilson et al. (2003); Aquila X-1—Rutledge et al. (2002a).

We plot the fitted optical depths for all observations in Figure 4-2. Also plotted are the average values for the AMP and atoll sources, excluding the fits where the electron temperature and τ were highly degenerate (the points below the dotted line). It is clear from these points that there is no measurable difference in the average optical depth of the AMPs and the atoll sources. Furthermore, one can see that there are observations in which AMP sources have a significantly higher optical depth than atoll sources.

4.3 Discussion and conclusions

Unlike the accretion-powered millisecond pulsars, most neutron stars LMXBs do not show persistent pulsations, although we know that many contain a rapidly-rotating neutron star. Titarchuk et al. (2002) suggested that a possible explanation was the presence of a scattering medium of high optical depth around the non-pulsing systems. To support this claim, they cited a number of observations of LMXB systems which had higher optical depths than the AMP SAX J1808.4−3658. However, the measured optical depth from an atoll LMXB is dependent on its spectral state, with higher optical depths occurring during the periods when the source in the banana branch (see, e.g., the study of 4U 1608−52 by Gierliński and Done 2002). In Chapter 3 we showed that the AMP sources spend virtually all their time in the extreme island state, so it is more reasonable to select comparison spectra from atoll sources while they are in the same state, as we have done here. Assuming that our fitted optical depths are indicative of the opacity of material surrounding the neutron star, our fit results imply that the scattering regions surrounding both AMP and atoll sources have very similar physical properties. Assuming that the scattering regions are also roughly the same size, this suggests that they are unlikely to be responsible for obscuring pulsed emission from the atoll sources.

Therefore, a different process may be needed to explain the fact that only a small subset of neutron stars in LMXBs exhibit persistent pulsations. As mentioned in § 4.1, a promising alternative is diamagnetic screening of the neutron star's surface dipole field by accreted material (Cumming et al. 2001). Since the amount of screening would be proportional to the accretion rate over the timescale of the re-emergence of the field ($\sim 100 - 1000$ yr), it would be expected that on this timescale, AMP sources would have a lower $\dot{M}$ than the non-pulsing atolls. Indeed, Gladstone et al. (2007) find that this appears to be the case: all the AMP systems (excluding HETE J1900.1−2455) accrete at lower rates than the atoll systems.

In fact, HETE J1900.1−2455 is a striking case of transitional behavior, perhaps an example of field burial on the very short timescale of months. Originally discovered in June 2005, this system exhibited persistent pulsations for only the first two months of its outburst (see also § 3.3.2.7). Since then, it has remained active as a low-luminosity X-ray transient for almost two years, many times longer than other AMP outbursts (the next longest being a 50-day outburst from XTE J1814−338; more typical ones last several weeks to a month). An attractive explanation for the disappearance of the pulsations is that the long-duration outburst allowed a critical amount of material to accrete and suppress the dipole field, diminishing its ability to channel accretion to the magnetic poles (Galloway et al. 2007b). This explanation is supported by the fact that the strength of the pulsations faded over the course of the initial part of the outburst, as would be expected if the field were becoming progressively more buried.

Another possibility is that the magnetic fields are similar, but the accretion geometry of

the atoll sources during outburst is significantly different from the AMPs as a result of their higher accretion rates. The inner disk radius will extend closer to the neutron star surface as the accretion rate increases, resulting in a greater fraction of material landing near the spin equator rather than the magnetic poles, suppressing the pulsation signal. Although this picture is consistent with the observed kHz QPO frequencies from non-pulsing LMXBs (Psaltis and Chakrabarty 1999), it does not explain why the atoll sources lack pulsations even at their lowest luminosities, which are comparable to the luminosities of the AMPs.

The continued discovery of new accretion-powered millisecond pulsars, as well as the monitoring of known pulsars, will allow for a more precise determination of their long-term accretion rates. In addition, other intermittent pulsars like HETE J1900.1−2455 may be discovered, which could help determine the differences (as well as links) between accretion-powered millisecond pulsars and non-pulsating atoll sources.
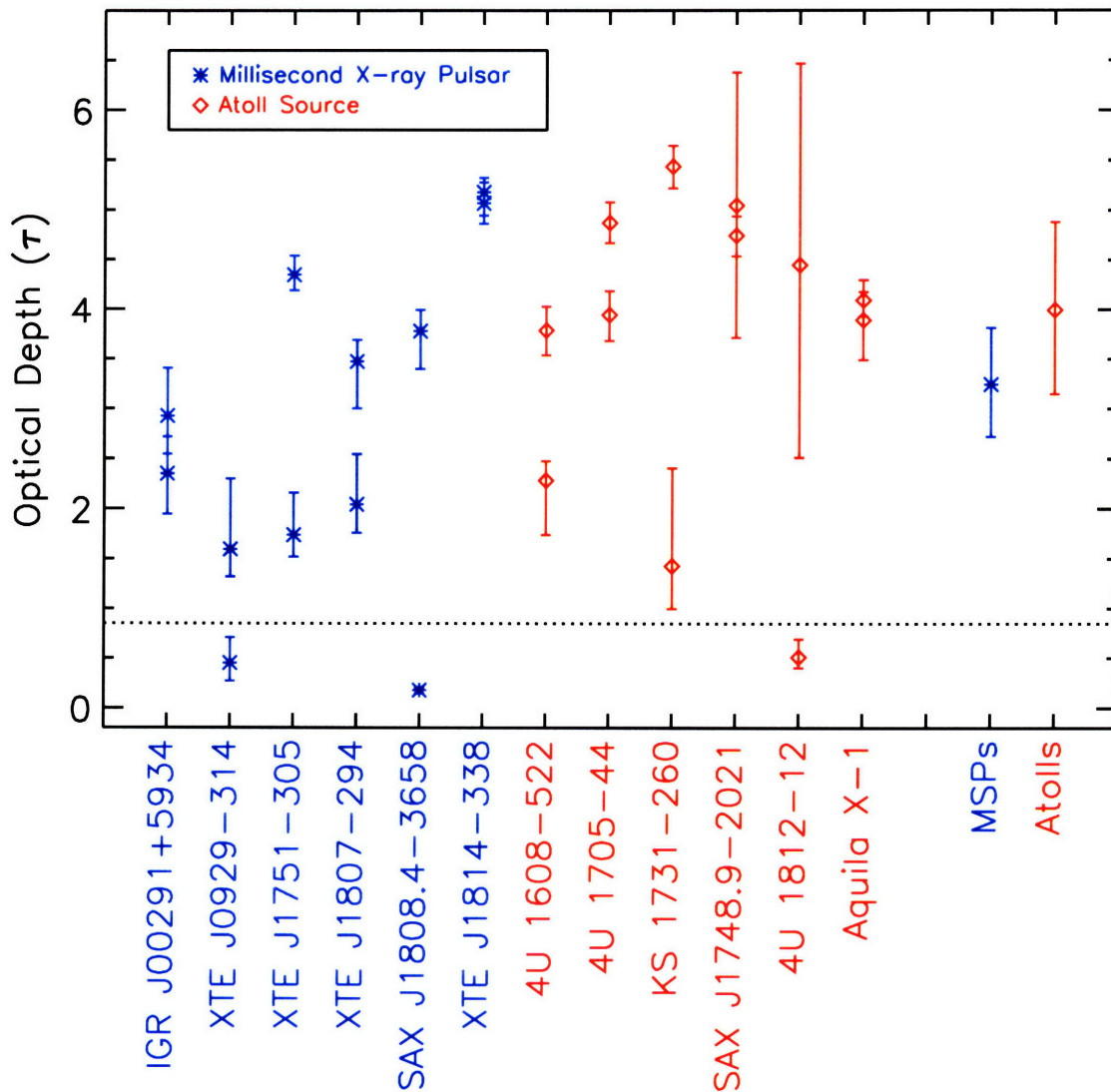
Figure 4-2: Fitted optical depths using the CompTT model. Measurements which fall below the dotted line are from fits where the electron temperature and optical depth were highly degenerate, and are excluded in determining the averages. Note that there is no significant difference in average optical depth between the two source classes.

Chapter 5

Looking for Jets from LMXBs: *Chandra* Observations of SAX J1808.4–3658 and XTE J1701−462

5.1 Jets from X-ray binaries

Astrophysical jets span many orders of magnitude in size and power, from the gargantuan radio lobes of Cygnus A that extend over 70 kpc from the center of their host galaxy and have a luminosity of $\sim 10^{44}$ ergs s^{-1}, to the diminutive jet of the symbiotic star CH Cyg which is only ≈ 0.005 pc (≈ 1000 AU) long and has a luminosity $\lesssim 10^{30}$ ergs s^{-1} (Galloway and Sokoloski 2004). Recently, the first X-ray jet from a neutron star was discovered in the X-ray binary system Circinus X-1 (Heinz et al. 2007). Despite their ubiquity, much about the formation and composition of jets remains unknown. However, recent observations of X-ray binary systems in our galaxy have allowed for their study of jets on easily accessible timescales. Among other important insights, this has furthered our understanding of the interaction of jets with accretion disks, providing a unique window on the processes which occur in the region where the jet first takes form.

A hallmark of jets is the presence of radio emission. This is a signature of the electrons (and possibly positrons) in the jet, which radiate via synchrotron emission, producing a power-law energy spectrum with a spectral index of $-0.4 \geq \alpha \geq -0.8$ (Fender 2006). Generally, it is unclear what, if any, is their baryonic content. The superluminal jets of SS 433 are the only to show spectral lines, indicating that they contain a significant population of baryons; other jets have apparently featureless continua, although this could be due to Doppler smearing of existing emission lines (Mirabel et al. 1997).

Although a number of jets have been imaged at radio (and even X-ray) wavelengths, many more are inferred from unresolved detections of radio emission (see, e.g., Stirling et al. 2001). This is well-justified for a few reasons. First, it is possible in many cases to estimate a minimum size for the synchrotron emission region, given a distance estimate and the assumption that the brightness temperature must be $\lesssim 10^{12}$ K (above which Compton losses would quickly deplete the jet energy). When sizes are estimated in this fashion, they are generally larger than the binary systems themselves, implying that the emitting material is not bound to the system and therefore is part of an outflow (Fender 2006). Furthermore, in the cases where the emitting regions are resolved, the geometry is almost always that of a jet or collimated blobs. Therefore, it is assumed that radio emission from X-ray binary

systems is indicative of a jet.

There are two distinct types of jet behavior. One is characterized by variable, punctuated radio emission, and is associated with spectral state changes in the X-ray binary (see, e.g., the study of simultaneous X-ray and radio observations of 4U 1728−34 in Migliari et al. 2003). The other is a weaker but steady jet, which is produced and sustained during the low/hard state of black hole binaries and island state of atoll sources. (It does not appear that high-field neutron stars, the classical X-ray pulsars, produce jets.) Despite their overall similarities, there are also some clear differences between binary systems with neutron star primaries and those containing black holes. Although both appear to "quench" their jets as the source enters a soft, disk-dominated state, the black hole systems do so completely, whereas the neutron star systems often still have some residual jet emission (Migliari and Fender 2006). In addition, the jet power (relative to X-ray emission) of atoll systems is ~ 30 times weaker than is seen in black hole or Z source systems (Fender 2006; Migliari et al. 2003). Finally, the neutron star and black hole systems appear to follow different radio/X-ray correlations: $L_{\rm R,BH} \propto L_{X,BH}^{0.5}$ whereas $L_{\rm R,NS} \propto L_{X,NS}$. Since the neutron star relationship is more steep, low-state neutron star systems will never enter a jet-dominated state. This could be due to the presence of a stellar surface, and therefore relatively more X-ray emission (Migliari and Fender 2006).

Jet emission has also been inferred from infrared and even optical photometry. Infrared emission in excess of what would be expected from an accretion disk plus companion star has been observed from a number of sources, including the accretion-powered millisecond pulsars XTE J1814−338 (Chapter 2), XTE J0929−314 (Rupen et al. 2002), and SAX J1808.4−3658 (Rupen et al. 2005). There is even enough spectral coverage of the ultracompact binary 4U 0614+091 to determine that the spectral index of the infrared excess is $\alpha = -0.57$, which is indicative of synchrotron emission from a relativistic outflow (Migliari et al. 2005). Jet emission from the black hole source V404 Cyg extends well into the optical regime, as is indicated by strong correlations between its optical and radio emission (Han and Hjellming 1992; Fender 2001b).

In a few cases, jets from black hole candidate X-ray binaries have actually been resolved at X-ray wavelengths. *Chandra* observations have revealed that shock-heated baryonic material produces the $\approx 6''$ ($\approx 10^{17}$ cm) jets observed from SS 433 (Migliari et al. 2002), whereas the emission from the larger (≈ 50 arcsecond, $\approx 4 \times 10^{18}$ cm) jets of XTE J1550−564 is probably due to synchrotron emission from shock-heated electrons and perhaps positrons (Corbel et al. 2002). An *XMM-Newton* observation of 4U 1755−33 after it had entered a quiescent state revealed a jet-like feature $3\rlap{.}'5$ across, corresponding to a distance of $\approx 10^{19}$ cm, but the origin of this emission is not clear (Angelini and White 2003). Recently, a *Chandra* observation of Circinus X-1 was able to resolve the first X-ray jet from a neutron star X-ray binary, and the inferred jet power is more than sufficient to create the observed large-scale radio lobes, and shows that at least some subset of neutron stars are as efficient at jet production as black holes (Heinz et al. 2007).

5.2 *Chandra* DDT observation of SAX J1808.4−3658

The accretion-powered millisecond pulsar SAX J1808.4−3658 is known to have both radio (Gaensler et al. 1999; Rupen et al. 2005) and infrared (Wang et al. 2001) emission associated with its outbursts which is likely produced by synchrotron emission from outflowing material. It is also the closest known AMP source ($d = 3.5$ kpc; see Table 3.1), so if the
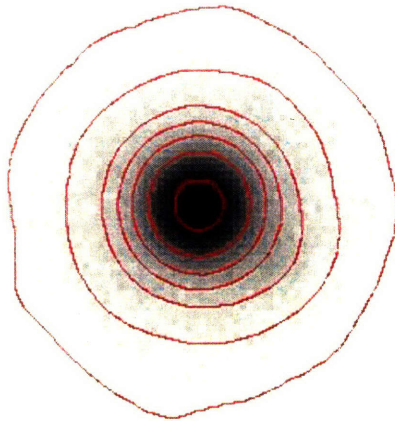
Figure 5-1: *MARX* simulation of an X-ray jet from SAX J1808.4−3658 using *Chandra* HRC-I. The jet is 1.5″ long and is 10 times fainter than the central point source. Contours are overplotted to make the enhancement due to the jet more easily visible.

outflowing material is collimated, it would be an ideal target for observing resolved jet structure. In Figure 5-1 we present a *MARX* simulation of a *Chandra* HRC-I observation of a 1.5″-long X-ray jet that is 10 times fainter than the central point source.

We observed the source at the end of its June 2005 outburst using the *Chandra* HRC-I, whose native resolution of 0.4″ corresponds to a distance of 8 light-days at the distance of SAX J1808.4−3658. This DDT observation (ObsID 6298) comprised a total of 5 ks and was performed on 20 June 2005.

The data were processed by the *Chandra X-ray Center* using CIAO vers. 3.2.2, and a comparison point source image was created using the *ChaRT* web-based ray-tracing utility.[1] The average count rate was 48.8 ± 0.2 counts s^{-1}, corresponding to a 0.5–10.0 keV flux of 1.7×10^{-9} ergs cm^{-2} s^{-1}. An image of the source is shown in Figure 5-2. There are no obvious jet features, although the presence of X-ray background emission causes the outermost contour to wander slightly from the smooth point source point spread function (PSF). Comparison with the idealized PSF created by *ChaRT* confirms that there is no statistically significant deviation and therefore no detected jet feature.

Although disappointing, the lack of a resolved X-ray jet in SAX J1808.4−3658 is not particularly surprising. At the time of the proposal, the source distance was thought to be 2.5 kpc, but this has subsequently been revised to 3.5 kpc. Given this greater distance, the angular size of any jet feature will be significantly less, and therefore more difficult to

---

[1]http://cxc.harvard.edu/chart/
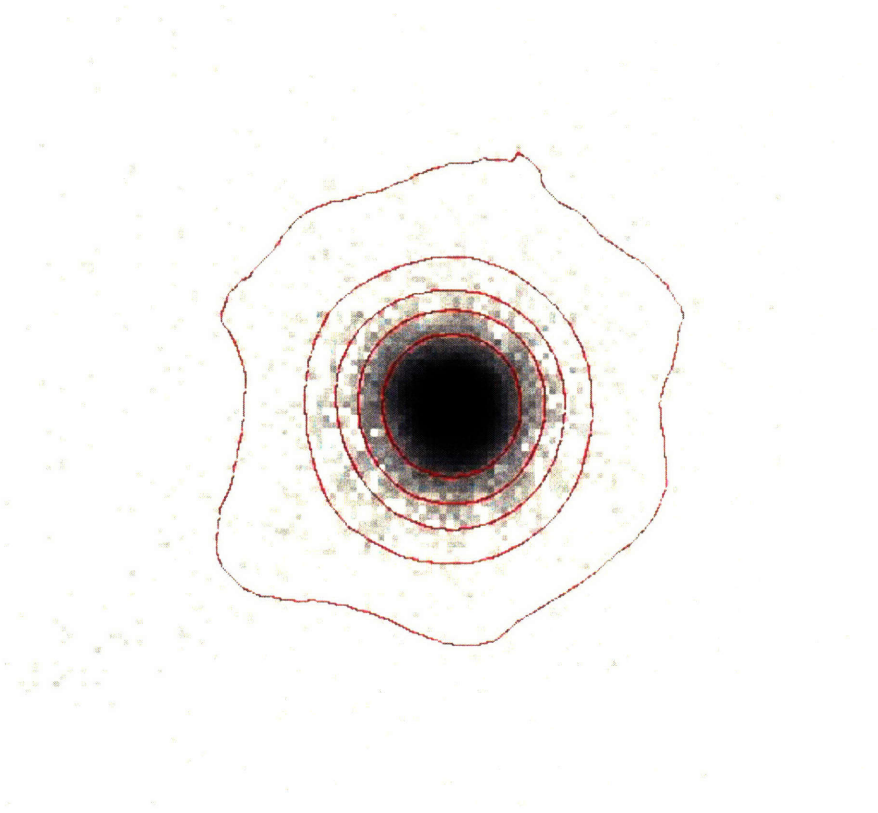
Figure 5-2: *Chandra* DDT observation of SAX J1808.4−3658 at the end of its 2005 outburst. X-ray contours are overplotted.

detect. However, it was still a worthwhile attempt, since a jet detection would have yielded extremely exciting results as both the first resolved X-ray jet from a known neutron star and the first from an object with a known magnetic field strength. Hopefully, future high spatial resolution X-ray observations of neutron star LMXBs will resolve X-ray jets from these objects.

5.3 Spurious jet-like feature in XTE J1701−462

The only known transient Z source, XTE J1701−462 first went into outburst in January 2006, and remains active over a year later. It was discovered by the *RXTE* ASM (Remillard et al. 2006), and optical (Maitra et al. 2006), near-infrared (Maitra and Bailyn 2006), and radio counterparts (Fender et al. 2006) have all been reported. Although XTE J1701−462 displays all the color and timing properties of a Z source, its track on the color-color diagram evolved dramatically during the first 10 weeks of the outburst. Initially, it appears similar to Cyg X-2 (a "Cyg-like" source), with a more vertically-oriented, Z-shaped track. As the outburst progresses and the X-ray flux decreases, the color track changes substantially and ultimately resembles that of Sco X-1 (a "Sco-like" source), which appears as a ν on the color-color diagram. Although other Z sources have mutable color tracks, none displays a complete switch between these two types of behavior (Homan et al. 2007). The correlation of X-ray flux with the color behavior of XTE J1701−462 suggests that the Cyg-like sources are intrinsically more luminous than the Sco-like sources.
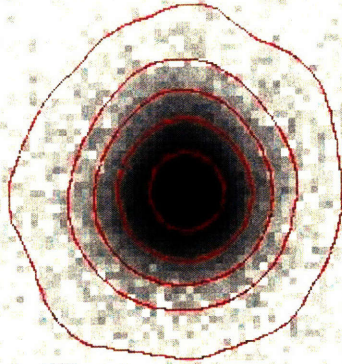
Figure 5-3: Unfiltered *Chandra* TOO observation of XTE J1701−462. X-ray contours are overplotted. Note the enhancement of emission to the north; this is due to error in the de-gapping correction—see text for discussion.

On 27 March 2006, *Chandra* observed XTE J1701−462 as part of our ongoing TOO program to obtain precise positions for neutron star transients. A 1.1 ks observation was obtained with the HRC-S, during which time the source had a mean count rate of 64.1 ± 0.2 counts s^{-1}, corresponding to a 0.5–10 keV flux of 7.6×10^{-9} ergs cm^{-2} s^{-1} (assuming a spectral shape that is consistent with a previous measurement by the *Swift* XRT; Kennea et al. 2006). We measured a source position of R.A. = $17^{h}00^{m}58\overset{s}{.}46$, decl. = $-46°11'08\overset{''}{.}6$ (J2000) with a 90% confidence radius of $0\overset{''}{.}6$.

An image of the source is presented in Figure 5-3. There is an apparent excess of X-ray emission to the north which is visible in the image as well as in comparisons with an idealized point-source PSF image created with *ChaRT*. Figure 5-4 shows one such comparison: here, counts are summed over discrete radial rings for both the source and PSF and the ratio is calculated, showing a pronounced excess at radii $\gtrsim 0.8''$. To determine the position angle of the excess emission, we took the same ratio over pie wedges using a radial range of 1.2–2.6″. A plot of the results is presented in Figure 5-5, from which it can be seen that the peak occurs at an angle of $\approx -7°$. This emission contains $\approx 4 \pm 1\%$ of the total X-ray flux, and if it were due to an actual ejection event which occurred at the start of the transient outburst, would indicate a superluminal apparent velocity of $1.27c$ (assuming XTE J1701−462 is at a distance of 10 kpc).

However, upon further examination, we found that the feature is actually an artifact
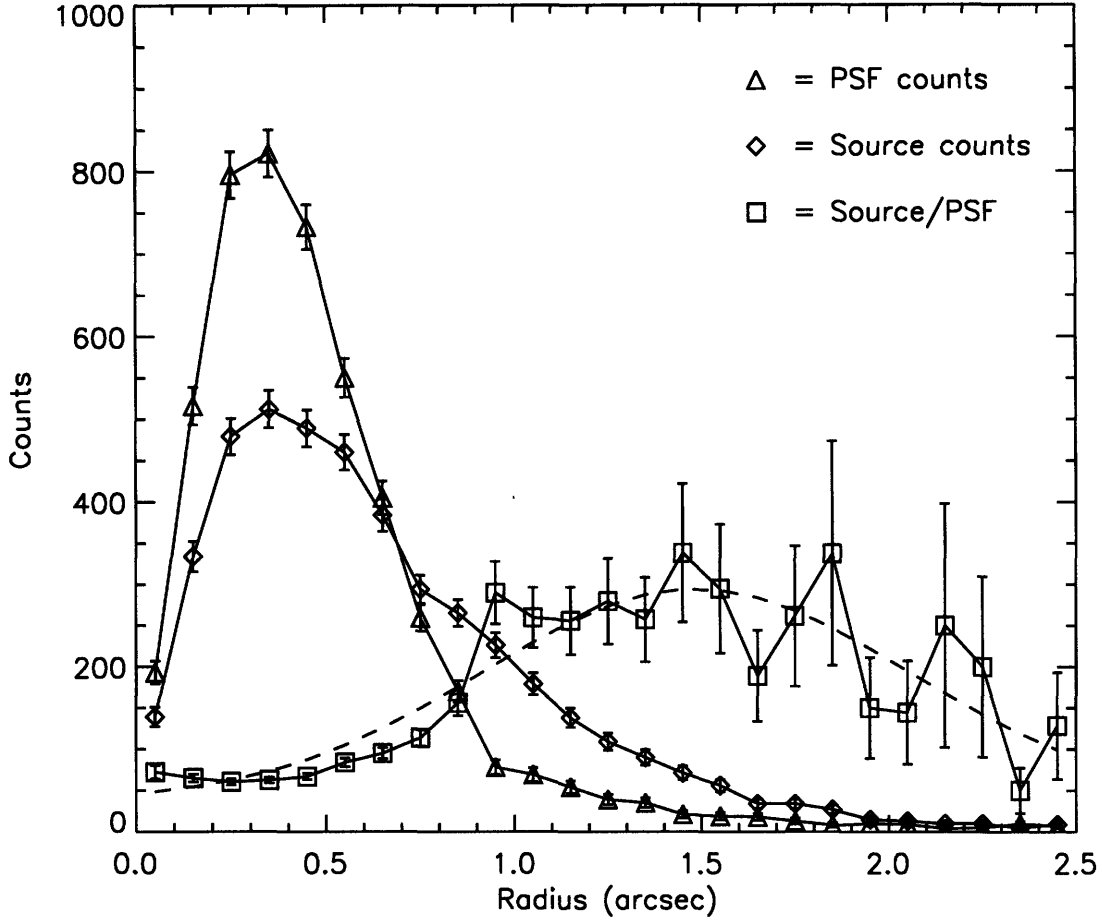
Figure 5-4: Apparent excess emission in the radial direction. The simulated point-source PSF (triangles), source data (diamonds), and source counts/PSF counts (squares; value has been multiplied by 100) are plotted as a function of distance from the source center. The dashed line is a Gaussian fit to the ratio.

caused by the algorithm that determines the position of events on the HRC-S detector. The standard algorithm uses information from the three amplifiers (taps) nearest to the charge cloud produced by an X-ray photon. While this works perfectly if the charge cloud is exactly centered on the middle tap, there are errors introduced if the cloud is off-center.[2] These errors result in "gaps" in the reconstructed image which occur in a grid of periodic intervals and are generally removed by standard data processing. Unfortunately, it is more difficult to apply a degapping correction when events occur in the intersections of the gaps. The dither pattern for our observation of XTE J1701−462 was such that a significant amount of time (40 s, corresponding to ≈ 4% of the observation) was spent in a region where the gaps intersect. For this period of time, the source position was incorrectly determined. This is particularly noticeable in a plot of the sky y-position with respect to time (see Figure 5-6). Although all HRC observations are similarly affected, the general result is a slight degradation of the PSF. In our observation, the combination of a short integration

---

[2]See http://hea-www.harvard.edu/~juda/calib/degap/degapping.html for more information.
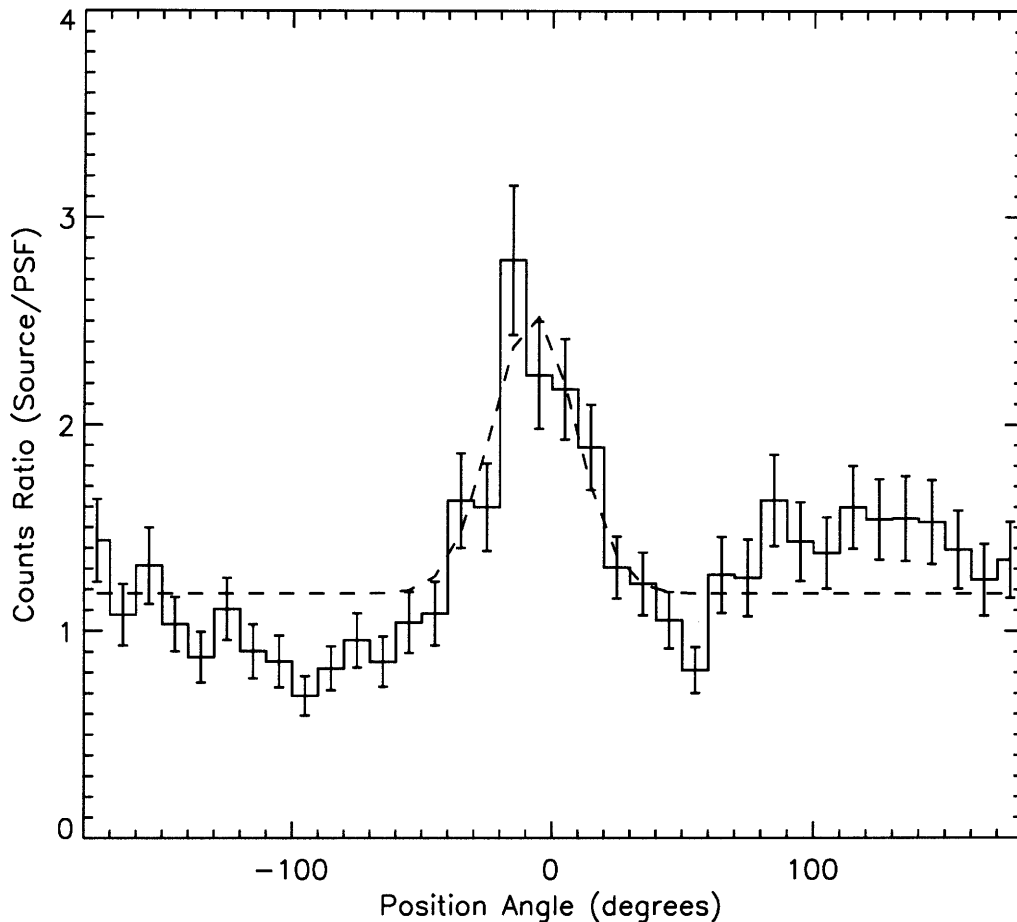
Figure 5-5: Ratio of source counts/PSF counts for an integrated radial range of 1.2–2.6″ as a function of position angle. The dashed line is a Gaussian fit to the ratio, and indicates that the peak occurs at a position angle of $-7°$.

time and a bright source caused a clearly visible spurious feature.

5.4 Conclusions

Jets have been inferred or observed from a significant population of astrophysical objects, including Galactic X-ray binaries. Unfortunately, our brief *Chandra* observations of SAX J1808.4−3658 and XTE J1701−462 were not able to detect any jet features. However, there is evidence of an infrared excess in three of the accretion-powered millisecond pulsars which could be attributed to synchrotron emission from a relativistic outflow. Furthermore, high–spatial-resolution X-ray observations have succeeded in resolving X-ray jets from a few black hole X-ray binaries, as well as, quite recently, the first neutron star X-ray binary. Therefore, the continued search for spatially resolved X-ray jets from neutron star X-ray binaries remains exciting and potentially very rewarding.
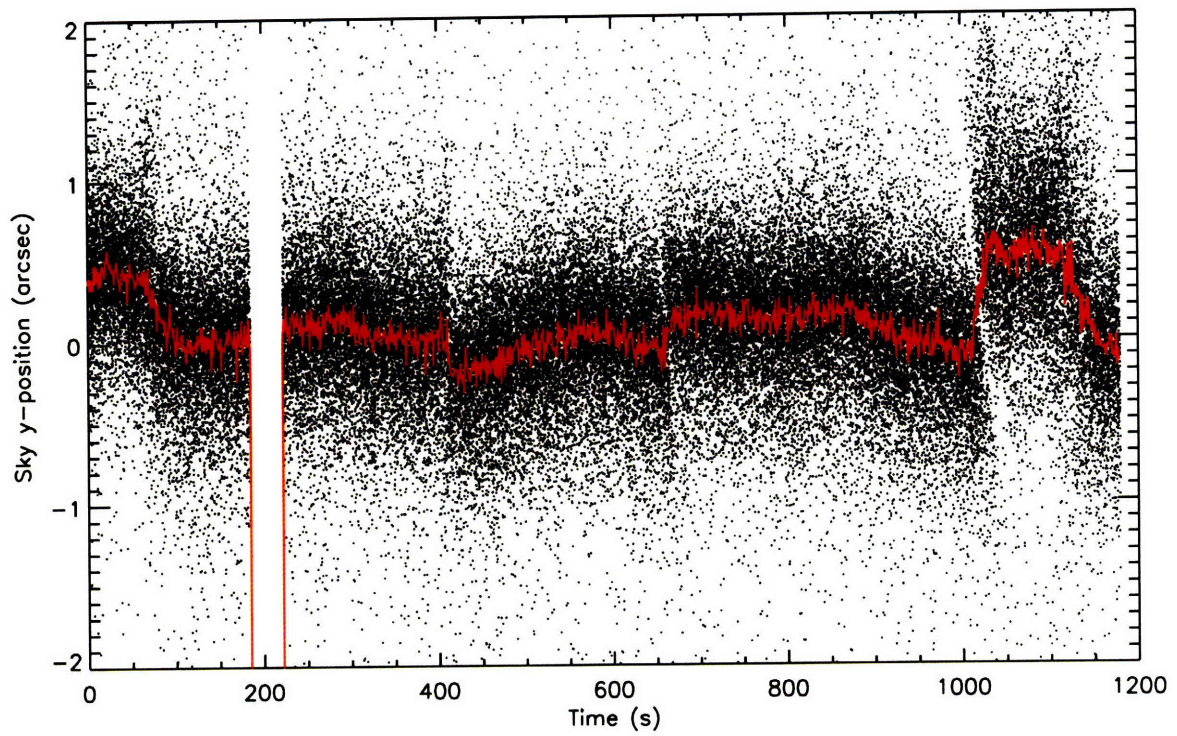
Figure 5-6: X-ray photon y-position as a function of observation time with an arbitrary zero-point offset. The red curve shows the average y-value for a 1-second integration, and makes the jumps in position due to incorrect degapping corrections more clear. This is what caused the jet-like feature visible in Figures 5-3–5-5.

Chapter 6

Temperature Distributions of Thermonuclear X-ray Bursts

6.1 Thermonuclear X-ray bursts: observations and physics

Neutron stars in X-ray binary systems accrete material from their companions at different rates, governed both by the size of the orbit and the evolutionary status and stellar structure of the companion. The mass accretion rate plays a central role in the observed characteristics of the binary system: for example, the previously discussed atoll and Z source classification is thought to be due primarily to differences in the average mass accretion rate (see Chapters 4 and 3). Likewise, the accretion rate determines whether a neutron star will exhibit thermonuclear X-ray bursts. For mass accretion rates lower than a critical rate for stable nuclear burning, $\dot{M} < 900$ g cm^{-2} s$^{-1}(Z_{CNO}/0.01)^{1/2}$ (where Z_{CNO} is the mass fraction of CNO), material will accumulate on the surface of the neutron star until it reaches the critical temperature and density necessary to undergo an unstable thermonuclear runaway and is observed as an X-ray burst (Strohmayer and Bildsten 2006). These explosions are commonly termed "type-I" X-rays bursts to distinguish them from the less common magnetically-regulated "type-II" bursts (i.e., the mechanism which governs MXB 1730−335, the "Rapid Burster").

Thermonuclear X-ray bursts are an extremely important observational tool. They are indisputable evidence of the presence of a surface and therefore of a neutron star (as opposed to black hole) primary. Furthermore, if there is a significant asymmetry in the distribution of the burst emission on the surface of the neutron star, there may be burst oscillations, which trace the neutron star spin frequency. Bursts may also attain super-Eddington luminosities, resulting in an expansion of the photosphere (a so-called *radius-expansion* burst). This observational determination of the Eddington luminosity can be used as a standard candle to produce a reliable ($\approx 30\%$) distance estimate (Basinska et al. 1984). Distances have been determined for quite a number of burst sources using this technique; see, e.g., Galloway et al. (2006).

It was also quickly recognized that thermonuclear X-ray bursts could be used to help answer an outstanding question in physics: what is the neutron star equation of state (EoS)? The EoS uniquely determines the radius (mass) of a neutron star given its mass (radius). The ratio of the mass of a neutron star to its radius, M/R, can therefore constrain EoS models and help reveal the fundamental physics of extremely dense material. Observations of thermonuclear X-ray bursts are a possible way to constrain M/R (van Paradijs 1979;

Goldman 1979). However, in order to use the measured blackbody radii from bursts, one must understand how they relate to the actual neutron star radii. This makes precision measurement of M/R and application to EoS models quite tricky. By contrast, if there are discrete spectral features which could be attributed to emission from the neutron star surface—for example, features that arise during a thermonuclear X-ray burst—they would be gravitationally redshifted by an amount

$$z = \left(1 - \frac{2GM}{Rc^2}\right)^{-1/2} - 1, \tag{6.1}$$

and could provide a direct measurement of M/R and therefore of fundamental neutron star properties (see, e.g. London et al. 1984; Foster et al. 1987). A number of papers have reported spectral features in low-resolution X-ray data (Waki et al. 1984; Turner and Breedon 1984, to name a few), but none of these features has ever been confirmed by higher-resolution instruments. Recently, the measurement of absorption lines in the *XMM-Newton* burst spectrum of EXO 0748−676 by Cottam et al. (2002) has renewed interest in the search for spectral features in X-ray bursts. The authors identify the features as arising from Fe XIV, Fe XV, and O VIII, all having a redshift of $z = 0.35$ which, for a standard range of neutron star masses, is in agreement with EoS models for normal nuclear material and excludes models for strange quark matter or kaon condensates. However, more recent attempts to find these features in other high-resolution observations of EXO 0748−676 have not been successful (Telis et al. 2004; Cottam et al. 2006). Therefore, it is important both to confirm the features seen in EXO 0748−676 and to find other systems with line features to provide further observational tests of neutron star EoS theory.

6.1.1 Atomic spectral features from thermonuclear X-ray bursts

What discrete features could be observable during a thermonuclear X-ray burst? The two main categories of features are spectral lines and edges. However, for either of these to be manifested, the elements which could produce such features must be present in the neutron star atmosphere. Heavy elements deposited by the accretion stream will sink below the photosphere on a timescale much shorter than the burst duration, and heavy elements created during nuclear burning will remain below the neutron star photosphere due to its significantly higher entropy (Joss 1977). Therefore, the most promising source of heavy elements is the accreting material which is just reaching the neutron star surface, particularly Fe and its spallation products (Bildsten et al. 2003).

Even if heavy elements are present, it does not necessarily mean that they will give rise to observable absorption edges or lines. Another important consideration is whether the temperature of the photosphere is low enough for an appreciable fraction of the nuclei to retain one or more electron. Bildsten et al. (2003) calculate the temperatures at which half of the nuclei will be in the hydrogenic state ($kT_{1/2}$; see their Table 1)—below this temperature there could be the formation of a photoionization edge. Similar temperatures of interest could be calculated for line features via the application of the Saha equation, and are in a similar range to the edge temperatures. For example, Fe XXVI (hydrogen-like) dominates at $kT > 1.2$ keV, whereas Fe XXV (helium-like) will be the predominant species for $kT < 1.2$ keV (Cottam et al. 2002).

Furthermore, on must take into account the effect of neutron star rotation on the observed spectral features. From the detection of burst oscillations as well as persistent pulsations we know that many neutron stars in LMXBs are rotating quite rapidly—usually in the

range of hundreds of Hz. Features which arise from the surface of a spinning neutron star will be affected in a number of ways, including relativistic Doppler broadening, frame dragging, and strong gravitational lensing (see, e.g. Özel and Psaltis 2003; Chang et al. 2006). As a result, intrinsic features will be distorted and broadened and will generally be more difficult to differentiate from the continuum emission. Of the 22 accreting neutron stars with known spin frequencies, the mean and median values of the spin are both ≈ 400 Hz. The only source with known spin less than 200 Hz is EXO 0748−676 (which has a spin of 45 Hz, in agreement with the minimal amount of Doppler broadening seen in its absorption lines Villarreal and Strohmayer 2004; Chang et al. 2005).

An obvious prerequisite to the analysis of X-ray burst spectra is the observation of thermonuclear bursts. Unfortunately, most sources do not burst at regular intervals, making the likelihood of detecting bursts a purely statistical exercise. For some sources, the burst rate is known to be anti-correlated with the accretion rate and therefore related to the source's spectral state. Furthermore, most sources do not burst very frequently—the average rate is 0.14 bursts hr^{-1}, or 4 bursts every 100 ks (Galloway et al. 2006). Ultimately, an important metric is the amount of burst fluence in the temperature range of interest that is expected over a given time interval, which will depend on the distance to the source as well as its burst properties.

Finally, it is important that the instrument used is capable of observing the bursts. Some X-ray observatories are better suited to this task than others. The ideal observatory would have a large collecting area to minimize the number of bursts needed to acquire the necessary amount of flux. It would also have a high enough spectral resolution to detect discrete spectral features. Also important is the ability of the instrument to handle the high count rates which occur during X-ray bursts without suffering problems like telemetry saturation or photon pile-up.

6.2 Temperature distributions of bursts

6.2.1 Source sample and data analysis

Both the flux and temperature evolve during the course of a thermonuclear X-ray burst. They peak and decay on similar timescales, although if there is a radius-expansion episode, the temperature will decrease as the flux is reaching its maximum value, since the blackbody radius is increasing as well. The temperatures generally peak at $\sim 2.5 - 3$ keV, and decay to below 1 keV in the tail of the burst.

We analyzed the burst temperature distributions from the *RXTE* data of all 45 burst sources included in Galloway et al. (2006). We considered all thermonuclear X-ray bursts observed from these sources, comprising a total of 1,158 bursts. For each burst, time-resolved spectra and matching response matrices were created, as were corresponding background spectra consisting of the persistent emission prior to the burst. The time intervals were determined based on the burst count rate and were adaptively lengthened as the flux decreased, varying from $0.25 - 2$ s. Each spectrum was then fitted with an absorbed blackbody, which generally provided a good fit ($\chi_\nu^2 \lesssim 2$). This yielded a blackbody temperature and normalization from which a bolometric flux was calculated. See Galloway et al. (2006) for a more detailed description of the fitting process.

All of the burst fit information is accessible via the MIT burst database, which includes all the thermonuclear burst sources observed by *RXTE*, and makes data manipulation quite straightforward for our large sample of sources. From the blackbody fits we were able to

calculate temperature profiles of the bursts—histograms of the burst fluence over a given temperature range. We were also able to construct various metrics to determine which sources are promising candidates for further study and future observations.

6.2.2 Burst temperature profiles

Using the temperature and bolometric flux from each fit, we constructed histograms of the integrated burst fluence for each of the burst sources. Since the number of bursts per source has a wide spread (several sources have only a single burst, whereas 4U 1636−53 has 170—see Table 6.1), the histograms vary greatly in their noise level, as can be seen by the relative smoothness or spikiness of the distributions.

The temperature profiles are plotted in Figures 6-1–6-3. There is a good deal of source-to-source variation, both in the shape of the distribution and in where the peak falls. Some sources have broad, rather flat histograms (e.g., 4U 1608−522) whereas others have a broad but distinctly peaked shape (e.g., 4U 1728−34). Some are very narrow, like GS 1826−24. Furthermore, the amount of low-temperature (< 1.5 keV) fluence is quite different depending on the source. For example, only 2% of the fluence from 1M 0836−676 lies below 1.5 keV, while for 4U 1724−307 it is 38%.

The variety in profile shapes is not particularly surprising considering the variety of burst types that have been combined to produce them. Ultimately, we are concerned with the amount of low-temperature fluence in the bursts from a given source, and not the characteristics of the individual bursts—therefore, we have combined all bursts for each source, be they long, short, weak, bright, or radius-expansion.

6.2.3 Low-temperature burst fluences

In order to determine which sources are most likely to have observable discrete spectral features, we have constructed a table that includes the most relevant parameters (Table 6.1). As discussed above, the temperature of the burst is important, since lower temperatures allow for lower ionization states and therefore the production of lines and edges. Observationally, one would like to maximize the amount of low-temperature fluence that would be expected in a given time interval, which is simply the fluence per burst multiplied by the burst rate. Using the burst rates presented in Galloway et al. (2006), we calculate the amount of low-temperature fluence expected for a 100 ks observation, which is listed in the next-to-last column of Table 6.1.

Even if a system has a substantial amount of low-temperature fluence, features produced during bursts may be obscured by effects from a high neutron star spin frequency (see above). The last column in Table 6.1 includes the spin frequencies where known. Although a smeared line or edge is not necessarily rendered undetectable, a substantially longer observing time would be necessary to distinguish it from the continuum level. From Figure 1 in Chang et al. (2006), it is clear that the line profile from a neutron star with $f_{\mathrm{spin}} \gtrsim 200$ Hz will be severely smeared. It is therefore somewhat discouraging that of the 15 bursters with known spin frequencies, only 1 is spinning more slowly than 200 Hz.

Another factor to consider in determining which sources would be optimal candidates for an observing campaign is whether the system is persistent or transient. It is impossible to predict exactly when a transient outburst will occur (or end), so any observation of a transient source would have to be conducted as a target of opportunity. Furthermore, for most transients, there is a non-negligible probability that no outburst will occur during a
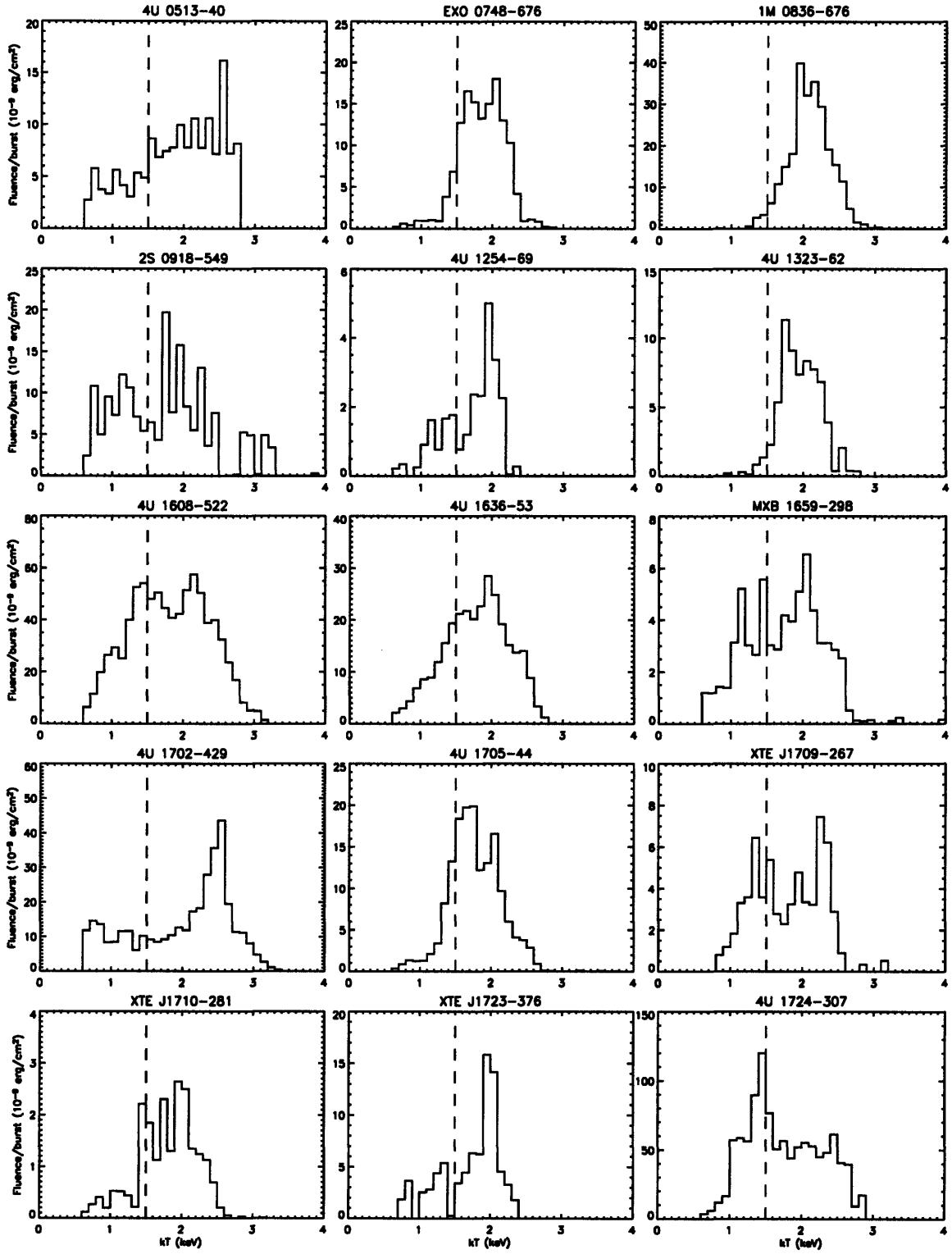
Figure 6-1: Histograms of the burst fluence with respect to the blackbody temperature in bursts observed by *RXTE*. A dashed line is plotted at $T = 1.5$ keV, and the histograms have been normalized by the number of bursts included to provide an average value for the fluence per burst at a given temperature.
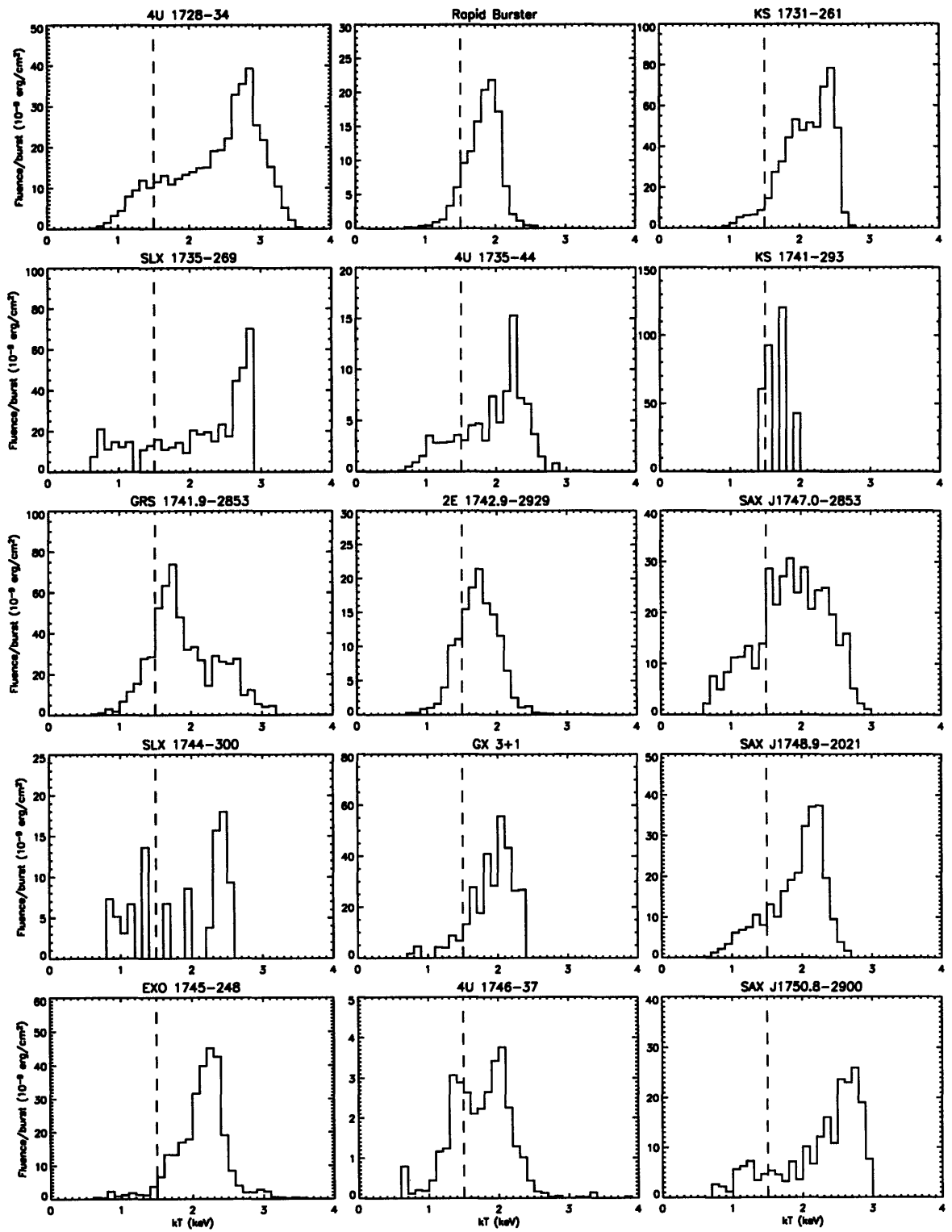
Figure 6-2: Same as Figure 6-1; second group of sources.
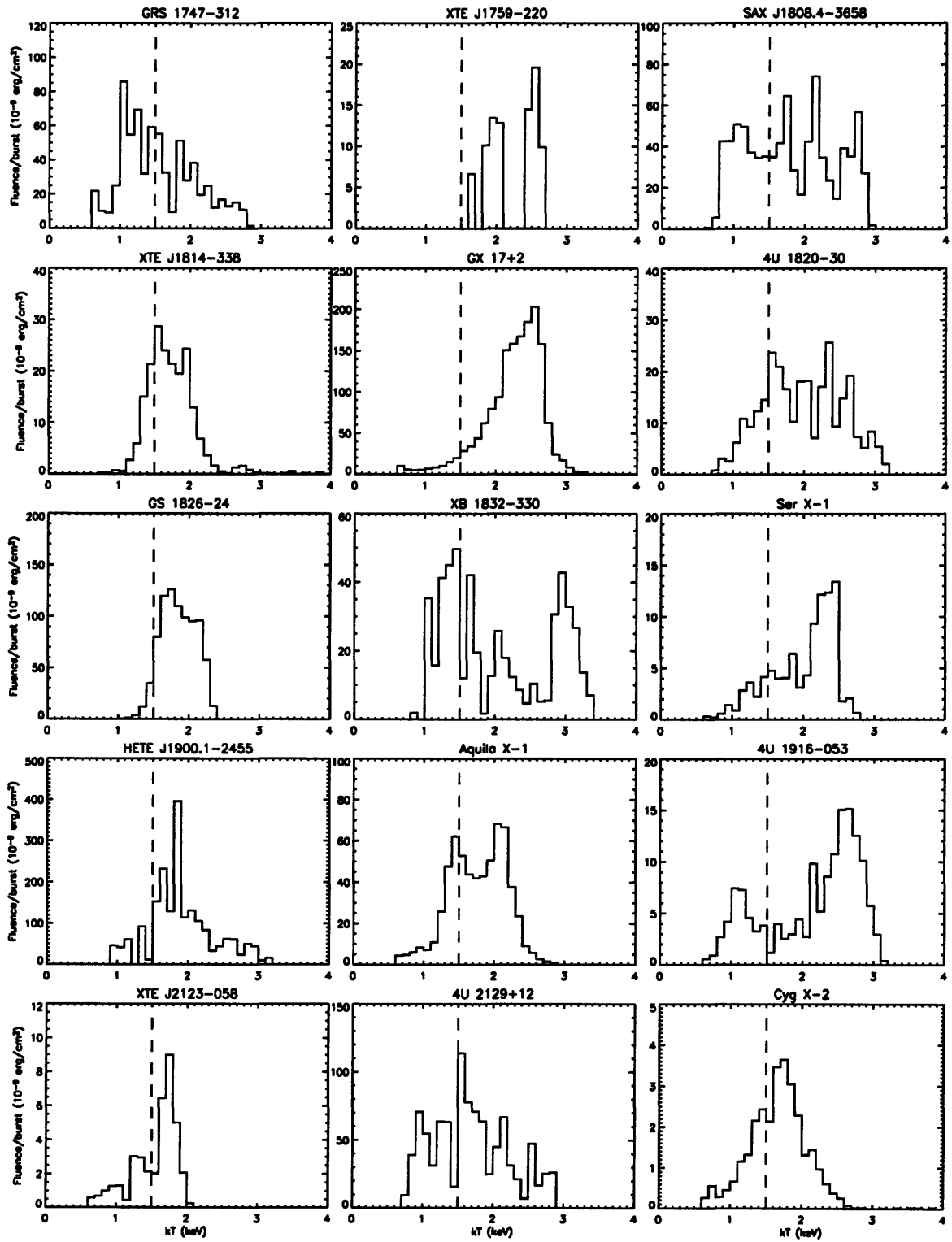
Figure 6-3: Same as Figure 6-1; third group of sources.

given observing cycle. We have indicated whether a source is persistent or transient by the letter "P" or "T" next to the source name. There are approximately equal numbers of persistent and transient bursters, and each class has approximately the same average value for its low-temperature fluence (though there is a large spread).

6.3 Conclusions and future work

The detection and measurement of discrete spectral features from the surface of neutron stars remains a promising way to learn about their fundamental physics. Thermonuclear X-ray bursts are a possible laboratory for the creation of such features, and the measurement of redshifted absorption lines in bursts from EXO 0748−676 was an exciting discovery that placed important constraints on the neutron star equation of state (Cottam et al. 2002). However, subsequent observations of this source have been unable to repeat this measurement, and observations of bursts from two other sources, GS 1826−238 and MXB 1728−34, have not detected any discrete features (Marshall et al. 2002; Galloway et al. 2007a).

A prerequisite for the formation of discrete spectral features in thermonuclear X-ray bursts is the presence of a significant fraction of atoms which retain one or more electrons. This necessitates a relatively low effective temperature, $kT \lesssim 1.5$ keV. We analyzed the temperature distributions of 1,158 bursts from 45 unique sources observed by the *RXTE* PCA, and find that the behavior of individual sources is quite varied. While some sources emit a significant fraction of their burst energy at low temperatures, others have virtually no fluence below 1.5 keV. In fact, the one source from which lines have been detected, EXO 0748−676, has only a small fraction—around 8%—of low-temperature burst fluence. The observations in which features were detected were fortunate to have captured bursts with lower-than-average temperature: the measured temperature was ≈ 1.2 keV. It is possible that the lack of line emission in subsequent observations has been due to more typical, higher burst temperatures. Furthermore, we note that both of the other sources from which bursts have been searched for features have relatively small fractions of low-temperature fluence.

We also stress the importance of neutron star spin in the suppression of detectable discrete spectral features. Neutron stars in accreting binary systems generally have spins in the range of 400 Hz, which would cause substantial smearing and distortion of the line profiles. Therefore, a strategy to detect discrete features arising from thermonuclear X-ray bursts must take into account both the burst temperature and the neutron star spin frequency. Observing sources with significant fluence but unknown spin would be one possible approach. Alternatively, simultaneous observations of EXO 0748−676, the only neutron star in an LMXB known to spin more slowly than 100 Hz, with a high–spectral-resolution and a high-throughput instrument could allow for the time-resolved determination of burst temperature, so that only the lower-temperature portions of the bursts are searched for line features.

Finally, we note that the future generation of high–time- and high–spatial-resolution, high-throughput X-ray observatories could improve the likelihood of the detection of discrete spectral features, both by improving the signal-to-noise of the spectrum, and also by allowing for time-resolved, and perhaps even pulse–phase-resolved, spectroscopy. The latter could help remove the detrimental effects of rapid neutron star spin, provided that a significant fraction of the burst flux arises from a spatially distinct region on the neutron star surface, as is the case for sources which exhibit burst oscillations.

Table 6.1. Low-Temperature Burst Fluences

Source (type)	# Bursts (RExp)[a]	Low-T Fluence (erg cm^{-2})[b]	$\overline{\text{Fluence}}$ Burst (erg cm^{-2})[c]	Low-T fraction[d]	Burst rate (hr^{-1})[e]	Low-T Fluence (erg cm^{-2})[f]	Spin Freq. (Hz)
4U 0513−40 (P)	7 (2)	153.7	22.0	0.17	0.021	12	...
EXO 0748−676 (T)	94 (3)	952.9	10.1	0.08	0.26	73	45
1M 0836−429 (T)	17 (0)	67.0	3.9	0.02	0.44	48	...
2S 0918−549 (P)	4 (1)	156.2	39.0	0.29	0.044	47	...
4U 1254−69 (P)	5 (4)	30.6	6.1	0.32	0.064	10	...
4U 1323−62 (P)	30 (0)	65.0	2.2	0.03	0.40	24	...
4U 1608−522 (T)	31 (13)	5260.2	169.7	0.24	0.070	329	619
4U 1636−53 (P)[g]	170 (52)	9405.9	55.3	0.22	0.19	292	581
MXB 1659−298 (T)	26 (12)	311.1	12.0	0.26	0.26	86	567
4U 1702−429 (P)	47 (6)	2597.3	55.3	0.18	0.13	199	330
4U 1705−44 (P)	47 (4)	1073.0	22.8	0.16	0.27	171	...
XTE J1709−267 (T)	3 (1)	46.8	15.6	0.30	0.075	32	...
XTE J1710−281 (T)	19 (1)	84.5	4.4	0.22	0.28	34	...
XTE J1723−376 (T)	3 (0)	51.1	17.0	0.22	0.32	151	...
4U 1724−307 (P)[g]	3 (3)	1100.9	367.0	0.38	0.021	214	...
4U 1728−34 (P)	106 (80)	1013.3	9.6	0.03	0.20	53	363
Rapid Burster (T)	66 (0)	685.2	10.4	0.09	0.13	37	306
KS 1731−261 (T)	27 (6)	354.5	13.1	0.03	0.20	72	524
SLX 1735−269 (P)	1 (0)	50.7	50.7	0.13	0.014	19	...
4U 1735−44 (P)	11 (8)	80.6	7.3	0.14	0.087	17	...
KS 1741−293 (T)	1 (0)	60.4	60.4	0.19	0.0018	3	...
GRS 1741.9−2853 (T)	8 (6)	731.3	91.4	0.16	0.014	35	...
2E 1742.9−2929 (P)	84 (2)	2298.0	27.4	0.20	0.15	113	...
SAX J1747.0−2853 (T)	17 (10)	846.4	49.8	0.16	0.030	41	...
SLX 1744−300 (P)	1 (0)	25.4	25.4	0.29	0.037	26	...
GX 3+1 (P)	2 (1)	39.4	19.7	0.09	0.014	7	...
SAX J1748.9−2021 (T)	16 (8)	483.3	30.2	0.13	0.44	369	[410]
EXO 1745−248 (T)	22 (2)	167.5	7.6	0.03	0.54	114	...
4U 1746−37 (P)	30 (3)	206.4	6.9	0.24	0.24	45	...
SAX J1750.8−2900 (T)	4 (2)	55.5	13.9	0.08	0.12	46	601
GRS 1747−312 (T)	7 (3)	1185.9	169.4	0.26	0.033	155	...
XTE J1759−220 (T)	1 (0)	0.0	0.0	0.0	0.034	0	...
SAX J1808.4−3658 (T)	6 (5)	883.0	147.2	0.24	0.012	49	401
XTE J1814−338 (T)	28 (1)	1111.6	39.7	0.21	0.23	253	314
GX 17+2 (P)	12 (9)	168.3	14.0	0.02	0.048	18	...
4U 1820−30 (P)	5 (5)	70.5	14.1	0.06	0.013	5	...
GS 1826−24 (T)	54 (0)	1802.0	33.4	0.04	0.25	231	...
XB 1832−330 (?)	1 (1)	151.3	151.3	0.33	0.036	151	...
Ser X-1 (P)	7 (3)	61.9	8.8	0.12	0.10	24	...
HETE J1900.1−2455 (T)	2 (2)	296.3	148.1	0.08	0.026	106	377
Aquila X-1 (T)	57 (10)	7358.9	129.1	0.23	0.10	358	549
4U 1916−053 (P)	14 (13)	127.6	9.1	0.09	0.12	30	270
XTE J2123−058 (T)	6 (0)	73.5	12.3	0.33	0.32	108	...
4U 2129+12 (P)	1 (1)	276.9	276.9	0.31	0.010	76	...
Cyg X-2 (P)	55 (15)	190.2	3.5	0.15	0.12	11	...

[a]The total number of *RXTE* PCA bursts presented here. In parentheses are the number of these bursts which showed a radius-expansion episode.

[b]The total fluence summed over the time when the burst was in the temperature range of 0.6–1.5 keV ("low-temperature" fluence).

[c]Total low-temperature fluence divided by the number of observed bursts.

[d]The fraction of burst fluence below 1.5 keV.

[e]Burst rates are from Galloway et al. (2006).

[f]Assuming a steady burst rate and average burst parameters, the expected 0.6–1.5 keV fluence for a 100 ks observation.

[g]Persistent but currently fading.

Chapter 7

High-Resolution X-ray Spectroscopy of the Ultracompact LMXB Pulsar 4U 1626−67

Abstract

We report results from four recent observations of the ultracompact low-mass X-ray binary pulsar 4U 1626−67. All the observations obtained high-resolution X-ray spectra of the system, two from the *Chandra X-ray Observatory* using the High Energy Transmission Grating Spectrometer, and two from the *XMM-Newton Observatory* using the Reflection Grating Spectrometer as well as the EPIC pn and MOS. These data allow us to study in detail the prominent Ne and O emission line complexes which make 4U 1626−67 unique among LMXBs. The observations were spaced over a period of 3 yr for a total observing time of 238 ks, allowing us to monitor the line regions as well as the overall source flux, continuum spectrum, and timing properties. The structure of the emission lines and the ratios of the components of the helium-like Ne IX and O VII triplets support the hypothesis that they are formed in the high-density environment of the accretion disk. We do not find any significant changes in the line widths or ratios over this time period, though we note that the line equivalent widths decrease. Using the most recent calibration products, we are able to place constraints on the strengths of the Ne K, Fe L, and O K photoelectric absorption edges. In contrast to the analysis of Schulz et al. (2001), the data do not require an overabundance of Ne or O in the system relative to the expected ISM values. We find that the pulsar is still spinning down, though the rate of decrease is greater than what was predicted by the ephemeris derived from previous *Compton*/BATSE monitoring. We also note that the pulse profile has changed significantly from what was found prior to the torque reversal in 1990, suggesting that this event may be linked to a change in the geometry of the accretion column. The flux of 4U 1626−67 continues to decrease, in keeping with the trend of the last $\approx$ 30 yr over which it has been observed. We expect the accretion rate to drop below the critical rate necessary to maintain a stable accretion disk in 2–15 yr, at which time 4U 1626−67 will enter a period of quiescence.

7.1 Introduction

The 7.7 s X-ray pulsar 4U 1626−67 was first discovered by *Uhuru* (Giacconi et al. 1972; Rappaport et al. 1977), and remains the only known high-field ($B \approx 4 \times 10^{12}$ G, Pravdo et al. 1979; Coburn et al. 2002) pulsar in an ultracompact low-mass X-ray binary (LMXB). This unique pairing of an apparently young neutron star with a very low-mass companion could indicate that the neutron star was originally a white dwarf whose mass, as a result of accretion, exceeded the Chandrasekhar limit (Joss et al. 1978 although see Verbunt et al. 1990). Although orbital motion has never been detected in X-ray data, pulsed optical emission reprocessed on the surface of the secondary allowed Middleditch et al. (1981) to infer an orbital period of 42 minutes, which was later confirmed by Chakrabarty (1998). It is therefore a member of the class of objects known as "ultracompact" binaries ($P_{orb} < 80$ minutes) which must have hydrogen-depleted secondaries to reach such short periods (Paczynski and Sienkiewicz 1981; Nelson et al. 1986). It has an extremely small mass function of $f \leq 1.3 \times 10^{-6}$ $M_{\odot}$, which corresponds to a secondary mass of 0.04 $M_{\odot}$ for $i = 18°$ (Levine et al. 1988). A very low mass secondary would account for the faint ($V \approx 17.5$) optical counterpart and the high optical pulsed fraction (McClintock et al. 1977, 1980).

Initially, 4U 1626−67 was observed to be spinning up with a characteristic timescale $P/\dot{P} \approx 5000$ yr, but in 1990 this trend reversed and the neutron star began to spin down on approximately the same timescale (Wilson et al. 1993; Chakrabarty et al. 1997). The torque reversal was abrupt, although the decrease in bolometric X-ray flux has been gradual and continuous over the past ≈ 30 yr. Assuming that the X-ray flux is a good proxy for the accretion rate onto the neutron star, these observational facts cannot be reconciled with current accretion disk–neutron star interaction theory. However, the fact that the pulsar underwent torque reversal implies that the radius at which the accretion disk is truncated by the neutron star's magnetic field is close to the corotation radius. With this assumption and a neutron star mass of 1.4 $M_{\odot}$, the measured $\dot{P}$ during spin-up can constrain the accretion rate to be $\gtrsim 2 \times 10^{-10}$ $M_{\odot}$ yr^{-1}, which implies a distance of $\gtrsim 3$ kpc (Chakrabarty et al. 1997). Alternatively, measurements of the optical and X-ray fluxes (assuming the albedo of the disk is $\gtrsim 0.9$) give a distance range to 4U 1626−67 of $5 \lesssim D \lesssim 13$ kpc (Chakrabarty 1998).

Perhaps the most unique characteristic of 4U 1626−67 is its X-ray spectrum. Angelini et al. (1995) first reported the presence of Ne and O emission lines in an *ASCA* spectrum, and they found similar features in an *Einstein* observation performed prior to the torque reversal. Using a subsequent observation by *Chandra*, we discovered double-peaked line structure indicative of formation in an accretion disk (Schulz et al. 2001 hereafter S01). Emission line features such as these are not seen in any other LMXB systems, and suggest that the donor is particularly rich in elements resulting from later stages of nuclear burning— perhaps a C-O-Ne or O-Ne-Mg white dwarf. A UV spectrum obtained with the *Hubble Space Telescope* Space Telescope Imaging Spectrograph (STIS) revealed both emission and absorption features from C, O and Si (Homer et al. 2002). The C absorption lines are stronger than expected from a purely interstellar medium (ISM) contribution, suggesting some local contribution, and the O V line has a pronounced double-peaked profile, indicating an accretion-disk origin similar to the X-ray lines. The spectrum is missing common N and He lines typically seen in UV spectra from high-excitation systems, likely because 4U 1626−67 is lacking in these elements. A high-S/N optical spectrum obtained by Werner et al. (2006) using the Very Large Telescope confirms the lack of He in the system, and

Table 7.1. X-Ray Observations

Observatory	Observation Start (UT)	Observation ID	Duration (ks)
Chandra.........	2000 Sep 16 14:57	104	40
XMM-Newton ...	2001 Aug 24 02:57	0111070201	17
Chandra.........	2003 Jun 3 02:30	3504	97
XMM-Newton ...	2003 Aug 20 05:55	0152620101	84

finds H lacking as well. The optical spectrum is dominated by C and O emission lines, but does not appear to contain any Ne lines. Given the current understanding of the model Ne atom, they find that Ne is present in 4U 1626−67 at $\lesssim 10\%$ by mass; or, equivalently, that Ne/O $\lesssim 0.2$.

We present a series of four high-resolution X-ray spectra spanning three years, two obtained with the High Energy Transmission Gratings (HETGS) aboard the *Chandra X-ray Observatory*, and two from the Reflection Grating Spectrometers (RGS) aboard *XMM-Newton*. We previously presented analysis of the first *Chandra* observation in S01, but this reanalysis uses improved calibration products and software. We describe the observations and data reduction procedures in § 7.2, and our spectral analysis in § 7.3. We present timing analysis is § 7.4. Finally, we discuss the implications of our observations in § 7.5.

7.2 Observations and data reduction

7.2.1 *Chandra*

The pulsar 4U 1626−67 has been observed twice with the HETGS on board the *Chandra X-Ray Observatory* (Canizares et al. 2005), first on 2000 September 16 and again on 2003 June 3. The HETGS comprises two sets of transmission gratings: the medium energy gratings (MEGs), with a spectral resolution of $\Delta\lambda = 0.023$ Å FWHM and a range of 2.5–31 Å (0.4–5.0 keV), and the high energy gratings (HEGs), which have $\Delta\lambda = 0.012$ Å FWHM and a range of 1.2–15 Å (0.8–10 keV). See Table 7.1 for a summary of the observations.

We obtained "level 1" event lists from the *Chandra* data archive[1] and reprocessed the data using the latest available version of the CIAO software (vers. 3.3) and the calibration database (CALDB vers. 3.2.1). This processing applied the gain, time-dependent gain, and charge transfer inefficiency (CTI) corrections. The CTI corrections improve the computation of event grade (used to filter out likely nonsource events) and the gain products improve the channel to energy mapping of events, which allows for more precise order-sorting of the dispersed spectra. We created grating responses that include the time-dependent effects of a contaminant present on the ACIS optical blocking filter (Marshall et al. 2004). Correcting for this contamination is necessary for precise spectral analysis, since it affects both spectral shape and normalization.

Neither *Chandra* observation contained any appreciable background flares. After reprocessing and filtering out bad pixels, we applied the standard grade filtering (retaining grades 0, 2, 3, 4 and 6), and used the `tgdetect` tool to determine the zeroth-order source position.

---

[1]http://cda.harvard.edu/chaser/mainEntry.do

The high source count rate caused the zeroth-order images to be quite piled up, but this did not hinder our ability to determine the source position. This position was used to sort the dispersed spectra into the proper orders, resulting in 62555 (101799) background-subtracted events in the first-order MEG spectrum and 35343 (59706) in the first-order HEG spectrum for ObsID 104 (3504). The dispersed spectra are not affected by pileup.

7.2.2 *XMM-Newton*

XMM-Newton has observed 4U 1626−67 four times, but only two of these observations contain a significant amount of science data (ObsIDs 0111070201, performed 2001 August 24, and 0152620101, performed 2003 August 20; see Table 7.1). Here, we analyze data from the three EPIC cameras (two MOS detectors and the pn), as well as the two reflection grating spectrometers (RGS1 and RGS2). The MOS (pn) detectors have nominal bandpasses of 0.15–12 (0.15–15) keV, and spectral resolutions of 70 (80) eV at 1 keV. The RGSs have bandpasses of 0.35–2.5 keV and first-order spectral resolutions of 0.04 Å FWHM. Both observations were performed after the failure of RGS1's CCD7 and RGS2's CCD4, resulting in gaps in the dispersed spectra that were filtered out for analysis.

The *XMM-Newton* science products were obtained from the *HEASARC*[2] archive. Both observations were affected by strong background flares in the MOS and pn detectors, which we filtered out prior to analysis, resulting in the loss of ≈ 5 ks of MOS data and ≈ 2 ks of pn data for ObsID 0111070201, and ≈ 25 ks of MOS and pn data and ≈ 12 ks of RGS data for ObsID 0152620101.

During ObsID 0111070201, the MOS1 detector was in timing mode, so was not easily susceptible to pileup. However, the source core is somewhat piled in the MOS2 detector, and was excised prior to analysis. During ObsID 0152620101, the MOS2 detector was in timing mode, and the MOS1 detector shows mild evidence of pileup, so we again removed the central portion of source data prior to analysis. The standard filters were applied, FLAG == 0 and PATTERN <= 12 (4), to the MOS (pn) data. The RGS data were reprocessed (using XMMSAS vers. 6.5.0) with refined source coordinates, resulting in updated source and background spectra as well as responses. Background spectra were created for the EPIC data using off-source regions, and scaled appropriately to match the source spectra. After processing, there were a total of 1.1×10^5 (1.7×10^5) background-subtracted counts in the MOS1 data, 7.3×10^4 (4.5×10^5) in the MOS2 data, 3.1×10^5 (1.04×10^6) in the pn data, 8366 (17289) in the RGS1 spectrum, and 9951 (21076) in the RGS2 spectrum for ObsID 0111070201 (0152620101).

7.3 Spectral analysis

We used the ISIS software package (vers. 1.3.3)[3] for spectral fitting. All source and background data, as well as response files, were read into ISIS, and normalized background counts were subtracted prior to fitting. We combined the ±1 spectral orders of the HETGS data, and used the −1 order of the RGS data. We employed Cash statistics throughout our analysis, and fit the data from different instruments simultaneously. All the quoted errors are 90% confidence limits unless otherwise noted.

---

[2]http://heasarc.gsfc.nasa.gov/db-perl/W3Browse/w3browse.pl
[3]http://space.mit.edu/CXC/ISIS/

Table 7.2. Continuum Spectral Fits

Observation	N_H $(10^{21} cm^{-2})$	Power Law		Blackbody		Flux[b]	C_ν (dof)[c]
		Norm[a]	Γ	$R^2_{km}/D^2_{10\ kpc}$	kT (keV)		
Chandra ObsID 104	$1.3^{+0.4}_{-0.3}$	12.1 ± 0.5	0.88 ± 0.03	600^{+400}_{-200}	0.21 ± 0.02	2.2	1.04 (1844)
XMM ObsID 0111070201	$1.39^{+0.07}_{-0.09}$	$8.0^{+0.1}_{-0.2}$	0.80 ± 0.01	330^{+30}_{-40}	$0.254^{+0.008}_{-0.005}$	1.7	1.15 (1888)
Chandra ObsID 3504	$1.0^{+0.4}_{-0.3}$	8.4 ± 0.2	0.81 ± 0.02	600^{+400}_{-200}	0.19 ± 0.01	1.7	1.10 (1926)
XMM ObsID 0152620101	$1.38^{+0.06}_{-0.04}$	$6.76^{+0.08}_{-0.07}$	$0.782^{+0.008}_{-0.007}$	290^{+30}_{-20}	$0.245^{+0.003}_{-0.005}$	1.5	1.38 (1857)

[a]Normalization of power-law component at 1 keV in units of 10^{-3} ergs cm^{-2} s^{-1} keV^{-1}.

[b]Absorbed 0.3–10.0 keV flux in units of 10^{-10} ergs cm^{-2} s^{-1}.

[c]The reduced Cash statistic and number of degrees of freedom for the fit.

7.3.1 Continuum fitting

For continuum fitting, we excluded the known emission-line regions and used the wavelength/energy ranges 1.2–17.0 (1.8–26.0) Å for the HEG (MEG) grating spectra, 7.0–34.0 Å for the RGS grating spectra, and 1.1–9.9 (1.1–8.3) keV for the MOS (pn) spectra. The lower energy ranges of the MOS and pn spectra were excluded because they contain unresolved Ne and O emission lines which artificially increase the overall continuum level. We also excluded regions in the RGS data that contain bad columns or fall across non-functioning CCD chips. During the second XMM-Newton observation (ObsID 0152620101), MOS2 was in timing mode, and its spectral calibration did not match that of the other instruments, so these data were omitted from the continuum fit.

We grouped the MOS data to have a minimum of 50 counts and the pn data to have a minimum of 500 counts bin^{-1}, and the RGS data to contain 6 channels bin^{-1} (resulting in $\cong$ 0.04 Å wavelength bins, comparable to the instrumental resolution). We grouped the HEG and MEG spectra to contain 4 channels and a minimum of 10 counts per bin (resulting in $\gtrsim$ 0.01 [0.02] Å wavelength bins for the HEG [MEG] data, again comparable to the instrumental resolution).

Although a simple power-law model gives a reasonable fit ($\chi^2_\nu \cong 1.2$), the residuals suggest the presence of an additional spectral component. This has previously been modeled as a second power-law or a blackbody component (S01). An F-test indicates that the addition of a blackbody component is preferred over a single power-law at the 8 σ level, and this is what we use for our continuum fits. To model the absorption, we used an updated version of the tbabs model, tbnew[4] (Wilms et al. 2007), which includes high-resolution structure for the Ne K, Fe L, and O K edges. The best-fit continuum models are presented in Table 7.2, and the combined continuum spectra are shown in Figure 7-1.

The 0.3–10 keV flux followed a decreasing trend, falling from 2.2×10^{-10} ergs cm^{-2} s^{-1} in 2000 September to 1.5×10^{-10} ergs cm^{-2} s^{-1} in 2003 August. Overall, 4U 1626−67 has decreased in flux since 1977, with no apparent change following the reversal in accretion torque in 1990 (see Fig. 7-2).

---

[4]http://astro.uni-tuebingen.de/~wilms/research/tbabs/

Table 7.3. Single-Gaussian Emission Line Fits

Instrument	MJD	$\Delta\lambda$ (Å)	V (km s^{-1})	FWHM (km s^{-1})	Flux[a]	EW (Å [eV])	C_ν (dof)[b]
Ne X Line at 12.13 Å							
Chandra	51803.6	0.021 ± 0.014	510 ± 340	6330^{+860}_{-690}	$41.3^{+4.6}_{-4.3}$	0.29 [24]	0.97 (115)
XMM-Newton.	52145.1	$0.016^{+0.033}_{-0.035}$	390^{+830}_{-880}	4800^{+1800}_{-1600}	$25.0^{+6.0}_{-5.7}$	0.21 [17]	1.22 (16)
Chandra	52795.1	$0.018^{+0.012}_{-0.013}$	440^{+310}_{-320}	5540^{+690}_{-590}	$19.4^{+2.2}_{-2.1}$	0.20 [17]	1.04 (134)
XMM-Newton.	52871.2	$0.019^{+0.021}_{-0.022}$	470^{+520}_{-540}	5540^{+1260}_{-990}	$20.4^{+3.0}_{-2.5}$	0.21 [18]	2.15 (16)
Ne IX Line at 13.55 Å							
Chandra	51803.6	$0.010^{+0.034}_{-0.032}$	210^{+740}_{-710}	4200^{+1800}_{-1200}	$13.2^{+4.5}_{-4.1}$	0.10 [6.8]	1.02 (91)
XMM-Newton[c]	52145.1	$\cdots$	$\cdots$	4200	$3.4^{+4.6}_{-3.4}$	0.030 [2.0]	1.03 (17)
Chandra	52795.1	$-0.019^{+0.036}_{-0.039}$	-430^{+800}_{-850}	4500^{+2000}_{-1700}	$7.2^{+2.6}_{-2.5}$	0.079 [5.4]	0.90 (102)
XMM-Newton[c]	52871.2	$\cdots$	$\cdots$	4500	$7.1^{+2.4}_{-2.1}$	0.070 [4.7]	0.81 (17)
O VIII Line at 18.97 Å							
Chandra	51803.6	$0.063^{+0.058}_{-0.079}$	1000^{+920}_{-1250}	7100^{+3200}_{-1700}	60^{+17}_{-15}	0.56 [19]	1.76 (45)
XMM-Newton.	52145.1	$0.025^{+0.034}_{-0.032}$	390^{+530}_{-500}	5510^{+1150}_{-860}	$39.1^{+6.6}_{-5.4}$	0.49 [17]	1.43 (60)
Chandra	52795.1	$-0.016^{+0.059}_{-0.060}$	-260 ± 940	6000^{+3400}_{-1600}	$28.8^{+9.6}_{-8.2}$	0.40 [14]	0.99 (56)
XMM-Newton.	52871.2	$-0.006^{+0.022}_{-0.021}$	-100^{+350}_{-340}	5840^{+890}_{-610}	$26.1^{+2.8}_{-2.3}$	0.40 [14]	1.34 (61)
O VII Line at 21.80 Å							
Chandra	51803.6	$-0.050^{+0.074}_{-0.077}$	-688^{+1015}_{-1057}	6154^{+1974}_{-1487}	$77.3^{+26.3}_{-24.3}$	0.87 [23]	0.98 (22)
XMM-Newton.	52145.1	$-0.027^{+0.070}_{-0.093}$	-380^{+960}_{-1280}	8900^{+4300}_{-1600}	72^{+18}_{-13}	0.96 [25]	1.08 (50)
Chandra	52795.1	$-0.020^{+0.093}_{-0.058}$	-280^{+1280}_{-800}	3700^{+3600}_{-1400}	31^{+16}_{-12}	0.50 [13]	0.91 (25)
XMM-Newton.	52871.2	$-0.051^{+0.022}_{-0.023}$	-710^{+310}_{-320}	5200^{+850}_{-490}	$47.6^{+5.2}_{-4.4}$	0.86 [23]	1.18 (51)

[a]The Gaussian normalization in units of 10^{-5} photons cm^{-2} s^{-1}.

[b]The reduced Cash statistic and number of degrees of freedom for the fit.

[c]Since the *XMM-Newton* data were not able to constrain the Ne IX lines, their positions and widths were fixed to the values found in the *Chandra* data.

7.3.2 Emission lines

There are prominent Ne and O emission lines in all four spectra (see Figs. 7-1 and 7-3). To explore the line characteristics, we added Gaussian features to the continuum models determined from the overall spectral fits. All the lines are well-fit by single Gaussian profiles. We note that the Ne IX lines are not reliably detected in the *XMM-Newton* data; for these lines, we fixed the line width and location to the *Chandra* values to obtain approximations of the line flux. The single-Gaussian line fits are presented in Table 7.3.

The single-Gaussian fits reveal lines which are quite broad ($\approx$6000 km s^{-1} FWHM). For a given line, the width does not vary significantly over the four observations. However, the line strengths of Ne X and O VIII decrease over the course of the observations (the trend is not so clear for Ne IX or O VII). To determine whether the line flux is decreasing more rapidly than the overall continuum flux, we fixed the line widths to their weighted averages and recalculated the line strengths, then fit the flux trends for the Ne X and O VIII lines. Fixing the widths did not change the flux values appreciably, and improved the errors on the fluxes by only a small amount. Over the $\approx$ 3 yr span of the observations, from 2000 September to 2003 August, the Ne X flux decreased to 51.6 $\pm$ 5.5% and the O VIII flux to 54.0 $\pm$ 8.7% of their initial values. This decrease is significantly more than the decrease in

the 0.3–10.0 keV continuum flux, which only fell to $76.4 \pm 6.6\%$ of its initial value. The fact that the line strengths decrease faster than the continuum strength is also reflected in the declining equivalent widths (EWs) of the lines. We find that the EWs of Ne X and O VIII decrease to $75.7 \pm 7.9\%$ and $74.3 \pm 12.3\%$ of their initial values, respectively (see Fig. 7-4, which also includes data from *ASCA* and *BeppoSAX*).

The *Chandra* Ne X and O VIII lines, as well as the *XMM-Newton* O VII line, show what appear to be double-peaked profiles (see Fig. 7-3). As S01 point out, the line shapes, combined with the apparent high-density environment of the line formation regions (as indicated by the dominance of the intercombination component of the He-like triplets; see below), suggest that the lines arise in an accretion disk. To derive physically meaningful values for the line parameters, we fit each line with a pair of Gaussians, fixing the width and absolute velocity of the red- and blueshifted components to be equal, thus approximating the expected disk-line "two-horn" profile. However, there are a number of instances in which it is not possible to constrain the width and velocity of a particular line. For these instances, we fixed the values to the weighted averages from the observations for which the line was well constrained. This allowed us to evaluate the approximate fluxes of the line components, with the assumption that the widths and velocities of a given line do not change substantially over the course of the observations. Where multiple measurements could be made, this is true both for the widths from the single-Gaussian fits and for the widths and velocities from the double-Gaussian fits, so we consider it to be a reasonable assumption. The Ne IX lines in the *XMM-Newton* data were too poorly constrained to be included in the double-Gaussian fits. Table 7.4 contains the values obtained from these fits.
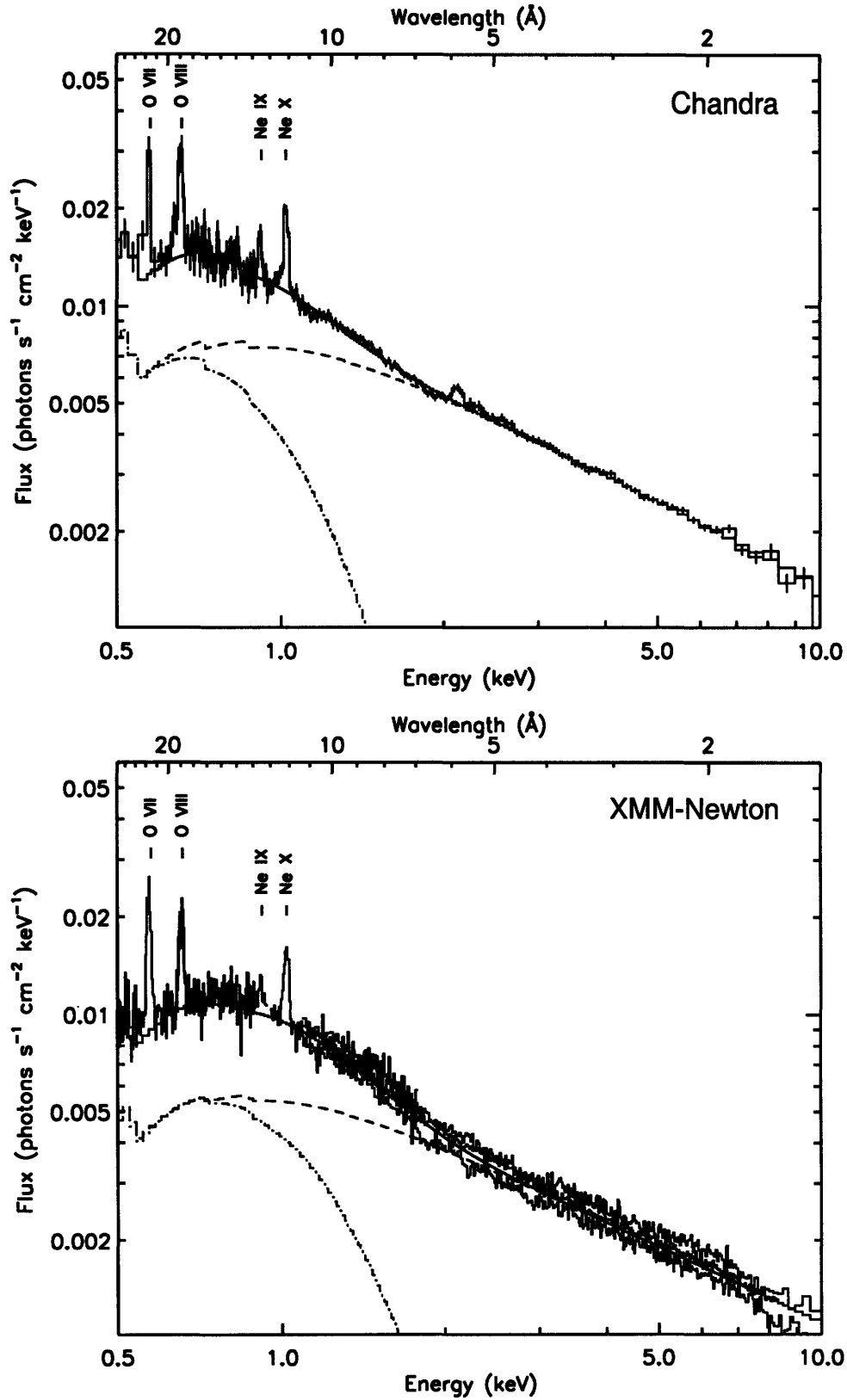
Figure 7-1: Combined *Chandra* (top) and *XMM-Newton* (bottom) spectra with representative continuum models comprised of absorbed blackbody plus power-law emission. The blackbody (dot-dashed line) and power-law (dashed line) contributions are also plotted.
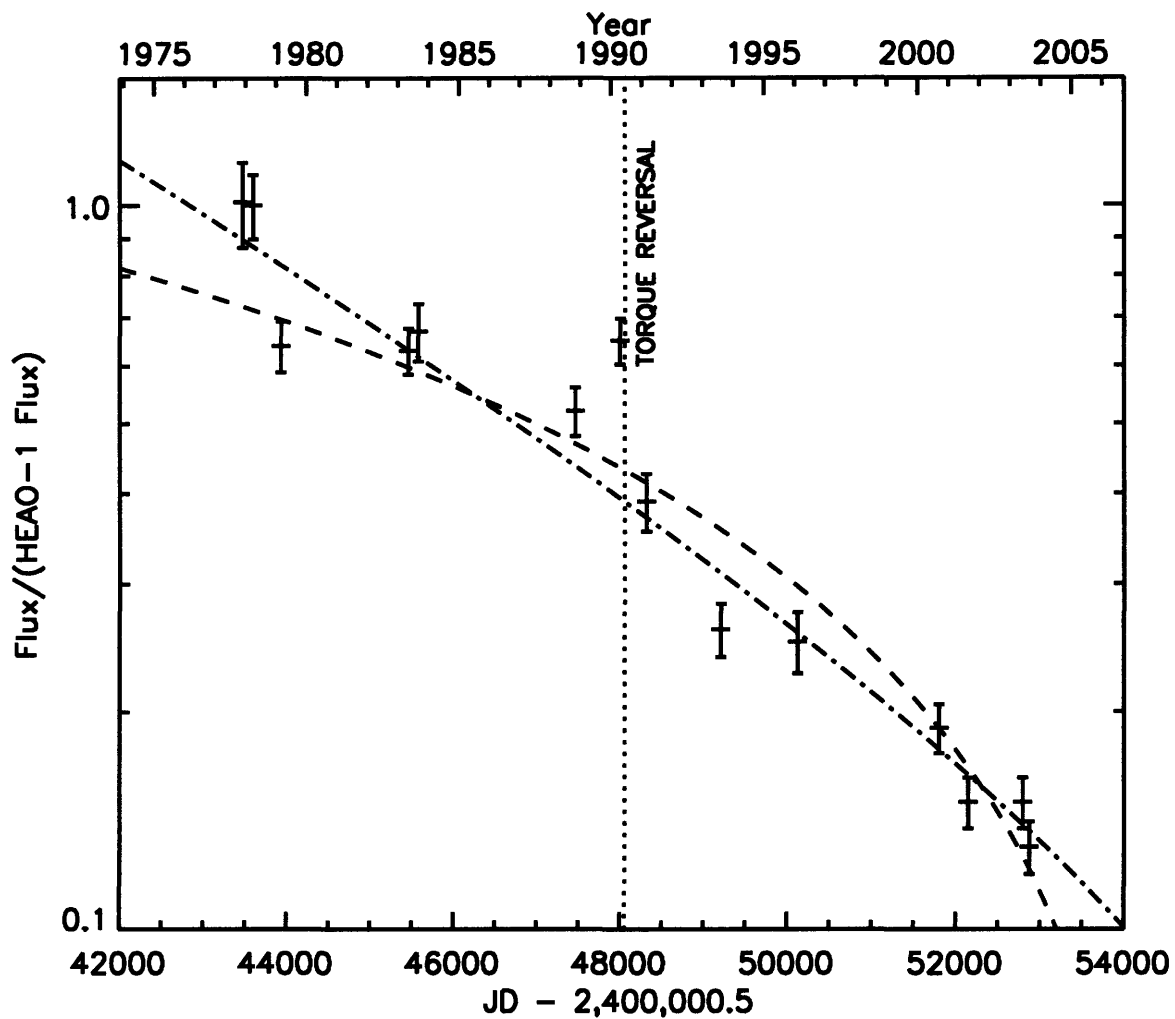
Figure 7-2: X-ray flux history of 4U 1626—67 from 1977 to 2003. The dashed line is a linear fit, the dot-dashed line a logarithmic fit to the data. Error bars represent the 1 σ confidence intervals. The most recent four data points represent the *Chandra* and *XMM-Newton* observations.
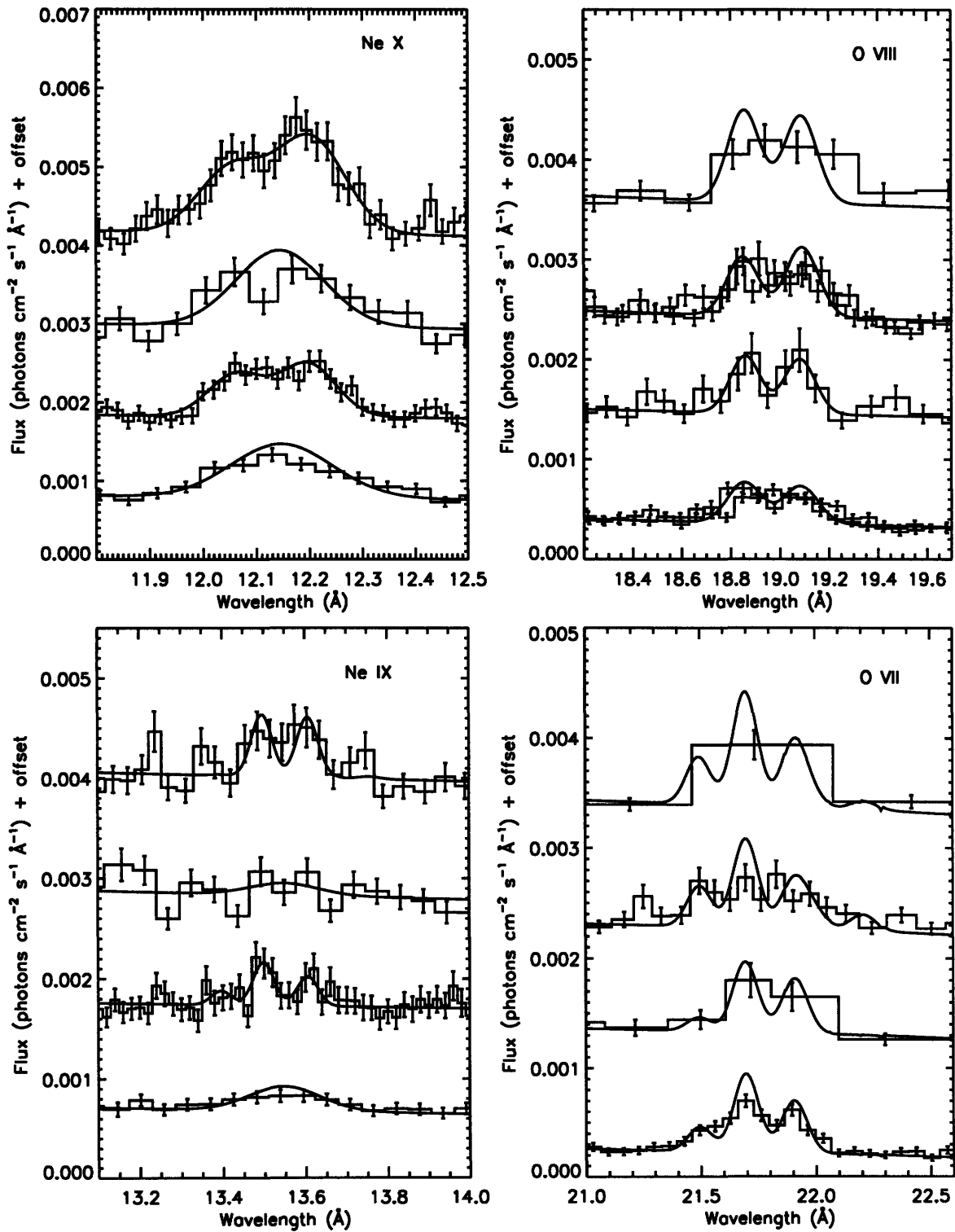
Figure 7-3: Emission-line regions for all four data sets. The hydrogen-like Ne X (left) and O VIII (right) ions are in the top panels, and the helium-like triples of Ne IX (left) and O VII (right) are in the bottom panels. Each panel contains (*top to bottom*) *Chandra* ObsID 104, *XMM-Newton* ObsID 0111070201, *Chandra* ObsID 3504, and *XMM-Newton* ObsID 0152620101.
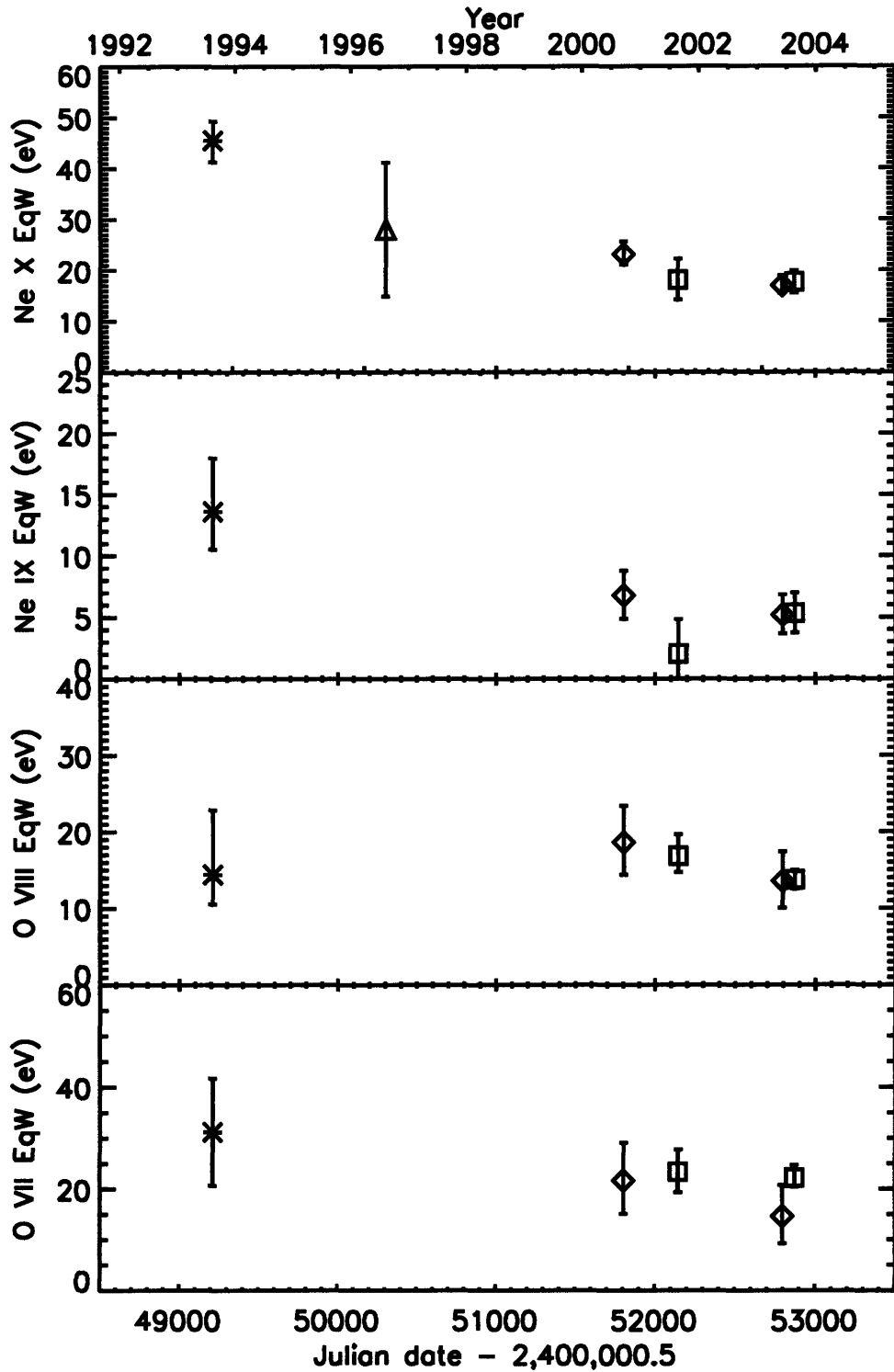
Figure 7-4: Line EWs from the literature and from the single-Gaussian fits presented in this chapter. The *ASCA* measurements are plotted with stars (Angelini et al. 1995), that from *BeppoSAX* with a triangle (Owens et al. 1997), and from *Chandra* with diamonds and *XMM-Newton* with squares; error bars represent the 90% confidence intervals.

Table 7.4: Double-Gaussian Emission Line Fits

Observatory	MJD	FWHM (km s^{-1})	$\Delta\lambda$ (Å)	V (km s^{-1})	Blueshifted Lines Flux[a]	EW (Å [eV])	Redshifted Lines Flux[a]	EW (Å [eV])	C_ν (dof)[b]
					Ne X Line at 12.13 Å				
Chandra..........	51803.6	3690^{+1190}_{-630}	$\pm0.075^{+0.011}_{-0.008}$	$\pm1840^{+270}_{-200}$	$15.8^{+3.1}_{-3.0}$	0.104 [8.84]	$23.8^{+3.8}_{-3.4}$	0.160 [13.36]	1.02 (246)
XMM-Newton.....	52145.1	1500^{+1800}_{-1500}	$\pm0.077^{+0.018}_{-0.017}$	$\pm1910^{+450}_{-430}$	$11.1^{+4.8}_{-4.6}$	0.092 [7.82]	$14.4^{+5.2}_{-4.7}$	0.120 [9.99]	1.15 (33)
Chandra..........	52795.1	3040^{+670}_{-440}	$\pm0.068\pm0.007$	$\pm1670^{+180}_{-170}$	$8.2^{+1.5}_{-1.4}$	0.083 [7.05]	$10.5^{+1.8}_{-1.6}$	0.107 [8.94]	1.10 (281)
XMM-Newton[c]....	52871.2	3085	$\pm0.072^{+0.017}_{-0.015}$	$\pm1780^{+420}_{-380}$	$11.3^{+2.6}_{-2.6}$	0.113 [9.45]	$9.0^{+2.5}_{-2.6}$	0.089 [7.60]	1.86 (34)
					Ne IX Resonance Line at 13.45 Å				
Chandra[d]..........	51803.6	1300	±0.055	±1210	$0.1^{+1.7}_{-0.1}$	0.001 [0.05]	$0.1^{+1.7}_{-0.1}$	0.001 [0.05]	1.09 (113)
Chandra..........	52795.1	1300^{+960}_{-610}	$\pm0.055^{+0.017}_{-0.018}$	$\pm1210^{+380}_{-400}$	$1.1^{+1.0}_{-1.0}$	0.012 [0.80]	$1.1^{+1.0}_{-1.0}$	0.012 [0.80]	0.86 (120)
					Ne IX Intercombination Line at 13.55 Å				
Chandra[d]..........	51803.6	1300	±0.055	±1210	$5.0^{+1.8}_{-1.9}$	0.037 [2.52]	$5.0^{+1.8}_{-1.9}$	0.037 [2.52]	1.09 (113)
Chandra..........	52795.1	1300^{+960}_{-610}	$\pm0.055^{+0.017}_{-0.018}$	$\pm1210^{+380}_{-400}$	$2.3^{+1.2}_{-1.1}$	0.021 [1.46]	$2.3^{+1.2}_{-1.1}$	0.021 [1.46]	0.86 (120)
					Ne IX Forbidden Line at 13.70 Å				
Chandra[d]..........	51803.6	1300	±0.055	±1210	$0.2^{+1.7}_{-0.2}$	0.001 [0.09]	$0.2^{+1.7}_{-0.2}$	0.001 [0.09]	1.09 (113)
Chandra..........	52795.1	1300^{+960}_{-610}	$\pm0.055^{+0.017}_{-0.018}$	$\pm1210^{+380}_{-400}$	$0.0^{+1.2}_{-0.0}$	0.0 [0.0]	$0.0^{+1.2}_{-0.0}$	0.0 [0.0]	0.86 (120)
					O VIII Line at 18.97 Å				
Chandra[e]..........	51803.6	2474	±0.116	±1840	$26.3^{+8.7}_{-9.9}$	0.258 [8.78]	$21.6^{+10.8}_{-6.4}$	0.210 [7.31]	1.72 (50)
XMM-Newton.....	52145.1	2450^{+900}_{-610}	$\pm0.122^{+0.016}_{-0.017}$	$\pm1930\pm260$	$17.6^{+4.7}_{-4.4}$	0.217 [7.58]	$21.9^{+4.9}_{-4.5}$	0.275 [9.36]	1.10 (73)
Chandra..........	52795.1	2320^{+1140}_{-650}	$\pm0.112^{+0.021}_{-0.023}$	$\pm1770^{+330}_{-370}$	$13.0^{+5.7}_{-4.9}$	0.179 [6.24]	$13.7^{+5.8}_{-5.0}$	0.191 [6.51]	0.98 (61)
XMM-Newton.....	52871.2	2600^{+870}_{-600}	$\pm0.115^{+0.012}_{-0.012}$	$\pm1810^{+180}_{-200}$	$12.7^{+2.1}_{-1.9}$	0.191 [6.66]	$12.4^{+2.0}_{-1.8}$	0.189 [6.43]	1.15 (76)

Table 7.4 – Continued

Observatory	MJD	FWHM (km s⁻¹)	Δλ (Å)	V (km s⁻¹)	Blueshifted Lines		Redshifted Lines		C_ν (dof)[b]
					Flux[a]	EW (Å [eV])	Flux[a]	EW (Å [eV])	
O VII Resonance Line at 21.60 Å									
Chandra[f]	51803.6	1750	±0.104	±1430	$12.8^{+11.2}_{-8.9}$	0.142 [3.82]	$12.8^{+11.2}_{-8.9}$	0.142 [3.82]	1.16 (22)
XMM-Newton[f]	52145.1	1750	±0.104	±1430	$11.7^{+5.4}_{-5.2}$	0.171 [4.60]	$11.7^{+5.4}_{-5.2}$	0.171 [4.60]	1.16 (47)
Chandra[f]	52795.1	1750	±0.104	±1430	$3.1^{+7.0}_{-3.1}$	0.048 [1.30]	$3.1^{+7.0}_{-3.1}$	0.048 [1.30]	0.95 (25)
XMM-Newton	52871.2	1750^{+560}_{-440}	$\pm0.104^{+0.016}_{-0.016}$	±1430 ± 220	$6.9^{+2.3}_{-0.6}$	0.122 [3.27]	$6.9^{+2.3}_{-0.6}$	0.122 [3.27]	0.96 (49)
O VII Intercombination Line at 21.80 Å									
Chandra[f]	51803.6	1750	±0.104	±1430	$19.8^{+12.6}_{-11.0}$	0.110 [2.89]	$19.8^{+12.6}_{-11.0}$	0.110 [2.89]	1.16 (22)
XMM-Newton[f]	52145.1	1750	±0.104	±1430	$15.3^{+5.5}_{-7.1}$	0.100 [2.63]	$15.3^{+5.5}_{-7.1}$	0.100 [2.63]	1.16 (47)
Chandra[f]	52795.1	1750	±0.104	±1430	$13.6^{+6.9}_{-7.2}$	0.159 [4.19]	$13.6^{+6.9}_{-7.2}$	0.159 [4.19]	0.95 (25)
XMM-Newton	52871.2	1750^{+560}_{-440}	$\pm0.104^{+0.016}_{-0.016}$	±1430 ± 220	$16.6^{+1.4}_{-2.6}$	0.156 [4.11]	$16.6^{+1.4}_{-2.6}$	0.156 [4.11]	0.96 (49)
O VII Forbidden Line at 22.10 Å									
Chandra[f]	51803.6	1750	±0.104	±1430	$2.8^{+10.0}_{-2.8}$	0.020 [0.52]	$2.8^{+10.0}_{-2.8}$	0.020 [0.52]	1.16 (22)
XMM-Newton[f]	52145.1	1750	±0.104	±1430	$5.7^{+5.3}_{-3.8}$	0.057 [1.46]	$5.7^{+5.3}_{-3.8}$	0.057 [1.46]	1.16 (47)
Chandra[f]	52795.1	1750	±0.104	±1430	$0.0^{+2.7}_{-0.0}$	0.0 [0.0]	$0.0^{+2.7}_{-0.0}$	0.0 [0.0]	0.95 (25)
XMM-Newton	52871.2	1750^{+560}_{-440}	$\pm0.104^{+0.017}_{-0.016}$	±1430 ± 220	$0.0^{+2.2}_{-0.0}$	0.0 [0.0]	$0.0^{+2.2}_{-0.0}$	0.0 [0.0]	0.96 (49)

[a]The Gaussian normalization in units of 10^{-5} photons cm^{-2} s^{-1}.

[b]The reduced Cash statistic and number of degrees of freedom for the fit.

[c]The Ne X line width was not well constrained for this observation, and its value was fixed to the weighted average of the values found in the other observations.

[d]The Ne IX line widths and velocities were not well constrained for this observation and were fixed to the values found in the *Chandra* observation of MJD 52795.1.

[e]The O VIII line width and velocity were not well constrained for this observation and were fixed to the weighted averages of the values found in the other observations.

[f]The O VII line width and velocity were not well constrained for this observation and were fixed to the values found in the *XMM-Newton* observation of MJD 52871.2.

Fitting the helium-like triplets of Ne IX and O VII with multiple Gaussians allowed us to estimate the strengths of the resonance, intercombination, and forbidden lines. The Ne IX intercombination line is clearly dominant in both *Chandra* observations (we were unable to fit this line in the *XMM-Newton* observations). While the intercombination line is the strongest of the O VII triplet as well, the resonance line contains significant flux, whereas the forbidden lines do not contribute substantially to any of the triplets. The lack of forbidden lines suggests that we are observing emission from a high-density plasma ($n_e \gtrsim 10^{12}$ cm^{-3}), which in turn supports the hypothesis that the lines arise in the accretion disk. We discuss this further in § 7.5.2.

7.3.3 Photoelectric absorption and elemental abundances

Since 4U 1626−67 shows prominent Ne and O emission lines, it is natural to ask whether this is a reflection of an overabundance of heavy elements in the system, or of the particular geometry and conditions inherent to this unique source. One way to constrain the local abundances is by measuring the strength of the absorption complexes within our spectral range. For the *XMM-Newton* and *Chandra* data this includes the Ne K , Fe L, and O K edges. While there could also be edges and absorption lines from ionized species of O and Ne, our data sets are not sensitive enough to detect these features. We fit the edges over the wavelength ranges 13.8–14.8, 16.5–18.0, and 22.2–25.3 Å, respectively, and used the tbnew model, which includes high-resolution modeling of the edge cross-sections (Wilms et al. 2007; Juett et al. 2004, 2006). In order to constrain the continuum over the restricted wavelength ranges, we used the same continuum model as was fitted to the full spectrum, restricting the model parameters to vary within the previously determined 90% confidence intervals. We present the fit results in Table 7.5. Although our results suggest a slight overabundance of these elements relative to the expected interstellar value of $N_H = (6.2\pm0.7)\times10^{20}$ cm^{-2} (measured directly from the Lyα line; Wang and Chakrabarty 2002), neither the *Chandra* nor the *XMM-Newton* data sets require a statistically significant local contribution to the interstellar column depth (see § 7.5.1 for further discussion). This differs from the results obtained by Schulz et al. (2001), which is likely due to changes in analysis technique as well as the improved instrumental calibration now available.

7.4 Timing analysis

All of the *Chandra* and *XMM-Newton* observations of 4U 1626−67 have high enough time resolution to determine the pulse period, and the *XMM-Newton* observations also allowed us to create energy-resolved pulse profiles. Prior to performing the timing analysis, we corrected the photon arrival times to the location of the solar system barycenter.

To determine the pulse period, we computed an overresolved power spectrum using the technique described in Chakrabarty (1998). We calculated the pulse frequency and frequency error using the methods and formulae presented in Ransom et al. (2002). The results are shown in Table 7.6, and Figure 7-5 contains a plot of the frequencies as well as the prediction curve and associated errors extrapolated from previous *Compton Gamma Ray Observatory* BATSE monitoring results (Chakrabarty et al. 1997). As can be seen from the plot, the pulsar is spinning down faster than was predicted, which is significant with respect to the stability of the timing during the BATSE era, but not unexpected considering the variable spin history of the source. We note that the QPO at 0.048 Hz is present in each of the observations, as has been seen previously (Shinoda et al. 1990; Chakrabarty 1998).

Table 7.5. 4U 1626−67 absorption edge fits

λ (Å)	Edge	Observatory (ObsID)	Total N_H[a] (10^{21} cm^{-2})	Implied N_Z[b] (10^{17} cm^{-2})
14.3	Ne K	Chandra (104)	$3.0^{+1.1}_{-2.5}$	$2.6^{+0.9}_{-2.2}$
		XMM-Newton (0111070201)	$1.9^{+0.2}_{-1.1}$	$1.67^{+0.17}_{-0.95}$
		Chandra (3504)	$0.9^{+2.2}_{-0.5}$	$0.8^{+1.9}_{-0.4}$
		XMM-Newton (0152620101)	$1.20^{+0.45}_{-0.33}$	$1.05^{+0.40}_{-0.29}$
17.5	Fe L$_{III}$	Chandra ObsID 104	$0.6^{+2.1}_{-0.3}$	$0.17^{+0.56}_{-0.07}$
		XMM-Newton (0111070201)	$1.38^{+0.70}_{-0.17}$	$0.37^{+0.19}_{-0.05}$
		Chandra (3504)	$0.5^{+1.8}_{-0.2}$	$0.13^{+0.48}_{-0.05}$
		XMM-Newton (0152620101)	$1.29^{+0.35}_{-0.18}$	$0.348^{+0.094}_{-0.049}$
23.3	O K	Chandra ObsID 104	$1.2^{+1.5}_{-0.7}$	$5.9^{+7.2}_{-3.4}$
		XMM-Newton (0111070201)	$1.38^{+0.42}_{-0.12}$	$6.7^{+2.1}_{-0.6}$
		Chandra (3504)	$1.7^{+0.6}_{-1.4}$	$8.4^{+3.0}_{-6.9}$
		XMM-Newton (0152620101)	$1.38^{+0.25}_{-0.04}$	$6.8^{+1.2}_{-0.2}$

[a]Fitted value of N_H, using the tbnew model (Wilms et al. 2007) and fitting over the immediate range of the absorption structure, restricting the continuum components to remain within their 90% confidence intervals (see text).

[b]Value of N_Z implied by the fitted N_H, assuming ISM abundances presented in Wilms et al. (2000).

Table 7.6. Pulse period of 4U 1626−67

Date	MJD	Pulse Period (s)	Observatory
2000 Sep 16	51803.6	7.6726(2)	Chandra
2001 Aug 24	52145.1	7.6736(2)	XMM-Newton
2003 Jun 5	52795.1	7.67514(5)	Chandra
2003 Aug 20	52871.2	7.67544(6)	XMM-Newton

The *XMM-Newton* pn data are ideal for creating energy-resolved pulse profiles. We made four energy cuts and divided the pulse period into 40 bins to create the profiles presented in Figures 7-6 and 7-7. The profiles have some significant differences from what was seen previously (see, e.g. Pravdo et al. 1979; Kii et al. 1986; McClintock et al. 1980; Levine et al. 1988). In the earlier observations, the pulse profile shows a dip at energies $\lesssim 2$ keV, then the emergence of two prominent peaks that flank this dip as the energy increases, reaching a maximum at ≈ 5 keV. By ≈ 13 keV, the dip has returned, and becomes both broader and deeper as the energy increases. We find that the current pulse profiles lack the double-peak feature that was seen before, and show only a dip which broadens at lower and higher energies. The profile is not entirely symmetric; there also appears to be a secondary dip at phase ≈ 0.85. Insofar as the pulse profile reflects the geometric and radiative properties of the accretion column and neutron star hot spot (see, e.g. Kii et al. 1986), changes in the pulse profile suggest that there have been fundamental changes in these regions of the system. While we do not speculate here as to the exact nature of these changes, we note that the accretion geometry may have changed at the time of torque reversal, affecting the accretion flow at the neutron star surface. Therefore, the changes that are seen in the pulse profile may be related to the change in the continuum spectrum of 4U 1626−67 that was observed around the time of the torque reversal (Angelini et al. 1995).

We also note that there were no flaring events seen in any of our observations, in contrast to what has been previously observed, when 4U 1626−67 was seen to flare dramatically in both X-ray and optical data on timescales of ≈ 1000 s (Joss et al. 1978; McClintock et al. 1980; Li et al. 1980). The cessation of flaring activity may have occurred at the same time as the torque reversal, although it is not clear what physical mechanism was responsible for the flaring or why it would be correlated with the change in sign of $\dot{P}$ (Chakrabarty et al. 2001).

7.5 Discussion

7.5.1 Absorption edge measurements

Four known or candidate ultracompact binary systems have X-ray spectra that show evidence of high Ne/O ratios (4U 0614+091, 2S 0918−549, 4U 1543−624, and 4U 1850−087; Juett et al. 2001; Juett and Chakrabarty 2003), although none of these systems have the X-ray emission-line complexes seen in 4U 1626−67. These unusually strong lines, which arise from highly ionized species of Ne and O, suggest that the donor must contain a significant quantity of these elements, and we have previously suggested that the donor may be the chemically fractionated core of a C-O-Ne or O-Ne-Mg white dwarf (S01). However, since the strength of the emission lines is very dependent on local plasma parameters, it is difficult to use them to determine elemental abundances. Alternatively, a way of determining local abundances is to measure the depths of the neutral absorption edges and to compare these with the value of the interstellar absorption along the line of sight as determined, for example, by the broader continuum fit. Any absorption in excess of what is expected from standard ISM abundances could be taken as an indication of material local to the system.

The Ne K, Fe L, and O K absorption edges do not appear strong in any of our observations, including the first *Chandra* observation (ObsID 104) that we analyzed in S01. Therefore, we are no longer able to argue for a significant overabundance of O or Ne in cool circumstellar material as we suggested in S01, at least not on the grounds of the absorption

edge analysis (see also § 7.3.3). Perhaps these elements are, in fact, overabundant in the disk (and thus the donor), but not much material is expelled from the system, or subsequently cools to form an absorbing medium. We note that our results agree with recent studies of the optical spectra of 4U 0614+091 and 4U 1626−67, which did not reveal any Ne emission features, only lines from C and O (Werner et al. 2006; Nelemans et al. 2006).

7.5.2 Emission line characteristics and physical implications

The emission lines have double-peaked profiles, and the line ratios imply that they are formed in a high-density environment, which suggests that they arise somewhere in the accretion disk (see also S01). If they are, in fact, disk features, then the measured velocities correspond to the actual disk velocities by the relation

$$v_{\text{obs}} = v \sin i = \sqrt{\frac{GM_X}{r}} \sin i. \tag{7.1}$$

The maximum disk velocity will occur at the inner edge of the accretion disk, which is likely truncated at the co-rotation radius of the neutron star at $\approx 6.5 \times 10^8$ cm. The Keplerian velocity at this radius is $\cong 5400$ km s^{-1}, whereas the line velocities are measured to be $\cong 1700$ km s^{-1} (note that this is the velocity at the center of the Gaussian in the double-Gaussian fits, which is therefore an underestimate of the absolute maximum velocity). If we take this to be the velocity at the inner disk edge, we are able to place a constraint on the inclination angle of the system: $\sin i \gtrsim 1700/5400 \cong 0.31$ ($i \gtrsim 22°$). We may combine this with the previously derived upper limit on the projected semi-major axis, given an orbital period of 42 min and limits on the timing noise (Chakrabarty et al. 1997), to find $3 \lesssim a_X \sin i \lesssim 8$ lt-ms.

The line ratio measurements are indicators of the plasma conditions in the line formation regions. Although we are not able to derive robust limits for the standard diagnostics, we note that the lack of detectable forbidden lines implies that the region is relatively high-density ($n_e \gtrsim 10^{12}$ cm^{-3}). Since the line velocities constrain the line formation regions to be associated with regions in the disk where $T_{\text{disk}} > 10^5$ K (see Equation 7.3), we expect that atomic collisions, not photoionization, will be the dominant process suppressing forbidden line emission. We also note that the relatively low value of the intercombination line (i) with respect to the resonance line (r), $r/i \approx 2$, suggests that the temperature of the line formation region is $\gtrsim 10^6$ K (Porquet and Dubau 2000). As discussed in S01, this temperature is characteristic of the highly ionized, optically thin outer layers of the accretion disk.

7.5.3 Long-term flux evolution

X-ray observations of 4U 1626−67 show that it has been decreasing in flux since 1977. Since this decrease appears to be bolometric—there is no sign of variable absorption, and the continuum spectrum is known to have undergone only one major change—we may use the X-ray flux to help determine other characteristics of the system. The long-term trend can be described by either an exponential decay or a linear decrease (see Fig. 7-2). If we take it to be logarithmic and integrate over the duration of the outburst, the fluence is 0.927 ergs cm^2 [giving a total energy of 1.1×10^{44} ($d/1$ kpc)^2 ergs]. Converting this to an average accretion rate, we find that

$$\dot{M}_{\text{ave}} \approx 2.2 \times 10^{-10} \, \Delta t_{\text{yr}}^{-1} \, d_{\text{kpc}}^2 \, M_\odot \, \text{yr}^{-1}, \tag{7.2}$$

where Δt_{yr} is the time between outbursts in years and d_{kpc} is the distance to the source in kpc. If we assume that the source is persistent and take $\Delta t \approx 30$ yr, we find that $d \lesssim 2$ kpc, which is less than the minimum distance of 3 kpc derived from considerations of the accretion torque during spin-up (Chakrabarty et al. 1997). If we assume a distance of $\gtrsim 3$ kpc, and take the long-term average accretion rate to be $\dot{M}_{\mathrm{GR}} = 3 \times 10^{-11}$ $M_{\odot}$ yr^{-1} (the value from gravitational-radiation–driven orbital evolution with a white dwarf donor; see Chakrabarty 1998), we find that $\Delta t \gtrsim 70$ yr, significantly longer than the known duration of the current outburst.

We may also combine current theory on disk stability with the flux data for 4U 1626−67 to obtain constraints on its distance and possible outburst duration. The accretion disk temperature will be determined both by viscous heating as well as X-ray heating from the central source (see, e.g. King et al. 1996; van Paradijs 1996), yielding a temperature profile of

$$T^4 = \frac{\eta \dot{M} c^2 (1 - \beta)}{4 \pi \sigma r^2} \left(\frac{dH}{dr} - \frac{H}{r} \right),$$ (7.3)

where η is the efficiency of the conversion of rest-mass energy into X-ray heating, β is the X-ray albedo of the disk, H is the scale height of the disk, and σ is the Stefan-Boltzmann constant. Following King et al. (1996), we take $\eta = 0.11, \beta = 0.9$, assume that $H/r \approx 0.2$ is constant, and that $H \propto r^n$, where $n = 9/8$ for shallow heating, where X-ray irradiation from the neutron star controls the temperature profile of the outer layers of the disk, but viscous dissipation heats the inner regions (Chakrabarty 1998). Assuming that the system is regulated by a disk instability mechanism, we can use the observed decline in flux to estimate when 4U 1626−67 will enter a quiescent state. The disk stability criterion requires that the temperature at the outermost disk radius remain $\gtrsim 6500$ K (Smak 1983) for an outburst to persist. Setting $r = r_{\mathrm{out}} \cong 2 \times 10^{10}$ cm, we derive a critical accretion rate of $\dot{M} = 3.6 \times 10^{-12}$ $M_{\odot}$ yr^{-1}. Note that this is lower than the value of $\dot{M}_{\mathrm{GR}}$ quoted above. Assuming that the accretion rate is directly proportional to the flux, and that it remained above the critical rate throughout the current outburst, we find the distance to 4U 1626−67 to be $\gtrsim 0.6$ kpc. Furthermore, if we assume a distance range of 3–13 kpc and an exponential (or linear) decline in flux commensurate with the current trend, we find that $\dot{M} \lesssim \dot{M}_{\mathrm{crit}}$ in the range 2018–2020 (or 2008 June–Sept). We would therefore expect 4U 1626−67 to become quiescent within 2–15 yr.

112
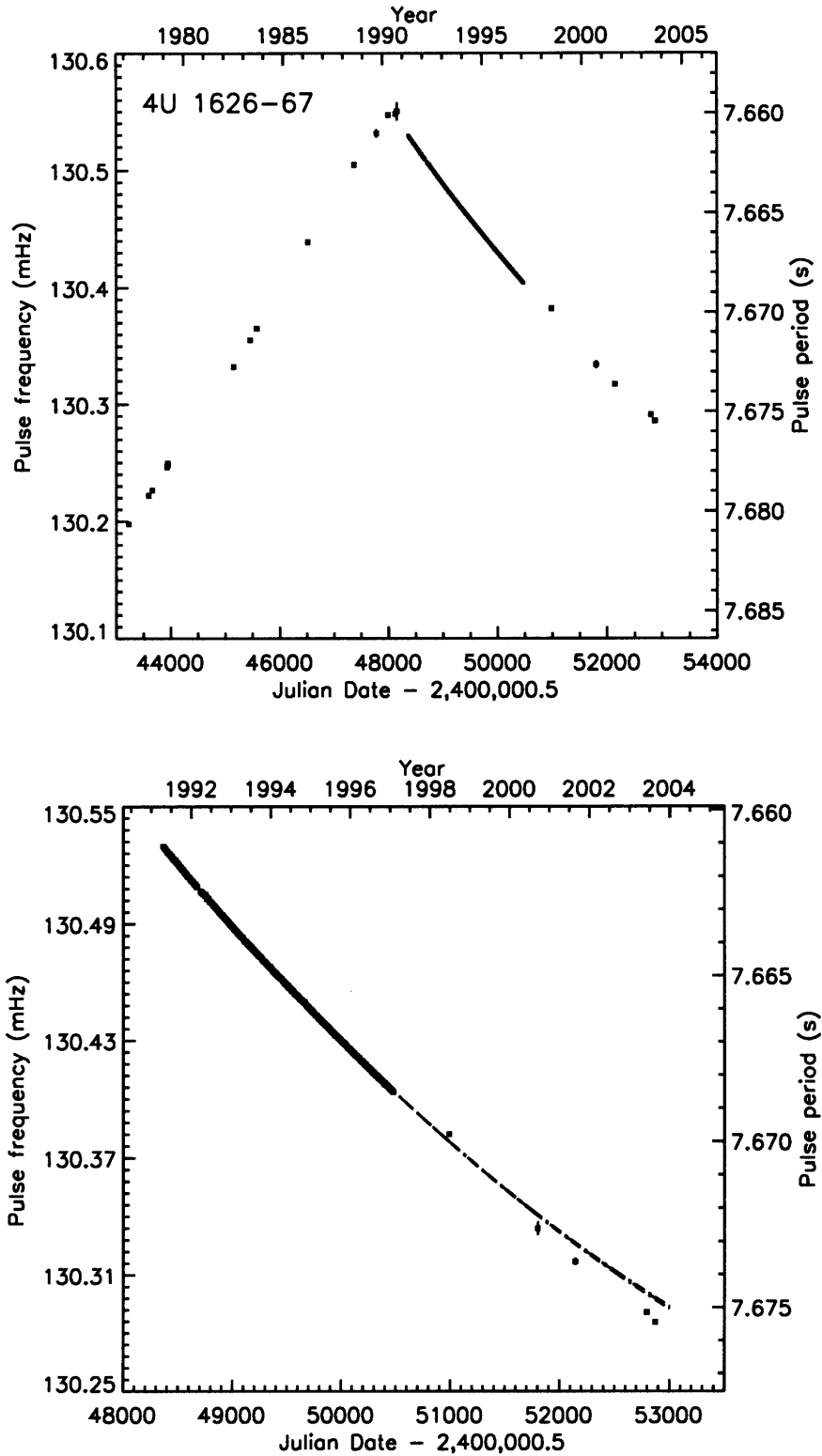
Figure 7-5: Frequency history of 4U 1626−67. **Top panel:** All data. **Bottom panel:** Expanded view of the *Compton* BATSE through the *Chandra* and *XMM-Newton* observations, along with the BATSE prediction (*solid curve with dot-dashed errors*). Pulse frequency data from other observatories, as well as the BATSE prediction, can be found in Chakrabarty et al. (1997) and Chakrabarty et al. (2001).
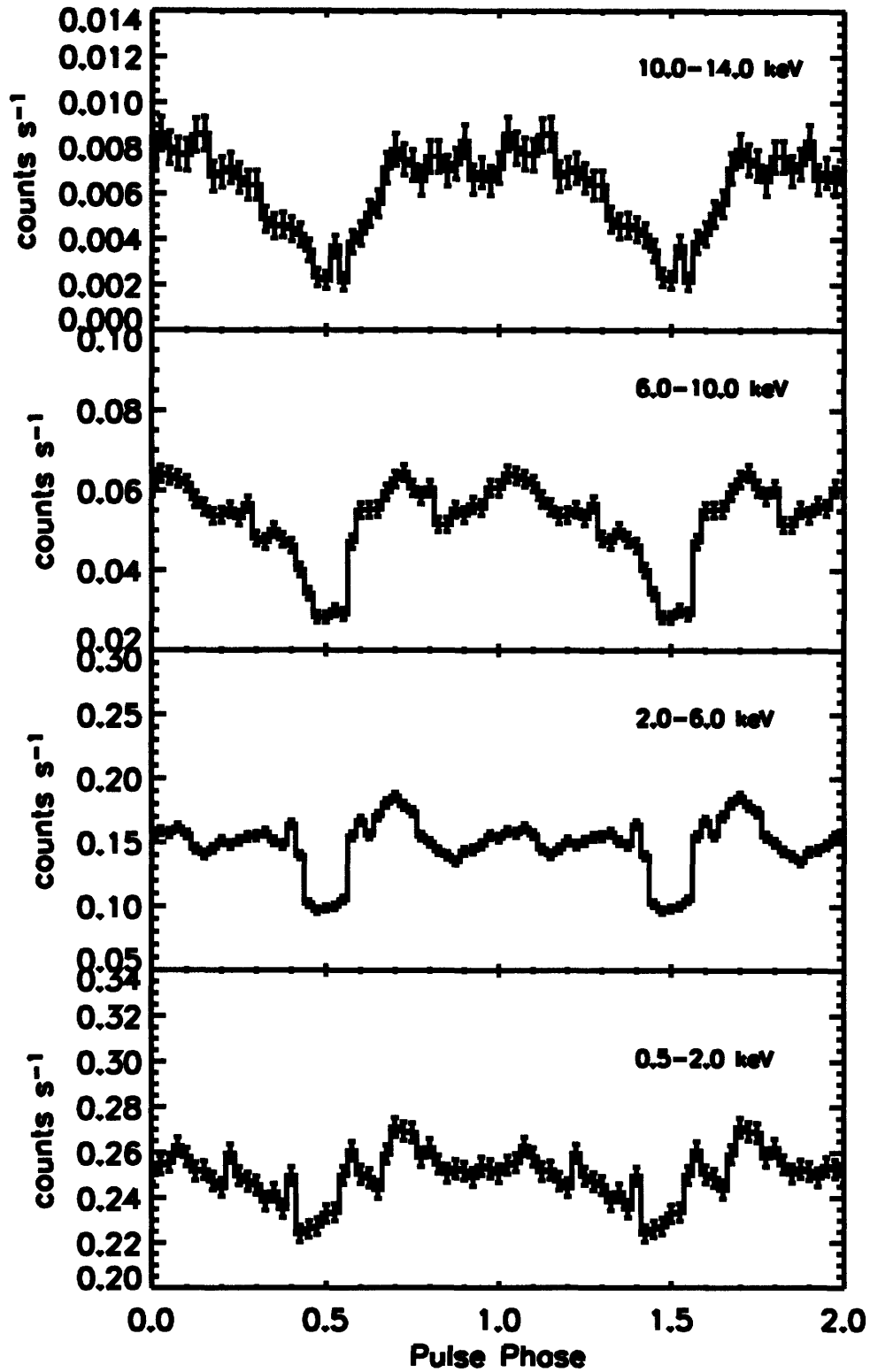
Figure 7-6: Folded pulse profiles of 4U 1626−67 from the *XMM-Newton* pn, ObsID 0111070201.
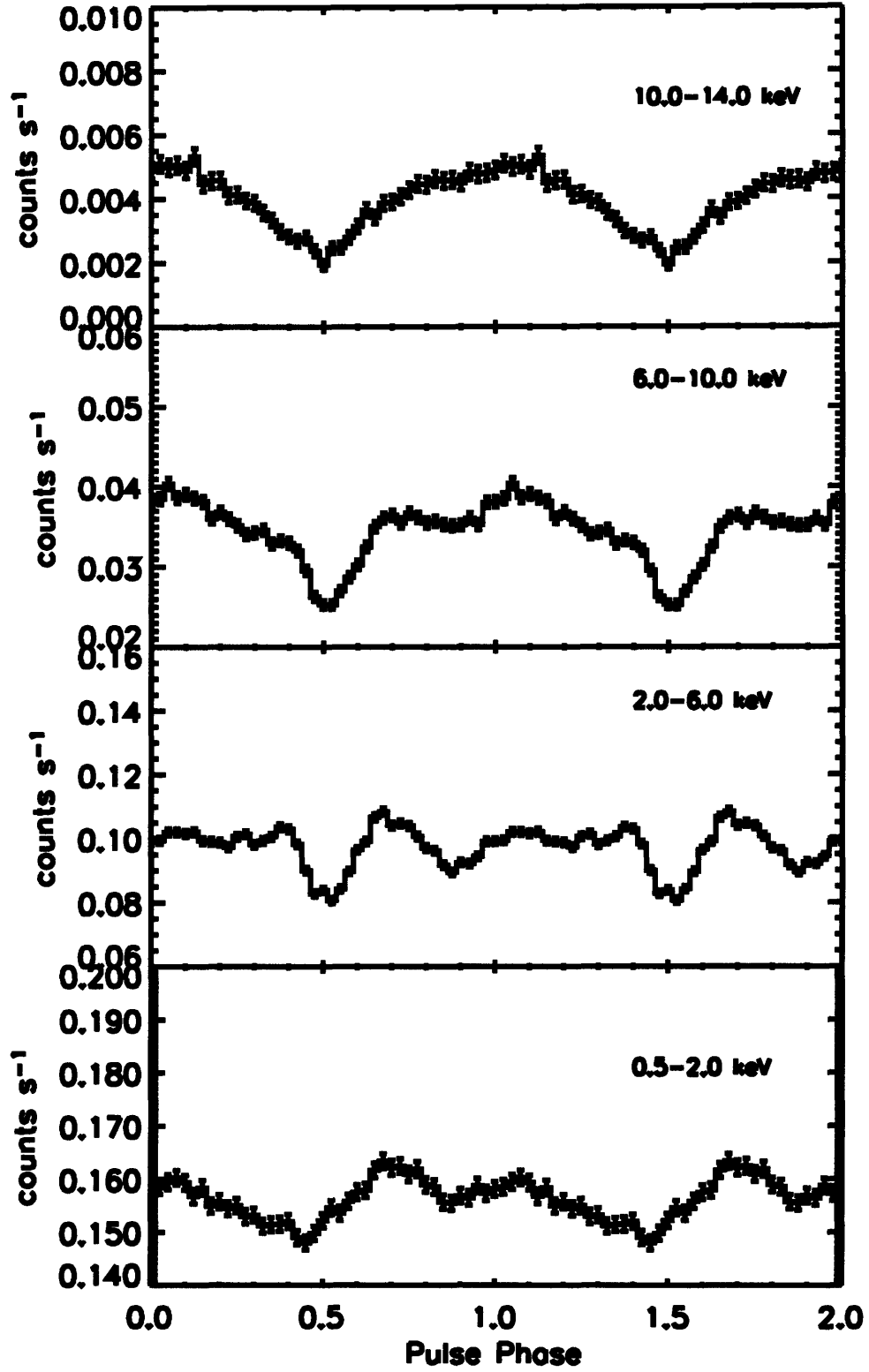
Figure 7-7: Same as Fig. 7-6 but for ObsID 0152620101.

Chapter 8

High-Resolution *Chandra* Spectroscopy of Galactic LMXBs

8.1 Introduction

The X-ray spectra of neutron star LMXBs are uniquely able to provide information about their geometry, composition, and emission mechanisms, since they offer a window into the high-energy regions and processes integral to these systems. Although some of these processes are well-understood, and the basic physical geometry of the systems reasonably well known, the origins of the basic spectral components are still a matter of debate. Softer spectral states are generally dominated by what can be modeled as a single- or multiple-temperature blackbody, but usually also require the presence of a harder component. However, whether this spectrum arises from a combination of disk emission and Comptonized blackbody emission from the neutron star surface (the *Eastern* model), or from emission due to an optically thick boundary layer plus a Comptonized component from the inner disk region (the *Western* model), or some other combination of physical components, remains unresolved. We discuss these models and the possible physical mechanisms through which X-ray spectra arise from neutron star LMXBs in § 1.1.9.

Recent X-ray missions such as *Einstein*, *ROSAT*, and *ASCA* have allowed for the broad study of large samples of Galactic LMXBs, and the resulting surveys have provided valuable insights into their spectral properties. In particular, Christian and Swank (1997) analyzed *Einstein* solid-state spectrometer (SSS) and monitor proportional counter (MPC) spectra from 49 LMXBs; this combination of instruments covers the energy range from 0.5–20.0 keV. All could be fit by a spectrum that included thermal bremsstrahlung or Comptonized emission plus a blackbody. Physically, these components could be due to optically thick emission from or close to the surface of the neutron star, optically thin emission originated farther out in the sytem, and possibly some contribution from the accretion disk. Schulz (1999) performed a survey of 23 LMXBs using the *ROSAT* position sensitive proportional counter (PSPC), fitting the spectra with power-law, thermal bremsstrahlung, blackbody, and blackbody plus power-law models. Unfortunately, the *ROSAT* PSPC has a very narrow bandpass (0.1–2.4 keV), making the task of determining continuum spectra rather difficult. As a result, the sensitivity of the fits was highly dependent on the strength of the absorbing column; sources with low column density often required the addition of a second spectral component. In addition, Church and Balucińska-Church (2001) studied *ASCA* spectra from ten LMXBs, fitting them with a set of simple models—combinations of

blackbodies and (cut-off) power-laws. They found that when fitting with a disk blackbody, unphysical values of the inner disk radius (i.e., smaller than the radius of the neutron star) were derived, suggesting that only a small fraction of the optically thick emission arises from the accretion disk. This result implies that the Western model could provide a more promising physical scenario.

The growing archive of public *Chandra*/HETG observations promises to provide a rich source of data for future surveys of X-ray spectra of neutron star LMXBs. In Chapters 2 and 7 we presented *Chandra*/HETG spectra of the accretion-powered millisecond pulsar XTE J1814−338 and the ultracompact binary 4U 1626−67. These are both in-depth studies which afford new insights into two unique and interesting systems. However, in the interest of facilitating a broader view of a larger sample of objects, we have constructed a database which makes the reduction of and access to *Chandra*/HETG spectra of Galactic LMXBs simple and straightforward. We describe the structure and content of this database, as well as the methods by which it is updated, in § 8.2. From the large number of neutron star LMXB sources with public *Chandra*/HETG observations, we have selected a representative sample of objects on which to perform spectral analysis. Although the scope of the sample included here is limited, we hope that the database structure and analysis techniques that we present are useful in future, larger-scale studies.

While some of the sources in our sample have been studied by other authors, we have the added benefit of analyzing the complete set in a self-consistent fashion. The data for each source have been reprocessed using the latest techniques and calibration products (as described in § 8.3, and the resulting spectra have been fit with a selection of standard models (see § 8.4). The high-resolution nature of the *Chandra*/HETG spectra also allows us to place constraints on the photoelectric absorption edges of many of the sources. This enables us to determine the continuum spectra in a more independent fashion than is possible with low-resolution spectral fits, where there is often a degeneracy between the continuum model parameters and the absorbing column. In particular, constraints on the absorbing column will allow for a more precise determination of the soft, i.e., blackbody, continuum component, since it is most strongly affected by uncertainties in absorption.

Our choice of models allows us to compare our fit results with previous studies of Galactic LMXBs, as well as to determine some possible physical parameters of the systems. Since we have chosen objects from different LMXB classes, we can also make comparisons across source type. § 8.5 and § 8.6 present the results of the continuum fits and the conclusions we are able to draw from our analysis.

8.2   The *Chandra* HETG LMXB database

8.2.1   Content and structure of the database

The *Chandra* HETG LMXB database contains all publicly available observations of Galactic LMXBs performed by *Chandra* using the HETGS (see Chapter 1 for a description of this instrument). After acquiring these observations from the *Chandra* archive, we have reprocessed them to apply the latest calibration products and wisdom. We also created, for each observation, spectra and responses to use for fitting, as well as a "summary" file that contains useful information and plots. In addition to this data, there are also two IDL database structures. The source database contains all known Galactic LMXBs and relevant parameters, and the observation database contains information about the *Chandra* observations of these sources (see Tables 8.1 and 8.2).

Basic information for the source database was first derived from Liu et al. (2001) with help from the RKcat[1]. More recently discovered sources were added by hand. Values for the Galactic hydrogen column density were first found using the ftools routine nh, which queries a map containing H I information from Dickey and Lockman (1990), and subsequently revised to reflect more precise measurements in the literature (references are found in the nhref field).

The observation database was constructed using queries to the HEASARC for each object in the source database. After the public data were downloaded and reprocessed, the database was further populated with information from the processed data as well as information from the fits file headers.

The database root directory is currently /nfs/cxc/r1/lmxb, which contains six subdirectories. The calibration directory contains the HETG RMF files (ARF files are created to match each observation). The catalogs directory contains IDL-readable versions of both the Liu et al. (2001) LMXB catalog and the RKcat, as well as the scripts needed to create and read these electronic versions. The idl directory contains IDL scripts for creating and updating the *Chandra* HETG LMXB database, as well as the IDL database structures and text-based data files. The scripts directory contains (non-IDL) scripts used for processing data and building the database. The sources directory contains subdirectories for each LMXB that *Chandra* has observed, which then contain subdirectories for each ObsID, in which the data and processed data products are placed. Finally, the summaries directory contains the summary files created for each reprocessed dataset.

8.2.2 Updating the database

Tables 8.1 and 8.2 list the files in which the database scripts find the various pieces of information that are used to update the database. The two scripts used to actually update the IDL databases are mkSrcDB.pro and mkObsDB.pro.

To add a new source to the database, the relevant information must be added on a new line in the file sourceList.dat, and the source provided with a unique source number. The name ("dirname") provided must, when any underscores are removed, be able to successfully query the Simbad database. Likewise, information should be added to a new line in the sourceInfo.dat file and the source coordinates to sourceCoords.dat (the last entry in this file is the number of Simbad references). To update any information on a source, the relevant field may be modified in one of these files. After all desired changes have been made, mkSrcDB.pro may be executed, which will create an updated database using all the information contained in the aforementioned files. It would be prudent to create backups of the database and the files used to create the database prior to editing them.

As new observations become public, it will also be necessary to periodically update the observation database. After the *Chandra* proposal cycle, but prior to the start of a new observing cycle, science targets are "ingested" into the Chandra archive. Currently, the list of ObsIDs in the observation database is updated through Cycle 8 targets. However, the date when data will become public is not known until after the observation is performed and the initial data processing completed. Therefore, one must periodically update the hetgobs.dat file, which is in the idl/chandra_obs directory. This is done by running the findChandraObs.pro script, and then deleting any lines in hetgobs.dat which are incorrect (generally duplicate) listings. These lines should be placed in the file hetgobs_deleted.dat

---

[1]http://physics.open.ac.uk/RKcat/

119

Table 8.1. *Chandra* HETG LMXB Source Database

Field	Description	Populated from
srcnum	Unique source identification number	sourceList.dat
name	Source name used for directory creation (Simbad-friendly)	sourceList.dat
catname	Source name used in Liu et al. (2001)	sourceList.dat
altname	Alternate source name from Liu et al. (2001)	sourceList.dat
asmname	Source name used in the ASM catalog	sourceList.dat
type	Source type (A=atoll, B=burster, D=dipper, G=globular cluster source, P=pulsar, M=AMP, T=transient, Z=Z source, U=ultrasoft spectrum)	sourceList.dat
ra	Right ascension (decimal degrees)	sourceCoords.dat
dec	Declination (decimal degrees)	sourceCoords.dat
porb	Orbital period (hours; if known)	sourceInfo.dat
pspin	Neutron star spin period (s; if known)	sourceInfo.dat
dist	Distance (kpc; if known)	sourceInfo.dat
vmag	Apparent V magnitude from Liu et al. (2001)	sourceInfo.dat
vmin	Min. apparent V magnitude if variable (vmag is max.)	sourceInfo.dat
bmv	$B - V$ color from Liu et al. (2001)	sourceInfo.dat
umb	$U - B$ color from Liu et al. (2001)	sourceInfo.dat
nh	Galactic absorption column (10^{22} cm^{-2})	sourceInfo.dat
nhref	Reference for absorption value[a]	sourceInfo.dat
simref	Number of references in Simbad as of last database update	sourceCoords.dat
notes	Field for notes	...

[a]If blank, the value of N_H was obtained via the `ftools` program `nh`.

for future reference. Then, run `mkObsDB.pro` to create the observation database from this information, and from data files already present in the Chandra HETG LMXB database.

After the observation database has been updated, `getChandraData.pro`[2] may be executed to download any publicly available data that has not already been obtained (the script checks for a directory named `sources/<sourcename>/<obsid>`; if it exists, it is assumed that the data has already been obtained). When the data have been downloaded, they can be reprocessed using `procData.pro`. In addition, `procDataTCut.pro` may be run if spectra for discrete time intervals are desired as well. After the data have been reprocessed, `mkObsDB` can be run a final time to populate the database with updated values for the source count rates.

8.3 Data reprocessing

The data that are downloaded from the *Chandra* database do not necessarily have the most current calibration applied, and have not all been processed in the same way. Therefore, we reprocessed all the timed-mode (though not the continuous-clocking mode) data to create

---

[2]As of 15 December 2006, the *Chandra* archive group discontinued the use of the provisional retrieval interface, which was used by the script `chandra_retrieve.sl` (called by `getChandraData.pro`) to obtain public observations. Therefore, this script will need to be reworked, probably to use John Davis' script ~`davis/bin/chandra-get`, before it can be successfully run.

Table 8.2. *Chandra* HETG LMXB Observation Database

Field	Description	Populated from
srcnum	Unique source identification number	sourceList.dat
obsid	*Chandra* observation ID	lmxb/idl/chandra_obs/hetgobs.dat
name	Source name used for directory creation	sourceList.dat
tname	Observation **target** name	lmxb/idl/chandra_obs/hetgobs.dat
pubdate	Date observation is public	lmxb/idl/chandra_obs/hetgobs.dat
status	Observation status[a]	lmxb/idl/chandra_obs/hetgobs.dat
obsdur	Observation duration (s)	lmxb/idl/chandra_obs/hetgobs.dat
pi	Principle Investigator of observation	lmxb/idl/chandra_obs/hetgobs.dat
mjdref	Reference MJD for **tstart** and **tstop**	lmxb/sources/<name>/<obsid>/repro/pha2.fits
tstart	Observation start time (s since **mjdref**)	lmxb/sources/<name>/<obsid>/repro/pha2.fits
tstop	Observation stop time (s since **mjdref**)	lmxb/sources/<name>/<obsid>/repro/pha2.fits
timedel	Observation frame time parameter	lmxb/sources/<name>/<obsid>/repro/pha2.fits
readmode	Detector read mode[b]	lmxb/sources/<name>/<obsid>/repro/pha2.fits
datamode	Detector data mode[c]	lmxb/sources/<name>/<obsid>/repro/pha2.fits
maxm1	Max. MEG-1 counts frame^{-1} (6 bins)$^{-1}$	lmxb/sources/<name>/<obsid>/repro/pha2.fits
maxp1	Max. MEG$+1$ counts frame^{-1} (6 bins)$^{-1}$	lmxb/sources/<name>/<obsid>/repro/pha2.fits
ra_pnt	Telescope pointing RA[d]	lmxb/sources/<name>/<obsid>/repro/pha2.fits
dec_pnt	Telescope pointing declination[d]	lmxb/sources/<name>/<obsid>/repro/pha2.fits
ra_targ	**target** RA[d]	lmxb/sources/<name>/<obsid>/repro/pha2.fits
dec_targ	**target** declination[d]	lmxb/sources/<name>/<obsid>/repro/pha2.fits

[a]Status is as of most recent database update.

[b]Possible read modes are TIME (timed event mode) and CC (continuous clocking mode).

[c]Possible data modes are FAINT, VFAINT, and GRADED.

[d]In decimal degrees.

spectral and response files using up-to-date calibration products. For each ObsID, we ran acis_process_events on the level 1 event file, applying the observation-specific bad pixel file, CTI correction, time-dependent gain correction, and removing the pixel randomization. We filtered the resulting file to include only grades [0,2,3,4,6], and status=0 except in the case where it has been flagged in pipeline processing by acis_detect_afterglow[3].

The zeroth-order source position was difficult to determine for a number of sources. Generally, using the standard tool tgdetect worked, but in cases where zeroth-order blocking was in place (for bright sources) or the position was otherwise incorrectly determined, we either used a script which traces the grating arms to find their intersection or determined the position by hand. After finding the correct position, we ran tg_create_mask with a reduced width factor of 20 (the default value is 35) to create an extraction region for the dispersed spectra. We used this region to produce ±1, ±2, and ±3 order source and background spectra for both the HEG and MEG, as well as matching grating ARF files. We used pre-determined grating RMF files for the spectral fitting.

After the data reprocessing was complete, we made a summary document containing useful information to check that the processing was successful as well as to give an idea of the basic properties of the source during the observation. For each ObsID, this file includes lightcurves binned at 100, 500, and 1000 s; a plot of the ASM lightcurve with the times of the *Chandra* observations indicated; an image of the ACIS field of view with the spectral extraction region overplotted; a table including basic source parameters, plots to estimate the amount of pileup present; and plots of the spectra in energy and in wavelength space. We also performed a final database update to incorporate the revised count rate information.

8.4 Spectral models and fitting

We chose a set of spectral models that are descriptive; i.e., are able to describe the functional form of the spectrum, as well as physically meaningful; i.e., from which we are able to derive physical parameters. All our spectral fitting was performed with the ISIS software package (vers. 1.4.7)[4] using models from the XSPEC fitting package[5]. These includes a power-law (powerlaw), thermal bremsstrahlung (bremss), a blackbody (bbodyrad), and, for one source, a multi-color disk blackbody (diskbb). To account for photoelectric absorption (both interstellar and local), we used the tbnew[6] model (Wilms et al. 2007), which allows for the independent variation of elemental abundances and includes high-resolution O K, Ne K, and Fe L edges.

Since we are interested in the shape of the continuum spectrum, we ignored any regions which contained lines while performing the fits. We also excluded time intervals which included thermonuclear X-ray bursts, eclipses, or X-ray dips (details for each source are given below). We combined the ±1 orders of the background-subtracted HEG and MEG spectra, and fit the two grating arms simultaneously, grouping the data to insure that each bin included at least 50 counts and 8 channels. This resulted in a spectral resolution of ≥ 0.02 (0.04) Å for the HEG (MEG). We analyzed the wavelength ranges 1.5–15.0 (1.8–25.0) Å for the HEG (MEG) data, and performed the fits using chi-squared statistics and

---

[3]See http://space.mit.edu/CXC/analysis/HETGS/AfterGlow/AfterGlow.html for a discussion of the importance of removing the afterglow correction for analysis of HETGS data.

[4]http://space.mit.edu/CXC/ISIS/

[5]http://heasarc.gsfc.nasa.gov/docs/xanadu/xspec/

[6]http://astro.uni-tuebingen.de/~wilms/research/tbabs/

Table 8.3. Source sample and *Chandra* observations

Source	Type[a]	ObsID	Observation time (ks)	Observation date
2S 0918−549	A, U[b]	701	28.5	19 Jul 2000
4U 1626−67	A, U, P	104	39.5	16 Sep 2000
		3504	94.8	3 Jun 2003
XTE J1814−338	B, T, M	4439	9.9	20 Jun 2003

[a]A = atoll source, U = ultracompact binary, B = thermonuclear X-ray burster, P = X-ray pulsar, T = transient system, Z = Z source, M = accretion-powered millisecond pulsar.

[b]2S 0918−549 is a candidate ultracompact binary based on its high Ne abundance (Juett et al. 2003).

subplex minimization (a variant of the Nelder-Mead simplex algorithm; Nelder and Mead 1964). Errors quoted are 90% confidence limits.

8.5 Source sample and individual fit results

Ideally, we would analyze every public observation in the *Chandra* HETG LMXB database. However, time constraints do not allow us to complete a project of such broad scope, so we have chosen a set of representative objects from standard source classes. These include the ultracompact binary system 4U 1626−67, the accretion-powered millisecond pulsar XTE J1814−338, and the atoll source 2S 0918−549. Both XTE J1814−338 and 4U 1626−67 have been discussed in previous chapters (2 and 7). Table 8.3 lists the sources and information about the *Chandra*/HETG observations analyzed here. Following are brief descriptions of of each source in our sample as well as the results of our spectral fitting.

8.5.1   2S 0918−549

The atoll source and candidate ultracompact binary system 2S 0918−549 has been observed once by *Chandra* (ObsID 701, performed 19 July 2000), during which time it was in the island state. It exhibits thermonuclear X-ray bursts, which have been used to determine a distance of 4.2 kpc (Cornelisse et al. 2002); however, there were no bursts present in the *Chandra* observation. A strong absorption edge in *ASCA* spectra revealed that 2S 0918−549 likely has a Ne-rich companion (Juett et al. 2001). The high-resolution *Chandra* spectrum, as well as one obtained with *XMM-Newton*, confirm that there is an excess of Ne in the system; $N_{\rm Ne} = (9.9\pm1.7)\times10^{17}$ cm^{-2} whereas $N_{\rm O} = (1.9\pm0.3)\times10^{18}$ cm^{-2}: the Ne column implies an H column ≈ 3 times greater than that inferred from the O column (Juett and Chakrabarty 2003). They also found the Fe column to be $N_{\rm Fe} = 1.0^{+0.6}_{-0.3}\times10^{17}$ cm^{-2}. In our continuum fits, we set the value of $N_{\rm H} = 3.9\times10^{21}$ cm^{-2} to match the column density of O (assuming ISM abundances; Wilms et al. 2000), and adjusted the Ne and Fe abundances appropriately.

Neither the thermal bremsstrahlung nor the blackbody model provide an acceptable fit. A power-law with photon index $\Gamma = 2.3$ provides a reasonable fit; $\chi^2_\nu = 1.05$. However, a plot
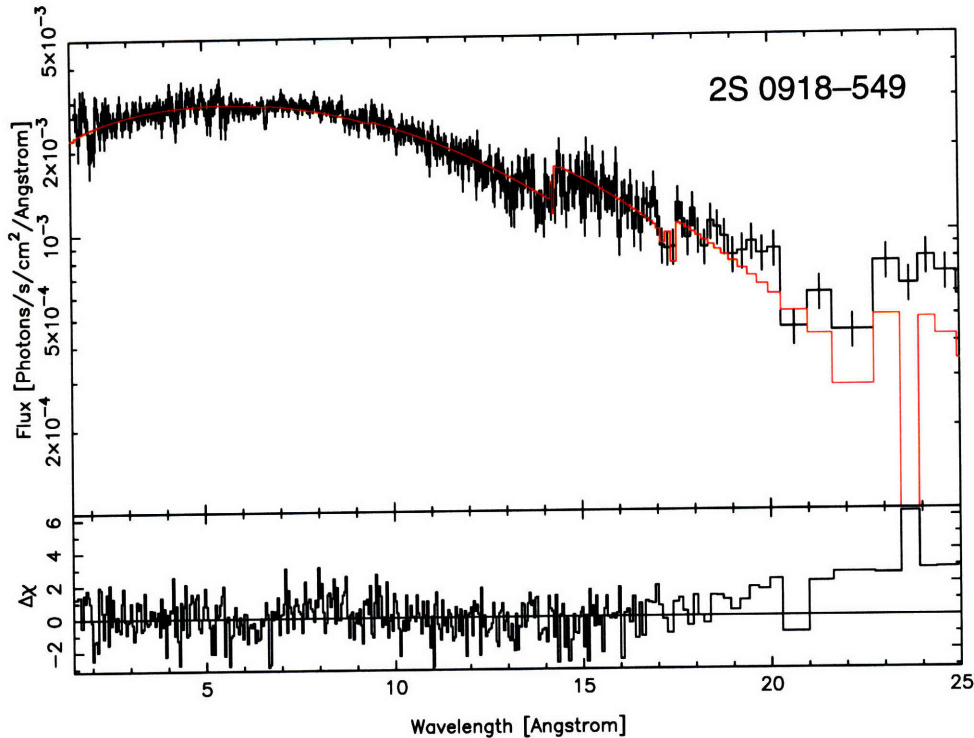
Figure 8-1: *Chandra*/HETG spectrum of 2S 0918−549. For plotting purposes, the MEG and HEG ±1 orders have been combined; the red curve is the power-law fit. Fit residuals are shown in the lower panel. Note the excess emission in the 20–25 Å range.

of the fit residuals shows an excess of soft emission in the 20–25 Å range (see Figure 8-1). To quantify the magnitude of this excess, we added a blackbody component while holding the photon index fixed. We find that the excess is well-accounted for by a very low-temperature (kT = 45 eV) blackbody with a radius of $\approx 2 \times 10^4$ km, or, alternatively, by a disk blackbody with an inner disk temperature of 53 eV and an inner radius of 2500 $(\cos^{-1/2} i)$ km (after applying the corrections described in Kubota et al. 1998). Unfortunately, neither of these allow for a realistic physical description. A single-temperature blackbody is generally thought to arise from the boundary layer or neutron star surface, but the fitted radius is far larger than either of these regions. While an accretion disk has a more substantial emitting area, the fitted inner disk radius and temperature do not agree with the X-ray heated accretion disk model (Equation 1.4). For a disk temperature of ≈ 50 eV, the corresponding radius should be ≈ 500 km; the fitted value is $\gtrsim 5$ times that amount.

8.5.2   4U 1626−67

We present a detailed description of the ultracompact binary 4U 1626−67 in Chapter 7. Briefly, this 42-min binary system contains a high–magnetic-field pulsar ($B \approx 4 \times 10^{12}$ G; $P_{\rm spin} = 7.7$ s), and its X-ray spectrum exhibits prominent Ne and O emission lines (Pravdo et al. 1979; Middleditch et al. 1981; Angelini et al. 1995). *Chandra* has observed 4U 1626−67 twice (ObsIDs 104 and 3504, performed 16 September 2000 and 3 June 2003), and we present analysis of both observations here.

The neutral absorbing column density to 4U 1626−67 is not high enough for us to

measure the depths of individual edges, so we allowed N_H to vary in all the fits. We also excluded the regions containing emission lines: 11.9–12.4 Å (Ne X), 13.3–13.8 Å (Ne IX), 18.7–19.3 Å (O VIII), and 21.4–22.1 Å (O VII) were removed prior to fitting. None of the single-component models—power-law, blackbody, or bremsstrahlung—provided a good fit for either observation ($\chi^2_\nu > 1.5$). However, the combination of a blackbody and power-law resulted in a good fit for both, $\chi^2_\nu = 1.1$, and we present plots of these fits in Figures 8-2 and 8-3. The blackbody has a temperature kT = 0.29 [0.28] keV and normalization $R^2_{km}/D^2_{10\ kpc} = 210$ [150] for ObsID 104 [3504]. Although the distance to 4U 1626−67 is uncertain, it is likely in the range 3–13 kpc. Assuming a distance of 3, 8, or 13 kpc, we derive a blackbody radius of 4, 12, and 19 km. The first two values are reasonable for emission arising from the surface of the neutron star, but the last is unreasonably large for most neutron star equations of state. The other likely site of blackbody emission is the accretion disk, but in this system, the disk is truncated at the corotation radius of the neutron star, $\approx 6.5 \times 10^3$ km. At this radius, the temperature of an X-ray heated accretion disk is ≈ 0.01 keV (Equation 1.4), substantially lower than the fitted temperature. Therefore, we consider it likely that the emission does arise from the surface of the neutron star, implying that 4U 1626−67 probably lies somewhere in the closer portion of its distance range.

We note that the parameters we derive from these fits are somewhat different from what is presented in Chapter 7. In order to explore these differences, we applied the same fitting methods to those data, and while the fitted values were slightly different, they agree within the 90% confidence regions with our previous results. Therefore, we attribute the differences we find here to the updated processing and newer calibration products.

8.5.3 XTE J1814−338

The accretion-powered millisecond pulsar XTE J1814−338 was observed once with the *Chandra* HETG for a total of 9.7 ks (ObsID 4439). We present detailed analysis of this observation, as well as optical data from the same outburst, in Chapter 2. There, we found evidence for an excess amount of infrared emission relative to an X-ray heated accretion disk model, suggesting that there is a synchrotron component in the spectrum. This emission could be attributed to a (perhaps jet-like) outflow from the system. XTE J1814−338 has also exhibited thermonuclear X-ray bursts, one of which shows evidence of Eddington-limited radius expansion, from which a distance of 8.0 ± 1.6 is derived (Strohmayer et al. 2003).

The absorption column is not high enough for us to fit individual edges, so we allow N_H to vary while fitting the continuum spectrum. A power-law and bremsstrahlung model both describe the spectrum quite well, giving, respectively, a photon index $\Gamma = 1.39$ and electron temperature kT = 27 keV. However, neither of these fits can perfectly account for emission in the 18–25 Å range, leaving a slight excess as can be seen in Figure 8-4. To better characterize the remaining emission, we added a blackbody component to the power-law, holding the photon index fixed but allowing the other parameters to vary. This results in a blackbody of temperature kT = 0.93 ± 0.09 keV. For a source distance of 8 kpc, this blackbody has a radius of 1.4 km, and could arise from a hot spot on the neutron star surface.
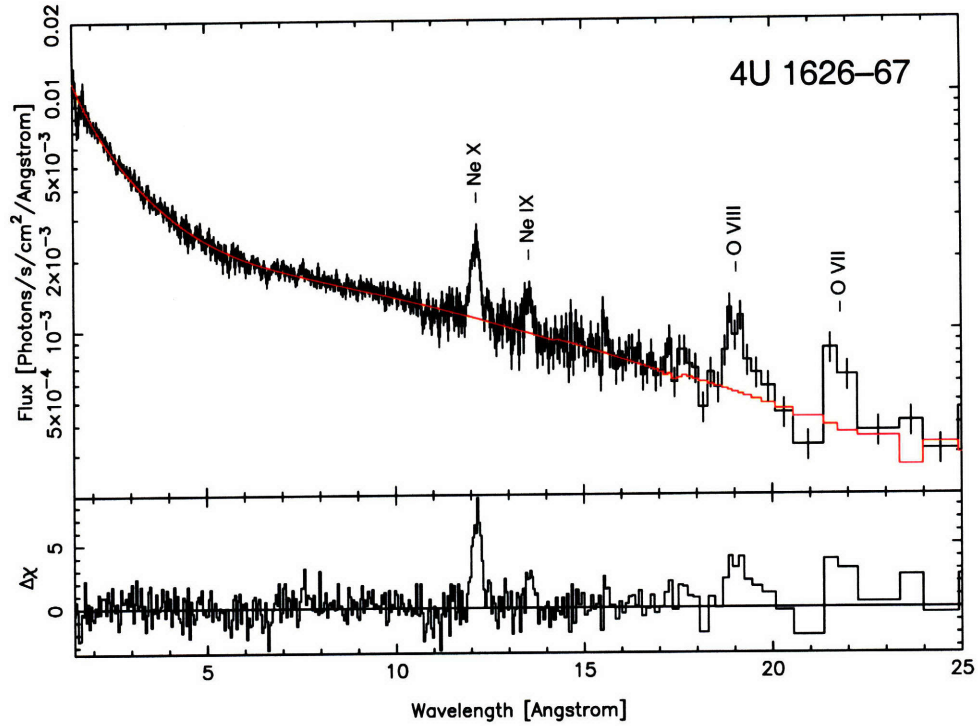
Figure 8-2: *Chandra*/HETG spectrum of 4U 1626−67, ObsID 104. For plotting purposes, the MEG and HEG ±1 orders have been combined; the red curve is the blackbody plus power-law fit. Fit residuals are shown in the lower panel. Note the strong O and Ne emission lines.
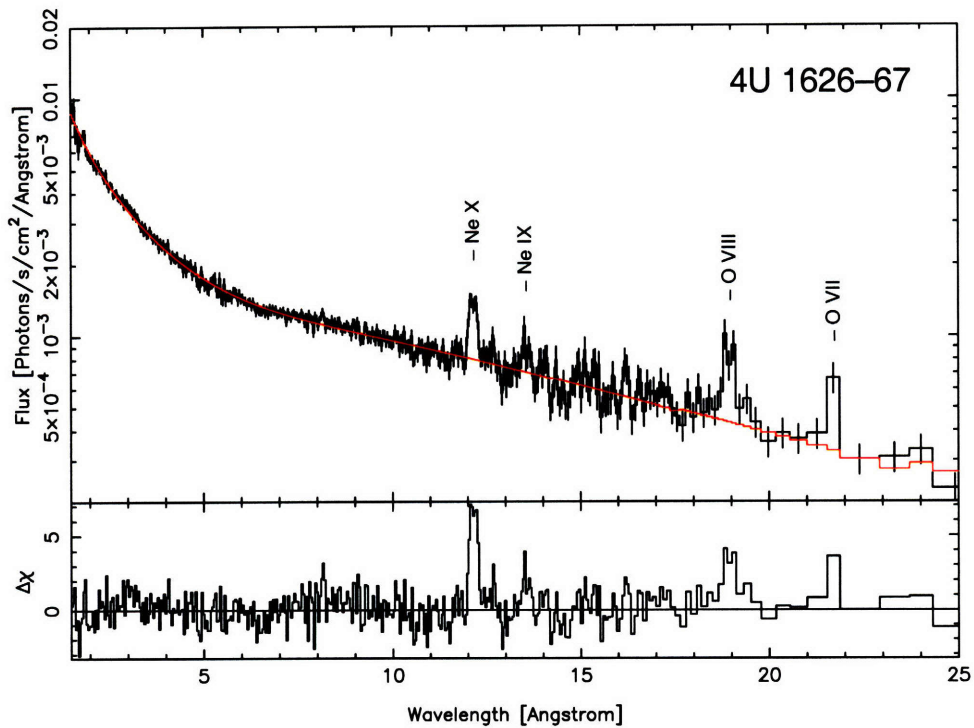
Figure 8-3: Same as Figure 8-2 but for ObsID 3504.

126
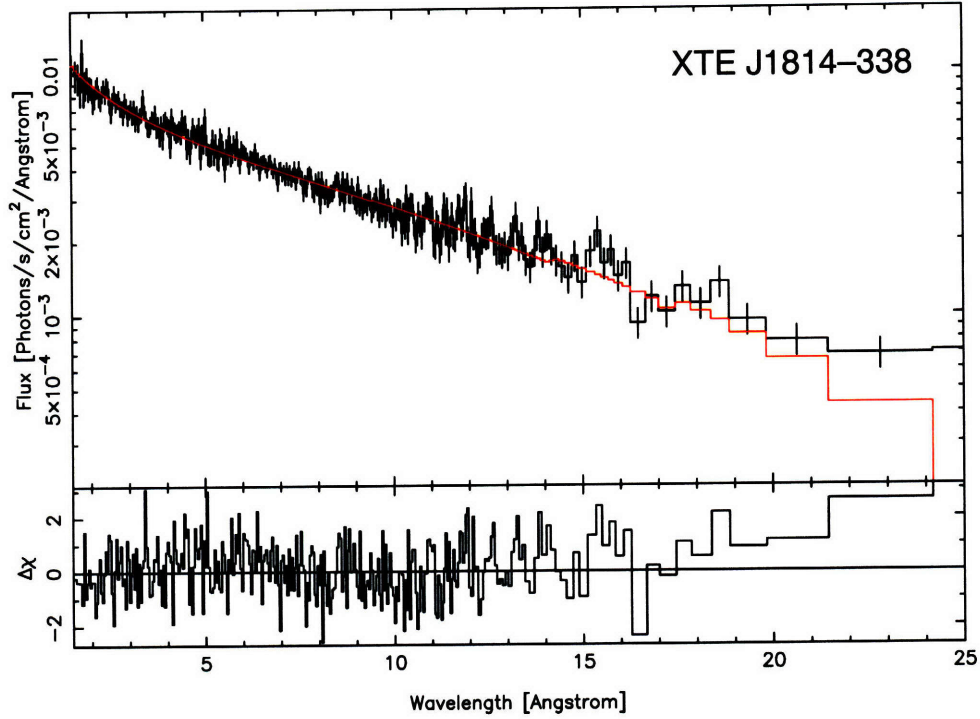
Figure 8-4: *Chandra*/HETG spectrum of XTE J1814−338; combined MEG and HEG ±1 orders with the power-law fit plotted in red and fit residuals shown in the lower panel. Note the excess of soft emission in the 18–25 Å range.

Table 8.4. LMXB power-law fits

Source	ObsID	$N_{\rm H}$ $(10^{21} {\rm cm}^{-2})$	Γ	Norm[a]	ν	χ^2_ν
2S 0918−549	701	3.90	2.29 ± 0.01	50.5 ± 0.5	795	1.05
4U 1626−67[b]	104	0.62	1.01 ± 0.01	13.4 ± 0.1	769	1.72
	3504	0.62	$\cdots$	$\cdots$	838	2.22
XTE J1814−338	4439	2.2 ± 0.3	1.39 ± 0.03	37 ± 1	566	0.95

[a]Power-law normalization at 1 keV in units of 10^{-3} erg cm^{-2} s^{-1} keV^{-1}.

[b]For these fits, $N_{\rm H}$ was frozen to its Galactic value; otherwise, the power-law fit forced it to zero.

Table 8.5. LMXB thermal bremsstrahlung fits

Source	ObsID	N_H $(10^{21}$ cm$^{-2})$	kT (keV)[a]	Norm[b]	ν	χ^2_ν
2S 0918−549	701	3.90	$\cdots$	$\cdots$	795	2.65
4U 1626−67	104	$0.39^{+0.07}_{-0.07}$	uncons.	uncons.	768	1.74
	3504	$\cdots$	$\cdots$	$\cdots$	837	2.77
XTE J1814−338	4439	1.7 ± 0.2	27^{+5}_{-4}	60 ± 1	566	0.92

[a]Electron temperature, assuming a thermal distribution of electrons.

[b]Bremsstrahlung normalization, $\frac{3.02 \times 10^{-12}}{4\pi D^2} \int n_e n_i dV$, where D is the distance to the source (cm) and n_e, n_i are the electron and ion densities (cm^{-3}).

Table 8.6. LMXB blackbody plus power-law fits

Source	ObsID	N_H $(10^{21}$ cm$^{-2})$	Blackbody		Power-law		ν	χ^2_ν
			kT (keV)	$R^2_\mathrm{km}/D^2_\mathrm{10\ kpc}$	Γ	Norm[a]		
2S 0918−549	701	3.90	0.05 ± 0.01	$4.4^{+365.9}_{-0.4} \times 10^7$	2.29	50.5 ± 0.3	794	1.03
4U 1626−67	104	0.8 ± 0.3	0.29 ± 0.02	210^{+70}_{-50}	0.69 ± 0.04	8.8 ± 0.5	766	1.09
	3504	0.4 ± 0.3	$0.28^{+0.02}_{-0.01}$	150^{+40}_{-30}	0.65 ± 0.03	6.2 ± 0.2	835	1.10
XTE J1814−338	4439	1.7 ± 0.3	0.93 ± 0.09	3 ± 1	1.391	33 ± 2	565	0.92

[a]Power-law normalization at 1 keV in units of 10^{-3} erg cm^{-2} s^{-1} keV^{-1}.

8.6 Discussion and conclusions

Not surprisingly, none of the pure blackbody fits were acceptable, and only one of the sources (XTE J1814−338) could be fit by a thermal bremsstrahlung spectrum. Of the models that we chose, the only one which provided an acceptable fit for all the sources was a blackbody plus power-law. Although it often provides a good description of the spectral shape, a power-law does not, by itself, have physical motivation. However, over the limited energy range investigated in *Chandra* HETG spectra, it is a reasonable approximation of the spectrum which would arise from Comptonization. As can be seen in the plots of Compton curves in Figure 1-7, the slope of the power-law is closely tied to the Compton β parameter, with steeper slopes occurring as a result of lower electron temperature and/or lower optical depth.

Two of the sources, 2S 0918−549 and XTE J1814−338, are reasonably well fit by a simple power-law, but show evidence for an excess of soft emission ($\lambda \gtrsim 20$ Å). 4U 1626−67 requires the presence of a soft component in its fits. In all cases, this soft component can be modeled by a single-temperature blackbody. However, some of the parameters from these blackbody fits agree more readily with standard models of neutron star LMXB systems than others. For example, the blackbody components in XTE J1814−338 and 4U 1626−67 could both arise from emission on the neutron star surface, although the emission radius derived for 4U 1626−67 becomes somewhat large for greater values of the source distance. In contrast, the blackbody component derived for 2S 0918−549 has an extremely low temperature, and very large normalization, resulting in a blackbody radius that is substantially larger than any physical model for a neutron star. If, instead, a multi-temperature disk blackbody is assumed, the resulting fit still does not agree with basic theoretical models of accretion disks—the radius of the inner disk is at a much larger value than would be expected from the inner disk temperature.

It is probable that fitting the soft X-ray emission with a blackbody is, in most cases, too naïve and likely unphysical. First, few astrophysical processes result in simple blackbody emission. Often, the emission is modified by other effects, such as processes in neutron star atmospheres or Comptonization from hot electrons. Furthermore, it is possible that the emission is completely unrelated to a blackbody process. This could easily be the case for 2S 0918−549, in which case the attempts to model the spectrum with blackbody emission result in apparently unphysical fit parameters.

Ultimately, undertaking the analysis of high-resolution X-ray spectra from a larger sample of sources will give a broader view of the spectral properties of different classes, and could help determine which spectral components provide the best physical descriptions of these systems. Although this is beyond the scope of this thesis, the framework of the *Chandra* HETG LMXB database should aid in the process of performing a survey of larger scope.

Chapter 9

Summary

In this thesis, I presented work spanning a wide variety of science topics concerning neutron star low-mass X-ray binaries. In Chapter 2, I presented analysis of the high-resolution *Chandra* spectrum of the accretion-powered millisecond pulsar XTE J1814−338. Although the X-ray spectrum is featureless, and was not able to provide much additional information about the system, the precise *Chandra* position allowed us to identify an optical counterpart. Analysis of optical observations of the counterpart also allowed us to place constraints on the inclination of the system. Furthermore, comparison of the optical magnitudes with the expected brightness of an X-ray heated accretion disk showed that there is a flux excess toward the infrared portion of the spectrum. This suggested that there is a non-thermal contribution which could arise from synchrotron emission, possibly due to the presence of a jet.

In Chapters 3 and 4, I found that the accretion-powered millisecond pulsars (AMPs)and a sample of atoll sources have very similar optical depths when fitted by a standard Comptonization model. This analysis used their color-color diagrams to ensure that the observations which I analyzed all came from a similar spectral state. Since the AMPs, with only one exception, exclusively occupy the extreme island state, this was the only state that we considered for the atoll sources as well. The observation that the AMPs do not explore the higher-luminosity regions of the color-color diagram, but otherwise have similar color properties to the atoll sources, suggests that they are an intrinsically lower-luminosity population. Furthermore, our determination that the two source classes have similar optical depths suggests that we cannot explain the lack of persistent pulsations in the atoll sources by invoking a scattering medium to obscure pulsed emission. It is more likely that the higher mass accretion rate in atoll sources could hinder the efficacy of the magnetic field in channeling the accretion flow, resulting in a lack of pulsations. Alternatively, it is possible that a higher overall accretion rate in the atoll sources has suppressed the magnetic field via diamagnetic screening, again affecting its ability to channel the accretion flow. This theory is supported by observations of the unique AMP HETE J1900.1−2455, which only appeared as a pulsar for the first two months of its almost two year, and still continuing, outburst.

In Chapter 5 I discussed our search of two *Chandra* observations of neutron star LMXBs, the AMP SAX J1808.4−3658 and the unique transient Z source XTE J1701−462, for X-ray jet features. As mentioned above, we have reason to believe that AMPs and other neutron star LMXBs may have jets, although much of the evidence is indirect, insofar as it not from spatially-resolved observations. Unfortunately, neither of our observations showed a bona

fide jet feature, though we discussed a spurious feature which could arise in temporally short observations of bright point sources.

In Chapter 6 I analyzed the burst temperature distributions from a large sample of thermonuclear X-ray bursts from Galactic LMXBs observed by *RXTE*. I found that there is a wide variety of behavior: some sources produce a substantially greater fraction of burst fluence at lower temperatures than others. Since the formation of discrete spectral features depends on the fraction of material on the neutron star surface which retains one or more electron, temperature can play an important role in the ability of such features to arise in burst spectra. This is relevant to current searches for lines and edges in the thermonuclear burst spectra of Galactic LMXBs, which has gained much recent attention due to its relevance in constraining models for the neutron star equation of state. For example, I found that the low-temperature fluence fractions are relatively small for all the sources from which searches have failed to detect discrete line features, or been unable, as in the case of EXO 0748−676, to repeat a previous measurement. I also stressed the importance of neutron star spin and its effect on the detectability of discrete features. Finally, I suggested some strategies, both current and future, for searching for discrete features in X-ray bursts.

In Chapter 7 I analyzed high-resolution *Chandra* and *XMM-Newton* spectra of the ultracompact LMXB pulsar 4U 1626−67. I found that the prominent Ne and O emission lines are consistent with an accretion disk origin, although the corresponding photoelectric absorption edges do not suggest an overabundance of neutral Ne or O in the system. Analysis of the current timing behavior showed that the pulsar continues to spin down, and the overall X-ray flux indicated that the system continues to fade, both in keeping with previously determined trends. I projected that 4U 1626−67 will enter a period of quiescence in approximately 2–15 years.

In Chapter 8 I described the *Chandra* HETG LMXB database, which contains high-spectral-resolution public observations of Galactic LMXBs. I analyzed three of these sources using a high-resolution absorption edge model to effectively account for photoelectric absorption, which provided strong constraints on the low-energy regions of the continuum spectra. For all three sources, the low-energy emission required the addition of a soft component which could be modeled by a blackbody. This blackbody can be interpreted as emission from the surface of the neutron star for XTE J1814−338 and 4U 1626−67. However, this is not the case for 2S 0918−549, suggesting that a blackbody model may not be appropriate. Analysis of a broader sample of sources will ultimately be necessary to better understand the physical interpretation of these spectra.

Bibliography

L. Angelini and N. E. White. An XMM-Newton Observation of 4U 1755−33 in Quiescence: Evidence of a Fossil X-Ray Jet. *ApJ*, 586:L71–L75, March 2003.

L. Angelini, N. E. White, F. Nagase, T. R. Kallman, A. Yoshida, T. Takeshima, C. Becker, and F. Paerels. Neon Line Emission in the X-Ray Spectrum of the Pulsar 4U 1626−67. *ApJ*, 449:L41–L45, August 1995.

K. Asai, T. Dotani, R. Hoshi, Y. Tanaka, C. R. Robinson, and K. Terada. ASCA Observations of Transient X-Ray Sources in Quiescence. *PASJ*, 50:611–619, December 1998.

D. Barret. Accretion flows around stellar mass black holes and neutron stars. In G. Bertin, D. Farina, and R. Pozzoli, editors, *AIP Conf. Proc. 703: Plasmas in the Laboratory and in the Universe: New Insights and New Challenges*, pages 238–249, April 2004.

D. Barret, J. F. Olive, and T. Oosterbroek. Simultaneous BeppoSAX and Rossi X-ray Timing Explorer observations of 4U 1812−12. *A&A*, 400:643–647, March 2003.

E. M. Basinska, W. H. G. Lewin, M. Sztajno, L. R. Cominsky, and F. J. Marshall. X-ray observations of the burst source MXB 1728−34. *ApJ*, 281:337–353, June 1984.

C. G. Bassa, P. G. Jonker, J. J. M. in 't Zand, and F. Verbunt. Two new candidate ultra-compact X-ray binaries. *A&A*, 446:L17–L20, February 2006.

R. D. Belian, J. P. Conner, and W. D. Evans. The discovery of X-ray bursts from a region in the constellation Norma. *ApJ*, 206:L135–L138, June 1976.

D. Bhattacharya and G. Srinivasan. The magnetic fields of neutron stars and their evolution, page 495. *X-ray Binaries*, eds. W.H.G. Lewin, J. van Paradijs, and E.P.J. van den Heuvel (Cambridge: Cambridge Univ. Press), 1995.

D. Bhattacharya and E. P. J. van den Heuvel. Formation and evolution of binary and millisecond radio pulsars. *Phys. Rep.*, 203:1–124, 1991.

S. Bhattacharyya, T. E. Strohmayer, M. C. Miller, and C. B. Markwardt. Constraints on Neutron Star Parameters from Burst Oscillation Light Curves of the Accreting Millisecond Pulsar XTE J1814−338. *ApJ*, 619:483–491, January 2005.

L. Bildsten and D. Chakrabarty. A Brown Dwarf Companion for the Accreting Millisecond Pulsar SAX J1808.4−3658. *ApJ*, 557:292–296, August 2001.

L. Bildsten, P. Chang, and F. Paerels. Atomic Spectral Features during Thermonuclear Flashes on Neutron Stars. *ApJ*, 591:L29–L32, July 2003.

R. J. Brissenden. Chandra X-ray Observatory Operations. In F. R. Harnden, Jr., F. A. Primini, and H. E. Payne, editors, *Astronomical Data Analysis Software and Systems X*, volume 238 of Astronomical Society of the Pacific Conference Series, pages 22–31, 2001.

L. Burderi, N. Robba, M. Guainazzi, D. Ricci, M. Capalbi, G. Celidonio, A. Coletta, R. Ricci, and M. Smith. 4U 1812−12. *IAU Circ.*, 6603, March 1997.

S. Campana, N. Ferrari, L. Stella, and G. L. Israel. XMM-Newton observations of two transient millisecond X-ray pulsars in quiescence. *A&A*, 434:L9–L12, May 2005.

S. Campana, M. Ravasio, G. L. Israel, V. Mangano, and T. Belloni. XMM-Newton Observation of the 5.25 Millisecond Transient Pulsar XTE J1807−294 in Outburst. *ApJ*, 594: L39–L42, September 2003.

S. Campana, L. Stella, F. Gastaldello, S. Mereghetti, M. Colpi, G. L. Israel, L. Burderi, T. Di Salvo, and R. N. Robba. An XMM-Newton Study of the 401 Hz Accreting Pulsar SAX J1808.4−3658 in Quiescence. *ApJ*, 575:L15–L19, August 2002.

S. Campana, L. Stella, S. Mereghetti, M. Colpi, M. Tavani, D. Ricci, D. D. Fiume, and T. Belloni. Aquila X-1 from Outburst to Quiescence: The Onset of the Propeller Effect and Signs of a Turned-on Rotation-powered Pulsar. *ApJ*, 499:L65–L68, May 1998.

C. R. Canizares, J. E. Davis, D. Dewey, K. A. Flanagan, E. B. Galton, D. P. Huenemoerder, K. Ishibashi, T. H. Markert, H. L. Marshall, M. McGuirk, M. L. Schattenburg, N. S. Schulz, H. I. Smith, and M. Wise. The Chandra High-Energy Transmission Grating: Design, Fabrication, Ground Calibration, and 5 Years in Flight. *PASP*, 117:1144–1171, October 2005.

B. W. Carroll and D. A. Ostlie. *An Introduction to Modern Astrophysics*. Reading, MA: Addison-Wesley, 1996.

D. Chakrabarty. High-Speed Optical Photometry of the Ultracompact X-Ray Binary 4U 1626−67. *ApJ*, 492:342–351, January 1998.

D. Chakrabarty, L. Bildsten, J. M. Grunsfeld, D. T. Koh, T. A. Prince, B. A. Vaughan, M. H. Finger, D. M. Scott, and R. B. Wilson. Torque Reversal and Spin-down of the Accretion-powered Pulsar 4U 1626−67. *ApJ*, 474:414–425, January 1997.

D. Chakrabarty, L. Homer, P. A. Charles, and D. O'Donoghue. Millihertz Optical/Ultraviolet Oscillations in 4U 1626−67: Evidence for a Warped Accretion Disk. *ApJ*, 562:985–991, December 2001.

D. Chakrabarty and E. H. Morgan. The two-hour orbit of a binary millisecond X-ray pulsar. *Nature*, 394:346–348, 1998.

D. Chakrabarty, E. H. Morgan, M. P. Muno, D. K. Galloway, R. Wijnands, M. van der Klis, and C. B. Markwardt. Nuclear-powered millisecond pulsars and the maximum spin frequency of neutron stars. *Nature*, 424:42–44, July 2003.

P. Chang, L. Bildsten, and I. Wasserman. Formation of Resonant Atomic Lines during Thermonuclear Flashes on Neutron Stars. *ApJ*, 629:998–1007, August 2005.

P. Chang, S. Morsink, L. Bildsten, and I. Wasserman. Rotational Broadening of Atomic Spectral Features from Neutron Stars. *ApJ*, 636:L117–L120, January 2006.

C. Chevalier and S. A. Ilovaisky. Discovery of a 19-hour period in Aquila X-1. *A&A*, 251: L11–L13, November 1991.

C. Chevalier, S. A. Ilovaisky, P. Leisy, and F. Patat. Magnitude, color and spectral type of Aql X-1 in quiescence. *A&A*, 347:L51–L54, July 1999.

D. J. Christian and J. H. Swank. The Survey of Low-Mass X-Ray Binaries with the Einstein Observatory Solid-State Spectrometer and Monitor Proportional Counter. *ApJS*, 109: 177–224, March 1997.

M. J. Church and M. Balucińska-Church. Results of a LMXB survey: Variation in the height of the neutron star blackbody emission region. *A&A*, 369:915–924, April 2001.

W. Coburn, W. A. Heindl, R. E. Rothschild, D. E. Gruber, I. Kreykenbohm, J. Wilms, P. Kretschmar, and R. Staubert. Magnetic Fields of Accreting X-Ray Pulsars with the Rossi X-Ray Timing Explorer. *ApJ*, 580:394–412, November 2002.

M. Cocchi, A. Bazzano, L. Natalucci, P. Ubertini, J. Heise, E. Kuulkers, J. M. Muller, and J. J. M. in 't Zand. Observations of Eddington-limited type-I X-ray bursts from 4U 1812−12. *A&A*, 357:527–532, May 2000.

S. Corbel, R. P. Fender, A. K. Tzioumis, J. A. Tomsick, J. A. Orosz, J. M. Miller, R. Wijnands, and P. Kaaret. Large-Scale, Decelerating, Relativistic X-ray Jets from the Microquasar XTE J1550−564. *Science*, 298:196–199, October 2002.

R. Cornelisse, J. Casares, D. Steeghs, A. D. Barnes, P. A. Charles, R. I. Hynes, and K. O'Brien. A detection of the donor star of Aquila X-1 during its 2004 outburst? *MNRAS*, 375:1463–1470, March 2007.

R. Cornelisse, F. Verbunt, J. J. M. in 't Zand, E. Kuulkers, J. Heise, R. A. Remillard, M. Cocchi, L. Natalucci, A. Bazzano, and P. Ubertini. BeppoSAX Wide Field Cameras observations of six type I X-ray bursters. *A&A*, 392:885–893, September 2002.

J. Cottam, F. Paerels, and M. Mendez. Gravitationally redshifted absorption lines in the X-ray burst spectra of a neutron star. *Nature*, 420:51–54, November 2002.

J. Cottam, F. Paerels, G. Telis, M. Audard, M. Mendez, L. Boirin, T. Lanz, W. Lewin, H. Marshall, L. Bildsten, and P. Chang. High Resolution Fe Lyman and Balmer Band Spectroscopy of the Bursts in EXO 0748−676. In *Bulletin of the American Astronomical Society*, page 2.05, September 2006.

A. Cumming, E. Zweibel, and L. Bildsten. Magnetic Screening in Accreting Neutron Stars. *ApJ*, 557:958–966, August 2001.

R. M. Cutri, M. F. Skrutskie, S. Van Dyk, J. M. Carpenter, T. Chester, T. Evans, J. Fowler, J. Gizis, E. Howard, J. Huchra, T. Jarrett, J. D. Kopan E. L.and Kirkpatrick, R. M. Light, K. A. Marsh, H. McCallon, S. Schneider, R. Stiening, M. Sykes, M. Weinberg, W. A. Wheaton, S. Wheelock, and N. Zacarias. *Explanatory Supplement to the 2MASS Second Incremental Data Release.* Technical report, IPAC/Caltech, 2001.

J. E. Davis. Event Pileup in Charge-coupled Devices. *ApJ*, 562:575–582, November 2001.

X. Delfosse, T. Forveille, D. Ségransan, J.-L. Beuzit, S. Udry, C. Perrier, and M. Mayor. Accurate masses of very low mass stars. IV. Improved mass-luminosity relations. *A&A*, 364:217–224, December 2000.

T. Di Salvo, R. Iaria, M. Méndez, L. Burderi, G. Lavagetto, N. R. Robba, L. Stella, and M. van der Klis. A Broad Iron Line in the Chandra High Energy Transmission Grating Spectrum of 4U 1705−44. *ApJ*, 623:L121–L124, April 2005.

J. M. Dickey and F. J. Lockman. H I in the Galaxy. *ARA&A*, 28:215–261, 1990.

M. Falanga, J. M. Bonnet-Bidaud, J. Poutanen, R. Farinelli, A. Martocchia, P. Goldoni, J. L. Qu, L. Kuiper, and A. Goldwurm. INTEGRAL spectroscopy of the accreting millisecond pulsar XTE J1807−294 in outburst. *A&A*, 436:647–652, June 2005a.

M. Falanga, L. Kuiper, J. Poutanen, E. W. Bonning, W. Hermsen, T. di Salvo, P. Goldoni, A. Goldwurm, S. E. Shaw, and L. Stella. INTEGRAL and RXTE observations of accreting millisecond pulsar IGR J00291+5934 in outburst. *A&A*, 444:15–24, December 2005b.

M. Falanga, J. Poutanen, E. W. Bonning, L. Kuiper, J. M. Bonnet-Bidaud, A. Goldwurm, W. Hermsen, and L. Stella. Simultaneous INTEGRAL and RXTE observations of the accreting millisecond pulsar HETE J1900.1−2455. *A&A*, 464:1069–1074, March 2007.

R. Fender. Energetics of jets from X-ray binaries. *Astrophysics and Space Science Supplement*, 276:69–77, 2001a.

R. Fender. Jets from X-ray binaries, pages 381–419. In *Compact Stellar X-ray Sources*, eds. W. H. G. Lewin and M. van der Klis, April 2006.

R. Fender, G. De Bruyn, G. Pooley, and B. Stappers. The radio counterpart of IGR J00291+5934. *The Astronomer's Telegram*, 361, December 2004.

R. Fender, B. Sault, and M. Dahlem. XTE J1701−462: possible radio counterpart. *The Astronomer's Telegram*, 710, January 2006.

R. P. Fender. Powerful jets from black hole X-ray binaries in low/hard X-ray states. *MNRAS*, 322:31–42, March 2001b.

E. C. Ford and M. van der Klis. Strong Correlation between Noise Features at Low Frequency and the KilohertzQuasi-Periodic Oscillations in the X-Ray Binary 4U 1728−34. *ApJ*, 506:L39–L42, October 1998.

E. C. Ford, M. van der Klis, M. Méndez, R. Wijnands, J. Homan, P. G. Jonker, and J. van Paradijs. Simultaneous Measurements of X-Ray Luminosity and Kilohertz Quasi-Periodic Oscillations in Low-Mass X-Ray Binaries. *ApJ*, 537:368–373, July 2000.

W. Forman, C. Jones, L. Cominsky, P. Julien, S. Murray, G. Peters, H. Tananbaum, and R. Giacconi. The fourth UHURU catalog of X-ray sources. *ApJS*, 38:357–412, December 1978.

W. Forman, C. Jones, and H. Tananbaum. UHURU observations of a transient X-ray source associated with the globular cluster NGC 6440. *ApJ*, 207:L25–L27, July 1976a.

W. Forman, H. Tananbaum, and C. Jones. UHURU observations of the galactic plane in 1970, 1971, and 1972. *ApJ*, 206:L29–L35, May 1976b.

A. J. Foster, A. C. Fabian, and R. R. Ross. The formation of iron features in the cooling spectrum of X-ray bursts. *MNRAS*, 228:259–268, September 1987.

D. B. Fox and S. R. Kulkarni. IGR J00291+5934 Optical Counterpart. *The Astronomer's Telegram*, 354, December 2004.

J. Frank, A. King, and D. J. Raine. *Accretion Power in Astrophysics*. Cambridge, UK: Cambridge University Press, February 2002.

H. Friedman, E. T. Byram, and T. A. Chubb. Distribution and Variability of Cosmic X-Ray Sources. *Science*, 156:374–378, April 1967.

B. M. Gaensler, B. W. Stappers, and T. J. Getts. Transient Radio Emission from SAX J1808.4−3658. *ApJ*, 522:L117–L119, September 1999.

D. K. Galloway, D. Chakrabarty, E. H. Morgan, and R. A. Remillard. Discovery of a High-Latitude Accreting Millisecond Pulsar in an Ultracompact Binary. *ApJ*, 576:L137–L140, September 2002.

D. K. Galloway and A. Cumming. Helium-rich Thermonuclear Bursts and the Distance to the Accretion-powered Millisecond Pulsar SAX J1808.4−3658. *ApJ*, 652:559–568, November 2006.

D. K. Galloway, C. B. Markwardt, E. H. Morgan, D. Chakrabarty, and T. E. Strohmayer. Discovery of the Accretion-powered Millisecond X-Ray Pulsar IGR J00291+5934. *ApJ*, 622:L45–L48, March 2005.

D. K. Galloway, H. L. Marshall, N. S. Schulz, C. R. Canizares, and Y. Yao. In preperation, 2007a.

D. K. Galloway, E. H. Morgan, M. I. Krauss, P. Kaaret, and D. Chakrabarty. Intermittent Pulsations in an Accretion-powered Millisecond Pulsar. *ApJ*, 654:L73–L76, January 2007b.

D. K. Galloway, M. P. Muno, J. M. Hartman, P. Savov, D. Psaltis, and D. Chakrabarty. Thermonuclear (type-I) X-ray bursts observed by the Rossi X-ray Timing Explorer. *ApJS*, submitted. astro-ph/0608259, August 2006.

D. K. Galloway and J. L. Sokoloski. An X-Ray Jet from a White Dwarf: Detection of the Collimated Outflow from CH Cygni with Chandra. *ApJ*, 613:L61–L64, September 2004.

R. Giacconi, S. Murray, H. Gursky, E. Kellogg, E. Schreier, and H. Tananbaum. The UHURU catalog of X-ray souces. *ApJ*, 178:281–308, December 1972.

M. Gierliński and C. Done. The X-ray spectrum of the atoll source 4U 1608−52. *MNRAS*, 337:1373–1380, December 2002.

A. B. Giles, J. G. Greenhill, K. M. Hill, and E. Sanders. The optical counterpart of XTE J0929−314: the third transient millisecond X-ray pulsar. *MNRAS*, 361:1180–1186, August 2005.

A. B. Giles, K. M. Hill, and J. G. Greenhill. The optical counterpart of SAX J1808.4−3658, the transient bursting millisecond X-ray pulsar. *MNRAS*, 304:47–51, March 1999.

J. Gladstone, C. Done, and M. Gierliński. Analysing the atolls: X-ray spectral transitions of accreting neutron stars. *MNRAS*, 378:13–22, June 2007.

I. Goldman. General relativistic effects and the radius and mass of X-ray bursters. *A&A*, 78:L15–L16, September 1979.

S. A. Grebenev, S. V. Molkov, and R. A. Sunyaev. An outburst of the accreting millisecond X-ray pulsar XTE J1751−305 detected with INTEGRAL. *The Astronomer's Telegram*, 446, March 2005.

J. G. Greenhill, A. B. Giles, and C. Coutures. A transient I-band excess in the optical spectrum of the accreting millisecond pulsar SAX J1808.4−3658. *MNRAS*, 370:1303–1308, August 2006.

J. E. Grindlay, J. E. McClintock, C. R. Canizares, L. Cominsky, F. K. Li, W. H. G. Lewin, and J. van Paradijs. Discovery of optical bursts from an X-ray burst source, MXB1735−44. *Nature*, 274:567–568, August 1978.

F. Haberl and L. Titarchuk. On the distance and mass-radius relation of neutron stars in X-ray burst sources. *A&A*, 299:414–420, July 1995.

X. Han and R. M. Hjellming. Radio observations of the 1989 transient event in V404 Cygni (=GS 2023+338). *ApJ*, 400:304–314, November 1992.

W. E. Harris. A Catalog of Parameters for Globular Clusters in the Milky Way. *AJ*, 112:1487–1488, October 1996.

J. M. Hartman, D. Chakrabarty, D. K. Galloway, M. P. Muno, P. Savov, M. Mendez, S. van Straaten, and T. Di Salvo. Discovery of 619 Hz Thermonuclear Burst Oscillations in the Low-Mass X-Ray Binary 4U 1608−52. In *Bulletin of the American Astronomical Society*, page 865, May 2003.

G. Hasinger and M. van der Klis. Two patterns of correlated X-ray timing and spectral behaviour in low-mass X-ray binaries. *A&A*, 225:79–96, November 1989.

S. Heinz, N. S. Schulz, W. N. Brandt, and D. K. Galloway. Evidence of a Parsec-Scale X-Ray Jet from the Accreting Neutron Star Circinus X-1. *ApJ*, 663:L93–L96, July 2007.

T. Hirano, S. Hayakawa, H. Kunieda, K. Masai, F. Nagase, F. Makino, and K. Yamashita. Energy spectra and time variations of the X-ray source Cygnus X-2. *PASJ*, 36:769–784, 1984.

J. Homan, M. van der Klis, R. Wijnands, T. Belloni, R. Fender, M. Klein-Wolt, P. Casella, M. Méndez, E. Gallo, W. H. G. Lewin, and N. Gehrels. Rossi X-Ray Timing Explorer Observations of the First Transient Z Source XTE J1701−462: Shedding New Light on Mass Accretion in Luminous Neutron Star X-Ray Binaries. *ApJ*, 656:420–430, February 2007.

L. Homer, S. F. Anderson, S. Wachter, and B. Margon. The Ultraviolet Spectrum of the Ultracompact X-Ray Binary 4U 1626−67. *AJ*, 124:3348–3357, December 2002.

X.-M. Hua and L. Titarchuk. Comptonization Models and Spectroscopy of X-Ray and Gamma-Ray Sources: A Combined Study by Monte Carlo and Analytical Methods. *ApJ*, 449:188–203, August 1995.

R. A. Hulse and J. H. Taylor. Discovery of a pulsar in a binary system. *ApJ*, 195:L51–L53, January 1975.

J. J. M. in 't Zand, A. Cumming, M. V. van der Sluys, F. Verbunt, and O. R. Pols. On the possibility of a helium white dwarf donor in the presumed ultracompact binary 2S 0918−549. *A&A*, 441:675–684, October 2005.

J. J. M. in 't Zand, J. Heise, J. M. Muller, A. Bazzano, M. Cocchi, L. Natalucci, and P. Ubertini. Discovery of the X-ray transient SAX J1808.4−3658, a likely low-mass X-ray binary. *A&A*, 331:L25–L28, March 1998.

J. J. M. in 't Zand, M. H. van Kerkwijk, D. Pooley, F. Verbunt, R. Wijnands, and W. H. G. Lewin. Identification of the Optical and Quiescent Counterparts to the Bright X-Ray Transient in NGC 6440. *ApJ*, 563:L41–L44, December 2001.

J. J. M. in 't Zand, F. Verbunt, T. E. Strohmayer, A. Bazzano, M. Cocchi, J. Heise, M. H. van Kerkwijk, J. M. Muller, L. Natalucci, M. J. S. Smith, and P. Ubertini. A new X-ray outburst in the globular cluster NGC 6440: SAX J1748.9−2021. *A&A*, 345:100–108, May 1999.

P. G. Jonker, S. Campana, D. Steeghs, M. A. P. Torres, D. K. Galloway, C. B. Markwardt, D. Chakrabarty, and J. Swank. Chandra observations of the millisecond X-ray pulsar IGR J00291+5934 in quiescence. *MNRAS*, 361:511–516, August 2005.

P. G. Jonker, G. Nelemans, Z. Wang, A. K. H. Kong, D. Chakrabarty, M. Garcia, P. J. Groot, M. van der Klis, T. Kerr, B. Mobasher, M. Sullivan, T. Augusteijn, B. W. Stappers, P. Challis, R. P. Kirshner, J. Hjorth, and A. Delsanti. A search for the optical and near-infrared counterpart of the accreting millisecond X-ray pulsar XTE J1751−305. *MNRAS*, 344:201–206, September 2003.

P. C. Joss. X-ray bursts and neutron-star thermonuclear flashes. *Nature*, 270:310–314, November 1977.

P. C. Joss, Y. Avni, and S. Rappaport. Accreting neutron stars in highly compact binary systems and the nature of 3U 1626−67. *ApJ*, 221:645–651, April 1978.

A. M. Juett and D. Chakrabarty. X-Ray Spectroscopy of the Low-Mass X-Ray Binaries 2S 0918−549 and 4U 1543−624: Evidence for Neon-rich Degenerate Donors. *ApJ*, 599: 498–508, December 2003.

A. M. Juett, D. K. Galloway, and D. Chakrabarty. X-Ray Spectroscopy of the Accreting Millisecond Pulsar XTE J0929−314 in Outburst. *ApJ*, 587:754–760, April 2003.

A. M. Juett, D. Psaltis, and D. Chakrabarty. Ultracompact X-Ray Binaries with Neon-rich Degenerate Donors. *ApJ*, 560:L59–L63, October 2001.

A. M. Juett, N. S. Schulz, and D. Chakrabarty. High-Resolution X-Ray Spectroscopy of the Interstellar Medium: Structure at the Oxygen Absorption Edge. *ApJ*, 612:308–318, September 2004.

A. M. Juett, N. S. Schulz, D. Chakrabarty, and T. W. Gorczyca. High-Resolution X-Ray Spectroscopy of the Interstellar Medium. II. Neon and Iron Absorption Edges. *ApJ*, 648: 1066–1078, September 2006.

P. Kaaret, E. H. Morgan, R. Vanderspek, and J. A. Tomsick. Discovery of the Millisecond X-Ray Pulsar HETE J1900.1−2455. *ApJ*, 638:963–967, February 2006.

P. Kaaret, J. J. M. i. Zand, J. Heise, and J. A. Tomsick. Discovery of X-Ray Burst Oscillations from a Neutron Star X-Ray Transient in the Globular Cluster NGC 6440. *ApJ*, 598:481–485, November 2003.

L. J. Kaluzienski, S. S. Holt, E. A. Boldt, and P. J. Serlemitsos. Recurrent X-ray outbursts from Aquila X-1. *Nature*, 265:606–607, February 1977.

N. Kawai and M. Suzuki. Estimated Distance to HETE J1900.1−2455. *The Astronomer's Telegram*, 534, June 2005.

J. A. Kennea, F. E. Marshall, D. Steeghs, C. Markwardt, D. N. Burrows, M. Torres, J. Miller, S. Hunsberger, J. Nousek, and N. Gehrels. Swift X-ray Spectrum and V-band Upper Limit for XTE J1701−462. *The Astronomer's Telegram*, 704, January 2006.

T. Kii, S. Hayakawa, F. Nagase, T. Ikegami, and N. Kawai. Anisotropic X-ray transfer in a strongly magnetized plasma of the X-ray pulsar 4U 1626−67. *PASJ*, 38:751–774, 1986.

A. R. King, U. Kolb, and L. Burderi. Black Hole Binaries and X-Ray Transients. *ApJ*, 464: L127–L130, June 1996.

W. Kluzniak and R. V. Wagoner. Evolution of the innermost stable orbits around accreting neutron stars. *ApJ*, 297:548–554, October 1985.

K. Koyama, H. Inoue, K. Makishima, M. Matsuoka, T. Murakami, M. Oda, Y. Osgawara, T. Ohashi, N. Shibazaki, Y. Tanaka, F. J. Marshall, I. S. Kondo, S. Hayakawa, H. Kunieda, F. Makino, K. Masai, F. Nagase, Y. Tawara, S. Miyamoto, H. Tsunemi, and K. Yamashita. Discovery of X-ray bursts from Aquila X-1. *ApJ*, 247:L27–L29, July 1981.

J. D. Kraus. *Radio Astronomy*. New York: McGraw-Hill, 1966.

M. I. Krauss and D. Chakrabarty. Why is it Difficult to Find Millisecond X-Ray Pulsars? In *Bulletin of the American Astronomical Society*, page 955, August 2004.

M. I. Krauss, A. Dullighan, D. Chakrabarty, M. H. van Kerkwijk, and C. B. Markwardt. XTE J1814−338. *IAU Circ.*, 8154, June 2003.

M. I. Krauss, Z. Wang, A. Dullighan, A. M. Juett, D. L. Kaplan, D. Chakrabarty, M. H. van Kerkwijk, D. Steeghs, P. G. Jonker, and C. B. Markwardt. The X-Ray Position and Optical Counterpart of the Accretion-powered Millisecond Pulsar XTE J1814−338. *ApJ*, 627:910–914, July 2005.

A. Kubota, Y. Tanaka, K. Makishima, Y. Ueda, T. Dotani, H. Inoue, and K. Yamaoka. Evidence for a Black Hole in the X-Ray Transient GRS 1009−45. *PASJ*, 50:667–673, December 1998.

E. Kuulkers, P. R. den Hartog, J. J. M. in 't Zand, F. W. M. Verbunt, W. E. Harris, and M. Cocchi. Photospheric radius expansion X-ray bursts as standard candles. *A&A*, 399: 663–680, February 2003.

E. Kuulkers, J. J. M. in 't Zand, M. H. van Kerkwijk, R. Cornelisse, D. A. Smith, J. Heise, A. Bazzano, M. Cocchi, L. Natalucci, and P. Ubertini. A half-a-day long thermonuclear X-ray burst from KS 1731−260. *A&A*, 382:503–512, February 2002.

A. U. Landolt. UBVRI photometric standard stars in the magnitude range 11.5–16.0 around the celestial equator. *AJ*, 104:340–371, July 1992.

A. Langmeier, M. Sztajno, G. Hasinger, J. Truemper, and M. Gottwald. EXOSAT observations of 4U 1705−44: Type I bursts and persistent emission. *ApJ*, 323:288–293, December 1987.

A. Levine, C. P. Ma, J. McClintock, S. Rappaport, M. van der Klis, and F. Verbunt. 4U 1626−67: The binary with the smallest known mass function. *ApJ*, 327:732–741, April 1988.

F. K. Li, J. E. McClintock, S. Rappaport, E. L. Wright, and P. C. Joss. 4U 1626−67 and the character of highly compact binary X-ray sources. *ApJ*, 240:628–635, September 1980.

D. Lin, R. A. Remillard, and J. Homan. Evaluating Spectral Models and the X-ray States of Neutron-Star X-ray Transients. *ApJ*, submitted. astro-ph/0702089, February 2007.

M. Linares, M. van der Klis, D. Altamirano, and C. B. Markwardt. Discovery of Kilohertz Quasi-periodic Oscillations and Shifted Frequency Correlations in the Accreting Millisecond Pulsar XTE J1807−294. *ApJ*, 634:1250–1260, December 2005.

Q. Z. Liu, J. van Paradijs, and E. P. J. van den Heuvel. A catalogue of low-mass X-ray binaries. *A&A*, 368:1021–1054, March 2001.

J. C. Lochner and D. Roussel-Dupre. Recurrence times and periodicities in 4U 1608−52 as observed by VELA 5B. *ApJ*, 435:840–847, November 1994.

R. A. London, W. M. Howard, and R. E. Taam. The spectra of X-ray bursting neutron stars. *ApJ*, 287:L27–L30, December 1984.

T. J. Maccarone and P. S. Coppi. Hysteresis in the light curves of soft X-ray transients. *MNRAS*, 338:189–196, January 2003a.

T. J. Maccarone and P. S. Coppi. Spectral fits to the 1999 Aql X-1 outburst data. *A&A*, 399:1151–1157, March 2003b.

D. Maitra and C. Bailyn. Near-Infra-Red Observations of XTE J1701−462 using SMARTS. *The Astronomer's Telegram*, 712, January 2006.

D. Maitra, C. Bailyn, J. Nelan, and J. Espinoza. Optical Counterpart of J1701−462. *The Astronomer's Telegram*, 706, January 2006.

D. Maitra and C. D. Bailyn. Evolution of Spectral States of Aquila X-1 during the 2000 Outburst. *ApJ*, 608:444–453, June 2004.

T. H. Markert, D. E. Backman, C. R. Canizares, G. W. Clark, and A. M. Levine. Observations of X rays from near NGC6440. *Nature*, 257:32–33, September 1975.

T. H. Markert, F. N. Laird, G. W. Clark, D. R. Hearn, G. F. Sprott, F. K. Li, H. V. Bradt, W. H. G. Lewin, H. W. Schnopper, and P. F. Winkler. The MIT/OSO 7 catalog of X-ray sources: Intensities, spectra, and long-term variability. *ApJS*, 39:573–632, April 1979.

S. Markoff, M. A. Nowak, and J. Wilms. Going with the Flow: Can the Base of Jets Subsume the Role of Compact Accretion Disk Coronae? *ApJ*, 635:1203–1216, December 2005.

C. B. Markwardt, D. K. Galloway, D. Chakrabarty, E. H. Morgan, and T. E. Strohmayer. Orbit Solution for the Millisecond Pulsar IGR J00291+5934. *The Astronomer's Telegram*, 360, December 2004a.

C. B. Markwardt, M. Juda, and J. H. Swank. XTE J1807−294. *IAU Circ.*, 8095, March 2003a.

C. B. Markwardt, E. Smith, and J. H. Swank. XTE J1807−294. *IAU Circ.*, 8080, February 2003b.

C. B. Markwardt, T. E. Strohmayer, and J. H. Swank. Revised Orbit and Burst Oscillations from the Millisecond Pulsar XTE J1814−338. *The Astronomer's Telegram*, 164, June 2003c.

C. B. Markwardt and J. H. Swank. XTE J1814−338. *IAU Circ.*, 8144, June 2003.

C. B. Markwardt, J. H. Swank, and T. E. Strohmayer. IGR J00291+5934 is a 598 Hz X-ray Pulsar. *The Astronomer's Telegram*, 353, December 2004b.

C. B. Markwardt, J. H. Swank, T. E. Strohmayer, J. J. M. in 't Zand, and F. E. Marshall. Discovery of a Second Millisecond Accreting Pulsar: XTE J1751−305. *ApJ*, 575:L21–L24, August 2002.

H. L. Marshall, R. E. Rothschild, and W. A. Heindl. High Resolution X-ray Spectra of Bursts from GS 1826-238. In *Bulletin of the American Astronomical Society*, volume 34, December 2002.

H. L. Marshall, A. Tennant, C. E. Grant, A. P. Hitchcock, S. L. O'Dell, and P. P. Plucinsky. *Composition of the Chandra ACIS contaminant*. In K. A. Flanagan and O. H. W. Siegmund, editors, X-Ray and Gamma-Ray Instrumentation for Astronomy XIII. Proceedings of the SPIE, Volume 5165, pages 497–508, February 2004.

J. E. McClintock, H. V. Bradt, R. E. Doxsey, J. G. Jernigan, C. R. Canizares, and W. A. Hiltner. Optical candidates for two X-ray bursters and an X-ray pulsar. *Nature*, 270: 320–321, November 1977.

J. E. McClintock, F. K. Li, C. R. Canizares, and J. E. Grindlay. Simultaneous X-ray and optical observations of the 7.7 second X-ray pulsar 4U 1626−67. *ApJ*, 235:L81–L85, January 1980.

P. Meszaros, W. Nagel, and J. Ventura. Exact and approximate solutions for the one-dimensional transfer of polarized radiation, and applications to X-ray pulsars. *ApJ*, 238: 1066–1080, June 1980.

J. Middleditch, K. O. Mason, J. E. Nelson, and N. E. White. 4U 1626−67: A prograde spinning X-ray pulsar in a 2500 s binary system. *ApJ*, 244:1001–1021, March 1981.

S. Migliari, R. Fender, and M. Méndez. Iron Emission Lines from Extended X-ray Jets in SS 433: Reheating of Atomic Nuclei. *Science*, 297:1673–1676, September 2002.

S. Migliari and R. P. Fender. Jets in neutron star X-ray binaries: a comparison with black holes. *MNRAS*, 366:79–91, February 2006.

S. Migliari, R. P. Fender, M. Rupen, P. G. Jonker, M. Klein-Wolt, R. M. Hjellming, and M. van der Klis. Disc-jet coupling in an atoll-type neutron star X-ray binary: 4U 1728−34 (GX 354-0). *MNRAS*, 342:L67–L71, July 2003.

S. Migliari, R. P. Fender, and M. van der Klis. Correlation between radio luminosity and X-ray timing frequencies in neutron star and black hole X-ray binaries. *MNRAS*, 363: 112–120, October 2005.

R. P. Mignani, S. Chaty, I. F. Mirabel, and S. Mereghetti. The infrared counterpart of the X-ray burster KS 1731−260. *A&A*, 389:L11–L14, July 2002.

J. M. Miller, R. Wijnands, M. Méndez, E. Kendziorra, A. Tiengo, M. van der Klis, D. Chakrabarty, B. M. Gaensler, and W. H. G. Lewin. XMM-Newton Spectroscopy of the Accretion-driven Millisecond X-Ray Pulsar XTE J1751−305 in Outburst. *ApJ*, 583:L99–L102, February 2003.

I. F. Mirabel, R. Bandyopadhyay, P. A. Charles, T. Shahbaz, and L. F. Rodriguez. The Superluminal Source GRS 1915+105: A High Mass X-Ray Binary? *ApJ*, 477:L45–L48, March 1997.

K. Mitsuda, H. Inoue, K. Koyama, K. Makishima, M. Matsuoka, Y. Ogawara, K. Suzuki, Y. Tanaka, N. Shibazaki, and T. Hirano. Energy spectra of low-mass binary X-ray sources observed from TENMA. *PASJ*, 36:741–759, 1984.

K. Mitsuda, H. Inoue, N. Nakamura, and Y. Tanaka. Luminosity-related changes of the energy spectrum of X1608−522. *PASJ*, 41:97–111, 1989.

D. G. Monet, S. E. Levine, B. Canzian, H. D. Ables, A. R. Bird, C. C. Dahn, H. H. Guetter, H. C. Harris, A. A. Henden, S. K. Leggett, H. F. Levison, C. B. Luginbuhl, J. Martini, A. K. B. Monet, J. A. Munn, J. R. Pier, A. R. Rhodes, B. Riepe, S. Sell, R. C. Stone, F. J. Vrba, R. L. Walker, G. Westerhout, R. J. Brucato, I. N. Reid, W. Schoening, M. Hartley, M. A. Read, and S. B. Tritton. The USNO-B Catalog. *AJ*, 125:984–993, February 2003.

M. P. Muno, D. Chakrabarty, D. K. Galloway, and P. Savov. Millisecond Oscillations and Photospheric Radius Expansion in Thermonuclear X-Ray Bursts. *ApJ*, 553:L157–L160, June 2001.

M. P. Muno, D. W. Fox, E. H. Morgan, and L. Bildsten. Nearly Coherent Oscillations in Type I X-Ray Bursts from KS 1731−260. *ApJ*, 542:1016–1033, October 2000.

M. P. Muno, F. Özel, and D. Chakrabarty. The Energy Dependence of Millisecond Oscillations in Thermonuclear X-Ray Bursts. *ApJ*, 595:1066–1076, October 2003.

M. P. Muno, R. A. Remillard, and D. Chakrabarty. How Do Z and Atoll X-Ray Binaries Differ? *ApJ*, 568:L35–L39, March 2002.

T. Murakami, H. Inoue, K. Koyama, K. Makishima, M. Matsuoka, M. Oda, Y. Ogawara, T. Ohashi, F. Makino, N. Shibazaki, Y. Tanaka, S. Hayakawa, H. Kunieda, F. Nagase, K. Masai, Y. Tawara, S. Miyamoto, H. Tsunemi, K. Yamashita, and I. Kondo. Discovery of two new X-ray burst sources XB1812−12 in Serpens and XB1940−04 in Aquila. *PASJ*, 35:531–537, 1983.

N. Nakamura, T. Dotani, H. Inoue, K. Mitsuda, Y. Tanaka, and M. Matsuoka. TENMA observation of X-ray bursts from X1608−52. *PASJ*, 41:617–639, 1989.

J. A. Nelder and R. Mead. A simplex method for function minimization. *The Computer Journal*, 7:308–313, 1964.

G. Nelemans, P. G. Jonker, and D. Steeghs. Optical spectroscopy of (candidate) ultracompact X-ray binaries: constraints on the composition of the donor stars. *MNRAS*, 370: 255–262, July 2006.

L. A. Nelson, S. A. Rappaport, and P. C. Joss. The evolution of ultrashort period binary systems. *ApJ*, 304:231–240, May 1986.

M. A. Nowak, A. Paizis, J. Wilms, K. Ebisawa, T. J.-L. Courvoisier, J. Rodriguez, R. Walter, M. del Santo, and P. Ubertini. IGR J00291+5934: an observation with Chandra. *The Astronomer's Telegram*, 369, December 2004.

J.-F. Olive, D. Barret, and M. Gierliński. Correlated Timing and Spectral Behavior of 4U 1705−44. *ApJ*, 583:416–423, January 2003.

J. A. Orosz, C. D. Bailyn, and K. Whitman. Infrared Observations of the Neutron Star X-ray Transient KS 1731−260. *The Astronomer's Telegram*, 75, September 2001.

S. Ortolani, B. Barbuy, and E. Bica. The low galactic latitude metal-rich globular cluster NGC 6440. *A&AS*, 108:653–659, December 1994.

A. Owens, T. Oosterbroek, and A. N. Parmar. The complex X-ray spectrum of the low-mass X-ray binary 4U 1626−67. *A&A*, 324:L9–L12, August 1997.

F. Özel and D. Psaltis. Spectral Lines from Rotating Neutron Stars. *ApJ*, 582:L31–L34, January 2003.

B. Paczyński. Gravitational Waves and the Evolution of Close Binaries. *Acta Astronomica*, 17:287–296, 1967.

B. Paczyński. Evolutionary Processes in Close Binary Systems. *ARA&A*, 9:183–208, 1971.

B. Paczynski and R. Sienkiewicz. Gravitational radiation and the evolution of cataclysmic binaries. *ApJ*, 248:L27–L30, August 1981.

A. Paizis, M. A. Nowak, J. Wilms, T. J.-L. Courvoisier, K. Ebisawa, J. Rodriguez, and P. Ubertini. Chandra and RXTE spectroscopy of the accreting msec pulsar IGR J00291+5934. *A&A*, 444:357–363, December 2005.

D. Pooley, W. H. G. Lewin, F. Verbunt, L. Homer, B. Margon, B. M. Gaensler, V. M. Kaspi, J. M. Miller, D. W. Fox, and M. van der Klis. Chandra Observation of the Globular Cluster NGC 6440 and the Nature of Cluster X-Ray Luminosity Functions. *ApJ*, 573:184–190, July 2002.

G. Pooley. IGR J00291+5934 - radio observation. *The Astronomer's Telegram*, 355, December 2004.

R. Popham and R. Sunyaev. Accretion Disk Boundary Layers around Neutron Stars: X-Ray Production in Low-Mass X-Ray Binaries. *ApJ*, 547:355–383, January 2001.

D. Porquet and J. Dubau. X-ray photoionized plasma diagnostics with helium-like ions. Application to warm absorber-emitter in active galactic nuclei. *A&AS*, 143:495–514, May 2000.

S. H. Pravdo, N. E. White, E. A. Boldt, S. S. Holt, P. J. Serlemitsos, J. H. Swank, A. E. Szymkowiak, I. Tuohy, and G. Garmire. HEAO 1 observations of the X-ray pulsar 4U 1626−67. *ApJ*, 231:912–918, August 1979.

W. Priedhorsky. Recurrent Population II X-ray transients—Similarities to SU UMa cataclysmic variables. *Ap&SS*, 126:89–98, October 1986.

J. E. Pringle. Soft X-ray emission from dwarf novae. *MNRAS*, 178:195–202, January 1977.

J. E. Pringle and M. J. Rees. Accretion Disc Models for Compact X-Ray Sources. *A&A*, 21:1–9, October 1972.

D. Psaltis and D. Chakrabarty. The Disk-Magnetosphere Interaction in the Accretion-Powered Millisecond Pulsar SAX J1808.4−3658. *ApJ*, 521:332–340, August 1999.

D. Psaltis and F. K. Lamb. Magnetic Fields of Neutron Stars in Low Mass X-Ray Binaries. In N. Shibazaki, editor, *Neutron Stars and Pulsars: Thirty Years After the Discovery*, page 179. Tokyo, Japan: Universal Academy Press, 1998.

S. M. Ransom, S. S. Eikenberry, and J. Middleditch. Fourier Techniques for Very Long Astrophysical Time-Series Analysis. *AJ*, 124:1788–1809, September 2002.

S. Rappaport, P. C. Joss, and R. F. Webbink. The evolution of highly compact binary stellar systems. *ApJ*, 254:616–640, March 1982.

S. Rappaport, T. Markert, F. K. Li, G. W. Clark, J. G. Jernigan, and J. E. McClintock. Discovery of a 7.68 second X-ray periodicity in 3U 1626−67. *ApJ*, 217:L29–L33, October 1977.

S. Rappaport, F. Verbunt, and P. C. Joss. A new technique for calculations of binary stellar evolution, with application to magnetic braking. *ApJ*, 275:713–731, December 1983.

P. Reig, M. Méndez, M. van der Klis, and E. C. Ford. Correlated Timing and Spectral Variations of the Soft X-Ray Transient Aquila X-1: Evidence for an Atoll Classification. *ApJ*, 530:916–922, February 2000.

P. Reig, S. van Straaten, and M. van der Klis. Timing Properties and Spectral States in Aquila X-1. *ApJ*, 602:918–930, February 2004.

R. A. Remillard, D. Lin, the ASM Team at MIT, and NASA/GSFC. New X-ray Transient, XTE J1701−462. *The Astronomer's Telegram*, 696, January 2006.

M. Revnivtsev and R. Sunyaev. A possible 38 day X-ray period of KS 1731−260. *A&A*, 399:699–702, February 2003.

M. P. Rupen, V. Dhawan, and A. J. Mioduszewski. XTE J0929−314. *IAU Circ.*, 7893, May 2002.

M. P. Rupen, V. Dhawan, and A. J. Mioduszewski. Radio detections of SAX J1808.4−3658. *The Astronomer's Telegram*, 524, June 2005.

R. E. Rutledge, L. Bildsten, E. F. Brown, G. G. Pavlov, and V. E. Zavlin. Quiescent Thermal Emission from the Neutron Star in Aquila X-1. *ApJ*, 559:1054–1059, October 2001.

R. E. Rutledge, L. Bildsten, E. F. Brown, G. G. Pavlov, and V. E. Zavlin. Variable Thermal Emission from Aquila X-1 in Quiescence. *ApJ*, 577:346–358, September 2002a.

R. E. Rutledge, L. Bildsten, E. F. Brown, G. G. Pavlov, V. E. Zavlin, and G. Ushomirsky. Crustal Emission and the Quiescent Spectrum of the Neutron Star in KS 1731−260. *ApJ*, 580:413–422, November 2002b.

G. B. Rybicki and A. P. Lightman. *Radiative Processes in Astrophysics*. New York, Wiley-Interscience, 1979.

D. J. Schlegel, D. P. Finkbeiner, and M. Davis. Maps of Dust Infrared Emission for Use in Estimation of Reddening and Cosmic Microwave Background Radiation Foregrounds. *ApJ*, 500:525–553, June 1998.

N. S. Schulz. ROSAT Energy Spectra of Low-Mass X-Ray Binaries. *ApJ*, 511:304–323, January 1999.

N. S. Schulz, D. Chakrabarty, H. L. Marshall, C. R. Canizares, J. C. Lee, and J. Houck. Double-peaked X-Ray Lines from the Oxygen/Neon-rich Accretion Disk in 4U 1626−67. *ApJ*, 563:941–949, December 2001.

N. S. Schulz, G. Hasinger, and J. Truemper. Spectral classification of low-mass X-ray binary (LMXB) energy spectra with color-color diagrams. *A&A*, 225:48–68, November 1989.

N. I. Shakura and R. A. Syunyaev. Black holes in binary systems. Observational appearance. *A&A*, 24:337–355, 1973.

S. E. Shaw, N. Mowlavi, J. Rodriguez, P. Ubertini, F. Capitanio, K. Ebisawa, D. Eckert, T. J.-L. Courvoisier, N. Produit, R. Walter, and M. Falanga. Discovery of the INTEGRAL X/γ-ray transient IGR J00291+5934: A Comptonised accreting ms pulsar? *A&A*, 432: L13–L16, March 2005.

K. Shinoda, T. Kii, K. Mitsuda, F. Nagase, Y. Tanaka, K. Makishima, and N. Shibazaki. Discovery of the quasi-periodic oscillations from the X-ray pulsar X1627−673. *PASJ*, 42: L27–L32, April 1990.

J. Smak. On the nature of dwarf novae. *ApJ*, 272:234–237, September 1983.

D. A. Smith, E. H. Morgan, and H. Bradt. Rossi X-Ray Timing Explorer Discovery of Coherent Millisecond Pulsations during an X-Ray Burst from KS 1731−260. *ApJ*, 479: L137–L140, April 1997.

D. Steeghs. XTE J1814−338. *IAU Circ.*, 8155, June 2003.

A. M. Stirling, R. E. Spencer, C. J. de la Force, M. A. Garrett, R. P. Fender, and R. N. Ogley. A relativistic jet from Cygnus X-1 in the low/hard X-ray state. *MNRAS*, 327: 1273–1278, November 2001.

T. Strohmayer and L. Bildsten. New views of thermonuclear bursts, pages 113–156. *Compact stellar X-ray sources*, eds. W. H. G. Lewin and M. van der Klis, April 2006.

T. E. Strohmayer and C. B. Markwardt. Evidence for a Millisecond Pulsar in 4U 1636−53 during a Superburst. *ApJ*, 577:337–345, September 2002.

T. E. Strohmayer, C. B. Markwardt, J. H. Swank, and J. in 't Zand. X-Ray Bursts from the Accreting Millisecond Pulsar XTE J1814−338. *ApJ*, 596:L67–L70, October 2003.

R. Sunyaev, M. Gilfanov, E. Churazov, V. Loznikov, N. Yamburenko, G. K. Skinner, T. G. Patterson, A. P. Willmore, O. Emam, A. C. Brinkman, J. Heise, J. Intzand, and R. Jager. The New X-Ray Transient Burster KS 1731−260. *Soviet Astronomy Letters*, 16:59–62, January 1990.

M. Sztajno, A. Langmeier, J. Frank, J. Trumper, G. Hasinger, W. Pietsch, and J. van Paradijs. U 1705−44. *IAU Circ.*, 4111, September 1985.

H. Tananbaum, L. J. Chaisson, W. Forman, C. Jones, and T. A. Matilsky. UHURU observations of 4U 1608−52: The 'steady' X-ray source associated with the X-ray burst source in Norma. *ApJ*, 209:L125–L130, November 1976.

A. Tarana, A. Bazzano, P. Ubertini, M. Cocchi, D. Götz, F. Capitanio, A. J. Bird, and M. Fiocchi. INTEGRAL high energy behaviour of 4U 1812−12. *A&A*, 448:335–339, March 2006.

G. Telis, F. Paerels, M. Audard, T. Lanz, J. Cottam, M. Mendez, L. Bildsten, P. Chang, and H. Marshall. Chandra High Resolution Spectroscopy of the Burst Spectrum of EXO 0748−67. In *Bulletin of the American Astronomical Society*, volume 36, page 954, August 2004.

J. Thorstensen, P. Charles, and S. Bowyer. The optical counterpart of Aquila X-1 (3U 1908+00). *ApJ*, 220:L131–L134, March 1978.

L. Titarchuk. Generalized Comptonization models and application to the recent high-energy observations. *ApJ*, 434:570–586, October 1994.

L. Titarchuk, W. Cui, and K. Wood. Why Is It Difficult to Detect a Millisecond Pulsar in Neutron Star X-Ray Binaries? *ApJ*, 576:L49–L52, September 2002.

C. A. Tout, P. P. Eggleton, A. C. Fabian, and J. E. Pringle. The evolution of irradiated stars. *MNRAS*, 238:427–438, May 1989.

C. A. Tout, O. R. Pols, P. P. Eggleton, and Z. Han. Zero-age main-seqence radii and luminosities as analytic functions of mass and metallicity. *MNRAS*, 281:257–262, July 1996.

M. J. L. Turner and L. M. Breedon. Spectral and temporal features in bursts from 2S 1636−536 observed with EXOSAT. *MNRAS*, 208:29P–36P, June 1984.

V. Šimon. The properties of outbursts and long-term activity of the soft X-ray transient 4U 1608−52 (QX Nor). *A&A*, 418:617–624, May 2004.

J. van Paradijs. Possible observational constraints on the mass-radius relation of neutron stars. *ApJ*, 234:609–611, December 1979.

J. van Paradijs. On the Accretion Instability in Soft X-Ray Transients. *ApJ*, 464:L139–L141, June 1996.

J. van Paradijs and J. E. McClintock. Optical and Ultraviolet Observations of X-ray Binaries, page 58. *X-ray Binaries*, eds. W.H.G. Lewin, J. van Paradijs, and E.P.J. van den Heuvel (Cambridge: Cambridge Univ. Press), 1995.

S. van Straaten, M. van der Klis, and R. Wijnands. Relations Between Timing Features and Colors in Accreting Millisecond Pulsars. *ApJ*, 619:455–482, January 2005.

R. Vanderspek, E. Morgan, G. Crew, C. Graziani, and M. Suzuki. Possible new X-ray burst source detected by HETE. *The Astronomer's Telegram*, 516, June 2005.

F. Verbunt, T. Belloni, H. M. Johnston, M. van der Klis, and W. H. G. Lewin. ROSAT observations of soft X-ray transients in quiescence. *A&A*, 285:903–911, May 1994.

F. Verbunt, M. H. van Kerkwijk, J. J. M. in 't Zand, and J. Heise. X-ray and optical follow-up observations of the August 1998 X-ray transient in NGC 6440. *A&A*, 359:960–966, July 2000.

F. Verbunt, R. A. M. J. Wijers, and H. M. G. Burm. Evolutionary scenarios for the X-ray binary pulsars 4U 1626−67 and Hercules X-1, and their implications for the decay of neutron star magnetic fields. *A&A*, 234:195–202, August 1990.

A. R. Villarreal and T. E. Strohmayer. Discovery of the Neutron Star Spin Frequency in EXO 0748−676. *ApJ*, 614:L121–L124, October 2004.

W. Voges, B. Aschenbach, T. Boller, H. Bräuninger, U. Briel, W. Burkert, K. Dennerl, J. Englhauser, R. Gruber, F. Haberl, G. Hartner, G. Hasinger, M. Kürster, E. Pfeffermann, W. Pietsch, P. Predehl, C. Rosso, J. H. M. M. Schmitt, J. Trümper, and H. U. Zimmermann. The ROSAT all-sky survey bright source catalogue. *A&A*, 349:389–405, September 1999.

S. D. Vrtilek, J. C. Raymond, M. R. Garcia, F. Verbunt, G. Hasinger, and M. Kurster. Observations of Cygnus X-2 with IUE: Ultraviolet results from a multiwavelength campaign. *A&A*, 235:162–173, August 1990.

S. Wachter, D. W. Hoard, C. D. Bailyn, S. Corbel, and P. Kaaret. A Closer Look at the Soft X-Ray Transient X1608−52: Long-Term Optical and X-Ray Observations. *ApJ*, 568: 901–911, April 2002.

I. Waki, H. Inoue, K. Koyama, M. Matsuoka, T. Murakami, Y. Ogawara, T. Ohashi, Y. Tanaka, S. Hayakawa, Y. Tawara, S. Miyamoto, H. Tsunemi, and I. Kondo. Discovery of absorption lines in X-ray burst spectra from X1636−536. *PASJ*, 36:819–830, 1984.

Z. Wang and D. Chakrabarty. Private communication, 2002.

Z. Wang, D. Chakrabarty, P. Roche, P. A. Charles, E. Kuulkers, T. Shahbaz, C. Simpson, D. A. Forbes, and S. F. Helsdon. The Optical Counterpart of the Accreting Millisecond Pulsar SAX J1808.4−3658 in Outburst: Constraints on the Binary Inclination. *ApJ*, 563: L61–L64, December 2001.

R. S. Warwick, N. Marshall, G. W. Fraser, M. G. Watson, A. Lawrence, C. G. Page, K. A. Pounds, M. J. Ricketts, M. R. Sims, and A. Smith. The Ariel V (3 A) catalogue of X-ray sources—I. Sources at low galactic latitude ($|b| < 10°$). *MNRAS*, 197:865–891, December 1981.

R. S. Warwick, A. J. Norton, M. J. L. Turner, M. G. Watson, and R. Willingale. A survey of the galactic plane with EXOSAT. *MNRAS*, 232:551–564, June 1988.

A. L. Watts and T. E. Strohmayer. The energy dependence of burst oscillations from the accreting millisecond pulsar XTE J1814−338. *MNRAS*, 373:769–780, December 2006.

K. Werner, T. Nagel, T. Rauch, N. J. Hammer, and S. Dreizler. VLT spectroscopy and non-LTE modeling of the C/O-dominated accretion disks in two ultracompact X-ray binaries. *A&A*, 450:725–733, May 2006.

N. E. White, A. Peacock, G. Hasinger, K. O. Mason, G. Manzo, B. G. Taylor, and G. Branduardi-Raymont. A study of the continuum and iron K line emission from low-mass X-ray binaries. *MNRAS*, 218:129–138, January 1986.

N. E. White, L. Stella, and A. N. Parmar. The X-ray spectral properties of accretion discs in X-ray binaries. *ApJ*, 324:363–378, January 1988.

R. Wijnands. An XMM-Newton Observation during the 2000 Outburst of SAX J1808.4−3658. *ApJ*, 588:425–429, May 2003.

R. Wijnands, M. Guainazzi, M. van der Klis, and M. Méndez. XMM-Newton Observations of the Neutron Star X-Ray Transient KS 1731−260 in Quiescence. *ApJ*, 573:L45–L49, July 2002.

R. Wijnands, J. Homan, C. O. Heinke, J. M. Miller, and W. H. G. Lewin. Chandra Observations of the Accretion-driven Millisecond X-Ray Pulsars XTE J0929−314 and XTE J1751−305 in Quiescence. *ApJ*, 619:492–502, January 2005.

R. Wijnands, J. M. Miller, C. Markwardt, W. H. G. Lewin, and M. van der Klis. A Chandra Observation of the Long-Duration X-Ray Transient KS 1731−260 in Quiescence: Too Cold a Neutron Star? *ApJ*, 560:L159–L162, October 2001.

R. Wijnands and M. van der Klis. A millisecond pulsar in an X-ray binary system. *Nature*, 394:344–346, 1998.

J. Wilms, A. Allen, and R. McCray. On the Absorption of X-Rays in the Interstellar Medium. *ApJ*, 542:914–924, October 2000.

J. Wilms, A. M. Juett, N. S. Schulz, and M. A. Nowak. In preparation, 2007.

C. A. Wilson, S. K. Patel, C. Kouveliotou, P. G. Jonker, M. van der Klis, W. H. G. Lewin, T. Belloni, and M. Méndez. Chandra Observations of the Faintest Low-Mass X-Ray Binaries. *ApJ*, 596:1220–1228, October 2003.

R. B. Wilson, G. J. Fishman, M. H. Finger, G. N. Pendleton, T. A. Prince, and D. Chakrabarty. *Compton Gamma Ray Observatory*. In M. Friedlander, N. Gehrels, and D. J. Macomb, editors, American Institute of Physics Conference Series, page 291, 1993.

K. S. Wood, J. F. Meekins, D. J. Yentis, H. W. Smathers, D. P. McNutt, R. D. Bleach, H. Friedman, E. T. Byram, T. A. Chubb, and M. Meidav. The HEAO A-1 X-ray source catalog. *ApJS*, 56:507–649, December 1984.

F. Zhang, J. Qu, C. M. Zhang, W. Chen, and T. P. Li. Timing Features of the Accretion-driven Millisecond X-Ray Pulsar XTE J1807−294 in the 2003 March Outburst. *ApJ*, 646:1116–1124, August 2006.

W. Zhang, K. Jahoda, R. L. Kelley, T. E. Strohmayer, J. H. Swank, and S. N. Zhang. Millisecond Oscillations in the Persistent and Bursting Flux of Aquila X-1 during an Outburst. *ApJ*, 495:L9–L12, March 1998.